The Design and Construction of an Experimental MgO Cold Cathode X-ray Tube for Use in XRF Spectrometry

by

Daniel Damjanovic.

Submitted in partial fulfilment of the requirements for the degree of Master of Science in Engineering in the School of Electrical and Electronic Engineering, University of Natal.

Durban. May 2000.

Abstract

An introduction to the fundamental concepts of X-ray physics and X-ray tube design is given. This discussion also includes a brief description of various X-ray tube types available commercially for a number of different industrial applications.

The design of a high-energy MgO cold cathode X-ray tube, which is to be used in an X-ray fluorescence (XRF) spectrometer, is described in detail with emphasis placed on the electron beam focusing mechanism and the theory of operation as well as the construction of the X-ray tube MgO cold cathode, which functioned as the electron emitter of the device. A detailed account is also given of the output characteristics of the X-ray tube power supply, which has a direct effect on the design requirements and consequently the performance of the X-ray tube.

An investigation into the manufacture of the vacuum envelope with particular attention focused on the production of reliable metal-to-ceramic seals was performed. A number of tests were conducted especially with regard to the maximum temperature that such seals may withstand without becoming permanently damaged. These tests were essential, since high temperature gradients tend to develop in an X-ray tube during operation, which the metal-to-ceramic seals of the tube must be capable of withstanding if damage to the device is to be avoided.

The set-up of the XRF spectrometer in which the completed X-ray tube was tested is discussed, in which the X-ray current and voltage measuring techniques are described. Furthermore a detailed account of the operation of the X-ray detector system and the multichannel analyser is given, which was used to detect and record spectra of the sample elements excited by the primary radiation of the X-ray tube.

Finally the measured X-ray tube performance characteristics are discussed and compared to the predicted results.

Preface

The author wishes to certify that the work in this document is his own work, unless specified to the contrary by named or numbered reference.

Acknowledgements

I would like to extend my gratitude to a number of people without whose support the performance of this work would not have been as constructive and enjoyable as it was.

Mr P. A. Thebock who supervised this work, whose often alternative ways of looking at a problem, which he tried to instil in me, led to a lot of thought provoking arguments and discussions, agreements and disagreements. I would also like to thank him for much of the guidance and support he provided throughout the performance of this work.

Professor A. Broadhurst who co-supervised this work, lending a reassuring hand during the completion of this work by helping ensure that this thesis was presented in good time.

Messrs J. Hunt and P. Shannon, the sponsors of this project, without whose financial and moral support its realisation would not have been possible.

Mr C. Booth who as Technical Officer in charge of the Materials Science Laboratory during the first year of this project provided much of his practical experience and technical know-how to manufacture the most intricately detailed parts needed for this project and taught me how to use the laboratory's facilities myself for the construction and testing of the X-ray tube.

Mr P. Hils, who as an academic visitor from the Institute of Thermodynamics at Karlsruhe University, Germany, was involved with the Materials Science Laboratory during the first year of the project providing good company and stimulation.

My parents, for the immense amount of moral support and encouragement during the course of this project.

Contents

1. Introduction.....page 1

2. The Theory of X-ray Tube Design.....page 4

2.1. Introduction.....page 4

2.2. The Definition of X-rays.....page 5

2.3. Emission of Characteristic X-ray Spectra.....page 6

2.4. Electronic States.....page 6

2.5. Critical Excitation Energies.....page 8

2.6. The Nature and Production of X-ray Spectra.....page 9

2.7. Construction of an X-ray Tube.....page 13

2.8. Design Considerations.....page 14

2.9. Excitation Efficiency.....page 16

2.10. Spectral Line Interference.....page 16

2.11. Cooling of the X-ray Tube.....page 17

2.12. Types of X-ray Tubes.....page 17

2.13. Properties of Vacuum.....page 19

2.14. Summary.....page 20

3. The Design of the X-ray Tube and the MgO Cold Cathode.....page 21

3.1. Synthesis of the End-window X-ray Tube.....page 21

3.1.1. Introduction.....page 21

3.1.2. The X-ray Power Supply.....page 22

3.1.3. Positive and Negative Space Charge in a Parallel-Plane Vacuum Diode.....page 25

3.1.4. Focusing of the X-ray Tube Electron Beam.....page 29

3.1.5. Design of the Cathode-Window Structure.....page 36

3.1.6. Design of the Anode and the Effect of the Target Geometry on the Electron and the X-ray Beam.....page 38

3.1.7. The Rating of the X-ray Tube.....page 41

3.1.8. Summary.....page 44

3.2. The Design of the MgO Cold Cathode.....page 46

3.2.1. Introduction.....page 46

3.2.2. Field Emission of Electrons by Solids.....page 47

3.2.3. Electron Emission due to the Schottky Effect.....page 48

3.2.4. Fowler-Nordheim Electron Emission from a Cold Cathode.....page 50

3.2.5. Cold Cathode Electron Emission due to Changing Electric Fields.....page 56

3.2.6. Determination of Current Emission from the MgO Cold Cathode.....page 60

3.2.7. Additional Electron Emission due to X-irradiation of the Cathode....page 65

3.2.8. Definition of Primary, Secondary and Tertiary Fluorescence.....page 67

3.2.9. Calculation of Primary Fluorescence.....page 67

3.2.10. Calculation of Relative Characteristic Line and Continuous Radiation Intensities of Nickel Excited by X-rays from a Tungsten target.....page 74

3.2.11. Effect of X-radiation on further Current Emission from the Cold Cathode.....page 82

3.2.12. Radiation by Moving Charges.....page 98

3.2.13. Summary.....page 102

4. The Construction of the X-ray Tube.....page 103

4.1. Introduction.....page 103

4.2. Metal-to-Ceramic Sealing.....page 103

4.3. Active Alloy Brazing.....page 105

4.4. Stress in Joints due to Thermal Expansion.....page 106

4.5. Thermal Shock.....page 108

4.6. Brazing and Testing of Experimental Metal-to-Ceramic Seals.....page 109

4.7. Assembly of the X-ray Tube.....page 112

4.8. Outgassing.....page 116

4.9. Lead Shielding and High Voltage Insulation of the X-ray Tube.....page 116

4.10. Summary.....page 117

5. The Spectrometer Set-up for the Evaluation of the X-ray Tube.....page 119

5.1. Introduction.....page 119

5.2. Measurement of the X-ray Tube Current and Supply Voltage.....page 120

5.3. Determination of the Photoefficiency of the MgO Cold Cathode.....page 122

5.4. Measurement of the Primary Radiation Intensity Distribution of the X-ray Tube.....page 122

5.5. X-ray Spectra Analysis using the Cold Cathode X-ray Tube.....page 124

5.3.1. The XR-100T-CZT Cadmium Zinc Telluride X-ray Detector.....page 125

5.3.2. The XR-100T Silicon X-ray Detector.....page 127

5.6. Safety and Protective Devices.....page 128

5.7. Summary.....page 130

6. Experimental Results.....page 131

6.1. The X-ray Tube Current and Voltage Characteristics.....page 131

6.2. Determination of the Photoefficiency of the MgO Cold Cathode.....page 132

6.3. Measurement of the Primary Radiation Intensity Distribution of the X-ray Tube.....page 133

6.4. Spectra Analysis using the Cold Cathode X-ray Tube.....page 135

6.4.1. Spectra Analysis with the
XR-100T-CZT Cadmium Zinc Telluride X-ray Detector.....page 135

6.4.2. Spectra Analysis with the
XR-100T Silicon X-ray Detector.....page 138

7. Discussion of Experimental Results .....page 142

7.1. The measured X-ray Tube Current and Voltage.....page 142

7.2. The Photoefficiency of the MgO Cold Cathode.....page 143

7.3. Measurement of the Primary Radiation
Intensity Distribution of the X-ray Tube.....page 143

7.4. Spectra Analysis using the Cold Cathode X-ray Tube.....page 144

8. Conclusion.....page 146

References.....page 148

Appendix 1. Computer Aided Design Drawings of the
Cold Cathode X-ray Tube.....page A-1

Appendix 2. Relative Intensities of the Tungsten Emission Lines
produced by the Cold Cathode X-ray Tube.....page A-6

Appendix 3. Wavelengths of the Principal Emission Lines
and Absorption Edges.....page A-8

Appendix 4. Mass Attenuation Coefficients of the Chemical Elements.....page A-11

Appendix 5. Excitation Energies of the Characteristic Excitation Lines
of Elements of the Periodic Table.....page A-12

Appendix 6. Fluorescent Yields of Elements of the Periodic Table.....page A-16

Appendix 7. Absorption Jump Factors of Elements of the Periodic Table.....page A-17

Appendix 8. Wavelengths of the Absorption Edges.....page A-18

Appendix 9. X-ray Spectra Measurements.....page A-19

List of symbols

A_0, Dushman constant: 1.2×10^{-2} A m^{-2} K^{-2};
B, magnetic field: T;
d, emitter collector distance (m);
e, electron charge: 1.602×10^{-19} C;
E, electric field (Vm^{-1});
E, absolute of electric field (Vm^{-1});
E, energy (Joules);
E_K, kinetic energy (Joules);
h, Planck's constant: 6.62×10^{-34} Js;
$i(t)$, X-ray tube current: A;
i_{AVE}, average X-ray tube current: A;
i_{field}, field current: A;
i_{photo}, photo current: A;
i_{char}, photo current due to characteristic X-radiation: A;
i_{cont}, photo current due to continuous X-radiation: A;
j_S, saturated thermal emission current density: A m^{-2};
j, current density: A m^{-2};
k, Boltzmann's constant: 1.38×10^{-23} J K^{-1};
K, relative dielectric constant;
m, rest mass of an electron: 9.1×10^{-31} kg;
T, absolute temperature (°K);
V, potential difference between emitter and collector (Volts);
ε, dielectric constant;
ε_0, 8.854×10^{-12} F m^{-1};
Φ, work function (eV);
Φ_0, work function in the absence of an exterior electric field acting on e.
σ_S, surface charge density (C m^{-2});
σ, conductivity: S m^{-1};
η, $\frac{e}{m} = 1.759\times10^{11}$ C kg^{-1};
P, power (Watts);
H, power (Watts);
k, thermal conductivity (W m^{-1} K^{-1});
r, distance from axis of electron beam (m);
r_0, cathode radius (m);
z, distance from cathode (m);
F, force (kg m s^{-2});
a, acceleration (m s^{-2});
v, velocity (m s^{-1});
c, speed of light: 3×10^8 m s^{-1};
p, momentum (kg m s^{-1});
p_{rel}, relativistic momentum (kg m s^{-1});
I_0, incident X-radiation intensity;
I_x, transmitted X-radiation intensity;
I_{char}, intensity of characteristic X-radiation;

I_{cont}, intensity of continuous X-radiation or *Bremsstrahlung*;
I_{int}, integral intensity of continuous X-radiation or *Bremsstrahlung*;
λ, wavelength (m);
λ_0, short wavelength limit of spectral distribution (m);
λ_{abs}, wavelength of absorption edge (m);
C, relative element concentration;
Ω, solid angle defined by a collimator;
h, specimen thickness (m);
ψ, incidence angle of primary X-radiation (degrees);
A_G, geometrical factor;
q, collimation factor;
μ, mass attenuation coefficient ($cm^2\ g^{-1}$);
ρ, density ($g\ cm^{-3}$);
θ_{max}, angle of maximum radiation intensity of a moving charge (degrees);

1. Introduction

Fig.1.1: The end-window cold cathode X-ray tube designed and built by the author [56].

Within only a year of Roentgen's discovery of X-rays in 1895 X-rays became widely applied in medical (including dental) and industrial radiography and fluoroscopy. However, the present widespread application of X-ray fluorescence spectrometry took place only once the development and commercial availability of reliable X-ray tubes and generators and electronic detection equipment had been realised for the readout of chemical labelling according to *Thebock, Damjanovic* and *Hils* [55].

In this study the development of a high-energy 85 kV cold cathode end-window X-ray tube capable of exciting elements with relatively high excitation levels, for instance the rare earth metals, is discussed in an attempt to present an improved and more functional alternative to common hot filament X-ray tube designs [56]. Furthermore the importance of the pulsed mode of operation of the cold cathode X-ray tube should not be overlooked either. The conceptualisation of the cold cathode end-window X-ray tube came about as a consequence of the realisation of the following problems associated with conventional hot filament X-ray tubes:

1. Conventional hot filament X-ray tubes are operated in the DC mode. This means that the overall power input to the tube, typically in the range of 2-5 kW [39], leads to a high temperature build-up, since in X-ray tubes no more than one per cent of the power applied to the tube is converted to useful X-radiation with the rest being dissipated as heat. High X-ray tube operating temperatures not only require large cooling systems thereby adding to the overall

tube dimensions to a considerable extent, but also lead to a faster evaporation rate of the target material thus reducing the overall life-time of the tube. According to *Bertin* [24] and *Spatz* and *Lieser* [46] the ideal minimum detection limit of an element can be obtained if the specimen containing that element is irradiated with X-rays having an energy greater than the critical excitation energy of the most energetic Kα characteristic emission line of that element by a factor of between 1.5 and 3.5. This factor has a specific value for each element and tends to increase for elements with higher atomic numbers. This means, that in the case of an X-ray tube operated in the DC mode the energy of the X-radiation will remain constant and so it will only be possible to detect a limited number of elements at minimum detection levels, which obviously poses a limitation on the X-ray tube.

2. The hot filament of a conventional X-ray tube, which, as part of the cathode, functions as the electron source of the tube, has a limited lifetime before filament burnout takes place, which is directly dependent on the gas pressure in the tube. Thus it is important that consistently high vacuum levels be maintained in hot filament X-ray tubes if a fast evaporation rate of the filament material and its consequent burnout is to be avoided. Furthermore in order to operate a hot filament a power supply capable of providing currents in the range of several Ampères is necessary in addition to the high voltage power supply needed to accelerate the electrons emitted by the filament towards the target of the X-ray tube.

In this study the author proposes an alternative solution to the aforementioned shortcomings associated with conventional X-ray tube designs [56]. After introducing the reader to general concepts in X-ray physics and X-ray tube design in Chapter 2, the cold cathode X-ray tube design is described in detail in Chapter 3. The central concept of the cold cathode X-ray tube is the magnesium oxide cold cathode that is used as an electron emitter. Besides the fact that such a cathode emits electrons purely due to the presence of a high potential difference applied across the X-ray tube, which means that a filament power supply discussed earlier becomes completely obsolete, it also requires a pulsed mode of operation for the X-ray tube. According to *Shroff* [2] emission from a cold cathode can be achieved by applying a continuous high voltage across the different layers of the cathode. However, to set off such an emission it is necessary to provide a starter mechanism. In Chapter 3 it is shown that one method of initiating the emission of electrons from a cold cathode is to repetitively apply high voltage pulses across the X-ray tube [56]. The author shows, using Maxwell's equations, that a changing potential with a negative rate of decay and therefore a changing electric field across the X-ray tube, and hence the different dielectric layers of the cold cathode, will create a magnetic field within the cathode which will produce a current in the cathode. Thus by using a pulsed high voltage power supply, which discharges voltage pulses across the X-ray tube in the form of a sawtooth waveform with each pulse having a negative slope, the emission of a current from the cathode can be effected [56]. Furthermore the pulsed mode of X-ray tube operation results in far lower heat dissipation while still providing the necessary high accelerating potential for the emitted electrons. According to *Thebock* [57] each voltage pulse across the X-ray tube will start at 85 kV and then decay to 0 kV, so that the entire range of voltages between these two values will be passed at one time or another during the discharge of a pulse across the tube, and therefore the optimal or minimum detection limit discussed by *Spatz* and *Lieser* [46] for each sample element below tungsten will be obtained at any one instant during the pulse discharge. By using an end-window geometry (see Chapter 3) for the X-ray tube further electron emission from the cold cathode can be obtained by allowing for part of the X-radiation produced at the target of the tube to irradiate the surface of the cathode. In

this way further electrons are photoemitted in addition to the field-emitted electrons. In this way the proposed pulsed end-window X-ray tube promises to operate at lower temperature levels, while at the same time providing a current which is produced as a result of the high voltage pulses applied across the tube and the irradiation of the cathode surface by X-rays. Finally, the limitation of a constant accelerating potential across the X-ray tube as far as the optimal detection limit for only a small number of elements is concerned is removed by discharging voltage pulses across the X-ray tube from 85 kV to 0 kV [56][57].

In Chapter 4 the general assembly considerations are illustrated, where an emphasis is placed on the metal-to-ceramic sealing techniques used to join the metal electrodes of the X-ray tube to its ceramic vacuum envelope to produce vacuum tight seals.

In Chapter 5 the spectrometer set-up for the evaluation of the X-ray tube is discussed. What is of primary interest in the characterisation of an X-ray tube are the characteristic voltage and current waveforms produced in the tube during operation, its photoefficiency as well as the absolute radiation intensity distribution of the tube. The results obtained are listed in Chapter 6 and finally discussed and interpreted in Chapter 7.

2. The Theory of X-ray Tube Design

2.1. INTRODUCTION

The principle of operation of an X-ray tube entails accelerating electrons through a vacuum from a cathode, either in the form of a heated filament or a cold cathode, through a potential V, typically in the range of several kilovolts, towards the target of the X-ray tube. Upon striking the target some of the energy of the electrons, which is directly dependent on the potential, is transformed into X-radiation containing continuous and characteristic line spectra of the target element. The electrode, towards which the electrons are accelerated, constitutes the anode and is placed at a potential that is positive with respect to the electron emitting electrode, namely the cathode. Once electrons strike the target material of the anode the electrons of the atoms in the target are excited to higher energy states and, on their return to their respective atomic shells, emit high energy photons in the form of X-rays. Because the strength of an electric field varies inversely with distance, the forces of repulsion increase in strength the closer the accelerated electrons approach the fields due to the orbital electrons of the target atoms. The accelerated electrons therefore loose kinetic energy very rapidly at the surface of the target, which either consists of a flat piece of a thin heavy metal embedded in the anode or constitutes the entire anode as such, and energy conversion takes place as a result. The kinetic energy of the accelerated electrons is converted in three principal ways [39]:

- A very small fraction, less than 1% in fact, is converted into X-radiation.
- Approximately 99% is converted into heat by increasing the thermal vibration of the atoms of the target material. This results in a temperature increase of the target material, which can be considerable.
- Most, if not all, of the accelerated electrons will have sufficient energy to eject orbital electrons from target atoms. These secondary electrons can escape the target surface and be accelerated back to the target to produce further X-radiation or heat.

Since electrons cannot be sufficiently accelerated in air or a gas, the cathode and the anode have to be sealed in an enclosure capable of maintaining low gas pressure or vacuum. This electrode arrangement, including the vacuum tight enclosure, constitutes an X-ray tube. It is the high potential difference between the cathode and the anode, that produces a high electric field, that accelerates the electrons from the cathode to the anode. The area of the target bombarded by the electrons is known as the focal spot. As will be shown in later chapters the X-ray tube is in fact an electronic vacuum diode, specifically designed to accelerate electrons towards its high potential anode and convert their energy to X-radiation. The following aspects distinguish an X-ray tube from a common vacuum diode:

- The length of the X-ray tube must be such, that arcing between the high potential electrodes both outside and inside of the tube does not take place. This problem can be avoided by producing a vacuum inside the tube as well as embedding it in an insulating medium, so that no arcs can be produced between the electrodes along the envelope of the X-ray tube.

- Because of the relatively high amount of heat generated in the anode of an X-ray tube during operation a cooling system has to be employed to remove this heat sufficiently, so that melting of tube components or thermal damage to the tube does not occur.

- The high potential across the tube and the tube current are parameters, that affect the intensity of the X-radiation produced by the X-ray tube. It is mainly the current that determines the intensity of the X-rays, while the high potential difference across the tube in conjunction with the target material determines the maximum energy that the overall X-radiation can have.

In the following sections of this chapter the theory surrounding X-ray tube design will be discussed after introducing some basic concepts of X-ray physics theory.

2.2. THE DEFINITION OF X-RAYS

Radiation may be defined as energy, in the form of waves or particles, emanating from its source through space in divergent straight lines [25]. However, radiation in the form of charged particles may be deflected from its linear path by electric and/or magnetic fields. All types of radiation have a dual nature in that they exhibit some properties best explained in terms of particles, and other properties best described in terms of waves. Most radiation has either predominantely corpuscular or wave properties, and it is convenient to classify all types of radiation in these two categories.

The corpuscular radiation includes alpha rays, helium nuclei, beta rays, electrons, positrons, positively charged electrons, neutrons and the cosmic rays, which consist of high-energy protons and helium nuclei.

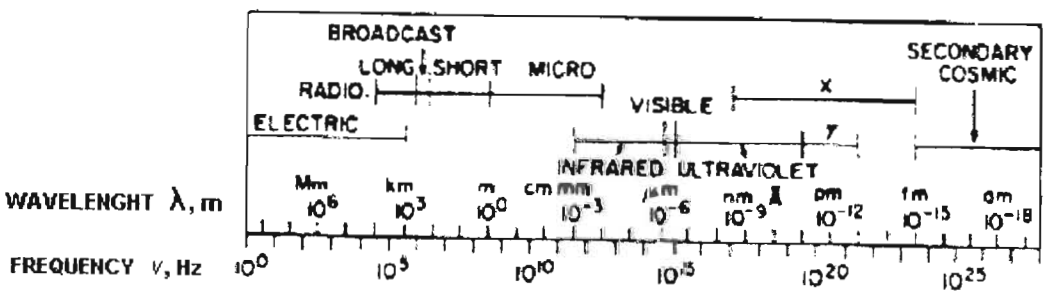

Fig. 2.1: The electromagnetic spectrum [25].

Wave radiation comprises the electromagnetic spectrum, which is divided into overlapping regions, as shown in Figure 2.1. The visible region (4000-7500 Å) is defined by human visual response. The gamma (γ) region comprises high-energy electromagnetic radiation originating in the nuclei of atoms undergoing radioactive decay. Secondary cosmic radiation results from the interaction of

primary cosmic radiation, which is corpuscular in nature, with terrestrial matter. The other spectral regions are defined somewhat arbitrarily on the basis of wavelength, or on the basis of the technology used to generate, produce, transmit, detect and apply the radiation in each region [25].

X-rays may be defined as electromagnetic radiation of wavelength between 10^{-5} and 100 Å produced by deceleration of high-energy electrons and/or by electron transitions in the inner orbits of the atoms.

2.3. EMISSION OF CHARACTERISTIC X-RAY SPECTRA

When a sufficiently energetic X-ray photon interacts with an atom, a transfer of the photon energy to one of the electrons of the atom, for instance a K-shell electron, takes place resulting in the ejection of the electron from the atom as illustrated in Figure 2.2 below

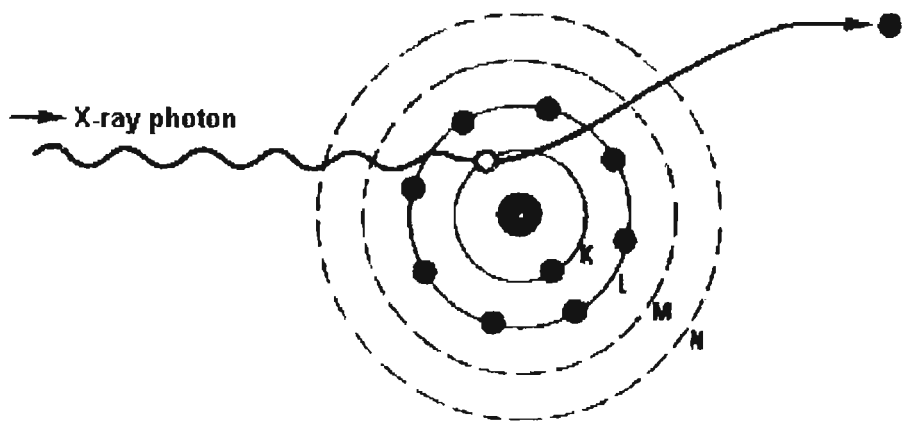

Fig. 2.2: Ionization of the K-shell electron by an incident X-ray photon [22].

After the initial ejection of an electron the vacancy produced in the atomic shell originally occupied by this electron is filled by an outer orbital electron from an outer shell and this transition is accompanied by the emission of a characteristic (fluorescent) X-ray photon with energy equal the difference in the energy between the two shells.

2.4. ELECTRONIC STATES

Except for the K shell of an atom all the other shells are subdivided into several subshells, where each one has its own specific energy value. The energy levels and the number of electrons assigned

to each shell is governed by the quantum theory of atomic structure, which states that every electron in a given atom moves on an orbital characterized by four quantum numbers [22]:

- n is the principal quantum number, or Bohr number, and is associated with successive orbitals. The binding energy between the electron and the nucleus is roughly related to $1/n^2$, where n is a positive integer 1, 2, 3, 4, ... representing the K, L, M, N, ... shells respectively.

- l, the angular quantum number, is a measure of the orbital angular moment which accounts for the existence of elliptic and circular orbitals. $l = 0$ corresponds to a circular orbit.

- m is the magnetic quantum number and can take all the integer values between $-l$ and $+l$, 0 included.

- s, the spin quantum number, can only take two possible values +1/2 and -1/2. s is often represented by + or -.

The Pauli Principle states that there can be no more than one electron in a given electronic state in any given atom. That means that each combination of four quantum numbers is exclusive to one electron [22]. Electronic states are usually designated by symbols containing a number and a letter, for instance 3d. The number designates the principal quantum number n while the letters s, p, d, f, g represent the l values 0, 1, 2, 3, 4, respectively. Thus the symbol 3d identifies the state $n = 3$ and $l = 2$. A small upper index after the letter indicates the number of electrons that have these two quantum numbers. For example $3d^6$ means that there are six electrons with $n = 3$ and $l = 2$. However, these electrons differ between each other by the values of the other two quantum numbers m and s. In Table 2.1 an example of an electron state in the K shell is given. The electrons in a shell do not have exactly the same energy. Their energies are represented by the transition levels in an energy diagram. The transition levels depend on the quantum numbers n and l and the internal or total quantum number j that represents the total (orbital plus spin) angular moment. Accordingly j can take the value of $l + \frac{1}{2}$ or $l - \frac{1}{2}$ with the restriction that j cannot be negative [22]. In Table 2.2 the transition levels are shown in both empirical and quantum notations.

Table 2.1: K shell electron states [22]. The maximum number of electrons is 2, i.e. $1s^2$.

n	1	1
l	0	0
m	0	0
s	+	-
Symbol	1s	1s

Table 2.2: Transition levels [22].

Empirical notation	l	j	Quantum notation
K	0	1/2	$1s_{1/2}$
L_I	0	1/2	$2s_{1/2}$
L_{II}	1	1/2	$2p_{1/2}$
L_{III}	1	3/2	$2p_{3/2}$
M_I	0	1/2	$3s_{1/2}$
M_{II}	1	1/2	$3p_{1/2}$
M_{III}	1	3/2	$3p_{3/2}$
M_{IV}	2	3/2	$3d_{3/2}$
M_V	2	5/2	$3d_{5/2}$
N_I	0	1/2	$4s_{1/2}$
N_{II}	1	1/2	$4p_{1/2}$
N_{III}	1	3/2	$4p_{3/2}$
N_{IV}	2	3/2	$4d_{3/2}$
N_V	2	5/2	$4d_{5/2}$
N_{VI}	3	5/2	$4f_{5/2}$
N_{VII}	3	7/2	$4f_{7/2}$

2.5. CRITICAL EXCITATION ENERGIES

By using the concept of energy levels it is possible to provide a more detailed description of the mechanism of characteristic X-ray emission. For a K electron to be ejected from an atom for instance, the incident photon has to overcome the binding energy E_K between the electron and the nucleus. Hence an incident photon must have an energy equal to or greater than E_K. This condition can be expressed in terms of the quantum energy $h\nu$ of the incident photon as shown below.

$$h\nu \geq E_K \tag{2.1}$$

where h denotes Planck's constant and ν is the photon frequency. In the case of an electron this condition can be expressed in terms of

$$eV \geq E_K \tag{2.2}$$

As shown in Table A5 (Appendix 5) E_K represents the critical excitation energy for an electron in the K shell. Similarly for electrons in the L shell E_K is replaced by E_{LI}, E_{LII} or E_{LIII} depending on the transition level of the ejected electron. The values of these minimum or critical excitation energies are recorded in Table A4 for the K and L shells. In the table the K number for the element W for example is 69.508 indicating that an incident electron must be accelerated to a potential of at least 69.508 kV to remove a K shell electron from the W atom [22]. In the case of excitation by an X-ray photon the latter must also have a minimum energy of

$$E = h\nu = 69.508\,\text{keV} \tag{2.3}$$

which corresponds to a critical wavelength of

$$\lambda = \frac{c}{\nu} = \frac{hc}{E} \approx 0.178\,\text{Å} \tag{2.4}$$

where λ is expressed in Angstrom and E in keV.

2.6. THE NATURE AND PRODUCTION OF X-RAY SPECTRA

The X-ray spectrum produced by electron bombardment of a metallic anode material consists of two parts, called the *continuous* spectrum, *continuum* or *Bremsstrahlung,* and the *characteristic* spectrum. The continuum is always present whenever primary electron radiation has energies within the X-ray band of the electromagnetic spectrum. The characteristic spectrum on the other hand, is only present when the exciting radiation has energies in excess of a critical excitation energy which is uniquely characteristic for each spectral series of each of the elements present in the emitting sample. The continuous spectrum is produced by the deceleration of incident electrons through inelastic collisions with atoms of the target material. Energy lost in each such collision is emitted as an X-ray photon of corresponding energy. Thus if an electron lost 12.4 keV of energy in a single collision, the result would be the emission of an X-ray photon with an energy of 12.4 keV. The proportion of the total energy that such an electron can loose in a collision can range from almost zero for so-called glancing collisions up to a 100 per cent if the total energy is lost in one collision. The X-ray spectrum produced in such a way will therefore consist of a continuous range of energies between the limits of zero on the one hand and the maximum energy of electrons on the other [29]. The maximum emitted X-ray energy will be given by

$$E_{max} = \frac{hc}{\lambda} = E_0 \tag{2.5}$$

where E_0 is the electron accelerating potential expressed in kV. The distribution of radiation between these limits is given by Kramers' formula:

$$I(\lambda)d\lambda = KiZ\left(\frac{\lambda}{\lambda_{min}} - 1\right)\left(\frac{1}{\lambda^2}\right)d\lambda \tag{2.6}$$

where i is the X-ray tube current, Z the mean atomic number of the target and K is a constant. The term $I(\lambda)$ represents the radiation intensity. The wavelength corresponding to the intensity maximum can be obtained by differentiating Kramers' formula:

$$I(\lambda) = KiZ\left(\frac{1}{\lambda}\frac{1}{\lambda_{min}} - \frac{1}{\lambda^2}\right) \tag{2.7}$$

and again,

$$\frac{dI}{d\lambda} = -\left(\frac{KiZ}{\lambda^2 \lambda_{\min}} - \frac{2KiZ}{\lambda^3} \right) \tag{2.8}$$

At the point of inflection $\lambda = \lambda_{\max}$ and $\frac{dI}{d\lambda} = 0$, so that

$$\frac{1}{\lambda_{\min}} = \frac{2}{\lambda_{\max}} \tag{2.9}$$

Therefore the wavelength of maximum intensity will be approximately twice the minimum wavelength. This relationship is only approximate because the continuum actually emitted from the target is considerably modified by self-absorption. This means that some of the X-ray photons are generated at depth within the target and may be absorbed in interaction with the target atoms. Increasing the accelerating potential V on the electrons will have two principal effects [29]:

- The short-wavelength limit of the continuum will shift to shorter wavelengths in accordance with the relationship

$$\lambda_{max} = \frac{hc}{V} \tag{2.10}$$

  where λ_{max} is in Å and V is in kV.

- The wavelength of maximum intensity will also shift towards lower wavelengths.

Since each such electron has more energy to lose in collisions, the intensity of any particular wavelength will also increase as V is increased (see Figure 2.3).

A continuous spectrum is produced whenever energetic electrons interact with matter provided they have energies in the X-ray range. In addition characteristic, or line, spectra are produced whenever the electrons have energies in excess of a critical excitation energy which varies from element to element in the target. In Figure 2.4 the spectra produced from a molybdenum target tube at a range of electron accelerating voltages from 10 to 25 kV is shown. It can be seen that only the continuous spectrum is excited at potentials below 20 kV. At 25 kV two sharp peaks appear, superimposed on the continuum at wavelengths below 1 Å. These lines are called the Kα and Kβ lines for the element Mo. They always appear at identical wavelengths in the spectra from any Mo-bearing samples, providing the accelerating voltage exceeds 20 kV, which is approximately the critical excitation voltage for the Mo spectrum (see Table A5, Appendix 5) [29].

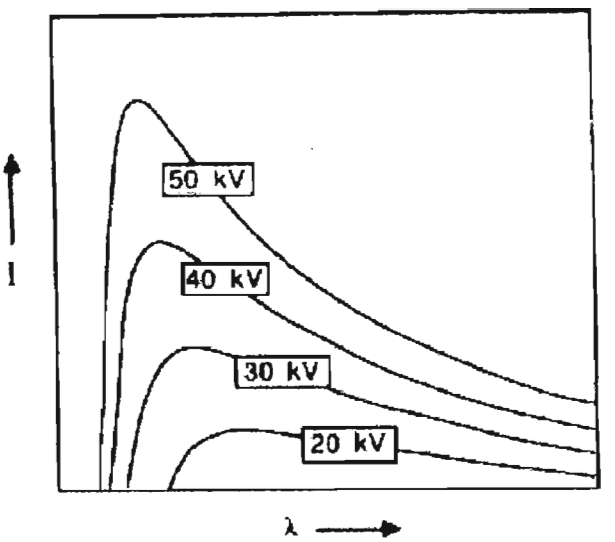

Fig. 2.3: The distributions of continuum intensities produced in an X-ray tube operated at different electron accelerating voltages [29].

The critical excitation voltage for the longer-wavelength, lower-energy Mo L lines spectrum is 2,9 keV. No other element emits identical lines at identical wavelengths. The characteristic spectrum is produced whenever the incident electrons have sufficient energy to excite electrons from the inner subshells of the target atoms to higher-energy orbital levels. Such excitation can take place only to a vacant energy level, which for a ground state atom means excitation beyond the Fermi level. The excited atom is unstable and regains its initial ground state by transfer of high-energy, neighbouring orbital electrons to the temporarily unfilled inner level. Such a transition has a far greater probability of occurring (e.g. $L \rightarrow K = K_{\alpha}$,$M \rightarrow K = K_{\beta}$, $M \rightarrow L = L_{\alpha}$ etc.) than one from an outer level, and has enough energy to produce an X-ray photon. Each such transition releases energy, which is then emitted as an X-ray photon whose energy in turn is equal to the difference between the initial and final energy states of the transferred electron:

$$E_{photon} = E_{initial} - E_{final} \tag{2.11}$$

Thus the wavelength of the emitted photon depends on the energy levels of the electron orbitals of the excited atom, which are quantized and characteristic of each atomic species [29].

To excite a characteristic line of an element the electrons interacting with that element have to have a kinetic energy, whose minimum value should be equal to the critical excitation energy of the characteristic line. Electrons with kinetic energies above that minimum value will also produce an emission of the given characteristic line. However, the detection limit for a characteristic X-ray line of an element will differ according to the accelerating potential applied. *Spatz* and *Lieser* [46]

investigated optimal accelerating potentials that would result in the emission of characteristic lines at minimum detection limits, which are measured in parts per million (ppm), for a number of different elements. In Table 2.3 the excitation potentials at which optimal or minimum detection limits were obtained for the characteristic emission lines of copper, molybdenum, tin and barium are shown. The listed elements were measured in samples consisting of a number of different elements. In Table 2.3 it can be seen, that the optimal excitation potential is roughly 1.5 to 3.5 times greater than the critical excitation potential for elements Cu, Mo, Sn and Ba. It can be seen that with an increasing atomic number of the element in question the optimal excitation potential to critical excitation potential ratio decreases. The findings of *Spatz* and *Lieser* are in accordance with *Bertin* [24], who states that generally the optimal detection limits for an element are obtained, if the electron accelerating potential applied across an X-ray tube is 1.5 to 2 times greater than the K line critical excitation energy of the X-ray tube target element.

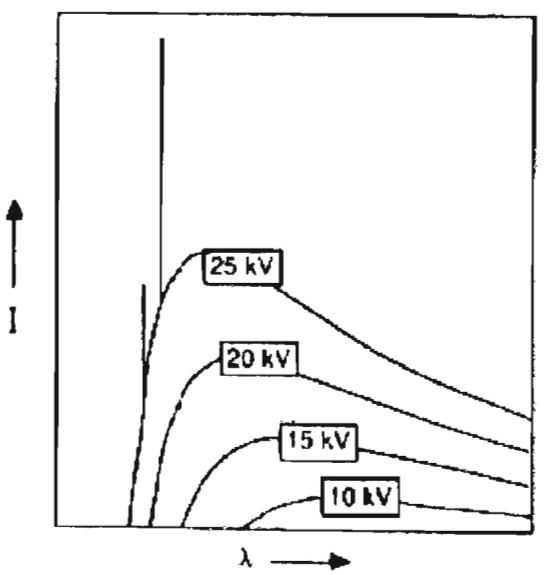

Fig. 2.4: The X-ray spectrum produced from a Mo target at electron accelerating potentials of 10-25 kV [29].

Table 2.3: Optimal excitation potentials for elements Cu, Mo, Sn and Ba [44].

Element	Optimal excitation potential , kV	Critical excitation potential for K line, kV	Ratio of optimal excitation potential to critical excitation potential
Cu	31.00	8.98	3.45
Mo	38.00	20.00	1.90
Sn	44.00	29.20	1.51
Ba	55.00	37.45	1.47

2.7. CONSTRUCTION OF AN X-RAY TUBE

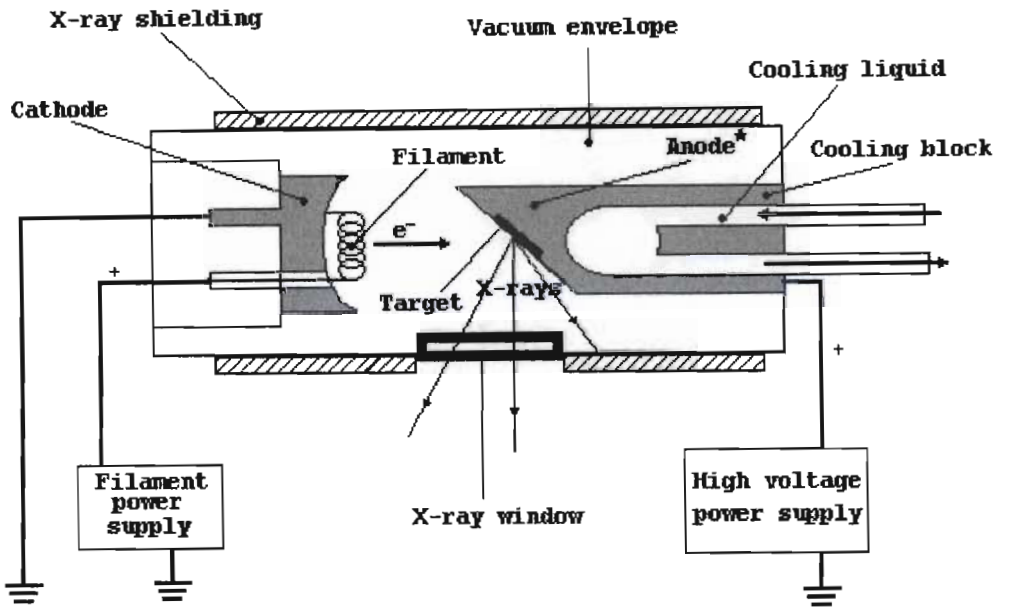

Fig. 2.5: Basic layout of an X-ray tube. The anode consists of the target and cooling block in the diagram.

The X-ray tube generates the primary X-ray beam that irradiates the sample and excites the characteristic line spectrum of its elements. The primary beam consists of the continuum and the spectral lines of the target and other elements contained in the X-ray tube components. The construction of an X-ray spectrometer tube is illustrated in Figure 2.5. The external features consist of a heavy ray proof metal sleeving that confines the X-radiation, a thin X-ray window that

permits emergence of the useful beam, and a glass or ceramic envelope that retains the vacuum in the X-ray tube and provides a long electrical insulation path between the cathode and the anode. The tungsten filament is heated to incandescence by an electric current passed through the filament terminals. The hot filament emits electrons that are roughly focused by a concave focusing electrode and attracted and accelerated to the target, which is operated at a high positive potential [25]. The target consists of a thin piece of metal embedded in a hollow copper block, through which a cooling liquid is circulated during operation to conduct heat away from the focal spot. The focal spot is the area bombarded by the filament electrons. It is the source of the primary X-rays. Target-to-window and target-to-sample distances are measured from the centre of the focal spot. The X-rays are emitted in all directions, but emerge from the metal sleeving only through the X-ray window. The angle between the normal to the window and the target surface is the target angle or anode angle. This angle is usually approximately 20°, so that the solid angle of the useful X-ray beam cone is 40°.

2.8. DESIGN CONSIDERATIONS

An X-ray tube is extremely inefficient. Only about 1% of the power dissipated by the target is converted to X-rays, the other 99% to heat [25]. Consequently the target has to be in close contact with a cooling device, so that the heat developed in the target material can be conducted away as much as possible. The target is typically positioned on a copper cooling block, which is an excellent heat conductor. This cooling block is water or oil cooled as shown in Figure 2.5. Unless the target metal is itself a very good heat conductor, it must be very thin, either a thin disk or plating. This presents no difficulties when it comes to the production of X-rays at the target surface since the electrons accelerated from the cathode penetrate only a very thin layer of the target.

The focal spot is usually very small, so the primary beam is highly divergent. At the target the useful cone subtends an angle of approximately 20° from the central ray. Thus, the primary beam obeys the inverse square law, and if the specimen or sample is to receive high primary intensity, the target-to-specimen, and hence the target-to-window, distance has to be as small as possible. Different manufacturers accomplish this by reducing the diameter of the tube, flattening the window side of the tube, or placing the focal spot, which is the area of the target bombarded by electrons, off axis in the direction of the window [25]. The target surface is inclined to the tube axis toward the window as shown in Figure 2.5. The angle between the target surface and the central ray or the useful primary X-ray cone emerging from the window is the target angle or anode angle and is typically 20°.

The window must be as transparent as possible to the X-rays, especially at the longer wavelengths, which are generated only inefficiently to begin with, and which are most efficient in exciting long-wavelength spectra [25]. The material typically used for such applications is beryllium, which is the most transparent practical window material. With a standard beryllium window thickness of 0.25 mm for instance only 10% of radiation at a wavelength of 5 Å is transmitted, and only 0.1% at a wavelength of 8 Å according to *Bertin* [25]. Beryllium of 25 μm transmits only 20% at 10 Å. Beryllium thinner than 25 μm and free of pinholes is difficult to make. As the atomic number increases, not only does the fraction of incident electrons that scatter increase, but the average angle between the scattered electrons and the target decreases, so that more of them actually strike

the window. The temperature of the window may rise to several hundred degrees centigrade, and, since beryllium is a relatively poor heat conductor, large temperature gradients may develop across its diameter. Thus if the window is too thin it may rupture. The higher the atomic number of the target and the smaller the target-to-window distance, the thicker the window must be. The high atomic number targets, such as molybdenum, tungsten, platinum and gold, have relatively thick windows (1 mm). Such tubes are typically used to excite the higher energy medium to short wavelength spectra, and the windows transmit these wavelengths efficiently. Chromium targets on the other hand are used to excite long wavelength spectra, and so the use of 0.25 mm thick beryllium windows is feasible [25]. Before the introduction of beryllium, however, aluminium was normally employed. Although the transmission characteristics of aluminium are slightly inferior to those of beryllium, it has the advantage of being far simpler to manufacture while at the same time displaying a capability of withstanding much higher temperature gradients across its surface. Bombardment of the window by scattered electrons can be precluded in reverse potential tubes, where the cathode is placed at ground potential and the anode is at the high positive potential. In this way secondary electrons ejected from the target surface are immediately accelerated back to the target due to their negative charges, rather than scattered across the window. Each X-ray tube design has its advantages and limitations. Thin-window tubes have high output flux, especially in the long wavelength region. However, these tubes are more fragile, shorter lived, and expensive, and have little advantage for the K lines of elements heavier than chromium. Tubes having off axis focal spots, side-window tubes in other words (see Figure 2.5), also have high output flux. However, they must be operated at lower power to avoid overheating the window from bombardment by electrons scattered from the nearby focal spot. Also intensity decreases more rapidly with life due to increased deposition of tungsten on the inside of the window. End-window tubes, which are briefly discussed later in this chapter, have the advantage of slower window deterioration due to the aforementioned factors because of a greater target-to-window distance.

The typical cathode assembly of the tube is illustrated in Figure 2.5. The tube shown in Figure 2.5 is an example of a hot cathode X-ray tube. The cathode is firmly sealed into the re-entrant glass or ceramic end of the tube. The cathode itself is typically composed of a nickel plate or focusing cup into which a filament is mounted. The filament is made of fine tungsten wire coiled to form a helix or vertical spiral [39], which allows for a greater electron emitting surface area rather than a straight piece of wire. Tungsten is usually chosen as the filament material because of its high melting point, and so it can be operated at incandescent temperatures without its shape or surface becoming distorted. Compared with other metals with similar melting points, tungsten produces relatively high electron emissions at a given temperature, and has good mechanical strength and physical properties which allow it to be drawn into fine wire and wound into a spiral. Its tendency to vaporize at high temperature is relatively low, and so the filament has a reasonably long lifetime. However, it must be noted, that this is only the case as long as the X-ray tube can maintain high vacuum levels within its vacuum tight glass or ceramic envelope. X-ray tubes are therefore very sensitive to variations in their gas pressure levels, since at higher pressures, or alternatively lower vacuum levels, the rate of vaporization of tungsten becomes significant resulting in a faster rate of filament deterioration.

2.9. EXCITATION EFFICIENCY

X-ray spectral lines of a given series are excited most efficiently by primary radiation having wavelengths near the short-wavelength side of the absorption edge associated with that series [25]. If the X-ray tube target has intense lines near this wavelength, they make the dominant contribution to the excitation. Otherwise, the continuum makes the dominant contribution. Target lines constitute a large portion of the primary spectrum. According to *Bertin* [25] measurements indicate that tungsten L lines constitute approximately 25% of the spectrum of a tungsten target, Cr K lines 75% of the spectrum of a chromium target. Whatever target is used it is therefore highly unlikely that an optimum target for all samples can be obtained. Consequently it is the continuum, which is usually relied on for excitation. When this is the case, given a certain tube excitation potential and current, the higher the atomic number, the more intense the continuum. Incidentally it has been noted, that at a specified X-ray tube current the continuum emerging from tungsten and chromium targets for instance should be the same, rather than proportional to Z, the atomic number of an element. This can be explained by the fact, that the continuum intensity is indeed proportional to the atomic number of the target for a specified electron current from filament to target. However, the X-ray tube current is actually the total electron current flowing within the tube from the filament to all the components connected to ground. As the atomic number of the target increases, an increasing fraction of the electrons arriving at the target is scattered, rather than connected by the target, so that the decreasing fraction is effective in generating the continuum [25]. The target current and the scattered current together constitute the total X-ray tube current. Thus for a high Z target, such as tungsten, a smaller fraction of the electrons is collected by the target, but these electrons generate continuum efficiently. Overall tungsten is probably the most widely used general-purpose target. Its high atomic number results in the generation of intense continuum. It is refractory having a melting point of 3410°C and withstands high target loading without pitting. It has intense L lines that contribute to the excitation of K and L lines of, respectively, germanium (Z 32) and iridium (Z 77) and neighbouring lighter elements. Platinum (Z 78) and gold (Z 79) are substantially equivalent to tungsten except in minor respects. They give a somewhat higher continuum intensity than tungsten. Molybdenum (Z 42) gives only about half the continuum intensity of tungsten, platinum, and gold, but, because of preferential excitation by its K lines, at the same excitation conditions molybdenum is advantageous to the tungsten for the K lines of niobium (Z 41) to arsenic (Z 33) [25]. Other target materials, that give substantially lower continuum intensities than tungsten, platinum and gold, are rhodium, palladium, silver, chromium and aluminium, which are typically used to analyze samples, that contain elements with relatively low critical excitation potentials.

2.10. SPECTRAL LINE INTERFERENCE

The primary spectrum of the X-radiation produced by an X-ray tube not only contains the spectra of the target element, but also the spectra of impurities in the target, spectra arising from the primary excitation of tube components other than the target by improperly focused or scattered electrons and spectra arising from secondary excitation of these components. In the determination of major constituents, especially in high atomic number matrices, scattered primary lines may be tolerable if a suitable way of measuring the background is used. However, if the necessity of measuring minor or trace concentrations of a given element arises, the target of that element should

not be used, and tubes containing lines of that element in their primary spectrum should be avoided. This presents a serious limitation to measuring elements, such as tungsten, iron, chromium, nickel, copper and so on, whose lines are almost always contained in the primary X-radiation of X-ray spectrometer tubes. Another condition that should be avoided if possible is the preferential excitation by target lines of an element having lines that interfere with sample lines [25].

2.11. COOLING OF THE X-RAY TUBE

Because of the high temperature development at the target during the operation of the X-ray tube (see Section 2.8), it is necessary to cool the cooling block and hence the tube by a continuous flow of water or oil typically at a rate of two litres per minute. Usually tap water is passed through the tube and discharged into the drain. The tap water should be filtered to prevent the accumulation of suspended matter in the cooling block. Alternatively the water may be circulated in a closed system. This method has the advantage that distilled or deionized water, rather than tap water, passes through the cooling system of the tube reducing the possibility of corrosion or obstruction. Furthermore, in a reverse potential tube, where the anode is operated at a high potential in the region of several tens of kilovolts, tap water containing ions may become electrically conductive leading to possible spark over in the spectrometer system. Transformer oil pumped through the tube in a closed system offers a better alternative to water due to its better heat conductivity and good electrical isolation properties. Operating the tube at powers exceeding its maximum rating, or within ratings with an inadequate amount of cooling liquid, results in the accelerated deterioration of the target. Operation without a cooling liquid for even a fraction of a minute may result in the complete destruction of the tube.

2.12. TYPES OF X-RAY TUBES

So far the basic functioning of an X-ray tube has been presented using the most common of X-ray tubes as an example, namely the side-window tube. Several other types of tubes, however, are of interest. As opposed to a single target tube, the use of dual target tubes is relatively common. The target of such a tube has two separate areas, one consisting of tungsten, platinum, or molybdenum, the other of chromium for example, and two filaments, each having its focal spot on one of the target areas. The filaments can be energized selectively. Such a tube allows for the high-energy excitation of both long-wavelength and short-wavelength spectra without having to change from one tube to another. However, such tubes generally are far more expensive than single target tubes and the filament power supply must be modified to provide for switching targets. Usually one target wears out more than the other contaminating the other target in the process. When either target of the tube becomes worn or only one of the filaments burns out the tube may be discarded [25].

Demountable tubes on the other hand, prove far more practical when it comes to a longer life-time since many of their components, such as different targets and burnt out filaments, can be easily replaced. Such tubes are continuously pumped during operation. Three excitation modes are feasible with demountable tubes [25]:

1. Primary excitation with the specimen on the target resulting in high sample line intensity.
2. Secondary excitation with the specimen external to the tube.
3. Secondary excitation with the specimen inside the tube and very close to the target.

Demountable tubes are therefore especially advantageous for the secondary excitation of trace samples. A target can be used that has a strong line near the short-wavelength side of the sample absorption edge. High X-ray tube power and thin windows can be used and the sample can be placed inside the tube exciting it to maximum intensity by placing it on the target. However, operation of the tube tends to be cumbersome since there is a need for constant pumping of the tube, and that means that a vacuum pump set-up has to be added to the overall X-ray spectrometer set-up. Another disadvantage is the fact, that there is always a need for dismantling the tube if the specimen has to be placed inside the X-ray tube.

The triode X-ray tube presents an example of a low power X-ray tube, which uses a grid positioned between the cathode and the anode as a third electrode that can be negatively biased to cut off the electron flow between the cathode and the anode. Such a tube is usually employed in energy dispersive X-ray spectrometers, where it is necessary to deal with dead time problems. The first pulse out of the detector can be used to trigger the negative grid bias on the tube. Thus the primary X-rays are immediately turned off and held off during the pulse processing time, so that no secondary X-rays are emitted from the specimen during this time. As soon as the first pulse has been processed and counted, the grid bias is removed and primary X-rays are generated until another pulse emerges from the detector once again restoring the bias [25]. In this way coincidence losses, where the tube pulse misses the detector pulse completely, and pulse pileup are completely eliminated. Tubes of this type may operate at high rates of exposure repetition [39].

The main advantage of a field emission X-ray tube is its cold field emissive cathode, either in the form of a metal point or an oxide cathode, which does not require an additional power supply, as is the case with hot filament X-ray tubes (see Figure 2.5), to energize the cathode. When a high potential is applied between the cathode and the anode or target an extremely high potential gradient is produced in the cold cathode, sufficient to withdraw electrons from the cathode, which then becomes a field emitter. Once electrons are emitted by the cathode they are then accelerated by the electric field between the cathode and the anode towards the target. The chief advantage here is the longer lifetime of the tube. Because the problem of vaporization of the tungsten filament is not existent, the vacuum levels in the tube can be significantly lower than those necessary in thermionic or hot filament tubes. In addition field emission or cold cathode X-ray tubes have longer life-times as the operating life-time of a metal point cold cathode is virtually unlimited. According to *Shroff* [2] the MgO cold cathode on the other hand displays only a slight deterioration in its average current emission capability after an operational time of approximately 10000 hours, which is far longer than the typical overall X-ray tube hot filament life-time of 2000 hours [39]. A serious disadvantage of field emission tubes is that the tube current cannot be varied independently of operating potential [25].

2.13. PROPERTIES OF VACUUM

The ultimate vacuum is defined as the limiting pressure approached in a vacuum chamber after pumping for sufficient time to establish that further reduction in pressure will be negligible [45]. No matter how high or good the vacuum the problem of the presence of rest gases and molecules in vacuum is an ever present one. One of the problems when evacuating a tube is the exhausting not only of the initially free gas molecules, but also the bound gases. The bound gases include adsorbed gasses, chemically combined impurities, permeable walls and virtual leaks produced by small almost closed gaseous pockets embedded in the inner surface of the vacuum chamber. These are the factors, that can significantly affect the degree of vacuum that can be achieved. According to *Smith* [35] it can for instance be shown that in releasing one monolayer of adsorbed gases into a tube maintained at a pressure of 10^{-10} Torr through warming of the tube, the tube pressure can rise to 0,17 Torr. Thus one monolayer of adsorbed gases can take the tube through the entire range of industrial vacua. Some of the effects of poor vacuum in tubes includes internal arcing, electron beam scattering, ion focussing and ion oscillations [19]. In evacuating an electronic vacuum tube the pressure changes from atmospheric pressure to a value as low as 10^{-9} Torr. Thus the pressure is reduced by over eleven orders of magnitude. This very wide pressure variation is usually divided into the following categories [37]:

Table 2.4: Table of practical vacuum ranges [35].

Pressure Range (Torr)	Degree of Vacuum
760 - 25	Low
25 - 10^{-3}	Medium
10^{-3} - 10^{-6}	High
10^{-6} - 10^{-9}	Very high
10^{-9} - 10^{-12}	Ultra high
< 10^{-12}	Extreme high

The unit Torr for pressure is a comparatively old fashioned unit that still remains in use because it is still widely accepted, and hence commonly used in vacuum technology. However, in line with the trend to introduce units which are orderly and consistent an increased use is being made of the conventional SI unit of pressure, the Pascal. One atmosphere is defined as 760 Torr and also as 101.32×10^3 Pascals. Hence 1 Torr is equivalent to 133.32 Pascals. If it is necessary to operate a vacuum tube under conditions of a good vacuum, one has to remove any substance within the tube that may lead to the degradation of the vacuum itself. As already indicated all components of the vacuum tube have different degrees of bound gases, and so it is of utmost importance to pretreat the different components of the X-ray tube prior to its assembly, so that bound gases can be eliminated as much as possible.

2.14. SUMMARY

Before proceeding with an introduction to X-ray tube technology, the reader was first familiarized with some general concepts of X-ray physics. It was shown, that X-radiation can be divided into continuous and characteristic line radiation, of which the former contributes most significantly to the primary radiation produced by an X-ray tube. The generation of X-rays is a highly inefficient process, in which only 1% of the power input to the tube is converted to X-radiation while the rest is dissipated as heat in the tube. It is therefore necessary to continuously cool an X-ray tube in order to avoid damage to the tube. Furthermore when designing an X-ray tube the target material has to be considered carefully. Because of its high melting point tungsten is typically used as a target material for the production of medium to short wavelength radiation. In standard X-ray tube design tungsten filaments are employed as electron emitters. Such tubes are known as thermionic X-ray tubes and represent the most common type of X-ray generating device. In Section 2.12, however, different types of X-ray tubes were presented, and it was shown, that an alternative to thermionic X-ray tubes is the field emission X-ray tube, which uses a cold cathode as an electron source thus eliminating the need for a filament power supply necessary to energize the electron emitter of a thermionic X-ray tube.

3. The Design of the X-ray Tube and the MgO Cold Cathode

3.1. SYNTHESIS OF THE END-WINDOW X-RAY TUBE

3.1.1. INTRODUCTION

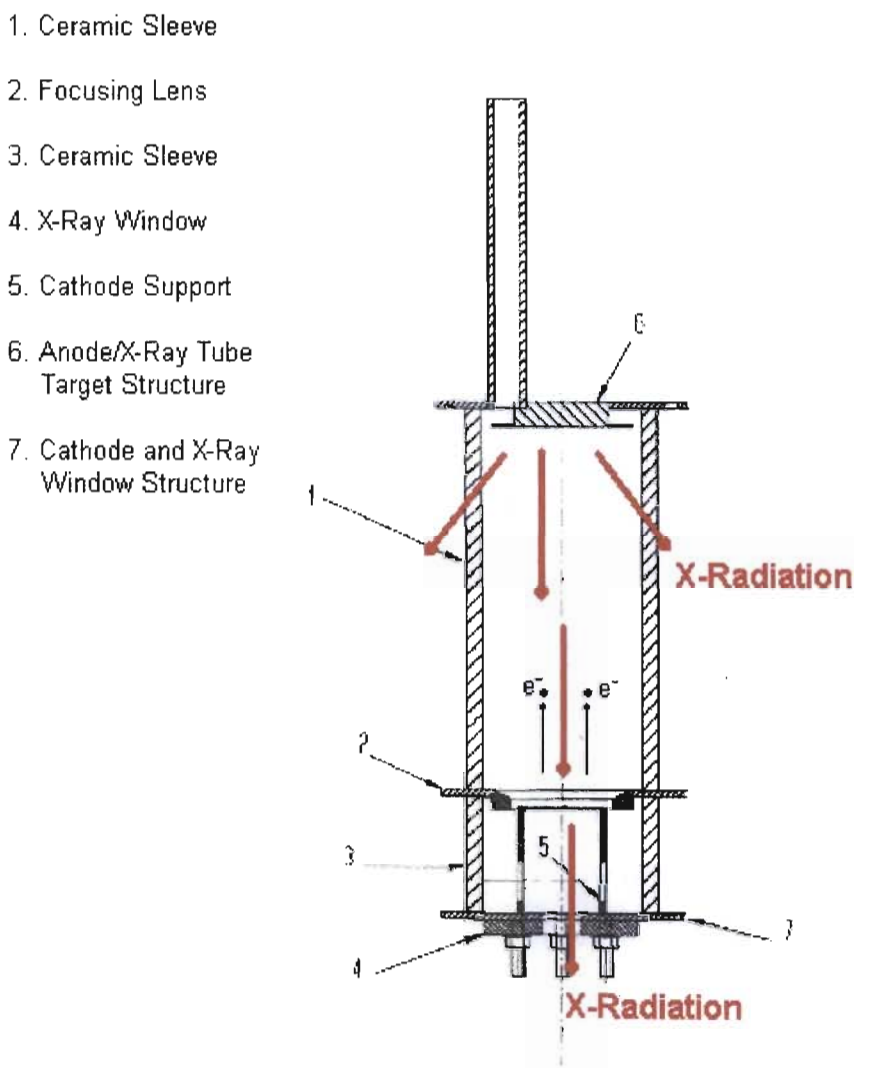

Fig. 3.1.1: Layout of the end-window X-ray tube as proposed by the author, where the directions of electron flow and X-radiation are shown [56].

The principle of operation of an X-ray tube entails accelerating electrons through a vacuum from a cathode, either in the form of a heated filament or, as in our case, a cold cathode, through a potential V towards the target of the X-ray tube. Upon striking the target some of the energy of the electrons, which is directly dependent on the potential, is transformed into X-radiation containing continuous and characteristic line spectra of the target element. It can be seen that the X-ray tube in fact functions in the same way as a vacuum diode. Besides the nature of the application the only significant difference between a vacuum diode and an X-ray tube is the fact, that in the case of an X-ray tube the target material has to be chosen in such a way, that the material required for this component would have to have a high melting point and heat capacity since roughly 99% of the energy applied to the X-ray tube is dissipated as heat in the target while only 1% results in the production of X-rays. Furthermore by selecting a material with a high atomic number radiation of higher energy can be produced at the target, so that a larger range of sample elements with higher radiative energy ranges can be excited. In addition an X-ray tube also incorporates an X-ray window, which functions as the X-ray exit of the tube. In order to transmit as much of the original radiation produced at the target as possible the window material not only needs to be as thin as possible, but also has to have as low an average absorption coefficient as possible.

In the design of the X-ray tube the tube can be treated as a vacuum diode. By using the two-electrode diode as a model for the X-ray tube this chapter, amongst other topics, sets out to document the flow of electrons between parallel plates and the use of an electron focusing method, that allows us to produce a uniform rectilinear electron flow between the cathode and the anode of the X-ray tube [56]. In an end-window X-ray tube design it is desirable to produce parallel electron flow, since upon striking the target the electrons produce X-rays radiating at peak intensity as close to 180° to the direction of the electron flow as possible. The end-window tube structure designed by the author is shown in Figure 3.1.1 and Figure A1a (see Appendix 1), where the direction of electron flow and X-radiation with respect to the X-ray window is clearly illustrated [56]. In describing this type of electron flow emphasis will be placed primarily on the phenomenon of space charge, which will finally lead to the derivation of the three-halves power law dependence of cathode current on applied anode voltage.

3.1.2. THE X-RAY POWER SUPPLY

A very important aspect, that has to be taken into account in the design of the end-window cold cathode X-ray tube, is the characteristic voltage and current output of the power supply, which, together with the X-ray tube, forms the X-ray generating unit of the spectrometer. In this case the power supply provided is capable of producing 85 kV pulses at a frequency of 111 Hz and a duty cycle of 33.3 %. The most important aspect of the power supply output is the pulse shape. Using Maxwell's law the author shows in Section 3.2.5 (Chapter 3.2), that in order to produce a current emission from the cold cathode X-ray tube the voltage and hence the electric field across the dielectric layers of the tube have to have a negative rate of decay, i.e. each voltage pulse has to be discharged across the tube in such a way, that it decays from 85 kV to 0 kV during each pulse (see Section 3.2.5). Furthermore an important aspect of a decaying voltage pulse is the fact, that all accelerating potentials from 0 kV to 85 kV will be discharged across the tube at a particular instant during each pulse. Hence according to *Spatz* and *Lieser* [46] and *Bertin* [24] (see Section 2.6) all sample elements having maximum characteristic excitation potentials between 0 kV and

approximately 70 kV will be excited at their minimum detection limits at a given instant during each pulse (see Section 2.6). In Figure 3.1.2 the voltage output of the power supply is shown.

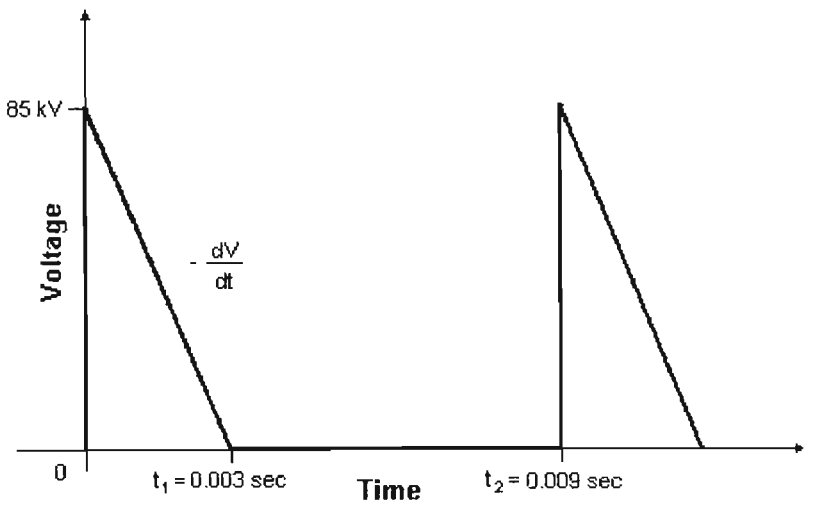

Fig. 3.1.2: Voltage waveform of the X-ray power supply, where t_1 is the pulse duration and t_2 the period.

From the plot in Figure 3.1.2 it can be deduced, that the voltage waveform expressed in terms of time satisfies the following relation:

$$V(t) = -2.83 \times 10^7 t + 8.5 \times 10^4 \text{ Volts} \tag{3.1.2}$$

The average voltage output V_{AVE} is given by the following equation:

$$V_{AVE}(t) = \frac{\int_0^{t_1} V(t)dt}{t_2} \text{ Volts} = \tag{3.1.3}$$

$$\frac{\int_0^{t_1} (-2.83 \times 10^7 t + 8.5 \times 10^4)dt}{t_2} \text{ Volts} =$$

$$\frac{\left[-1.415 \times 10^7 t^2 + 8.5 \times 10^4 t\right]_0^{t_1}}{t_2} \text{ Volts} = 14.183 \text{ kV};$$

where t_1 = 0.003 seconds represents the pulse duration and t_2 = 0.009 seconds is the period of the voltage waveform.

By regarding the X-ray tube as a capacitor it is evident, that the current developing across the tube will increase as the potential across it decreases. However, with the power supply having a current limit of 30 mA, the tube current eventually saturates at that value. In Section 3.2.11 the author predicts, that the tube current will have an approximately square waveform (see Figure 3.2.19, Section 3.2.11) as shown in the figure below.

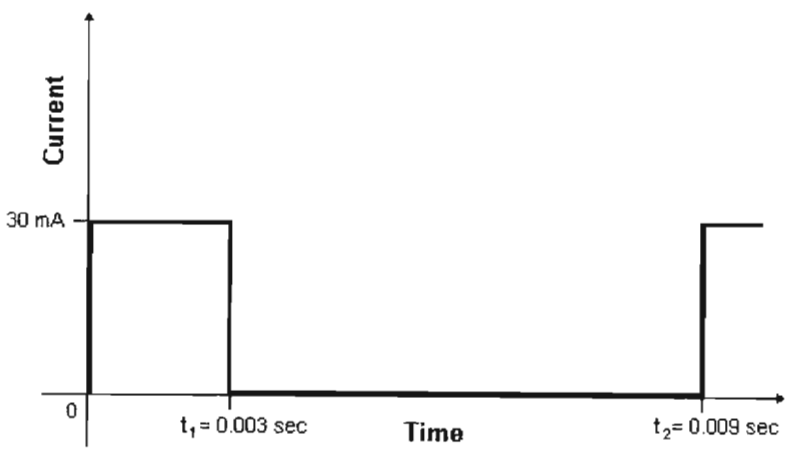

Fig. 3.1.3: The current waveform of the X-ray power supply.

As in the case of the average voltage output of the power supply V_{AVE} the average output current i_{AVE} can be determined using the following relation:

$$i_{AVE}(t) = \frac{\int_0^{t_1} i(t)dt}{t_2} \text{ mA} = \tag{3.1.4}$$

$$\frac{\int_0^{t_1} 30 \cdot dt}{t_2} \text{ mA} =$$

$$\frac{[30t]_0^{t_1}}{t_2}\ \text{mA} = \frac{[30t]_0^{0.003}}{0.009}\ \text{mA} = 10\ \text{mA};$$

Having established the values for the average power supply voltage and current output to the cold cathode X-ray tube the average power output P_{AVE} across the tube, which is the product of V_{AVE} and i_{AVE}, is therefore approximately142 Watts. This value represents the quantity used in the computation of the overall heat dissipation in the tube in the later sections of this chapter.

3.1.3. POSITIVE AND NEGATIVE SPACE CHARGE IN A PARALLEL-PLANE VACUUM DIODE

If we consider a number of electrons being accelerated through a vacuum and take one electron as our particle under consideration, then the free electrons in the vicinity of this particular electron will all contribute to the net force, which acts to move this particle. The field, which exists at the location of a particle, depends upon the positions of neighbouring particles. The motion of these, in turn, depends upon the field. The solution to such a space charge problem is far more complex than the electron-trajectory solution in known fields [33].

The most significant aspect of space-charge flow in a diode is to limit the current drawn from the space-charge limited cathode to a value determined by the three-halves power of the applied voltage and to cause the potential variation within the tube to be non-linear. A practicable approach to the problem of space charge is possible simply because with such multitudes of particles, electrons in this case, no one particular electron is important. The charge, which is concentrated at the locations of the electrons, is considered as though it was smeared out through the region. Using this approximation Poisson's equation and the concept of discrete charges become compatible.

The complexity of the space-charge problem even in geometrically simple situations is illustrated by the parallel-plane diode (see Figure 3.1.5). Let us consider a hypothetical diode consisting of two infinite parallel planes (Figure 3.1.5). If no electrons were present in the space between the planes, a potential difference between the two plates would result in a uniform electric filed. A single electron emitted at the cathode would move toward the anode with constant acceleration. With a large number of emitted electrons, however, the effect on the field becomes significant. The presence of the negative charge between the plates, which is particularly dense near the cathode surface where the electrons move relatively slowly, causes the potential to be lower than it would be otherwise. The electric field is therefore not uniform, and the electron acceleration is not constant [33]. To solve this problem we start with Poisson's equation, which in the one-dimensional case is

$$\frac{d^2V}{dx^2} = -\frac{\rho}{\varepsilon_0} \tag{3.1.5}$$

where V is the potential a distance x from the cathode in Volts and ρ is the charge density in coulombs per cubic metre. The electron velocity v is related to the potential by the equation

$$\frac{1}{2}mv^2 = eV \tag{3.1.6}$$

The continuity equation states, that the space derivative of the product $\rho \cdot v$ is zero under steady state conditions. This means, that the product of ρ and v is constant for all distances x and must be equal to the magnitude of the current density j in Ampères per square metre. By substituting $-j = \rho \cdot v$, where the negative sign is due to the negative charge density, and equation 3.1.6 into equation 3.1.2 results in

$$\frac{d^2V}{dx^2} = \frac{j}{\varepsilon_0}\sqrt{\frac{m}{2eV}} \tag{3.1.7}$$

where m denotes the mass of an electron and e is the charge of an electron.

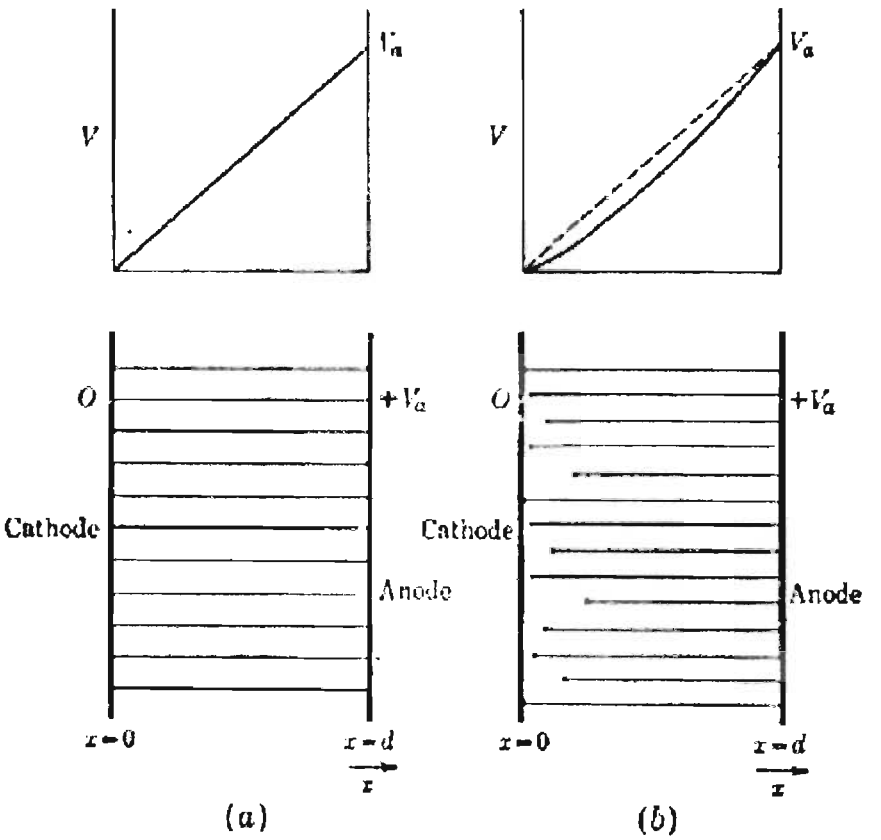

Fig. 3.1.5: Electric lines of force and potential variation with distance in a parallel-plane diode (a) without space charge and (b) with space charge.

To obtain the potential variation within the diode the differential equation (equation 3.1.7) must be solved. This can be achieved by multiplying both sides by $2\frac{dV}{dx}$ and integrating, giving

$$\left(\frac{dV}{dx}\right)^2 = \frac{4j}{\varepsilon_0}\sqrt{\frac{m}{2e}}V^{\frac{1}{2}} + C_1 \tag{3.1.8}$$

The constant of integration C_1 is the square of the value of the electric field at the point where the potential is zero. If we assume an unlimited supply of electrons, this constant may be taken to be zero for the following reason:

With no space charge between the electrodes there exists an accelerating field at the surface of the cathode as is indicated in Figure 3.1.6a. This causes electrons to leave the vicinity of the cathode which, in turn, lowers the potential in the interelectrode space. The rate at which the electrons leave the cathode is limited only by the lowering of the potential near the surface to the point where the electric field at the surface is practically zero (Figure 3.1.6c) [33].

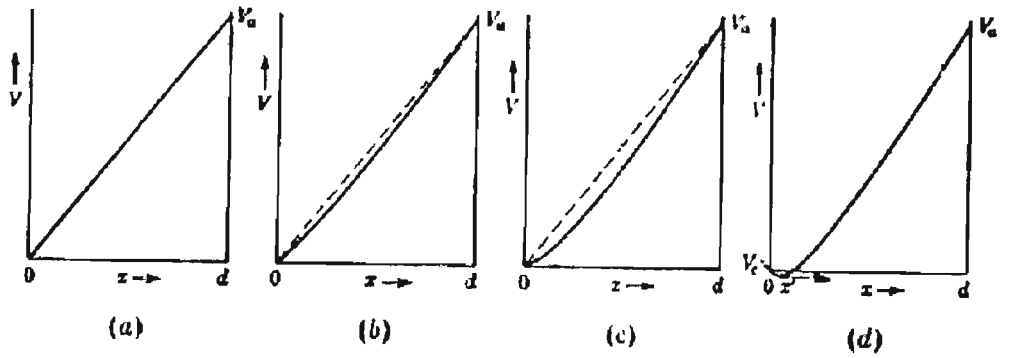

Fig. 3.1.6: Variation of potential with distance in a parallel-plane diode (a) with no space charge, (b) with a limited supply of electrons, (c) with an unlimited supply of zero-initial velocity electrons, and (d) with a space-charge-limited condition but finite initial velocities.

By assuming that the electrons leave the cathode with the same average initial velocity and taking the zero level of potential as corresponding to zero velocity, it can be reasoned, that the cathode has in fact a slight positive potential. In this case space charge will build up until a region of zero potential and zero electric field as shown in Figure 3.1.6d limits the current flow. Such a region is known as a *virtual cathode*[33]. If C_1 is zero we simply take the square root of both sides of equation 3.1.8 and integrate to obtain

$$V^{\frac{3}{4}} = \frac{3}{4}\sqrt{\frac{4j}{\varepsilon_0}\sqrt{\frac{m}{2e}}}x + C_2 \qquad (3.1.9)$$

If $V = 0$ at $x = 0$, C_2 is zero, and so equation 3.1.9 can be rearranged to obtain the following expression for the space charge limited current density

$$j = \frac{4\varepsilon_0}{9}\sqrt{\frac{2e}{m}}\frac{V^{\frac{3}{2}}}{x^2} \qquad (3.1.10)$$

where j is expressed in terms of Ampères per square metre of cathode surface. This is the *Child-Langmuir law* of space-charge-limited flow, which states, that the current varies as the three halves power of the anode potential and inversely as the square of the electrode potential. As will be shown in Section 3.2 the electrons accelerated in the X-ray tube through potentials of up to 85 kV will reach relativistic velocities. According to *Harman* [33] the relativistic form of the *Child-Langmuir law* is

$$j = \frac{4\varepsilon_0}{9}\sqrt{\frac{2e}{m}}\frac{V^{\frac{3}{2}}}{x^2}\left(1 - \frac{3}{28}\frac{V}{V_n}\right) \qquad (3.1.11)$$

where V_n is the normalizing voltage [33] defined by

$$V_n = \frac{mc^2}{e} = 5.11 \times 10^5 \text{ Volts} \qquad (3.1.12)$$

It can therefore be seen, that at high voltages the current will be somewhat reduced from the Child-Langmuir value. This can be explained by the fact that for any given voltage the electron velocity is less than that calculated from nonrelativistic relations. Equation 3.1.11 will enable us to determine the maximum current that the cathode of the X-ray tube will be able to provide. The total current emitted from a cathode of surface area A can be obtained by multiplying the current density j by A:

$$i = \frac{4\varepsilon_0}{9}\sqrt{\frac{2e}{m}}\frac{V^{\frac{3}{2}}}{x^2}\left(1 - \frac{3}{28}\frac{V}{V_n}\right) \cdot A \qquad (3.1.13)$$

where i is the relativistic cathode current in Ampères. The above expression is used in Section 3.2, in which the current emission from the magnesium oxide cold cathode is discussed in order to establish what effect space-charge will have on the maximum emission current of the X-ray tube. By substituting the accelerating potential applied across the X-ray tube, namely $V(t) = -2.83\times10^7 t + 8.5\times10^4$ Volts (see Section 3.1.2), the maximum space charge limited current, that can flow in the tube, can be obtained. In this case equation 3.1.13 can be expressed as follows:

$$i(t) = (-2.83 \times 10^{7} t + 8.5 \times 10^{4})^{\frac{3}{2}} \cdot \left(5.530 \times 10^{-7} t + 9.154 \times 10^{-8}\right) \text{ Volts} \qquad (3.1.14)$$

The space charge limited current, that can be discharged by a vacuum diode, or as is the case here a cold cathode X-ray tube, if a voltage pulse $V(t) = -2.83\times10^{7}t + 8.5\times10^{4}$ Volts is applied across the tube is shown in Figure 3.1.7. It should be noted, that the maximum current values in Figure 3.1.7 do not represent physically attainable tube currents, which are in fact limited by the power supply output current, which is 30 mA (see Section 3.1.2), as well as the current emission capabilities of the cold cathode of the X-ray tube (see Chapter 3.2).

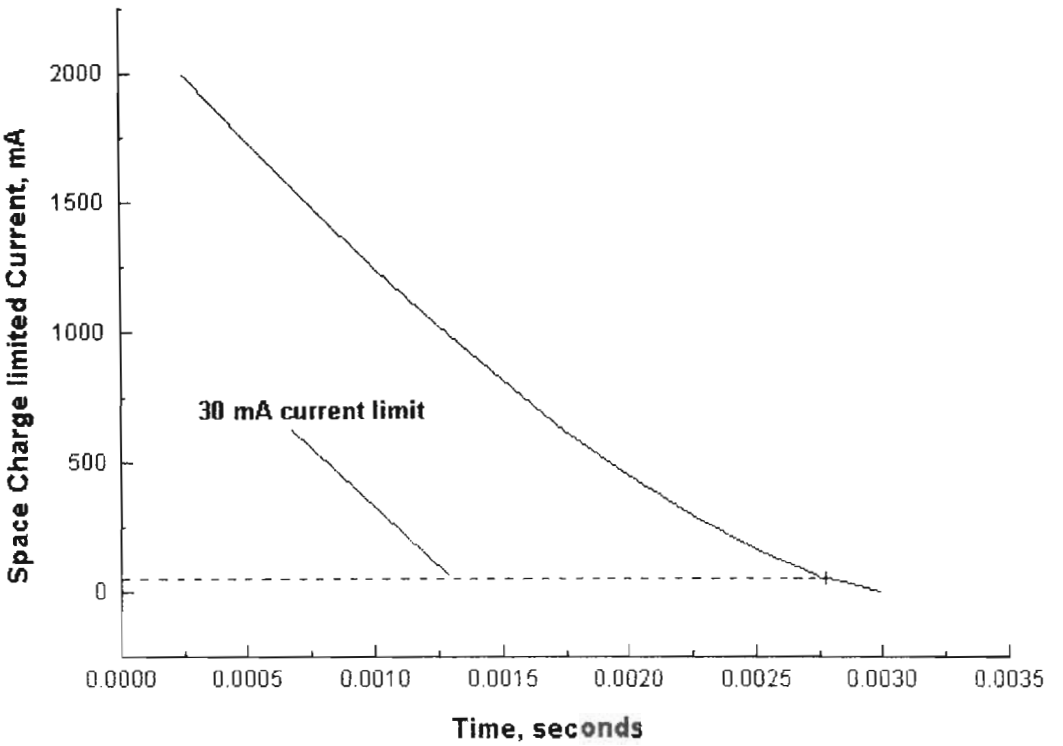

Fig. 3.1.7: Maximum space charge limited current for a voltage pulse of the form $V(t) = -2.83\times10^{7}t + 8.5\times10^{4}$ Volts. The actual physical current limit due to the X-ray tube power supply is indicated by the dashed line.

3.1.4. FOCUSING OF THE X-RAY TUBE ELECTRON BEAM

In order to produce X-radiation of maximum intensity by considering all limitations of the X-ray tube it is necessary for the force acting on the accelerated electrons, that collide with the target to

produce X-ray photons, to be as large as possible. The Newtonian and the relativistic forms of the relations expressing the force F in terms of the electron mass m_e and its acceleration a are shown in equations 3.1.15a and 3.1.15b respectively.

$$F = m_e \cdot a \tag{3.1.15a}$$

$$F = \frac{m_e \cdot a}{\left(1 - \frac{v^2}{c^2}\right)^{\frac{3}{2}}} \tag{3.1.15a}$$

From the above two expressions it can be seen, that the force F is directly proportional to the acceleration a. The kinetic energy E_K of an electron accelerated by a potential V is

$$E_K = eV = \frac{1}{2} m_e \cdot v^2 \tag{3.1.16}$$

where v is the velocity of the charged particle. The velocity v is directly proportional to the accelerating potential V of the tube. If one takes V, the potential of the anode with respect to the cathode, as having a constant value, then the velocity of the electron at the instant of its impact on the target will be constant as well. The acceleration of a particle is the rate at which its velocity changes:

$$a = \frac{dv}{dt} \tag{3.1.17}$$

If dv is to be constant in value the time dt for an electron to travel from the cathode to the anode of the tube will have to be as short as possible in order to produce greater acceleration of the electron and hence a larger force F acting on it.

In this way X-radiation of optimum intensity can be produced at the target of the X-ray tube. For an electron to travel from the cathode to the anode within the shortest possible time it will have to traverse the shortest possible distance d as well. The force F acting on an electron can also be expressed as the product of its charge and the electric field present:

$$F = e\mathrm{E} = e \cdot \frac{V}{d} \tag{3.1.18}$$

Once again it can be seen that by decreasing the distance through which the electron travels the force will increase provided that the term eV in equation 3.1.18 is kept constant. In the proposed X-ray tube design an electron will traverse the shortest distance, if it moves in a direction normal to the surfaces of the cathode and the target (see Figure 3.1.8).

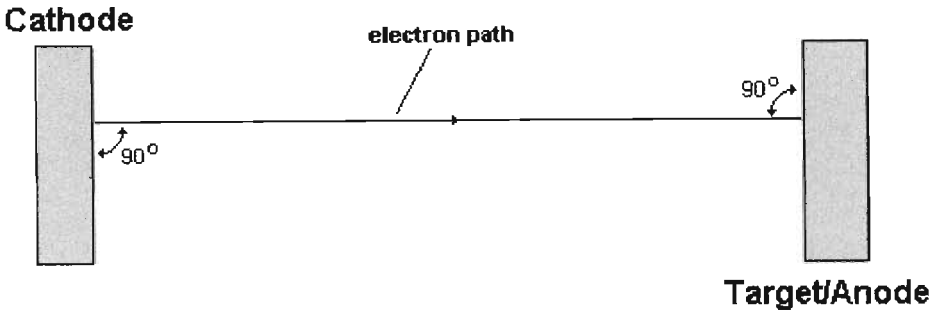

Fig. 3.1.8: The direction of an electron travelling from the cathode to the anode of the X-ray tube.

By taking into account the situation illustrated in Figure 3.1.8 above it is evident, that parallel or rectilinear electron flow will produce X-radiation of optimal intensity. When dealing with electron beams the following two basic problems have to be dealt with [37]:

1. The electrostatic repulsion forces between electrons tend to cause the beam to diverge.

2. The current density required in the electron beam is normally far greater than the emission density of the cathode.

In dealing with the repulsion force problem one should examine the problem of attempting to cause the electrons to travel in parallel paths as they leave the cathode as indicated in Figure 3.1.9.

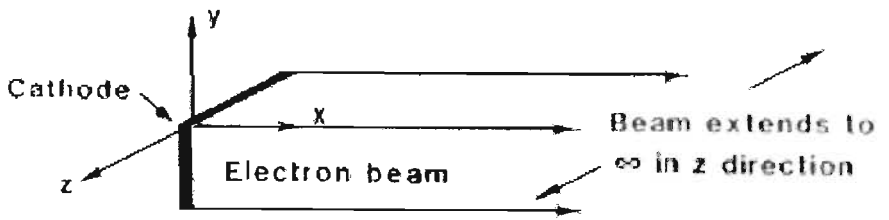

Fig. 3.1.9: Parallel electron flow from a planar cathode [37].

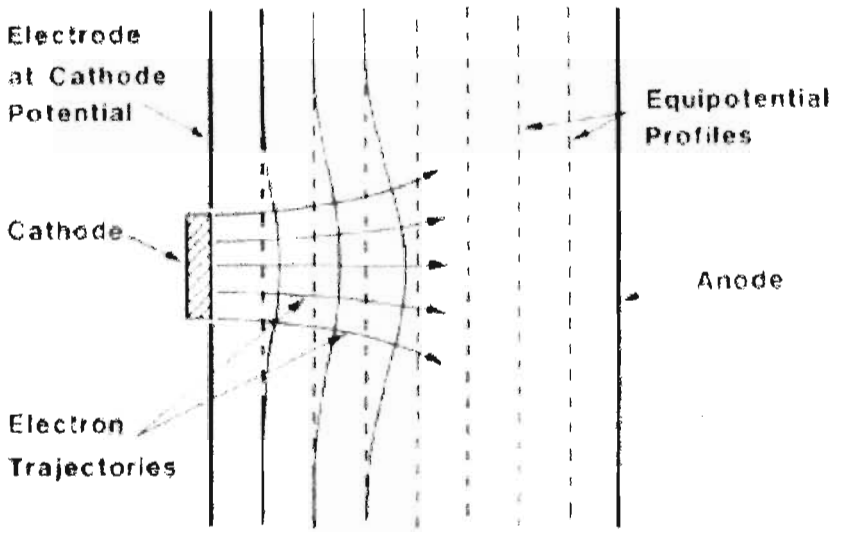

Fig. 3.1.10: Equipotential profiles without (dashed lines) and with (solid lines) electrons [37].

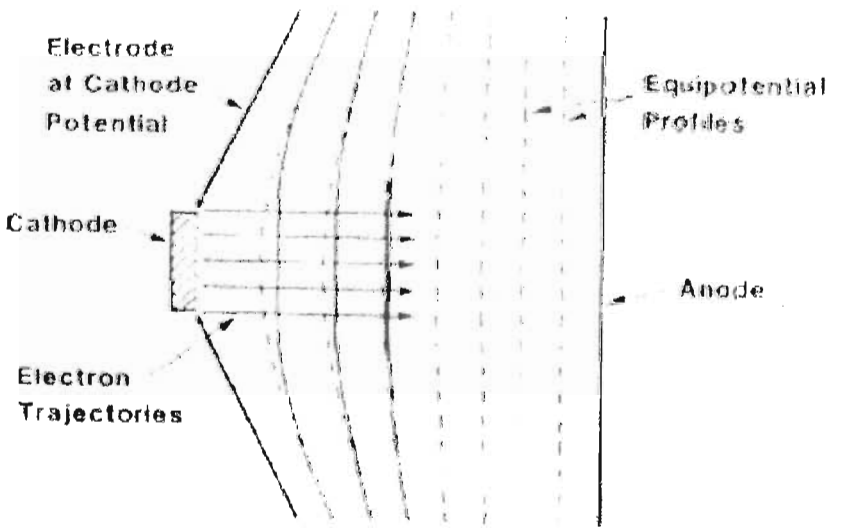

Fig. 3.1.11: Straightening of equipotential profiles in an electron beam [37].

Firstly the equipotential profiles in a parallel-plane diode containing no electrons are parallel and spaced equal distances apart for equal voltage increments. This is shown by the dashed lines in Figure 3.1.10. When electrons are present, however, the equipotential profiles are deflected to the right as indicated by the solid lines. Electrons tend to move perpendicular to the equipotential profiles, so the electron trajectories diverge as the electrons move away from the cathode. This is simply another way of saying that the electrons are pushing on each other and causing their trajectories to diverge [37]. By introducing an electrode arrangement that could straighten the equipotential profiles even though electron space charge forces were present, the electrons could travel along parallel paths. Intuitively it can be seen that if the electrodes adjacent to the cathode are tipped towards the anode, as indicated in Figure 3.1.11, then the equipotential profiles are straightened.

In the absence of electrons the profiles curve toward the cathode. The presence of electron charges causes them to move toward the anode. The mathematical solution that leads to a definition of the electrode configuration for parallel electron flow is similar to the solution for the problem of space-charge-limited flow discussed in Section 3.1.3. The main difference now is that the equations must be solved inside and outside the electron stream, and then the solutions must match at the edge of the beam. The resulting electrode and equipotential profiles for parallel electron flow are given in Figure 3.1.12 [38].

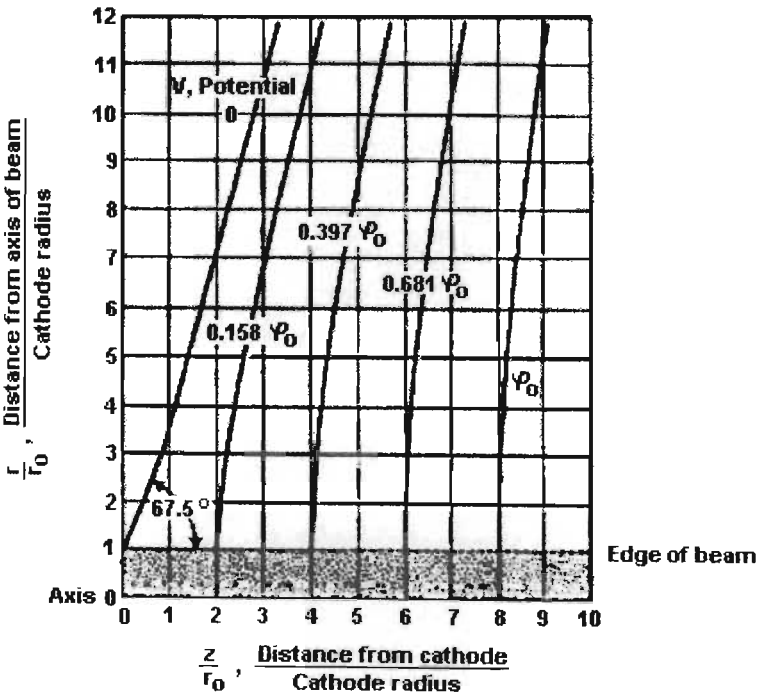

Fig. 3.1.12: Electrodes for obtaining axially symmetrical electron flow of uniform diameter [38].

Figure 3.1.12 shows electrode shapes which were derived by Pierce [36][38] for parallel flow from a space-charge-limited cathode in a cylindrical beam according to equations 3.1.19 and 3.1.20 [36][38]:

$$V = f(x) = Ax^{\frac{4}{3}} \tag{3.1.19}$$

$$A = \left(\frac{9i}{4\varepsilon_0 \left(\frac{2e}{m_e} \right)^{\frac{1}{2}}} \right)^{\frac{2}{3}} = 5.69 \times 10^3 i^{\frac{2}{3}} \tag{3.1.20}$$

where V = the accelerating potential in Volts;
x = the distance travelled by an electron in metres;
i = the tube current in Ampères;
ε_0 = the permittivity of vacuum (8.854×10^{-12} F/m);
e = the charge of an electron (1.602×10^{-19} C);
m_e = the mass of an electron (9.11×10^{-31} kg);

The shape of the equipotentials in Figure 3.1.12 is independent of the absolute magnitude of the potentials involved and of the units in which distance is measured. Therefore, in Figure 3.1.12 potential is indicated in terms of an arbitrary potential, $V = \varphi_o$, assigned to one equipotential potential surface. The potential of the cathode is taken as zero and the distance is measured in arbitrary units, with the origin located at the edge of the cathode. *Pierce* [38] showed that the zero potential surface is a plane which meets the edge of the cathode ($x = y = 0$) making an angle of 67.5° with the normal to the cathode (the x axis). The equipotentials that are remote from the cathode are those which give $V = Ax^{\frac{4}{3}}$ along the axis [38]. In Section 3.1.5 and Chapter 3.2 a cathode radius r_0 of 7 mm is chosen. In Figure 3.1.12 above the term $\frac{z}{r_0}$ denotes the ratio between the electrode-cathode distance and the cathode or beam radius. Obviously the electrode, which is placed at $V = \varphi_o$, is in fact the anode of the tube. Hence with $\frac{z}{r_0} = 8$ and $r_0 = 7$ mm we obtain

$$z = 56 \text{ mm},$$

where z, which is actually equivalent to x, is the distance between the cathode and the anode of the X-ray tube.

We have now not only determined the shape of the focusing electrode, which will be positioned at an angle of 67.5° to the edge of the electron beam at the cathode, but also what the spacing between the cathode and the anode should be in order to achieve rectilinear electron flow. By choosing a ceramic sleeving for the X-ray tube of 25 mm inside diameter we will choose a lens that has an outer diameter of 22 mm, which means that the distance from the axis of the beam to the edge of the lens r (see Figure 3.1.12) is 11 mm. Therefore the ratio $\frac{r}{r_0}$ will be

$$\frac{r}{r_0} = \frac{11\text{ mm}}{7\text{ mm}} \approx 1.57$$

From the graph in Figure 3.1.12 we can see, that at that value the anode will have virtually no curvature.

In Figure 3.1.13 the relative positions of the focusing electrode, the anode and the cathode with respect to each other are illustrated [56]. To complete the synthesis of the X-ray tube it is now necessary to proceed with the design of the cathode, the anode and the window.

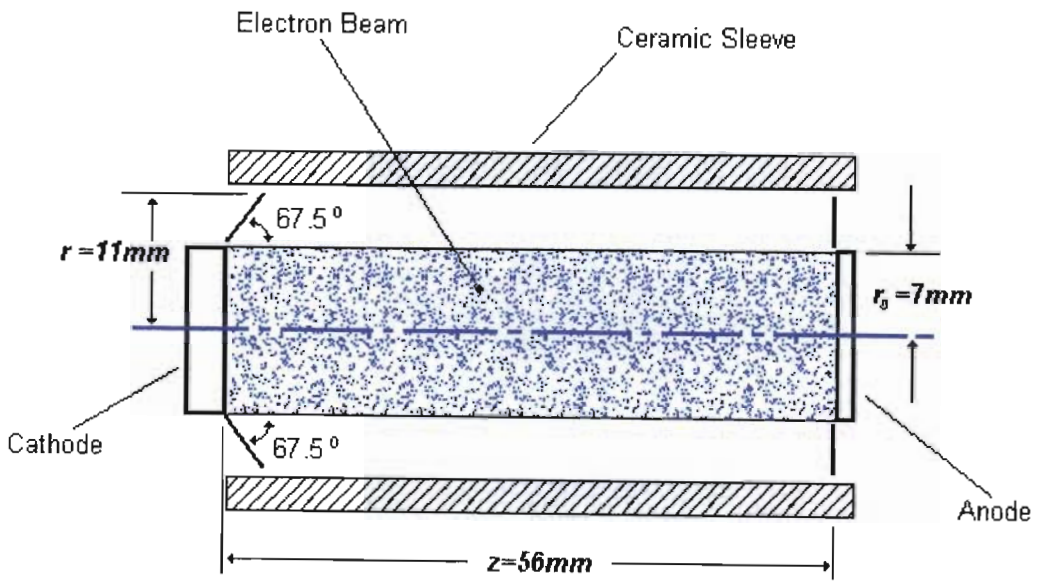

Fig. 3.1.13: Positions of the focusing lens, the cathode and the anode relative to each other [56].

3.1.5. DESIGN OF THE CATHODE-WINDOW STRUCTURE

As can be seen from the layout of the X-ray tube in Figure 3.1.1 the cathode and the window of the tube are integrated. Its principle of operation is illustrated once more in Figure 3.1.15. While the exact design and construction of the cathode will be described in exact detail in Section 3.2, we shall concentrate on the X-ray window for now. The basic function of the X-ray window is that of an exit for the X-radiation produced by the tube and of an interface separating the vacuum inside the tube from the outside environment. Since it is advantageous to have as little attenuation of the X-rays as possible as they pass through the window towards a given analyte, it is necessary to choose a material for the window that has relatively low attenuation coefficients across a wide range of radiation energies. Although beryllium windows are more commonly used in the manufacture of X-ray windows due to their excellent transmission characteristics as compared to aluminium, which used to be more commonly used for X-ray windows before the introduction of beryllium windows, we shall choose aluminium as our window material for the following reasons:

1. Unlike beryllium aluminium is easily machined.

2. Beryllium, which is a highly volatile material especially in the form of dust and vapour, is extremely toxic and can have a deadly effect on humans through accumulation on the skin, the mucous membrane or in the lungs.

Typical window thicknesses are between 0,1 mm and 1 mm. According to *Bertin* [25] the higher the atomic number of the target and the smaller the target-to-window distance, the thicker the window must be.

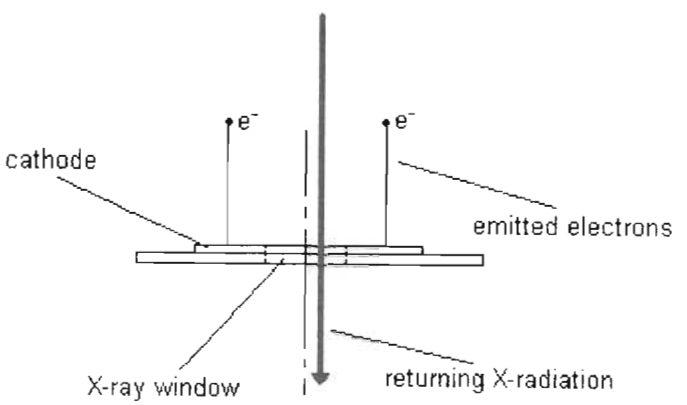

Fig. 3.1.14: Principle of operation of the cold cathode X-ray window structure of the X-ray tube.

The transmission of X-rays through a given material can be expressed as [22]:

$$\frac{I_x}{I_0} = \exp(-\mu\rho x) \tag{3.1.21}$$

where $\frac{I_x}{I_0}$ = the ratio between the transmitted and the incident radiation;

μ = the mass attenuation coefficient of the material ($cm^2\ g^{-1}$);

ρ = the density of the material ($g\ cm^{-3}$);

x = the thickness of the material (cm);

We will now compare the transmission characteristics of circular aluminium windows of 0.1 mm and 1 mm thicknesses for a number of radiation energies. The density of aluminium ρ is 2.7 g cm^{-3}. The attenuation coefficients are taken from Table A4 (Appendix 4). From Table 3.1.1 it is obvious that the thinner 0.1 mm aluminium X-ray window is a far better transmitter of X-rays than the 1 mm window. Already at energies above 50 keV more than 99% of the radiation produced at the target of the tube is transmitted through the 0.1 mm window. This means that the K lines of the tungsten target, which lie well above 50 keV (see Table A5a, Appendix 5), will all have an intensity $I_x \geq 0.99 \cdot I_0$ after transmission through the aluminium window. The L lines on the other hand, with critical excitation energies of at least 10 keV, will have at least 49% of their radiation transmitted. It can therefore be said, that a 0.1 mm aluminium window is an excellent transmitter of medium and especially high energy X-rays. In the case of low energy radiation both the 0.1 mm and 1 mm are extremely poor X-ray transmitters absorbing almost all of the incident radiation.

Table 3.1.1: Transmission ratios of a 0.1 mm and a 1 mm aluminium X-ray window.

Photon energy, keV	μ, $cm^2\ g^{-1}$	$\frac{I_x}{I_0}$ (x=**0.01cm**)	$\frac{I_x}{I_0}$ (x=**0.1cm**)
2	2260	3.15×10^{-27}	0
5	193	5.46×10^{-3}	2.34×10^{-23}
10	26.2	0.49	8.47×10^{-4}
20	3.44	0.91	0.395
50	0.368	0.99	0.905
100	0.170	0.995	0.955
200	0.122	0.997	0.968

In Figure 3.1.15 and Figure A1c (refer to Appendix 1) the final design of the X-ray window-cold cathode structure is illustrated. It should be pointed out, that the aluminium window is not actively soldered onto the structure, as is the case with the cathode support and the cathode-window support. Instead it is epoxied onto the cathode-window support and held in place by the X-ray window support, which is screwed onto the structure. This is due to the fact, that active soldering of the ceramic and steel components of the X-ray tube takes place at temperatures above 800°C, which is well above the melting point of aluminium. The exact procedures of active

soldering and metal to ceramic joining used in the manufacture of the X-ray tube will be described in closer detail in Chapter 4.

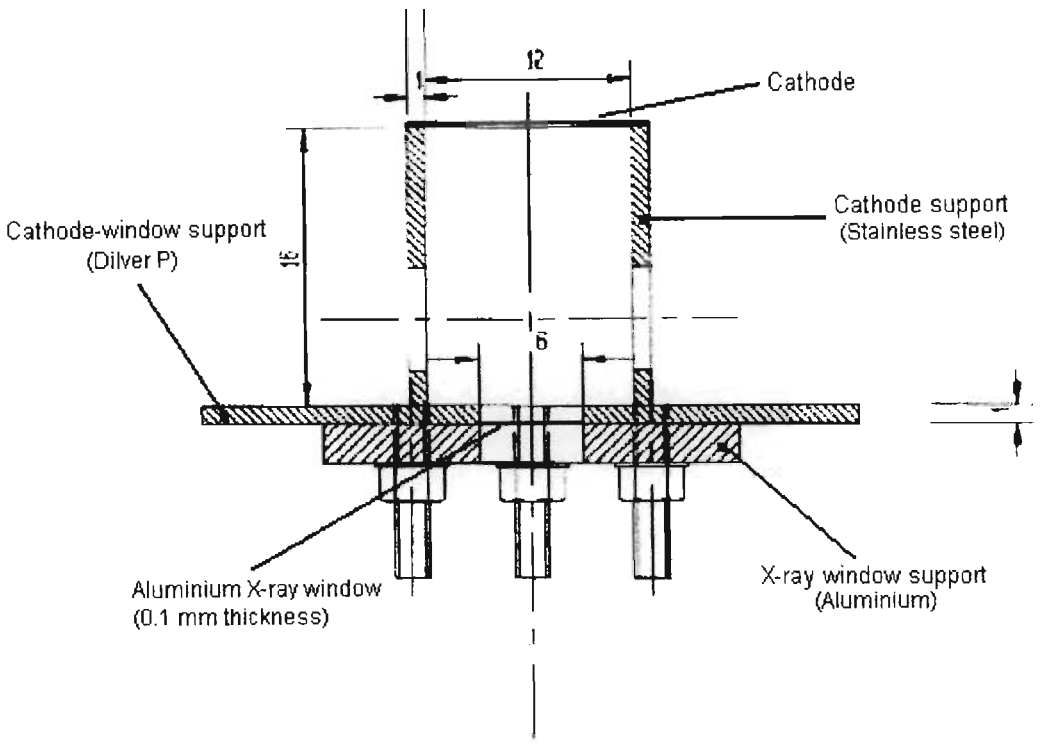

Fig. 3.1.15: The final design of the X-ray window-cold cathode structure [56].

3.1.6. DESIGN OF THE ANODE AND THE EFFECT OF THE TARGET GEOMETRY ON THE ELECTRON AND THE X-RAY BEAM

In the design of an anode or target for an X-ray tube it is important to take the following parameters into account:

1. The *focal spot* of an X-ray tube determines the area, that will be bombarded by electrons emitted by the cathode. The focal spot is not in itself a part of the X-ray optical system, and consequently may be relatively large. The larger size of the focal spot, that is affected by the oncoming electrons, allows for greater power dissipation.

2. The angle θ between the central X-ray and the cone of the resulting radiation (see Figure 3.1.16) in a common side-window X-ray tube is limited by the angle ϕ, that the target face forms with the central X-ray beam.

In our design of the cold cathode end-window X-ray tube, the target is positioned in such a way, that its face is parallel to the cathode. This produces a collimated X-ray beam rather than a divergent one, which is the case in tubes with targets placed at an angle other than 90° to the electron beam.

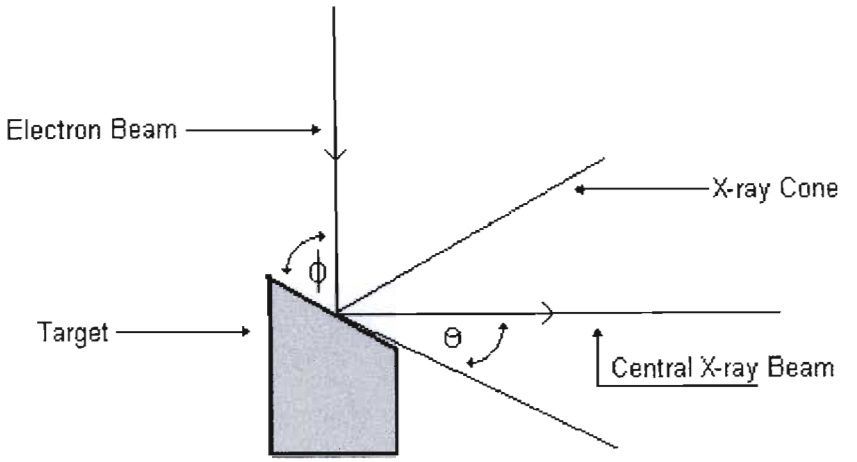

Fig. 3.1.16: Target position relative to the electron and central X-ray beams in a side window tube.

In such a parallel cathode-anode structure the collimated beam can be utilized in such a way, that the central portion of the beam *A* (see Figure 3.1.17) can leave the tube via a central opening in the cathode and the X-ray window of the tube. The rest of the collimated X-ray beam will impinge on the cathode causing the photoemission of further electrons from its surface.

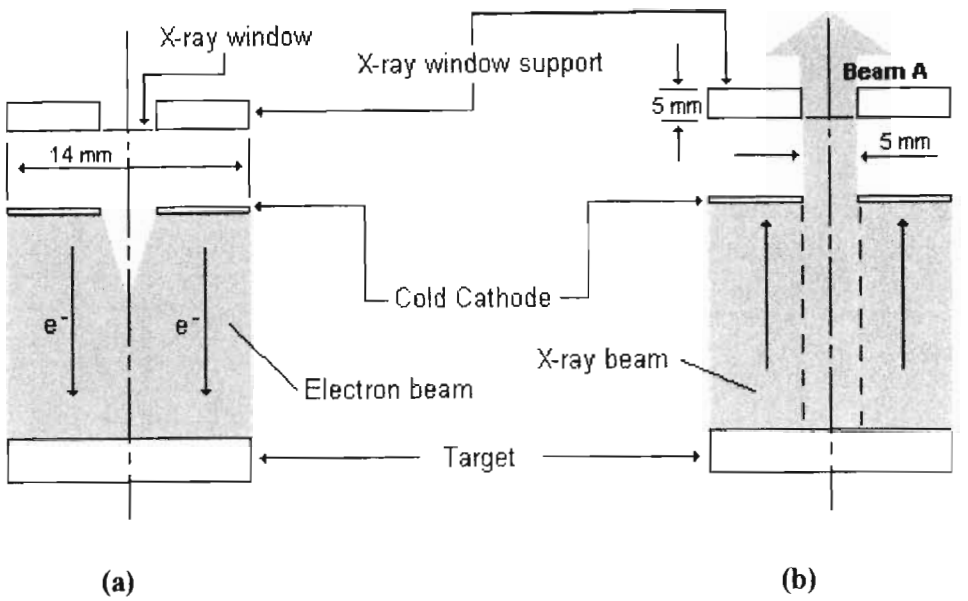

Fig. 3.1.17: (a) The electron beam (shaded region) travelling from the cathode to the target, and (b) the X-ray beam propagating from the target to the window. Only the central beam of 5 mm diameter (beam A) emerges from the window with the rest of the beam acting on the cold cathode.

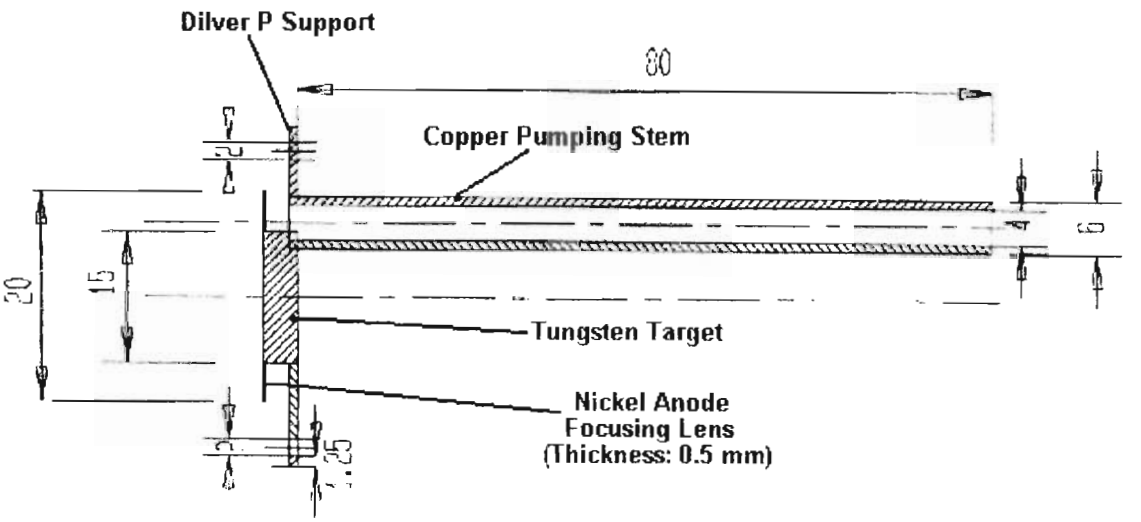

Fig. 3.1.18: The anode of the end-window X-ray tube.

Figure 3.1.17 illustrates this case, where the emission of the electrons (see Figure 3.1.17a) and the X-ray beam (see Figure 3.1.17b) is shown. The useful beam, namely the X-radiation emerging from the X-ray window of the tube to excite the analyte, is cylindrical in shape. The diameter of the useful X-ray beam will be determined by the diameter of the opening in the cathode, and especially the diameter of the window itself, while the remainder of the X-ray beam will irradiate the cathode leading to further electron emission. The diameter chosen for the window is 6 mm and the overall electron beam and hence X-ray beam diameter is determined by the outer diameter of the cathode, which is 14 mm (see Figure 3.1.17). Obviously the more energetic short wavelength components of the beam acting on the cathode will, to a certain extent, pass through it and continue propagating towards the window. The window support, consisting of 5 mm thick aluminium as shown in Figure 3.1.15 in Section 3.1.5 will absorb these X-rays sufficiently, so that their intensities will be significantly smaller than those of the collimated useful beam emerging from the X-ray window. By considering the design of the electrode system described earlier in this section (see Section 3.1.3) it can be seen, that the anode will indeed have to be parallel to the cathode if a uniform rectilinear electron beam is to be produced. This is illustrated in Figure 3.1.12 and Figure 3.1.13 in Section 3.1.4. Therefore this shows, that a parallel cathode-anode structure will focus the emitted electrons in such a manner, that they will move within a rectilinear beam striking the face of the anode at right angles and hence produce a collimated X-ray beam, which will leave the anode in a direction normal to its surface. The final design of the anode, including its dimensions, is shown in Figure 3.1.18 and Figure A1b (see Appendix 1). The anode in Figure 3.1.18 above is shown in Figure 3.1.1 and Figure A1a (refer to Appendix 1) as Component 6.

3.1.7. THE RATING OF THE X-RAY TUBE

The total load, in terms of average power output and exposure time, which can be safely applied at a single exposure to an X-ray tube is limited by the possibility that the heat generated may melt or cause thermal damage to the target or anode. The maximum temperature to which a tungsten target may be raised is generally considered to be approximately 3000°C. There is considerable vaporization of tungsten at temperatures above 3000°C [19]. Even though that temperature could be considered the maximum permissible temperature for operating the tube without causing any damage to the target, the actual maximum temperature should be well below that. In the case of the tube described here it is shown in Chapter 4, where the materials used in the manufacture of the tube and the brazing techniques employed in joining metal to ceramic to produce vacuum tight seals are described, that the tube should not reach temperatures higher than approximately 160°C, if damage to the tube through cracking of its vacuum tight joints is to be avoided. The maximum allowable power input to the tube, that will cause a steady-state temperature development of up to 160°C in the tube, has to be determined in order to establish the maximum rating of the X-ray tube. In Figure 3.1.19 below the X-ray target attached to a hollow copper block, through which transformer oil is pumped, is shown. The transformer oil, which is of standard type 982-68, functions as the cooling liquid ensuring that the inner surface of the copper plate touching the anode of the tube, is kept at room temperature.

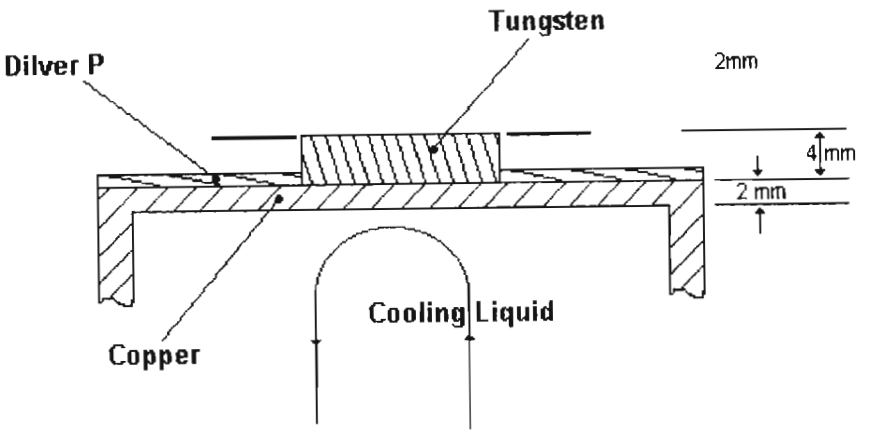

Fig.3.1.19: Cooling of the anode.

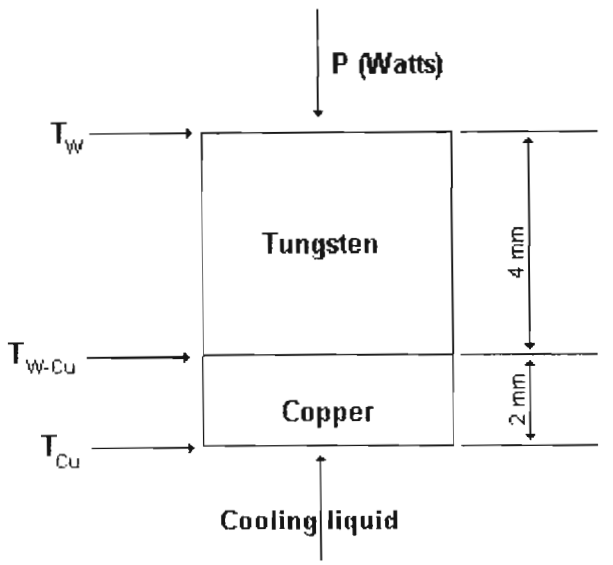

Fig. 3.1.20: Temperatures, that develop at the tungsten surface, the tungsten-copper interface and the copper surface, which is kept at 24°C room temperature by the cooling liquid.

By using equation 3.1.22 [40] the maximum power, that may be dissipated across the tungsten target and the copper plate of the cooling block attached to the target before the surface of the

target reaches 160°C, can be determined. In Figure 3.1.20 the tungsten copper junction is illustrated once more this time displaying the temperatures that develop at the different interfaces of the anode. Under steady-state conditions the heat flow across the tungsten target and copper plate is equal. Therefore we can use equation 3.1.22 [40] to equate the heat flows across tungsten and copper.

$$H = \frac{k_W \cdot A_W \left(T_W - T_{W-Cu}\right)}{L_W} = \frac{k_{Cu} \cdot A_{Cu} \left(T_{W-Cu} - T_{Cu}\right)}{L_{Cu}} \qquad (3.1.22)$$

where H = the dissipated power (W);

k_W = the thermal conductivity of tungsten (154 W $m^{-1}K^{-1}$ at 160°C);

k_{Cu} = the thermal conductivity of copper (395 W $m^{-1}K^{-1}$ at 24°C);

A_W = is the cross sectional area of the tungsten target. The diameter of the target surface is 15 mm. Thus $A_W = 1.77 \times 10^{-3}$ m^2;

A_{Cu} = is the cross sectional area of the copper plate. The diameter of the copper plate is 38 mm. Thus $A_{Cu} = 9.07 \times 10^{-3}$ m^2;

L_W = the thickness of the tungsten target (0.004 m);

L_{Cu} = the thickness of the copper plate (0.002 m);

T_W = the temperature of the target surface. In this case the maximum permissible temperature of 160°C shall be considered.

T_{W-Cu} = the temperature of the tungsten-copper interface;

T_{Cu} = the temperature of the copper plate surface, which is kept at room temperature (24°C) by the cooling liquid;

By inserting all the values above into equation 3.1.22 [40], one can now solve for the tungsten-copper interface temperature T_{W-Cu}, which is equal to 29°C. Having thus calculated the copper-tungsten interface temperature, T_{W-Cu} can now be substituted back into equation 3.1.22 using either the parameters for tungsten or for copper to obtain the heat flow through the anode structure. Under steady-state conditions the heat dissipation across tungsten and copper will be the same:

$$H_W = \frac{k_W \cdot A_W \left(T_W - T_{W-Cu}\right)}{L_W} =$$

$$\frac{\left(154 \text{ W m}^{-1}K^{-1}\right) \cdot \left(1.77 \times 10^{-3} \text{ m}^2\right) \cdot \left(160 - 28.97\right) ^\circ\text{C}}{0.004 \text{ m}} \approx$$

8.9 kW for tungsten,

and

$$H_{Cu} = \frac{k_{Cu} \cdot A_{Cu}\left(T_{W-Cu} - T_{Cu}\right)}{L_{Cu}} =$$

$$\frac{\left(396.16\ \mathrm{W\ m^{-1}K^{-1}}\right)\cdot\left(9.07 \times 10^{-3}\ \mathrm{m^2}\right)\cdot\left(28.97 - 24\right)\ ^{\circ}\mathrm{C}}{0.002\ \mathrm{m}} \approx$$

8.9 kW for copper;

The maximum permissible heat flow or power dissipation across the X-ray tube has now been established and is equal to 8.9 kW. In Sections 3.1.2 it is shown, that the overall average power dissipation across the tube will be 142 Watts. By inserting that value with all the corresponding parameters for either tungsten or copper back into equation 3.1.22 the temperature of the target surface T_W can be calculated, and is found to be 29°C, which is obviously far below the maximum allowed temperature of 160°C. The X-ray tube can therefore be operated safely, if 142 Watts of power is dissipated across it under steady-state conditions. The design of the copper cooling block which is attached to the X-ray tube is shown in Figure A1e in Appendix 1.

3.1.8. SUMMARY

After having introduced the overall design of the end-window X-ray tube structure in order to present an overview of the X-ray tube components and their respective functions in Section 3.1.1 and then presenting the reader with the X-ray tube power supply characteristics (see Section 3.1.2), it was subsequently established, that an X-ray tube operates according to the same principles as a simple vacuum diode with the sole exception, that a target with a high atomic number is placed at the anode. As electrons are accelerated through the tube from the cathode to the anode high energy X-rays can be produced as the electrons strike the target, which in this case is manufactured from tungsten. Having shown, that the X-ray tube can also be treated as a vacuum diode, the problem of positive and negative space charge in a parallel-plane vacuum diode had to be considered, which places a limit to the maximum current, that can be emitted by a cathode. The expression developed for this current (equation 3.1.13) is used in Section 3.2, in which the current emission from a magnesium oxide cold cathode is discussed, to determine the waveform of a current pulse in the X-ray tube under the given conditions.

Having developed expressions for the space-charge limited current in a tube, the problem of electron beam focusing onto the target was tackled. In order to produce a collimated X-ray beam in the end-window tube radiating with maximum intensity in a direction 180° to that of the electrons travelling towards the target, Pierce type focusing was applied in the design of the tube. By introducing a Pierce type lens in the focusing system of the tube it is possible to overcome the effects of space-charge, namely the tendency of the electron beam to diverge as it approaches the target thus producing a smaller current density at the target. With Pierce focusing the current density at the cathode is theoretically equal to the current density at the target, because the electrons are now focused in such a way, that they travel along rectilinear or parallel paths. In this way the current at the anode or target reaches a maximum, which in turn results in the production of X-radiation with maximum intensity.

Finally the design of the integrated cathode-window structure was described. It was shown, that an aluminium X-ray window of 0.1 mm thickness was sufficient to allow for the X-rays to leave the tube with a minimal amount of attenuation while passing through the window. The radiation exiting the tube through the X-ray window is known as the useful beam. It is this X-radiation, that excites the elements in a given sample or analyte. The anode, as part of the Pierce type focusing system, had to be designed in such a way, that the target and the anode focusing lens effectively formed a single surface parallel to the cathode. Another important aspect, that has to be taken into consideration in the design of the X-ray tube, is the determination of the maximum permissible loading of the X-ray tube. The maximum permissible loading is a quantity, that gives an indication of the maximum power input, that can be dissipated across the tube without causing damage to the tube, principally in the form of cracking of the ceramic sleeving as well as the metal-to-ceramic joints. In order to avoid such damage, which would result in the loss of vacuum in the tube, it was found that the average power input to the tube should not exceed 8.9 kW under steady-state conditions and the use of target cooling. By allowing for an average heat flow of 142 Watts through the tube it was shown, that the target would eventually reach a steady-state temperature of 29°C at its surface provided that target cooling is employed.

3.2. DESIGN OF THE MgO COLD CATHODE

3.2.1. INTRODUCTION

In order to prolong the life-time of the X-ray tube, which is directly dependent on the vacuum and hence the filament or hot cathode life-time in such a device, a cold cathode consisting of a MgO layer on a nickel substrate is used. Such an electron emitter is capable of functioning at lower levels of vacuum, which in the case of a hot filament usually result in fast evaporation rates of the cathode material and hence a shorter life-time of the X-ray tube. The phenomenon of electron emission from MgO is similar to the Malter effect [9][7], which can be found to be the case with a whole range of materials such as aluminium oxide, silicon oxide and potassium chloride. However, out of all these materials MgO seems to be best suited as an electron emitter with regard to its ability to produce high current densities for prolonged periods of time. As far as the emission mechanism of such a cathode is concerned, it is generally believed that an electron avalanche takes place in the porous MgO layer as a result of the presence of a high electric field applied between the MgO layer and the nickel substrate. These fields are a result of the build up of high potentials on the magnesium oxide surface. By triggering the electron emission with a starter means such as ultraviolet light, intensive visible light, electron bombardment, radioactivity or the discharge from a Tesla coil [10], electron avalanching is produced in the oxide layer which in turn causes further avalanching due to the pair production between electrons drawn out of the nickel substrate under the influence of the electric field and holes within the MgO layer. As a number of electrons are thus able to attain enough energy to leave the cathode material and enter the vacuum of the tube, where they are then accelerated towards the anode of the X-ray tube as a result of the potential difference between the anode and the cathode, the production of holes is maintained resulting in a continuation of the recombination processes between the electrons and the holes, and therefore the electron avalanching, for as long as a high electric field is maintained across the oxide layer. The formation of a nickel oxide layer between the nickel base and the MgO layer leads to an even greater acceleration of the electrons from the nickel base to the MgO surface of the cathode [2][7][10]. While it is commonly accepted, that electron emission from cold cathodes is not due to the Schottky effect, the Fowler-Nordheim equation [2][3][4] on the other hand, which relates the current emitted from a cold surface to the electric field across it, has often been used to describe this phenomenon. The author will show in this chapter, that the Fowler-Nordheim relation does not explain cold cathode emission in a satisfactory manner either, and therefore an alternative mechanism is suggested. As will be seen in the later sections of this chapter an alternative way to initiating and maintaining electron emission from the MgO cold cathode is to apply a changing electric field across its dielectric layers, namely the NiO and the MgO layers. The author will show, that, according to Maxwell's third law, a changing electric field in a dielectric material creates a circular magnetic field in it, which ultimately results in the electrons being accelerated from the nickel substrate through the NiO and the MgO layers into the vacuum of the X-ray tube. Incidentally Maxwell's relation mentioned above also explains why electron emission from a cold cathode can also be maintained when a constant electric field is applied provided an initial current is present. At the same it will also be shown (see sections 3.2.7 to 3.2.11), that due to the geometry of the X-ray tube, the cathode will be irradiated by the X-rays produced at the tungsten target resulting in the emission of photoelectrons from the cathode in addition to the field emitted electrons. In considering this problem one needs to take both the characteristic line and the continuous radiation from the tungsten target into account, both of which contribute to the emission of photoelectrons from the cathode. In this way the total current emitted from the cathode of the X-

ray tube will in fact be the sum of the current produced by the application of a changing electric field across the X-ray tube and the current resulting from the photoemission of electrons due to the X-irradiation of the cathode surface.

3.2.2. FIELD EMISSION OF ELECTRONS BY SOLIDS

Note should be taken of the fact that in studying electron emissions from various solids under ideal conditions the phenomenon of electron emission greatly depends on the gas condition of the discharging surface. Hence experiments on emission should be conducted only once the surfaces to be tested have been carefully outgassed, so that results can be obtained characteristic of gas free surfaces. Electrons may be emitted by surfaces at high temperature called thermionic emission or by electron or ion bombardment. In this case focus will be placed on the effect of high-surface fields on cold cathodes characteristics. Under the influence of fields of the order of 10^5 Volts/cm and greater electrons can effectively be pulled out of cold surfaces solely by the action of the field. This effect is known as cold or autoelectronic emission [1]. When taking the emissive characteristics of MgO into account the nature and type of the metal support, which functions as a substrate for the MgO layer of the cold cathode, also has an effect on electron emission from the cold cathode. According to *A.M Shroff* [2] this fact can be proven by using a layer composed of 50% MgO and 50% $MgO.MgCO_3$ on a layer of MgO_2 that has a mass 15% of that of the previous oxide layer and is deposited on the different metals in Table 3.2.1 below.

Table 3.2.1: The values of the work function ϕ of the pure metals and the heat necessary for the formation of their oxides [2].

Metal.	Φ (eV).	Q (kcal/mol).
Platinum	5.3	17
Nickel	4.6	58.4
Tantalum	4.1	500

Table 3.2.1 gives the work functions and the heat values necessary for the formation of oxides of the metals platinum, nickel and tantalum in their pure forms. In Figure 3.2.1 one can see that the electron emission is in fact raised as the work function of the metal support decreases or as the oxidation heat is increased [2].

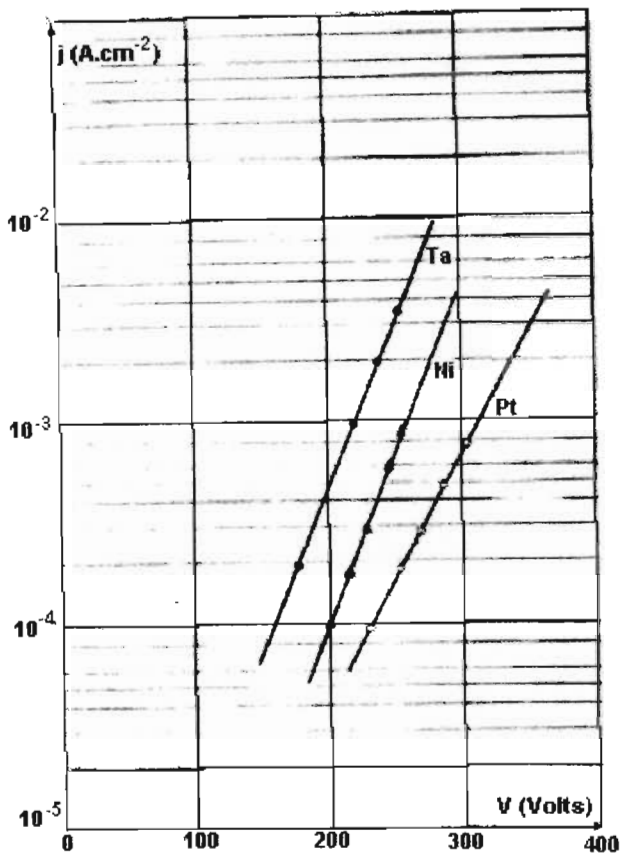

Fig. 3.2.1: Influence on electron emission by the metal support [2]

3.2.3. ELECTRON EMISSION DUE TO THE SCHOTTKY EFFECT

If the phenomenon of electron emission is due to the Schottky [3] effect, then, according to *Shroff* [2], the Richardson-Dushman equation (equation 3.2.1) can be used, so that the thermoelectronic functioning of the cathode at temperature T under conditions of saturation is taken into account. Under such circumstances it follows, that once the cathode is exposed to an exterior electric field E, the emission current then becomes proportional to the temperature of the emitter [2]. Thermal electron emission from all types of cathodes can be adequately described by the Richardson-Dushman equation:

$$j_S = A_o T^2 \exp\left[-\frac{\Phi}{kT}\right] \tag{3.2.1}$$

The value of the work function Φ varies approximately linearly with temperature according to the relation

$$\Phi = \Phi_0 + \alpha \cdot T \tag{3.2.2}$$

where Φ_0 = work function at $T = 0$ °K and $\alpha = d\Phi / dT$, the temperature coefficient of the work function. According to *W. H. Kohl* [19], equations 3.2.1 and 3.2.2 above can be combined into one expression:

$$j_S = A_o T^2 \exp\left[\frac{-\alpha}{k}\right] \cdot \exp\left[-\frac{\Phi_0}{kT}\right] \tag{3.2.3}$$

In equation 3.2.3 the term $A_o \cdot \exp\left[\frac{-\alpha}{k}\right]$ is also referred to as the Richardson or emission constant of a material. While its value lies typically between 30×10^4 and 70×10^4 A m^{-2} deg^{-2} for pure metal surfaces [19], for oxide cathodes and thin films the emission constant assumes a value close to 1×10^4 A m^{-2} deg^{-2} and even less according to *W. H. Kohl* [19]. For the following calculation it will therefore be assumed, that the MgO film of the cold cathode will have an emission constant of 1×10^4 A m^{-2} deg^{-2}. Hence by substituting $A_o \cdot \exp\left[\frac{-\alpha}{k}\right] = 1\times10^4$ A m^{-2} deg^{-2}, $T = 293$ °K and $\Phi_0 = 3.1$ eV, the work function of MgO [1], into equation 3.2.3 the following value for the saturated thermal emission current density j_S is obtained:

$$j_S = \left(293^0\,\mathrm{K}\right)^2 \cdot \left(1\times10^4\,\mathrm{A\,m^{-2}\,deg^{-2}}\right) \cdot \exp\left[\frac{-3.1\mathrm{eV}\times1.602\times10^{-19}\,\mathrm{C}}{1.38\times10^{-23}\,\mathrm{J\ ^0K^{-1}}\cdot 293\ ^0\mathrm{K}}\right]$$

$$\approx 1.336\times10^{-47}\ \mathrm{A\,m^{-2}}$$

$$= 1.336\times10^{-51}\ \mathrm{A\,cm^{-2}}$$

Using a disk shaped cathode which has an outside diameter of 1.4 cm and an inner diameter of 0.6 cm and hence a total surface area of $A = 1.256$ cm^2, the thermal saturation current i_S can then be calculated by multiplying the emission area A of the cathode with j_S:

$$i_S = A \cdot j_S = \tag{3.2.4}$$

$$(1.256\ \mathrm{cm^2}) \cdot (1.336\times10^{-51}\ \mathrm{A\,cm^2}) =$$

$$1.678\times10^{-51}\ \mathrm{A} = 1.678\times10^{-48}\ \mathrm{mA}$$

Clearly this current is practically negligible and it will be shown in the following sections that autoelectronic emission from the MgO cathode is due to effects other than the Schottky effect. Table 3.2.2 presents further values for i_S at still higher temperatures. These values were computed using the same approach as above for a MgO cold cathode with an emission surface area of 1.256 cm^2. Even at temperatures as high as 1100 °K the emission current is only 9.411×10^{-5} mA.

So far the above calculations were performed with respect to a single MgO layer without taking into account the entire cathode structure i.e. the Ni-NiO-MgO structure. With the work function of Ni equal to 5 eV and MgO equal to 3.1 eV, it is obvious that the work function of the Ni-NiO-MgO structure will have a value between 3.1 eV and 5 eV. By substituting values for the work

function greater than 3.1 eV into equation 3.2.3 the values for j_S and hence i_S will be even lower than those obtained in Table 3.2.2 at the corresponding temperatures. The quantities obtained in Table 3.2.2 may therefore be considered the maximum currents, that a MgO cathode may emit provided its substrate, which is nickel in our case, has a work function ≥ 3.1 eV.

Table 3.2.2: Absolute currents (mA) at different temperatures emitted by a MgO film of 1.256 cm^2 surface area assuming the entire cathode structure has a minimum work function of 3.1 eV.

T/°K	I_S/mA
293	1.678×10^{-51}
300	9.053×10^{-48}
500	1.734×10^{-26}
700	2.898×10^{-18}
900	4.385×10^{-12}
1100	9.411×10^{-5}

3.2.4. FOWLER-NORDHEIM ELECTRON EMISSION FROM A COLD CATHODE

The density of the emitted current dependent on the electric field can also be described by the Fowler-Nordheim relation [2][21][26]:

$$j = j_0\left(\frac{E}{E_0}\right)^2 exp\left[-\frac{E_0}{E}\right] \tag{3.2.5}$$

where

$$E_0 = \frac{4\sqrt{2m}}{3\eta e}\Phi^{\frac{3}{2}} = 6.383\times10^{-8}\ \Phi^{\frac{3}{2}} \ ,$$

$$j_0 = \frac{2em}{9\eta^3\pi^2}\Phi^2 = 6.037\times10^{-85}\ \Phi^2 \ ,$$

$$E = \frac{V}{d} \ ,$$

where $\eta = e/m$, V is the voltage applied across the dielectric medium and d refers to the thickness of the dielectric medium.

It can be seen that the above expression is independent of temperature, which is a characteristic of the field effect. According to *Shroff* [2] the above expression can finally be presented as shown in equation 3.2.6:

$$\frac{d\log\frac{j}{V^2}}{d\frac{1}{V}} = -0.3d\Phi^{\frac{3}{2}} \qquad (3.2.6)$$

Using the above expression *Shroff* [2] determined the thickness d of the NiO layer, that is formed between the MgO layer and the nickel substrate. If one considers the graph in Figure 3.2.2 as an example one can see that the logarithm of current density j is plotted as a function of $\frac{1}{V}$ for various nickel based MgO samples, which *Shroff* [2] used in his investigations of MgO cold cathodes.

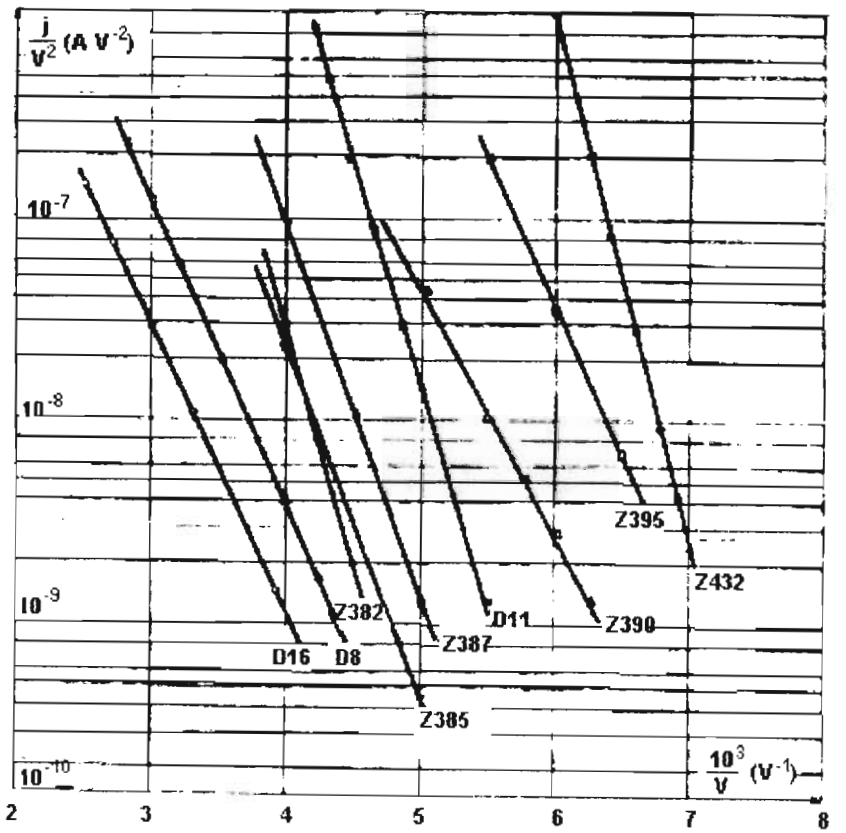

Fig.3.2.2: The characteristic $\log\frac{j}{V} = f\left(\frac{1}{V}\right)$ **[2].**

The gradients of these curves, namely $\frac{d\log\frac{j}{V^2}}{d\frac{1}{V}}$, enabled *Shroff* [2] to evaluate d, the dielectric layer thickness in question, provided its work function Φ is known. By considering the work

function Φ of MgO to have a value 3.1eV, he then found d to be equal to 780 Å [2]. He deduced that this value represented the thickness of a nickel oxide interface between the metal and the magnesium oxide layer, and approximated it to 1000 Å. Furthermore he verified the existence of such a layer by a simple X-ray examination of the cathode and by an evaluation of the Debye-Scherrer diagram obtained from such an analysis. Even though the value for the thickness of the NiO layer has thus been established by applying the Fowler-Nordheim relation, the author disagrees with *Shroff's* statement, that the electron emission from the MgO cold cathode is one of the Fowler-Nordheim type. However, before elaborating further on this point, it is necessary to first calculate the different voltages and electric fields that develop not only across the Ni-NiO-MgO structure of the cold cathode, but also across the cold cathode-vacuum-anode structure of the entire X-ray tube. In Figure 3.2.3 a working model and a band structure model for Ni-NiO system is displayed.

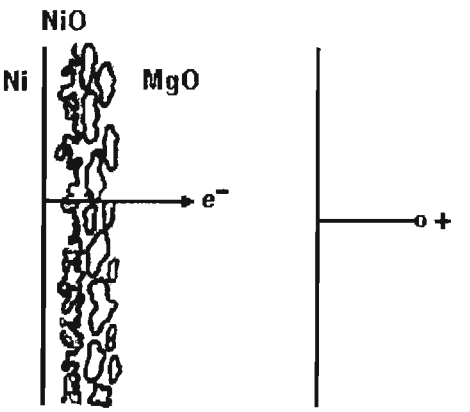

Fig. 3.2.3.a: Working model of a Ni-NiO-MgO structure [2].

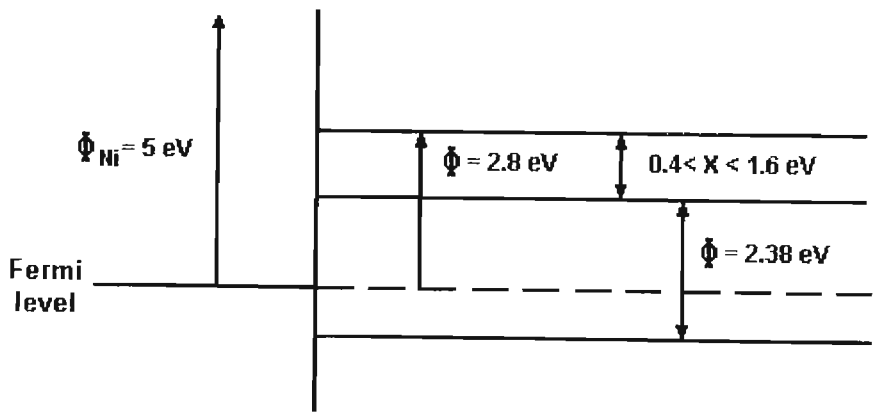

Fig. 3.2.3.b: Band structure model for a Ni-NiO system [2].

By taking into account the work function of Ni (Φ = 5 eV) and the electron affinity of NiO (χ = 1.6 eV) and thus establishing an overall work function for the Ni-NiO system of 3.4 eV, *Shroff* [2] showed that the Schottky effect was practically negligible even for fields of the order of 10^8 V cm^{-1} (of the order of 10^{-33} A cm^{-2} at T = 300 °K as compared to orders of 10^{+8}A cm^{-2} for the field effect at the same temperature). The fact, that the Schottky effect does not take place in field dependent electron emission has also been verified in section 3.2.3 earlier. This means, that the electron emission from a cold MgO cathode subjected to a high electric field is affected by temperature to a negligible extent, and so it can be stated that *autoelectronic emission* can be treated as a field dependent phenomenon only. Taking that into account the following emitter-collector structure representative of a cold cathode X-ray tube must be considered:

Ni-NiO-MgO-vacuum-anode.

Here one can see the presence of three dielectric layers, namely the nickel oxide, the magnesium oxide and the vacuum layers, whereby the substrate (i.e. Ni) and the anode are functioning as the electrodes [2]. The following material thicknesses, dielectric constants and electric fields are taken into consideration:

1. d_1, ε_1, E_1 for NiO;
2. d_2, ε_2, E_2 for MgO;
3. d_3, ε_3, E_3 for the vacuum;

Similarly one must consider the corresponding potential differences V_1, V_2 and V_3 which add up to a total accelerating voltage between the end electrodes of the X-ray tube V = 85 kV. With

$$\varepsilon_1 E_1 = \varepsilon_2 E_2 = \varepsilon_3 E_3,$$

one obtains the following expressions for V_1, V_2 and V_3:

$$V_1 = \frac{d_1}{\varepsilon_1} \frac{V}{\frac{d_1}{\varepsilon_1} + \frac{d_2}{\varepsilon_2} + \frac{d_3}{\varepsilon_3}} = \frac{d_1}{\varepsilon_1} AV,$$

$$V_2 = \frac{d_2}{\varepsilon_2} AV,$$

$$V_3 = \frac{d_3}{\varepsilon_3} AV.$$

One can now find the following values for V_1, V_2 and V_3:

$V_1 = 1.279 \times 10^{-2}$ V for $d_1 = 1 \times 10^{-7}$ m,

$V_2 = 15.73$ V for $d_2 = 1 \times 10^{-4}$ m,

$$V_3 = 84980.79 \text{ V for } d_3 = 0.056 \text{ m.}$$

where

$\varepsilon_1 = \varepsilon_0 K_1 = 1.05\times10^{-10}$ F m^{-1} and K_1, the relative dielectric constant for NiO, = 11.9 [20],

$\varepsilon_2 = \varepsilon_0 K_2 = 8.54\times10^{-11}$ F m^{-1} and K_2, the relative dielectric constant for MgO, = 9.65 [20],

$\varepsilon_3 = \varepsilon_0 K_3 = 8.85\times10^{-12}$ F m^{-1} and K_3, the relative dielectric constant for vacuum, = 1,

d_1 = the thickness of the NiO layer (m),

d_2 = the thickness of the deposited MgO layer on the nickel substrate (m),

d_3 = the anode-cathode spacing of the X-ray tube (m), which has been derived in Section 3.1.3, where it is denoted as z.

Using the above values for V_1, V_2 and V_3 and d_1, d_2 and d_3 the corresponding electric fields E_1, E_2 and E_3 can be found:

$$E_1 = 1.279\times10^5 \text{ V m}^{-1},$$

$$E_2 = 1.573\times10^5 \text{ V m}^{-1},$$

$$E_3 = 1.518\times10^6 \text{ V m}^{-1}.$$

Cobine [1] states that electrostatic fields of the order of 10^5 V m^{-1} are sufficient to cause autoelectronic emission. From the above values for the electric fields it can therefore be seen that these values are sufficient for cold cathode electron emission to take place. Another aspect of this type of emission, which has to be mentioned, is the existence of superficial charges at the NiO-MgO interface. According to *Shroff* [2] the electric field can also be expressed as the ratio between the surface charge density σ_S (C m^{-2}) and the dielectric constant ε of a given material, i.e. $E = \frac{\sigma_S}{\varepsilon}$ [14]. By taking the earlier obtained values of $E_2 = 1.573\times10^5$ V m^{-1} and $\varepsilon_2 = 8.54\times10^{-11}$ F m^{-1}, σ_S is obtained as

$$\sigma_S \approx 1.343\times10^{-5} \text{ C m}^{-2}.$$

which, when divided by the charge value for the elementary charge $e = 1.602\times10^{-19}$ C, is equivalent to approximately 8.385×10^{13} charges cm^{-2}. If one takes into account, that the electrons are actually drawn from the nickel base of the cathode through the NiO and MgO layers during avalanching, it becomes apparent that the number of free electrons must exceed the minimum charge density of 8.385×10^{13} charges cm^{-2} in order for electron emission from the cathode under the presence of high electric fields to take place. Figure 3.2.4 illustrates the equilibrium potentials with and without such charges. It can be shown that nickel contains 9.129×10^{22} atoms cm^{-3}, which means that the number of available electrons is clearly even higher than both that value and the required minimum

of available charges of 8.385×10^{13} charges cm^{-2}. Therefore a nickel substrate will be sufficient to supply electrons into the NiO and MgO layers, so that the required MgO surface potentials can develop for autoelectronic emission to take place. In Figure 3.2.4 the initial equilibrium potentials across the NiO, MgO and vacuum layers, i.e. the equilibrium potentials in the absence of charges, are illustrated. Once a steady flow of charges is established across these layers, so that practically a short connection is established across the vacuum, the entire voltage applied to the tube develops across the NiO and the MgO layers (see curve denoted 'equilibrium state with charges' in Figure 3.2.4). As can be seen below most of that potential drop then develops across the NiO, thus making it the layer most prominent in accelerating the electrons from the nickel substrate.

It can therefore be said, that by having theoretically established the thickness of a NiO layer that forms in a nickel based MgO cold cathode it is possible to establish the equilibrium potentials and electric fields within the different dielectric layers (i.e. NiO, MgO, vacuum). The calculations for these fields have shown, that the application of an accelerating potential of 85 kV in the aforementioned X-ray tube structure will indeed produce field magnitudes within the different dielectric layers high enough to produce electron emission. Also it can be seen that the electron emission from a cold MgO cathode would in this case be one arising from the presence of high electric fields within the different dielectric layers of the cathode rather than from the temperature dependent Schottky type. Having established a value for the electric field $E = E_2$ across the MgO layer and keeping in mind that the work function Φ of MgO is 3.1 eV, the value for the emitted cold cathode current density j can be determined by substituting the above values into equation 3.2.5. In this way one finds, that

$$E_0 = \frac{4\sqrt{2m}}{3\eta e}\Phi^{\frac{3}{2}} = 2.235\times10^{35}\ \text{V m}^{-1}$$

and

$$j_0 = \frac{2em}{9\eta^3\pi^2}\Phi^2 = 1.489\times10^{121}\ \text{A m}^{-1},$$

and so, with E in equation 3.2.5 equal to E_2,

$$j = j_0\left(\frac{E}{E_0}\right)^2 exp\left[-\frac{E_0}{E}\right] = 7.384\times10^{-42}\ \text{A m}^{-1} \approx 0\ \text{A m}^{-1}.$$

With the current density j in equation 3.2.5 attaining a value approaching zero it can therefore be stated, that even though the electron emission from the cold cathode is entirely dependent on an applied electric field, the Fowler-Nordheim concept of electron emission from a MgO cold cathode does not offer a satisfactory description for this phenomenon at all. Note should be taken of the fact, that the value assumed for the NiO layer thickness of 1×10^{-7} m is merely an approximation made by *Shroff* [2], which he attempted to explain via the Fowler-Nordheim equation (equation 3.2.5), yet only verified by X-ray examination of the cathode.

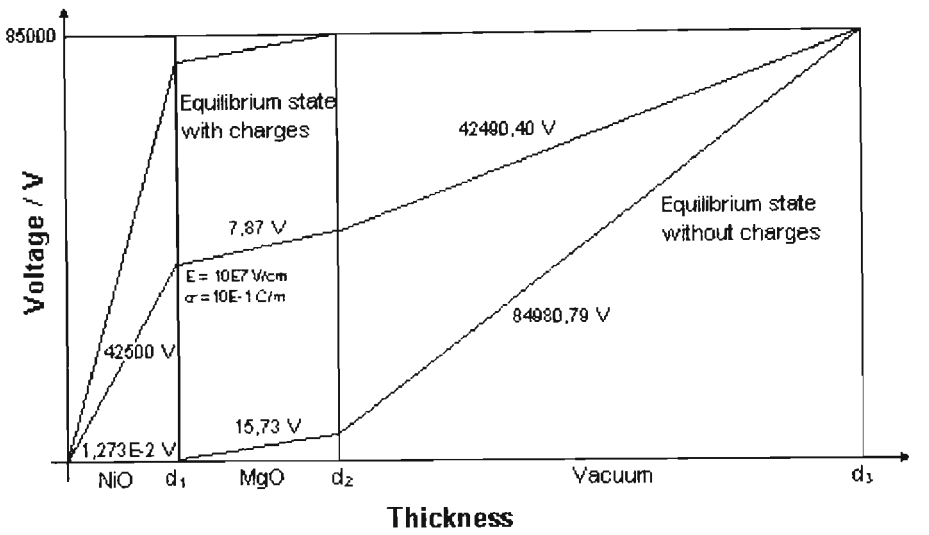

Fig. 3.2.4: Equilibrium potentials with and without surface charges.

3.2.5. COLD CATHODE ELECTRON EMISSION DUE TO CHANGING ELECTRIC FIELDS

So far it has been established that emission from a cold MgO cathode is merely due to high electric fields within the different dielectric layers of the X-ray tube, namely the NiO, the MgO and the vacuum layers, and that the Schottky effect is not applicable in this case. It has also been shown that the Fowler-Nordheim relation cannot be used to describe electron emission from a cold cathode either. It is necessary to point out, however, that electron emission from a cold cathode cannot take place simply by the application of a constant high electric field [2][3][4][6][9][10]. According to *Daglish* [9] the emission of electrons from the cold magnesium oxide depends upon the establishment and maintenance of a positive potential on the oxide surface, and upon the existence of a suitable field outside the coating, which is within the vacuum space between the cathode and the anode of the X-ray tube. This field is provided by applying a positive potential to the anode of the X-ray tube. No current passes when this potential is applied until primary emission is initiated by a starter means such as electron bombardment of the cathode, a high-frequency discharge from a Tesla coil across the tube and other mechanisms that cause initial electron emission from the cathode [9]. It will be shown, however, that the need for the aforementioned starter mechanisms can be completely avoided, if a changing electric field instead of a constant electric field is applied across the dielectric layers of the X-ray tube. This can evidently be achieved by using a pulsed 85 kV power supply rather than a constant voltage supply to power up the X-ray tube. The above statement can be explained using the basic laws of electricity or magnetism. If one considers N to be the density of molecules per cubic metre in MgO, then

$$\mathbf{P} = N\mathbf{p} = N\alpha\mathbf{E}_{loc} \tag{3.2.7}$$

is the volume density of dipole moments, where $\mathbf{p}$ denotes the average polarization per molecule, α represents the total polarizability of the material and $\mathbf{E}_{loc}$ is the local electric field applied across

the MgO layer. According to *Elliott* [18] equation 3.2.7 may also be expressed in the form of the following equation:

$$\mathbf{P} = \frac{N\alpha}{1 - \frac{\gamma}{\varepsilon_0} N\alpha}\mathbf{E} \tag{3.2.8}$$

Thus under the restrictions of this analysis the polarization **P** is linearly proportional to the macroscopic field [18]. For this reason one may write

$$\mathbf{P} = \chi_e \varepsilon_0 \mathbf{E} \tag{3.2.9}$$

in which χ_e is a dimensionless constant, called the *dielectric susceptibility*, and is given by

$$\chi_e = \frac{\frac{N\alpha}{\varepsilon_0}}{1 - \gamma \frac{N\alpha}{\varepsilon_0}} \tag{3.2.10}$$

where γ is a constant. According to *Elliott* [18] the flux density in the material is

$$\mathbf{D} = \varepsilon_0 \mathbf{E} + \chi_e \varepsilon_0 \mathbf{E} = \varepsilon_0 (1 + \chi_e)\mathbf{E} = \varepsilon \cdot \mathbf{E} \tag{3.2.11}$$

The relative dielectric constant K_r can be expressed using the following relation [16]:

$$K_r = \frac{\varepsilon}{\varepsilon_0} = 1 + \chi_e \tag{3.2.12}$$

where ε is the permittivity of the dielectric and ε_0 is the permittivity of space. Therefore, with the relative dielectric constant for MgO being 9.65, χ_e is easily computed using equation 3.2.12 and is found to be equal to 9.65. From equation 3.2.9 we can therefore express the volume density of dipole moments for MgO also in the form of equation 3.2.13:

$$\mathbf{P} = (2{,}5 \cdot 8.854 \times 10^{-12}\ \mathrm{F.m^{-1}}) \cdot \mathbf{E} =$$

$$2.214 \times 10^{-11} \cdot \mathbf{E} \tag{3.2.13}$$

Using equations 3.2.11 and 3.2.13 one can now relate a changing electric field $\partial\mathbf{E}/\partial\mathbf{t}$ to a magnetic field and the motion of charges, or better still a current, within a dielectric medium. If a dielectric material is considered at the microscopic level to consist of an aggregation of charged particles, then the free-space Maxwell's equation, also known as Ampère's law,

$$\nabla \times \mathbf{B} = \mu_0 \mathbf{j_t} + \frac{1}{c^2} \cdot \partial\mathbf{E}/\partial\mathbf{t} \tag{3.2.14}$$

is applicable, with $\mathbf{j}_t = \mathbf{j} + \mathbf{j}_b$ representing the total current density due to motions of both primary charges $\mathbf{j}$ and the bound charges ($\mathbf{j}_b$) within the dielectric. *R. S. Elliott* [18] goes on to show that

$$\mathbf{D} = \varepsilon_0 \mathbf{E} + \mathbf{P}$$

and therefore

$$\dot{\mathbf{D}} = \varepsilon_0 \dot{\mathbf{E}} + \dot{\mathbf{P}} = \varepsilon_0 \dot{\mathbf{E}} + \mathbf{j}_t - \mathbf{j}$$

With the dielectric material being nonmagnetic as in the case of MgO we can then also express Maxwell's equation (equation 3.2.14) in the form

$$\nabla \times \mathbf{B} = \mu_0 \left(\mathbf{j} + \dot{\mathbf{D}} \right) \tag{3.2.15}$$

Substituting equation 3.2.11 into equation 3.2.15 one obtains

$$\nabla \times \mathbf{B} = \mu_0 \mathbf{j} + \mu_0 \varepsilon_0 \left(1 + \chi_e\right) \partial \mathbf{E} / \partial t \tag{3.2.16}$$

From equation 3.2.16 it can be seen that the changing electric field $\partial \mathbf{E}/\partial t$ and the current density $\mathbf{j}$ have the same signs, which means that in order for a current to be emitted from the MgO layer of the cathode, i.e. in order for $\mathbf{j}$ to be a positive quantity, $\partial \mathbf{E}/\partial t$ would obviously have to be positive (see Figure 3.2.5 and 3.2.6). According to *Young* [31] if one takes the electric field $\mathbf{E}$ as a vector quantity, then it is equal to $-V/d$, where V to the voltage applied across a medium of length d. Thus in order to produce electric fields with positive gradients across the 85 kV X-ray tube a pulsed X-ray tube power supply has to be used, that generates a saw tooth waveform with voltage pulses, that have negative slopes (see Figure 3.2.6). At the same time $\nabla \times \mathbf{B}$ in equation 3.2.16 shows that a circular magnetic field arises around the current present in the dielectric medium as a result of the electric field gradient $\partial \mathbf{E}/\partial t$. It is also important to note, that equation 3.2.16 also explains why current emission can take place in the case of a constant electric field across the MgO film provided that the emission is initiated by a starter mechanism. With $\mathbf{E}$ having a constant value $\partial \mathbf{E}/\partial t$ becomes 0, so that equation 3.2.16 can be reduced to

$$\nabla \times \mathbf{B} = \mu_0 \mathbf{j} \tag{3.2.17}$$

From equation 3.2.17 one can deduce, that if the initial current emission from the cathode is equal to zero or if no starter mechanism is applied to the cathode under a constant electric field, then no magnetic field will be able to develop within the MgO layer of the cathode. Hence no current emission will be able to take place. However, as long as the condition that a nonzero initial current is provided is fulfilled, a magnetic field will be able to develop, even though $\partial \mathbf{E}/\partial t = 0$, and a constant current equal to the initial current will develop. Equation 3.2.16 is therefore in perfect agreement with the observations made by *Daglish* [9] and *Shroff* [2], that in order to cause electron emission form a cold cathode under a constant electric field it is necessary to create an initial current from the cold cathode by an external starter mechanism. All in all it can therefore be seen, that the starter mechanisms mentioned above for constant electric fields become completely

redundant for cold cathode X-ray tubes, if a changing electric field is introduced by applying pulsed voltages across the tube.

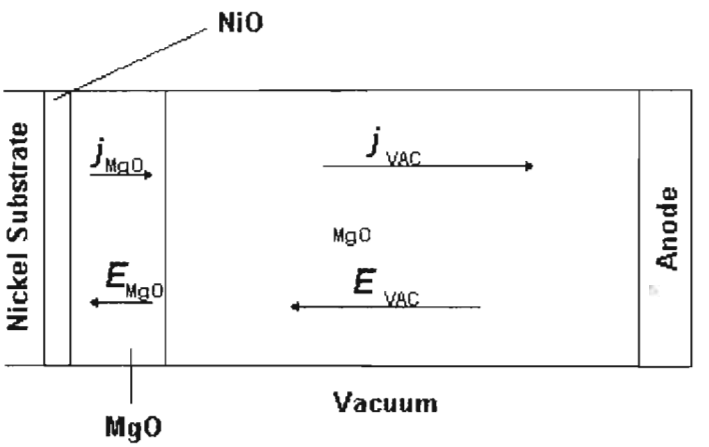

Fig. 3.2.5: Graphic representation of X-ray tube dielectric layers and the directions of the electric field E and the current density j across them.

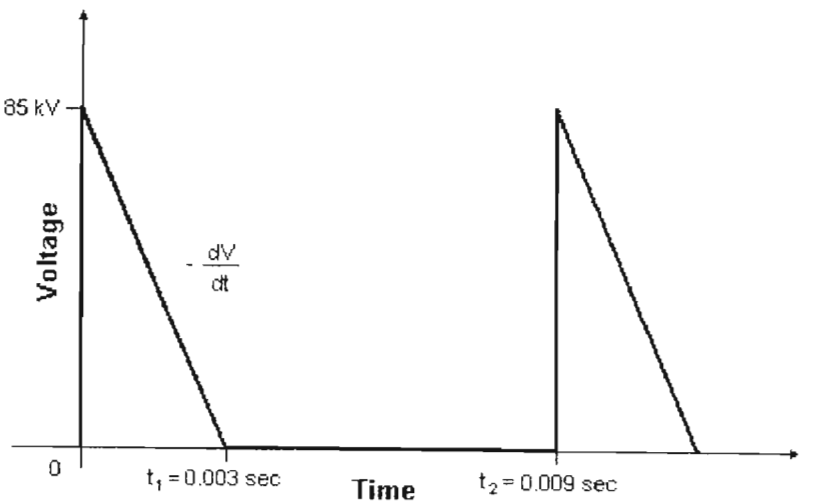

Fig. 3.2.6: Voltage waveform of an 85 kV X-ray power supply with negative gradient.

3.2.6. DETERMINATION OF CURRENT EMISSION FROM THE MgO COLD CATHODE

In order to determine theoretical values for currents produced by the MgO cold cathode it is necessary to determine the conductivity σ of MgO at room temperature (293 °K). The previous sections have shown that the total field enhanced secondary emission is caused by an intense electric field in the magnesium oxide film. This is a direct result of the formation of positive surface charges. It is therefore sufficient to merely consider the electron emission properties of MgO, since an equilibrium between the charging of the MgO surface and recombination with charges from the nickel substrate of the cathode is established during the electron emissive process [6]. The MgO sample to be measured for its conductivity was prepared as follows:

Magnesium oxide (MgO light) was mixed in a one-to-one ratio with magnesium carbonate ($MgCO_3$), where 2g of each substance were used. This mixture was then rolled in 15 cm^3 of amyl acetate and then diluted in 15 cm^3 of 1-propanol. The magnesium oxide cathode was prepared using this $MgO.MgCO_3$ mixture as it promised the highest emission rate according to measurements made by *Shroff* [2] (see figure 5.10, of this section). The amyl acetate and 1-propanol mixtures were employed as binders for the $MgO.MgCO_3$ powder as suggested by *Daglish* [9]. In this way it was possible to spray the final mixture onto a surface. Once applied to an insulating ceramic surface the amyl acetate and 1-propanol mixture was then allowed to evaporate from the $MgO.MgCO_3$ mixture by heating the prepared sample to a temperature of 40°C for an hour in a vacuum oven under a pressure of 10^{-4} Torr.

The conductivity of the MgO. $MgCO_3$ mixture was then determined experimentally using the four point method. By connecting a current source across a 3mm long MgO slab of cross sectional area $A = (0.4\times10^{-3}\ \text{m}) \cdot (3\times10^{-3}\ \text{m}) = 1.2\times10^{-6}\ \text{m}^2$, as illustrated in Figure 3.2.7, a potential difference of $\varphi = 27$ V was measured at an applied current of 10 μA. By applying these values in equation 3.2.18 [16] the conductivity σ of MgO was found to be $9.26\times10^{-4}\ \text{S m}^{-1}$.

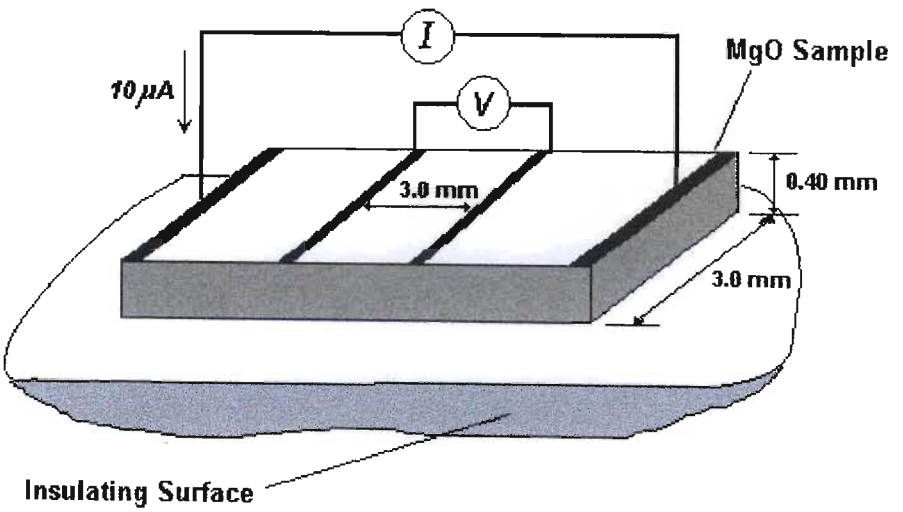

Fig. 3.2.7: Measurement of the conductivity of MgO using the four point method.

$$\frac{\varphi}{I} = \frac{l}{\sigma \cdot A} \tag{3.2.18}$$

Using a 111 Hz 85 kV power supply to operate the X-ray tube (see Figure 3.2.8 for voltage waveform) an expression for the power supply voltage output and hence the electric fields across the tube can be found. The equation for one voltage pulse of 0.003 sec duration across the entire tube (see equation 3.1.2, Section 3.1.2), i.e. the NiO-MgO-vacuum structure, is

$$V(t) = \frac{-8.5 \times 10^4}{0.003} t + 8.5 \times 10^4 \text{ Volts} \tag{3.2.19}$$

In section 3.2.4 it was found that V_2, the voltage across the magnesium oxide film, was 15.73 V when a voltage of 85 kV was applied across the tube. Therefore the voltage waveform across the MgO layer will have the same shape as that provided by the power supply (see Figure 3.2.8). However, the potential across the MgO film will peak at 15.73 V (see Section 3.2.4) rather than 85 kV while for the NiO layer the peak will be at 1.279×10^{-2} V. Thus the potentials developing inside the MgO and NiO layers during one pulse can be expressed using equations 3.2.20a and 3.2.20b:

$$V_{MgO}(t) = \frac{-15.73}{0.003} t + 15.73 \text{ Volts} \tag{3.2.20a}$$

$$V_{NiO}(t) = \frac{-1.279 \times 10^{-2}}{0.003} t + 1.279 \times 10^{-2} \text{ Volts} \tag{3.2.20b}$$

Therefore E_2 from section 3.2.4, namely the electric field across the MgO layer, can now be expressed as

$$E_2 = E_{MgO}(t) = \frac{V_2}{d_2} =$$

$$\frac{\frac{-15.73}{0.005} t + 15.73}{1 \times 10^{-4}} =$$

$$-5.243 \times 10^7 t + 1.573 \times 10^5 \text{ V m}^{-1} \tag{3.2.21a}$$

and E_1, the electric field across the NiO layer, can be written as

$$E_1 = E_{NiO}(t) = \frac{V_1}{d_1} =$$

$$\frac{\frac{-1.279 \times 10^{-2}}{0.003} t + 1.279 \times 10^{-2}}{1 \times 10^{-7}} =$$

$$-4.263 \times 10^{7} t + 1.279 \times 10^{5} \text{ V m}^{-1} \qquad (3.2.21b)$$

where the values for V_1 and V_2 are taken from equation 5.20 and $d_1 = 1\times10^{-7}$ m and $d_2 = 1\times10^{-4}$ m are the thicknesses of the NiO and MgO layers respectively. Keeping in mind that the current density $j = \sigma E$, the current density j emitted by the MgO film can be obtained by substituting the electric field E by E_2 in equation 3.2.22:

$$j\left(\frac{A}{m^2}\right) = \sigma \cdot E_2 \qquad (3.2.22)$$

The total current i_{field} emitted due to the electric field in the MgO layer into the vacuum of the X-ray tube by the cathode can be computed by multiplying the total surface area A of the MgO cathode by j. With the cathode having an outer radius of 0.014 m and an inner radius of 0.006 m, its surface area A is found to be equal to 1.256×10^{-4} m^2. Therefore the time dependent field current i_{field} becomes

$$i_{field}(t) = A \cdot j = 1.256\times10^{-4} \cdot \sigma \cdot E_{MgO}(t) \text{ Ampères}$$

$$1.256 \times 10^{-4} \text{ m}^2 . 9.26 \times 10^{-4} \text{ S m}^{-1} . \left(-5.243 \times 10^{7} t + 1.573 \times 10^{5} \text{ V m}^{-1}\right) =$$

$$-6.098t + 0.018 \text{ Ampères} \qquad (3.2.23a)$$

This relation is plotted in Figure 3.2.9 below illustrating how the current emitted during a single pulse by the MgO cold cathode decays with a negative electric field gradient $\partial\mathbf{E}/\partial\mathbf{t}$ according to the method described above.

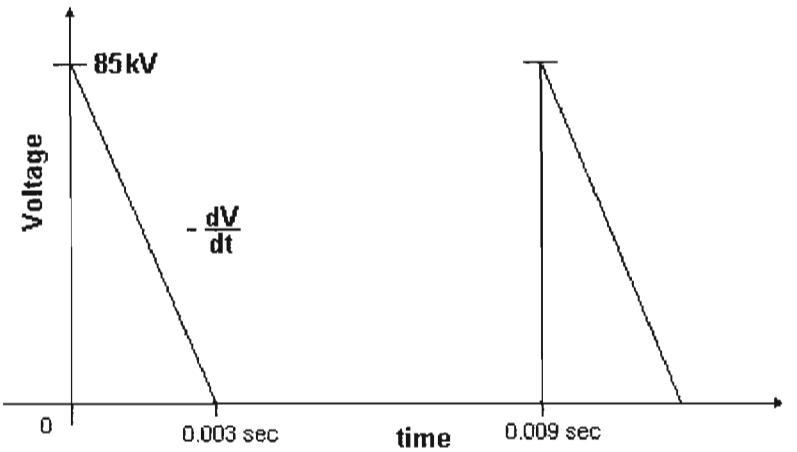

Fig. 3.2.8: Voltage waveform of a 111Hz 85 kV X-ray power supply with a 33,33% duty cycle.

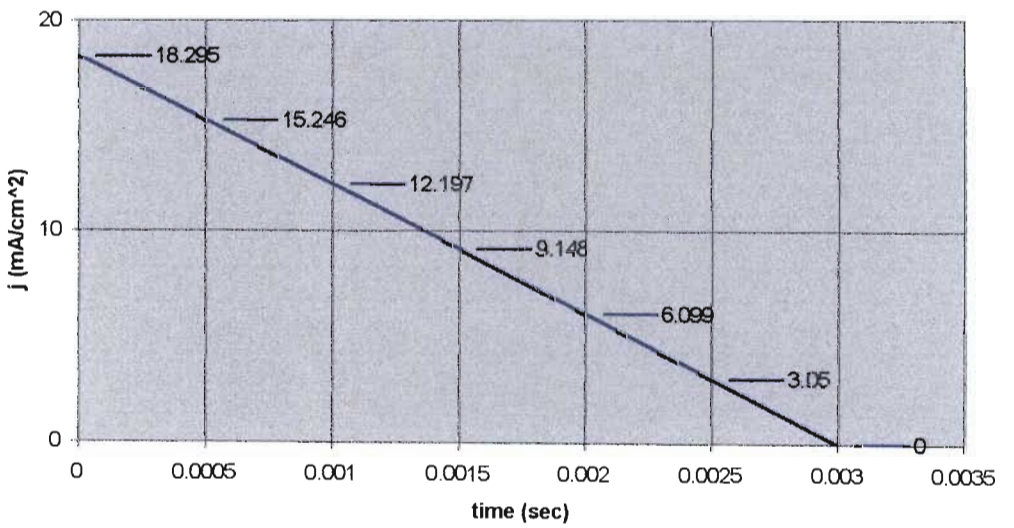

Fig. 3.2.9: Chart of current i_{field}(t) emitted by MgO cold cathode during one voltage pulse. The voltage waveform is shown in fig. 5.8.

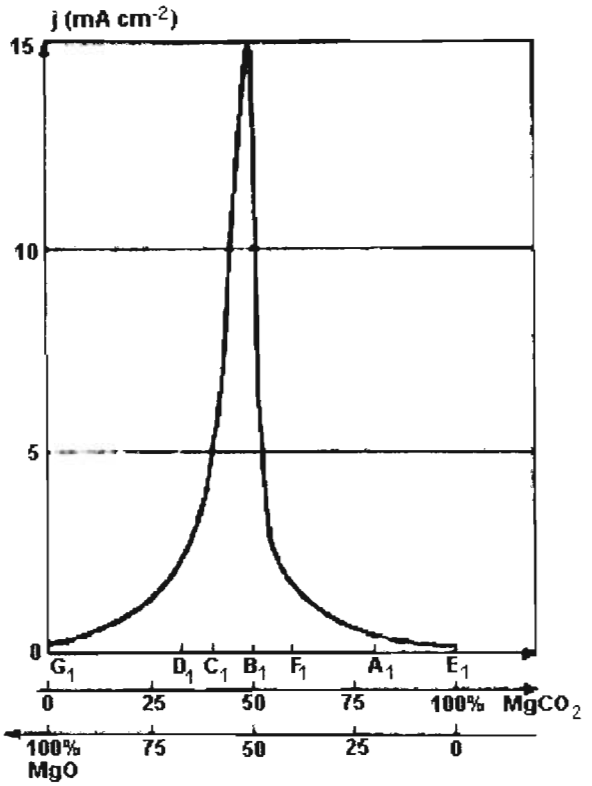

Fig. 3.2.10: Current density of emitted electrons versus cold cathode composition [2]

According to Figure 3.2.10 a maximum electron emission current density can be obtained, if MgO is mixed with $MgCO_3$ in a one-to-one weight ratio, so that a current emission density of 15 $mAcm^{-2}$ can be obtained [2]. This implies that a MgO cathode of 1.4 cm outside and 0.6 cm inside diameter would be capable of providing current densities of up to 19 mA cm^{-2}. It can be seen, that the maximum cathode current i_{field} = 18.295 mA, or alternatively the emitted current density j = 14.566 mA cm^{-2}, calculated using equation 3.2.23a, which is plotted in Figure 3.2.10, is somewhat lower than that measured by *Shroff* [2] (see Figure 3.2.10). However, one can say that the above two predictions (see Figure 3.2.9 and 3.2.10) are roughly in agreement with each other, whereby the total maximum emitted current i_{field} = 19 mA predicted by *Shroff* differs only by 3.88 % from the current value of 18.295 mA predicted by equation 3.2.23a. As in the case of the average power supply output current i_{AVE} (see Section 3.1.2) the average field current $i_{ave.field}$ can be obtained from equation 3.2.23a as follows:

$$i_{ave.field} = \frac{\int_0^{t_1} i_{field}(t)}{t_2} = \frac{\int_0^{t_1} -6.098t + 0.018}{t_2} =$$

$$\frac{\left[-3.049t^2 + 0.018t\right]_0^{0.003}}{0.009} =$$

$$3.048\times10^{-3} \text{ Ampères} = 3.048 \text{ mA}; \qquad (3.2.23b)$$

In conclusion we can see that electron emission from a MgO cold cathode can neither be attributed to the Schottky effect nor can it be explained via the Fowler-Nordheim relation (equation 3.2.5). At temperatures as high as 1100 °K a MgO cathode with a surface area of 1.256 cm^2 would be capable of providing a negligible current of only 9.411×10^{-5} mA (see Table 3.2.2, section 3.2.3), which leads us to exclude the possibility of the Schottky effect taking place in the cold cathode under the influence of a high electric field. At the same time one can see, that any value calculated for the emitted current density j using the Fowler-Nordheim equation approaches zero. This result would indicate that no current would be emitted from a MgO cold cathode under the influence of high electric fields, which, however, is not the case according to experimental observations [2,3...13]. With Maxwell's third law, or Ampère's law, however, it is evident that not only will a current pass through a dielectric medium provided a changing electric field is present across it, but that this is primarily due to a circular magnetic field, namely $\nabla \times \mathbf{B}$, that builds up in the dielectric layers of the cold cathode. Even if a constant electric field is applied across the dielectric medium, MgO in our case, a constant current will develop across the material together with a rotating magnetic field provided an initial current is present at the start of the emission process.

3.2.7. ADDITIONAL ELECTRON EMISSION DUE TO X-IRRADIATION OF THE CATHODE

From the end-window tube construction described in Chapter 3.1 (see Figure 3.1.1) one can see, that, once electrons have struck the target surface of the tube, the X-ray photons thus produced will not only leave through the window of the tube to irradiate a given specimen, but will also strike the surface of the cold cathode thus exciting further electrons in the nickel substrate of the MgO cathode. However, instead of falling back into their shells causing further X-ray photons to be emitted from the cathode itself, the electrons will, under the influence of the electric fields present in the NiO, MgO and vacuum layers of the tube, be able to travel all the way to the target [56]. As a result of this more electrons will be emitted from the cathode in addition to those being emitted solely under the influence of the electric fields mentioned above. In Figure 3.2.11 we can see how the cathode is positioned with respect the target face of the tube. In the figure one can clearly see that the cathode itself will receive X-radiation from the target [56].

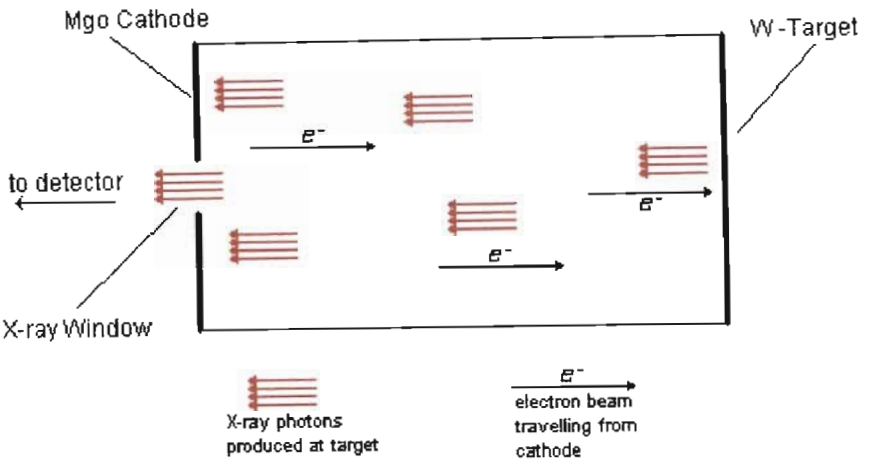

Fig. 3.2.11: Position of the MgO cold cathode with respect to the target/anode face of the tube [56].

According to *R. H. Fowler* [23] photoemission of electrons from a material can be considered as directly proportional to the photon energy incident on the surface of the material. Obviously it is this photon energy, be it in the form of visible or ultraviolet light, X-ray or radioactive radiation and so on, that causes electrons to be photoemitted from a given material. When a specimen is subjected to a bombardment of highly energetic electrons, X-rays will be produced from the specimen. This type of excitation is referred to as electron excitation, and the intensity of a K line resulting from such an interaction between the electrons and the specimen can be expressed in terms of equation 3.2.24:

$$I_K \propto i(V - V_K)^{\approx \beta} \tag{3.2.24}$$

where I_K is the intensity of a specific K line or the spectral intensity distribution of the primary radiation, V_K is the K-excitation potential (kV), V can be either the peak or the constant X-ray tube potential in kV, i is the X-ray tube current (mA) and β is a constant equal to 1.7 [24]. The quantity $(V - V_K)$ is the *overpotential* or *overvoltage*, while the exponent is a constant which has a value typically between 1.5 and 2. From equation 3.2.24 we can therefore see, that I_K is directly proportional to the tube current i. If we take this current to represent the photoemitted electrons described earlier it follows, that the K line intensity I_K of nickel is also directly proportional to the amount of electrons emitted from the nickel substrate of the cold cathode as a result of X-rays from the target striking it. Hence

$$I_K \propto i \tag{3.2.25}$$

where i is the X-ray tube current. In order to determine how much photocurrent is produced by the cold cathode and therefore how high the total tube current $i = i_{photo} + i_{field}$, where i_{field} is the

current emitted due to the field alone (see Figure 3.2.9, section 3.2.6), is it is necessary to calculate the fluorescence intensities of the fluorescent X-radiation emitted from nickel assuming that no electric fields are present and therefore no electrons are emitted. In the treatment of this problem it will also be assumed, that the X-rays emitted from the target of the X-ray tube will completely pass through the thin and porous MgO and NiO layers of the cathode causing emission of photoelectrons from its nickel sleeve. The intensities calculated in this manner will then be directly related to the total tube current i, which arises from the combined effect of the X-irradiation of the nickel substrate of the cathode and the high electric fields present in the dielectric layers of the tube i.e. the NiO, MgO and vacuum layers. In Section 3.2.11 of this chapter an idealised case be presented, in which it is assumed that all the electrons excited and removed from their atomic shells will be accelerated through the high electric fields present in the vacuum space of the tube towards the anode rather than undergo processes of recombination. The symbols that will be used in the intensity calculations in this section are illustrated in Table 3.2.3.

3.2.8. DEFINITION OF PRIMARY, SECONDARY AND TERTIARY FLUORESCENCE

Primary fluorescence results from the direct effect of the incident beam or primary radiation on the element considered, which in this case is nickel. To illustrate this point the K fluorescence line of Ni will be taken as an example. The incident radiation is that of a continuous spectrum I_λ starting at the short wavelength limit λ_0, which is defined as

$$\lambda_0 = \frac{hc}{E} = \frac{12.398}{E} \tag{3.2.26}$$

where λ_0 is expressed in Å units and E, the acceleration energy which in fact is the accelerating potential V in this case, is in keV. One basic rule for excitation is that only X-ray photons with an energy higher than that of the absorption edge can excite the K fluorescence of Ni. The remaining portion of the radiation cannot contribute to Ni K emission [22]. The primary fluorescence is the major contributor to emission in the specimen, and is solely responsible for fluorescent emissions in specimens of pure elements or when the fluorescent element is associated with elements with longer wavelength fluorescence lines [22]. Since we will concern ourselves merely with the impact of X-radiation on Ni it will be sufficient to take the primary fluorescence into account for our intensity calculations in the next section. Secondary fluorescence is often associated for an element of higher atomic number than that of the fluorescent element [22]. For instance if one has a Ni-Ag alloy submitted to an incident radiation from a W target, then both elements will be excited by the primary radiation from the target. Keeping in mind that one is looking at increasing excitation energies as one moves from Ni to Ag to W, it can be seen that the Ag Kα lines will be energetic enough to excite the Ni atoms. In this way an additional Ni emission will take place, which is referred to as secondary emission. Finally tertiary fluorescence can be explained in a similar way as secondary fluorescence. If we are looking at an alloy consisting of the three elements Cr-Ni-Ag and irradiate it with X-rays from a W target, then the secondary fluorescence of Ni will irradiate the less energetic Cr atoms thus producing tertiary fluorescence of Cr.

3.2.9. CALCULATION OF PRIMARY FLUORESCENCE

Consider a flat homogeneous specimen *s* of thickness h_{spec}, containing the fluorescent element *x* at the relative concentration C_x (Figure 3.2.12).

Table 3.2.3: Definitions of symbols used in intensity calculations [22].

Symbol	Description
ψ_1, ψ_2	incidence angle of primary radiation and emergence angle of fluorescent radiation, respectively, measured from the specimen surface (fig.5.12).
$A_G = \frac{\sin\psi_1}{\sin\psi_2}$	Geometrical factor.
$q = \frac{sin\psi_1}{sin\psi_2}\frac{\Omega}{4\pi}$	Collimation factor.
p	specimen density.
h_{spec}	specimen thickness.
C_x, C_y, C_z	relative concentrations of elements *x, y, z....*
I_λ	spectral intensity distribution of primary radiation.
λ	Wavelength.
λ_0	short wavelength limit of the spectral distribution.
$\lambda_{abs,x}, \lambda_{abs,y}, \lambda_{abs,z}$	Wavelengths of absorption edges of elements *x, y, z....*
$\lambda_x, \lambda_y, \lambda_z$	Wavelengths of fluorescent radiations of *x, y, z...*
μ_S	mass absorption coefficient of specimen *s* at wavelength λ.
$\mu_x \mu_y, \mu_z$	mass absorption coefficient of elements *x, y, z* at wavelength λ.
P_x	primary fluorescence of element *x* for a given spectral line.

The primary beam, of known spectral intensity distribution I_λ which is equivalent to I_K in equation 3.2.24, is assumed to be parallel and incident at an angle Ψ_1. The fluorescent radiation is observed at an emergence angle Ψ_2 [22]. The intensities are expressed in photons or counts per second and unit section^{-1} of the X-ray beams. The following calculations refer to the emission of the Kα line of Ni. According to *R. Tertian et al.* [22] with P_i the total fluorescence intensity the contribution $dP_i(\lambda, x)$ of the spectral band between λ and $\lambda + d\lambda$, and the volume element between x and $x + dx$ (see Figure 3.2.12), is dependent on the following factors:

1. The radiation intensity, represented by the factor *a*, that reaches the volume element is the incident intensity $I_\lambda d\lambda$, after attenuation by the path length $\frac{x}{\sin\psi_1}$,

$$a = I_\lambda d\lambda \exp\left[-\mu_{Ni,\lambda}\rho_{Ni}\frac{x}{\sin\psi_1}\right] \qquad (3.2.27)$$

where $\mu_{Ni,\lambda}$ is the mass absorption coefficient of the nickel specimen at wavelength λ. The limits of λ will be established later on in this section. The density of nickel, ρ_{Ni}, is equal to 8.9 g cm^{-3}.

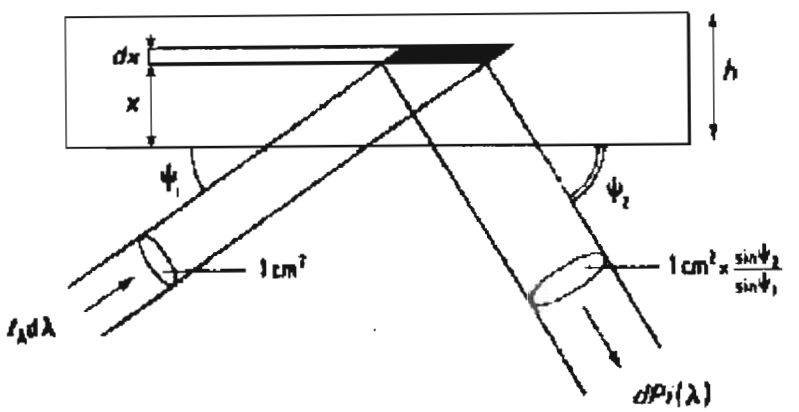

Fig. 3.2.12: Components in the calculation of primary fluorescence [22].

2. The fraction of the primary radiation that is absorbed in the volume element of nickel is

$$\mu_{Ni,\lambda}\rho_{Ni}\frac{dx}{\sin\psi_1} \tag{3.2.28}$$

From Figure 3.2.11 it can be seen, that the incidence angle of the primary radiation to the nickel surface is $\frac{\pi}{2}$ rad. Therefore $\sin\psi_1 = 1$, so that expression 3.2.28 can be rewritten as

$$\mu_{Ni,\lambda}\rho_{Ni}dx\ ;$$

3. The Kα fluorescence emission for instance is obtained by multiplying the number of absorbed photons by the excitation factor E_i

$$E_i = \frac{r_K - 1}{r_K}\omega_K g_{K\alpha} \tag{3.2.29}$$

which is the product of three probabilities: $\frac{r_K - 1}{r_K}$ is the probability of K excitation, $g_{K\alpha}$ is the probability emission of a Kα line in preference to other K lines and ω_K is the probability of the emitted Kα photon escaping from the atom [22]. In the case of the emission of K lines from a

given specimen the emission probability of a K line g_K in preference to other K lines is given by the intensity ratios $\frac{I(K\alpha_2)}{I(K\alpha_1)}$ for the $K\alpha_2$ line and $\frac{I(K\beta)}{I(K\alpha)}$ for the $K\beta$ line. The probability of emission of a $K\alpha_1$ line is 1. These probability values are given in Table 3.2.4 below for elements with atomic numbers 24 to 32.

Table 3.2.4: Intensity ratios for K spectra [27][28].

Element	$\frac{I(K\alpha_2)}{I(K\alpha_1)}$	$\frac{I(K\beta)}{I(K\alpha)}$
$_{24}$Cr	0.505	0.133
$_{26}$Fe	0.507	0.134
$_{28}$Ni	0.508	0.135
$_{30}$Zn	0.510	0.135
$_{32}$Ge	0.512	0.148

However, when taking the emission of L lines into account the emission probability of an L line in preference to another L line g_L can be expressed in terms of the vacancy distribution of L lines n_{KL_i}. One has to bear in mind, that when an atom has been ionised in an inner shell, in our case a K shell, it is deexcited through radiative or Auger transitions. In the radiative process the X-ray photon escapes from the atom as an excited L-shell electron falls back into its shell, while in the Auger transition the photon is absorbed within the atom itself on its way out and ionises the atom in an outer shell. For instance a Kα photon can leave an atom entirely in a radiative process or it can eject an L, M or N electron in an Auger transition. The values for $n_{KL_i}(A)$ due to Auger transitions and $n_{KL_i}(R)$ due to radiative transitions calculated from experimental data by *Rao et al.* [27][28] are illustrated in Table 3.2.5 for elements with atomic numbers 24 to 32.

Table 3.2.5: Average number of primary L_i subshell vacancies produced by transitions to the K shell: $n_{KL_i}(A)$ due to Auger transitions and $n_{KL_i}(R)$ due to radiative transitions. Also listed is the total number of primary L vacancies produced by Auger transitions [$n_{KL_i}(A)$], by radiative transitions [$n_{KL_i}(R)$], and by all transitions (n_{KL}) to the K shell [27][28].

Element	$n_{KL1}(A)$	$n_{KL2}(A)$	$n_{KL2}(R)$	$n_{KL3}(A)$	$n_{KL3}(R)$	$n_{KL}(A)$	$n_{KL}(A)$	n_{KL2}
$_{24}$Cr	0.214	0.559	0.083	0.474	0.165	1.247	0.248	1.495
$_{26}$Fe	0.201	0.485	0.103	0.447	0.203	1.133	0.306	1.439
$_{28}$Ni	0.185	0.415	0.123	0.410	0.242	1.010	0.365	1.375
$_{30}$Zn	0.170	0.353	0.142	0.372	0.279	0.895	0.421	1.316
$_{32}$Ge	0.154	0.298	0.159	0.333	0.311	0.785	0.470	1.255

According to *Williams* [29] the probability ω of a photon escaping from an atom, which is also known as the fluorescence yield, refers to a situation where the photon emission is caused by accelerating electrons colliding with the atoms of a given material. This means that ω_K, ω_L and ω_M are the probability of a K photon, a L photon and a M photon escaping from an atom respectively. In our case we therefore have to consider the target material of the X-ray tube, which is tungsten, in order to determine the values of ω_K, ω_L and ω_M. According to *Bertin* [25] (see Appendix 6) the values of ω_K, ω_L and ω_M for tungsten have been found to be 0.944, 0.304 and 0.018 respectively. The graph in Figure 3.2.13 is a plot of fluorescence intensity ω in terms of atomic number Z. The probability of K excitation $\frac{r_K - 1}{r_K}$ and L excitation $\frac{r_L - 1}{r_L}$ on the other hand, which is also known as the absorption jump factor, has to be used in reference to the irradiated material, which is the nickel substrate of the cold cathode of the X-ray tube. In Table 3.2.6 the selection of parameters for characteristic fluorescence is illustrated, where G denotes the element excited by element H.

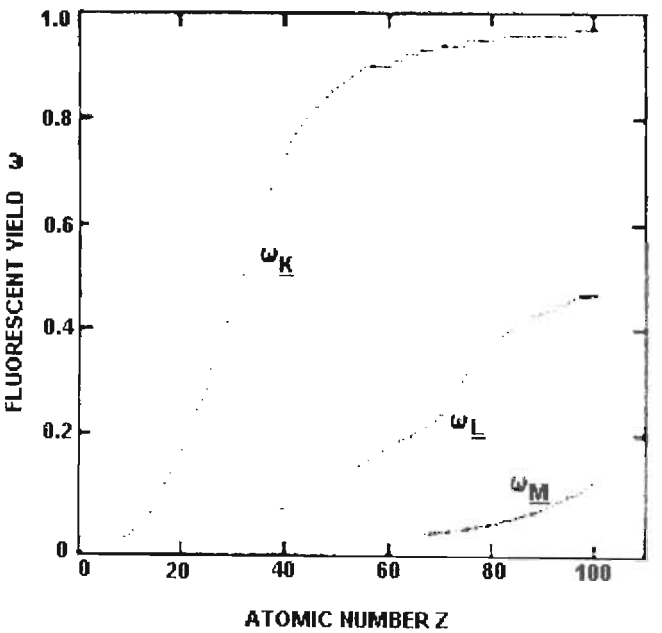

Fig. 3.2.13: Graph of fluorescence yields ω_K, ω_L and ω_M as a function of atomic number Z. Data taken from ref. 24.

Table 3.2.6: Selection parameters for characteristic fluorescence (excitation of element G by element H) [29].

	For $\omega(H)$, use	For $\omega(G)$, use
$K_H \rightarrow K_G$	$\omega_K(H)$	**K edge**
$K_H \rightarrow L_G$	$\omega_K(H)$	**L edge**
$L_H \rightarrow K_G$	$\omega_L(H)$	**K edge**
$L_H \rightarrow L_G$	$\omega_L(H)$	**L edge**

In Figure 3.2.13 one can see the fluorescence yields ω plotted as a function of atomic number Z. Both the K and L absorption jump factors are given in Table 3.2.7 below.

Table 3.2.7: K and L absorption jump factors for elements Co, Ni and Cu. Data taken from ref. 25 (see Appendix 7).

Element	$\frac{r_K - 1}{r_K}$	$\frac{r_L - 1}{r_L}$
$_{27}$Co	0.881	-
$_{28}$Ni	0.873	0.639
$_{29}$Cu	0.874	0.652

4. The fluorescent radiation is emitted uniformly in every direction and the fraction that enters the collimator is

$$c = \frac{\Omega}{4\pi} \tag{3.2.30}$$

where $d\Omega$ is the solid angle defined by a collimator, i.e. the angle between the electron beam incident on the target and the reflected primary X-ray beam emerging from a collimator [22]. In the case of the end window cold cathode X-ray tube (see Section 3.1) no collimators are used. However, the primary X-ray beam will be at an angle of π radians to the electron beam incident upon the target due to the end window design of the X-ray tube (see Section 3.1). Hence Ω can be assumed to being equal to π radians and so the factor c can be evaluated as

$$c = \frac{\pi}{4\pi} = \frac{1}{4}$$

5. The fluorescent radiation λ_{Ni} emitted in the direction of the collimator is in turn attenuated by the path length $\frac{x}{\sin\psi_2}$ in the nickel, and the transmitted fraction is

$$d = exp\left[-\mu_{s,\lambda_{Ni}}\rho_{Ni}\frac{x}{sin\psi_2}\right] \tag{3.2.31}$$

The emergence angle of fluorescent radiation ψ_2 is equal to $\frac{\pi}{2}$ rad i.e. $\sin\psi_2 = 1$.

6. An additional factor

$$e = \frac{\sin\psi_1}{\sin\psi_2} = 1 \tag{3.2.32}$$

must be applied to adjust the intensity to a unit section of the emergent beam [22]. The intensity $dP_i(\lambda,x)$ is the product of the factors a,b,c,d,e and E_i. By defining

$$q = \frac{sin\psi_1}{sin\psi_2}\cdot\frac{\Omega}{4\pi} \tag{3.2.33}$$

and rearranging terms one obtains the following expression [22]:

$$dP_i(\lambda,x) = qE_iC_i\frac{\rho_{Ni}}{\sin\psi_1}\mu_{Ni,\lambda}I_\lambda d\lambda\exp\left[-\rho_{Ni}x\left(\frac{\mu_{s,\lambda}}{\sin\psi_1}+\frac{\mu_{s,\lambda_{Ni}}}{\sin\psi_2}\right)\right]dx \tag{3.2.34}$$

By integrating from $x = 0$ and $x = h_{spec}$ the fluorescence intensity from the $I_\lambda d\lambda$ element of the incident radiation becomes

$$dP_i(\lambda) = qE_iC_i\left\{1-exp\left[-\rho_{Ni}h_{spec}\left(\frac{\mu_{s,\lambda}}{sin\psi_1}+\frac{\mu_{s,\lambda_{Ni}}}{sin\psi_2}\right)\right]\right\}\frac{\mu_{Ni,\lambda}I_\lambda d\lambda}{\mu_{s,\lambda}+\frac{sin\psi_1}{sin\psi_2}\mu_{s,\lambda_{Ni}}} \tag{3.2.35}$$

Thus if one integrates over the useful range λ from λ_0 to $\lambda_{abs.Ni}$ the total or integrated fluorescence intensity becomes

$$P_i = qE_iC_i\int_{\lambda_0}^{\lambda_{abs.Ni}}\left\{1-exp\left[-\rho_{Ni}h_{spec}\left(\frac{\mu_{s,\lambda}}{sin\psi_1}+\frac{\mu_{s,\lambda_{Ni}}}{sin\psi_2}\right)\right]\right\}\frac{\mu_{Ni,\lambda}I_\lambda d\lambda}{\mu_{s,\lambda}+\frac{sin\psi_1}{sin\psi_2}\mu_{s,\lambda_{Ni}}} \tag{3.2.36}$$

According to *Tertian et al.* [22] a specimen is defined as thick when h_{spec} in equation (3.2.36) is

sufficiently large to make the exponential term negligible compared to unity. By defining the geometrical factor

$$A = \frac{\sin\psi_1}{\sin\psi_2} \tag{3.2.37}$$

equation (3.2.36) then reduces to

$$P_i = qE_iC_i \int_{\lambda_0}^{\lambda_{abs}} \frac{\mu_{i,\lambda} I_\lambda d\lambda}{\mu_{s,\lambda} + A\mu_{s,\lambda_i}} \tag{3.2.38}$$

This formula is most important as in practice the majority of intensities measured can be considered as emanating from thick specimens, since h_{spec} is generally larger than a few mm. In actual fact h can be less than 1 mm and still be considered thick. In equation (3.2.36) $\mu_{s,\lambda}$ and μ_{s,λ_i} have equal values since one is dealing with a clean metal containing nickel only. If we consider the case of $K\alpha_1$ emission, then we have a wavelength of 1.658 Å for the $K\alpha_1$ line of nickel (see Appendix 3). At that wavelength the mass attenuation coefficient for nickel is equal to an estimated 50 cm^2g^{-1} (see Appendix 4). With ρ_{Ni}, the density of nickel, equal to 8.9 g cm^{-3} and h_{spec} = 0.02 cm one obtains the following value for the exponent in equation 3.2.36:

$$exp\left[-\rho h_{spec}\left(\frac{\mu_{s,\lambda}}{sin\psi_1} + \frac{\mu_{s,\lambda_i}}{sin\psi_2}\right)\right] =$$

$$\exp\left[-8.9\ \mathrm{g\ cm^{-3}} \cdot 0.02\mathrm{cm} \cdot \left(\frac{50\mathrm{cm^2\ g^{-1}}}{1} + \frac{50\mathrm{cm^2\ g^{-1}}}{1}\right)\right] \approx$$

$$1.86\times10^{-8},$$

which is indeed negligible compared to unity. Therefore it can be concluded, that equation 3.2.38 is certainly applicable for the calculation of the primary fluorescence of nickel P_{Ni}.

3.2.10. CALCULATION OF RELATIVE CHARACTERISTIC LINE AND CONTINUOUS RADIATION INTENSITIES OF NICKEL EXCITED BY X-RAYS FROM A TUNGSTEN TARGET

In order to calculate the contribution made by each emission line of nickel to the overall relative radiation intensity of nickel when excited by X-ray photons from the tungsten target of the X-ray tube, in terms of the K line fluorescence yield ω_K, the L line fluorescence yield ω_L and the M line fluorescence yield ω_M of tungsten, it is necessary to first take the voltage pulse of the X-ray tube power supply into account (see Figure 3.2.8, Section 3.2.6). In Figure 3.2.14 we can see the same voltage pulse, but additional information is also given as to the time values, at which the pulse will pass a critical excitation energy point of a given line.

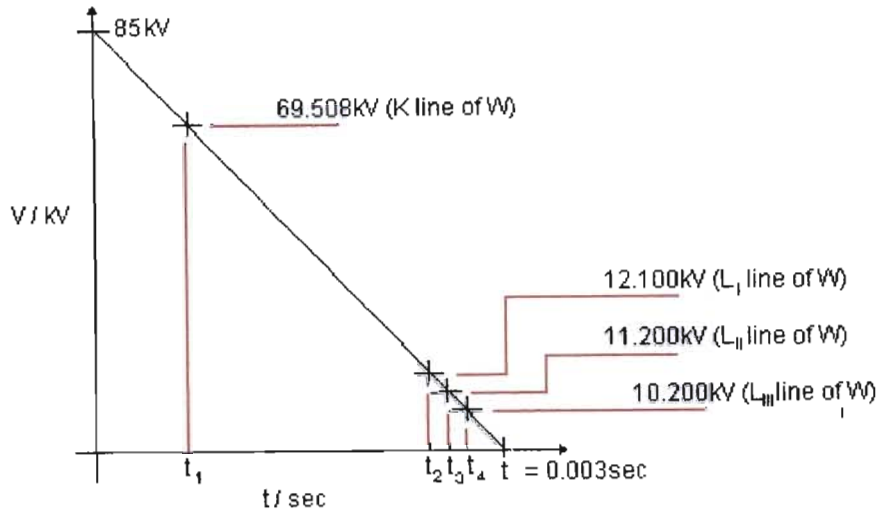

Fig. 3.2.14: Accelerating potential curve for the X-ray tube with times at which the different critical excitation potentials of W are passed.

As in Section 3.1.2 and 3.2.6 the voltage waveform of the pulse in Figure 3.2.14 above is given by

$$V(t) = -\frac{85}{0.003}t + 85 =$$

$$-28333t + 85 \ \text{kV} \tag{3.2.39}$$

where the accelerating potential V is given in kV and the time t is given in seconds. From equation 3.2.39 and Figure 3.2.14 one can easily compute the time intervals $0 \rightarrow t_1$, $t_1 \rightarrow t_2$, $t_2 \rightarrow t_3$, $t_3 \rightarrow t_4$ and $t_4 \rightarrow t = 0.003$ sec. Their values are given below in Table 3.2.8.

Table 3.2.8: Time intervals between the critical excitation potentials for the K and L lines of W during one voltage pulse.

	$V_{crit,n}$ (kV)	$t_n(\text{sec}) = \frac{V_{crit.} - 100}{-20000}$	$t_n - t_{n-1}(\text{sec})$
$0 \rightarrow t_1$, n=1	69.508	5.474×10^{-4}	5.474×10^{-4}
$t_1 \rightarrow t_2$, n=2	12.100	2.576×10^{-3}	2.029×10^{-3}
$t_2 \rightarrow t_3$, n=3	11.538	2.596×10^{-3}	2.000×10^{-5}
$t_3 \rightarrow t_4$, n=4	10.200	2.643×10^{-3}	4.700×10^{-5}

For the time interval $0 \rightarrow t_1$ all the emission lines of the tungsten target act on the nickel, and so the primary intensities of nickel in terms of the K fluorescence yield ω_K and the L fluorescence yield ω_L of tungsten must be taken into account. During the intervals $t_1 \rightarrow t_2$, $t_2 \rightarrow t_3$ and $t_3 \rightarrow t_4$ the K-lines of the tungsten target are no longer excited, because the accelerating potential becomes lower than the critical excitation potential of 69.508 kV. Only the photons emitted from the L and M shells of tungsten act on the nickel, which are still sufficiently energetic to excite the K shell electrons of nickel (E_K = 8.332 keV, see Appendix 5). From the Table in Appendix 5 we can see that even the least energetic photon produced by an electron in the M shell of tungsten ($E_{M\zeta_1}$ = 1.384 keV for W as compared to $E_{L\eta}$ = 0.762 keV, the energy of the least energetic electron in the L shell of Ni) is still energetic enough to have an impact on all the electrons in the L shell of the nickel atoms. Thus during these intervals the fluorescence intensities depend on ω_L and ω_M. During the interval $t_4 \rightarrow t$ = 0.003 sec only the photons produced by the M shell electrons of the tungsten target have an effect on the nickel atoms. At this stage the radiation from the tungsten is sufficient to excite the L shell electrons of the nickel atoms only. The energies of the Ni M lines are so small (E_M = 0.065 keV), that their contribution to the fluorescence intensity and hence the electron emission from nickel can be considered insignificant. In Table 3.2.9 all the parameters that need to be taken into account for each of the aforementioned intervals are given.

Table 3.2.9: Parameters used in the calculation of Ni fluorescence intensities P_i for the different time intervals during one voltage pulse (see Figure 3.2.14) applied across the X-ray tube.

Time interval	Fluorescence yield ω of element W	Absorption jump factor $\frac{r-1}{r}$ of element Ni	Ni shells subjected to electron excitation
$0 \rightarrow t_1$	ω_K, ω_L and ω_M	$\frac{r_K-1}{r_K}$ and $\frac{r_L-1}{r_L}$	K , L
$t_1 \rightarrow t_2$	ω_L and ω_M	$\frac{r_K-1}{r_K}$ and $\frac{r_L-1}{r_L}$	K , L
$t_2 \rightarrow t_3$	ω_L and ω_M	$\frac{r_K-1}{r_K}$ and $\frac{r_L-1}{r_L}$	K , L
$t_3 \rightarrow t_4$	ω_L and ω_M	$\frac{r_K-1}{r_K}$ and $\frac{r_L-1}{r_L}$	K , L
$t_4 \rightarrow t$ = 0,003 sec	ω_M	$\frac{r_L-1}{r_L}$	L

Before going on with the calculations of the relative intensities of the X-radiation from nickel during each of the aforementioned time intervals attention should be drawn to the fact, that the overall intensity during each time interval obtained constitutes the sum of all the intensities of the different nickel emission lines during that interval i.e.

$$P(\Delta t) = \sum P_i(\omega) \tag{3.2.40}$$

where $P(\Delta t)$ denotes the overall nickel radiation intensity during the time interval Δt and $\sum P_i(\omega)$ is the sum of all the individual emitted photons in a nickel atom depending on the K, L and M fluorescence yields of tungsten. With $q = \frac{1}{4}$, $\mu_{i,\lambda} = \mu_{s,\lambda}$, $C_i = 1$ and $A = 1$ (see section 3.2.9) equation 3.2.38 can also be expressed as follows:

$$P_i = \frac{1}{4} \times E_i \times 1 \times \int_{\lambda_0}^{\lambda_{abs,i}} \frac{1}{2} \cdot I_\lambda d\lambda =$$

$$P_i = \frac{1}{2} \cdot \frac{1}{4} \times E_i \times 1 \times \int_{\lambda_0}^{\lambda_{abs,i}} I_\lambda d\lambda =$$

$$P_i = \frac{1}{8} \cdot E_i \cdot [\lambda]_{\lambda_0}^{\lambda_{abs,i}} \cdot I_\lambda =$$

$$P_i = \frac{1}{8} \cdot E_i \cdot \left[\lambda_{abs,i} - \lambda_0\right] I_\lambda \tag{3.2.41}$$

By substituting equation 3.2.29 into equation 3.2.41 P_i becomes

$$P_i = \frac{1}{8} \cdot \frac{r-1}{r} \omega \cdot g \cdot \left[\lambda_{abs,i} - \lambda_0\right] I_\lambda \tag{3.2.42}$$

where $\frac{r-1}{r}$ is the absorption jump factor of an emission line of the irradiated material, ω is the fluorescence yield for an emission line of the element which excites the specimen element and g is the probability of emission of a given line in preference to another line for the irradiated specimen, which is nickel in our case. Again it is important to point out, that λ_0 is the critical wavelength or minimum wavelength given by

$$\lambda_0 = \frac{12.396}{V} \tag{3.2.43}$$

where the tube potential V and the critical wavelength λ_0 are given in kV and Å respectively as given by equation 3.2.39, which can then be substituted into equation 3.2.43 to give us the following expression:

$$\lambda_0 = \frac{12.396}{-28333t + 85} \text{ Å} \tag{3.2.44}$$

Substituting this into equation 3.2.42 we finally obtain

$$P_i = \frac{1}{8} \cdot \frac{r-1}{r} \omega \cdot g \cdot \left[\lambda_{abs,i} - \frac{12.396}{-28333t + 85} \right] I_\lambda =$$

$$P_i = \frac{1}{8} \cdot \frac{r-1}{r} \omega \cdot g \cdot \left[\frac{\lambda_{abs,i}(28333t + 85) + 12.396}{28333t + 85} \right] I_\lambda \qquad (3.2.45)$$

The above calculation can be accomplished for every nickel emission line in this way. In Table A2 (see Appendix 2) the different values for the selection parameters and their respective relative intensities $P_i(t)$ discussed above are listed for each nickel emission line in terms of the tungsten fluorescence yields ω_K, ω_L and ω_M (see Table A2, Appendix 2). If we take the $K\alpha_1$ line emitted from nickel under the influence of an incident tungsten K line for instance, the calculation of the relative intensity of such a nickel line is obtained in the following manner:

The value for $P_{K\alpha_1(K)}(t)$, the relative fluorescence intensity of nickel when irradiated by a tungsten K line, is determined using equation 3.2.45, which we have derived in this section. Since we are considering the intensity of a nickel $K\alpha_1$ line, the absorption jump factor for the K line of nickel has to be used, which is $\frac{r_K - 1}{r_K}$ = 0.873 (see Table 3.2.7). The values for the term $\frac{r-1}{r}$ for the nickel K and L lines are taken from Table 3.2.7 in Section 3.2.9. The emission of this particular line is a result of the interaction of a tungsten K line and nickel, so that the fluorescence yield for the K line of tungsten, ω_K = 0.873, has to be used. The values for the different fluorescence yields ω in Table A2 (Appendix 2) are plotted in the graph of Figure 3.2.13 and have been determined both theoretically and experimentally by *Reed* [30] whereas *Bertin* [25] lists values for the absorption jump factors and the fluorescence yields that were commonly accepted before *Reed's* findings. The transition probability g for the $K\alpha_1$ line of nickel is 1, since the transition lines for all the other emission lines of nickel are expressions relative to the $K\alpha_1$ line. The transition probabilities for all the other nickel lines are given in Tables 3.2.4 and 3.2.5. As discussed earlier the excitation factor E_i is a product of the fluorescence yield, the absorption jump factor and the transition probability. Substituting the above probability values, $\lambda_{abs,Ni(K)}$ and the expression derived for λ_0 in equation 3.2.44 into equation 3.2.45 a value for the relative intensity $P_{K\alpha_1(K)}(t)$ of the nickel $K\alpha_1$ line due to its irradiation by a tungsten K line can be found. For this particular case we therefore obtain

$$P_{K\alpha_1(K)}(t) = \frac{4342.02t + 14.31}{28333t + 85} I_\lambda$$

All the other values for $P_i(t)$ can be obtained in a similar manner and are listed in Table A2 (Appendix 2).

Earlier in this section it was pointed out, that during one voltage pulse applied across the X-ray tube all the emission lines of the tungsten target act on the nickel surface initially. Once the critical excitation energy for the tungsten K line has been passed during the pulse only the L and M emission lines emitted from the tungsten target will affect the nickel substrate of the cold cathode structure. As the output voltage of the pulse continues to drop the same process as above takes place again once the point of critical excitation for the L lines has been passed leaving only the M lines to excite the nickel (see Figure 3.2.14). Therefore the pulse has been divided into time intervals, namely the time intervals between the different excitation energies, so that the overall contribution of the emission lines from tungsten to the characteristic line emission from nickel during each time interval can be assessed. In Table 3.2.11 the five time intervals under consideration (see Figure 3.2.14) are listed. Also shown in the Table are the tungsten emission lines which act on nickel during each of the aforementioned time intervals. The term $\sum P_i(t)$ is the sum of all the relative intensities of the nickel emission lines and hence the total emission intensity of the characteristic emission lines of nickel during each time interval. In Table 3.2.10 the total intensities $\sum P_i(t)$ in terms of each tungsten fluorescence yield ω_K, ω_L and ω_M i.e. each total intensity value due to the K, L and M emission lines respectively, are shown.

Table 3.2.10: Total intensity $\sum P_i(t)$ for every tungsten emission line.

Tungsten emission line	Tungsten fluorescence yield	Total intensity $\sum P_i(t) \times I_\lambda$
K	ω_K	$\frac{125478.16t + 382.39}{28333t + 85}$
L	ω_L	$\frac{40406.56t + 123.15}{28333t + 85}$
M	ω_M	$\frac{2392.62t + 7.28}{28333t + 85}$

Table 3.2.11: Total intensities $\sum P_i(t)$ for every time interval $t_{n-1} - t_n$ during one voltage pulse of the form $V = -28333t + 85$ kV.

Time interval	Tungsten emission lines acting on nickel during the time interval	Nickel emission lines produced during the time interval	Total relative intensity $\sum P_i(t)$ of nickel emission lines during the time interval
$0 \rightarrow t_1$	K, L, M	K, L, M	$\frac{168277.34t + 512.82}{28333t + 85} I_\lambda$
$t_1 \rightarrow t_2$	L, M	K, L, M	$\frac{42799.18t + 130.43}{28333t + 85} I_\lambda$
$t_2 \rightarrow t_3$	L, M	K, L, M	$\frac{42799.18t + 130.43}{28333t + 85} I_\lambda$
$t_3 \rightarrow t_4$	L, M	K, L, M	$\frac{42799.18t + 130.43}{28333t + 85} I_\lambda$
$t_4 \rightarrow 0{,}003\,\text{sec}$	M	K, L, M	$\frac{2392.62t + 7.28}{28333t + 85} I_\lambda$

So far only the X-irradiation of the cathode in terms of the tungsten characteristic emission lines has been discussed. In addition to that, however, the radiation due to *Bremsstrahlung* also has to be taken into account. The *continuous spectrum*, also known as the *continuum*, *white* spectrum, *general* spectrum, and *Bremsstrahlung*, is characterised by four major features: a continuous range of wavelengths (analogous to white light), having an abrupt short wavelength limit at $\lambda_{\min}$, rising to a maximum intensity λ_{imax}, then gradually decreasing in intensity at longer wavelengths [24]. In Figure 3.2.15 a typical example of such a continuum profile with the K, L and M characteristic line spectra is shown. The relative intensity at any given wavelength λ of such a continuum can be approximated by the Kramers formula,

$$I_\lambda \propto iZ\left(\frac{1}{\lambda_{\min}} - \frac{1}{\lambda}\right)\frac{1}{\lambda^2} \tag{3.2.46}$$

where I_λ is the intensity at wavelength λ, $\lambda_{\min}$ is the short-wavelength limit, i is the X-ray tube current, and Z is the atomic number of the X-ray tube target.

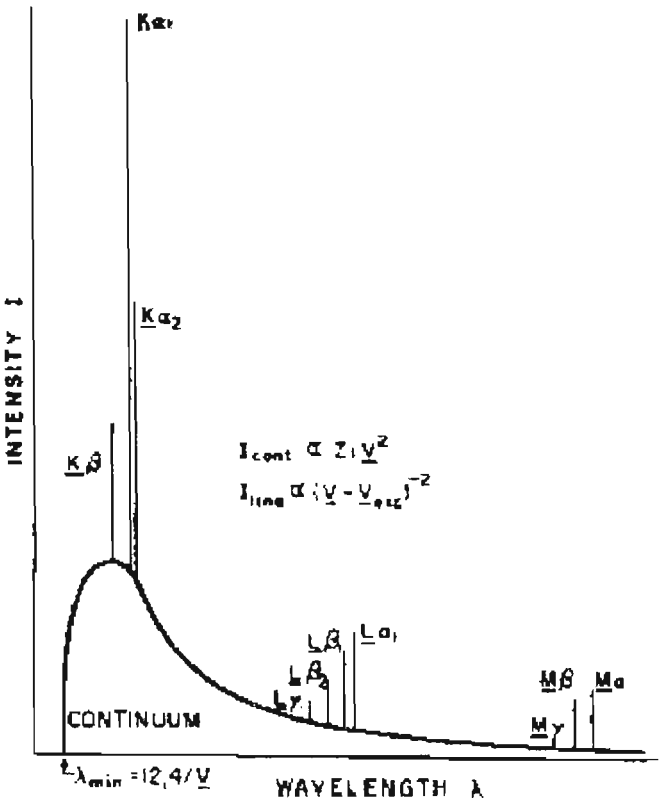

Fig. 3.2.15: Typical X-ray spectrum of a heavy element, showing the continuous spectrum and K, L and M characteristic line spectra [24].

The continuum arises when high speed electrons undergo stepwise deceleration in matter. The principal source of high intensity continuum is in fact the X-ray tube. If we consider an electron moving from the cathode to the target of the X-ray tube operating at potential V, then the shortest wavelength λ_{min} that this electron can generate is emitted if the electron upon striking the target decelerates to zero in a single step, giving up all its energy as one X-ray photon [24]. This wavelength is given by equation 3.2.43, namely

$$\lambda_{min} = \frac{12.396}{V}$$

The term V refers to the maximum accelerating potential, that an electron experiences at any given time. However, most electrons actually give up their energy in numerous unequal decrements ΔV resulting in the production of X-ray photons of wavelength $\lambda = \frac{12.396}{\Delta V} > \lambda_{min}$. The overall result of electrons bombarding the target undergoing such stepwise deceleration is the generation of a continuous spectrum of wavelengths $\geq \lambda_{min}$. The effect of X-ray tube target atomic number Z,

current i, and potential V on the integrated continuum intensity can be expressed by the Beatty formula [24]

$$I_{int} = \left(1.4 \times 10^{-9}\right) ZiV^2 \tag{3.2.47}$$

where I_{int}, i and V are in watts, amperes, and volts, respectively [24]. It is obvious that none of these parameters substantially affects the general profile of the continuum. While the short-wavelength limit is merely affected by V, a change in the X-ray tube current causes a proportional change in continuum intensity since the number of electrons interacting with the target is directly proportional to the current. The target atomic number Z has much the same effect as the number of orbital electrons in each target atom is directly proportional to Z. It is evident, that the X-rays produced at the target of the tube will contain a continuum for the entire duration of a single voltage pulse (see Figure 3.2.14, section 3.2.10) applied across the X-ray tube. As the voltage drops with time during one pulse, so the continuum intensity will diminish and at the same time the short-wavelength limit will increase. Overall the continuum of the X-radiation will excite the atoms in the nickel substrate of the cathode in addition to the characteristic line radiation described in the previous sections of this chapter. It should be borne in mind, that the excited electrons in the nickel under the influence of a high electric field will be unable to return to their previous states thus releasing an X-ray photon each, but will instead be accelerated through the dielectric layers of the tube to the target thus adding to the overall tube current. It is important to point out, that not all of the electrons contained in a given energy level of a nickel atom in the cathode will be removed. The fluorescence yield ω of a given energy level of an element gives the number of electrons in a given shell that effectively leave the atom under the influence of X-radiation. Only these electrons can then be accelerated as photoelectrons under the influence of an electric field from the cathode to the anode of the X-ray tube rather than recombine. It can therefore be said that the current in the tube will arise due to a combination of the changing high electric field present in the cathode and the X-irradiation, consisting of the tungsten characteristic lines as well as the tungsten continuous spectra, of its surface.

3.2.11. EFFECT OF X-RADIATION ON FURTHER CURRENT EMISSION FROM THE COLD CATHODE

If we take into account that the photoemission of electrons from a material can be considered as being directly proportional to the photon energy incident on the surface of the material [23] (see section 3.2.7), then it can be seen, that the values calculated for the relative fluorescence intensities of nickel when excited by tungsten can be directly related to the electron emission from nickel under the combined influence of a high electric field and X-irradiation of the nickel surface. In section 3.2.10 the relative intensities of nickel were calculated assuming that no electric fields were present. Therefore once excited by the X-rays produced by the tungsten anode the nickel substrate of the cold cathode will only emit X-ray photons as the excited electrons of the nickel atoms fall back into their shells. However, under the influence of a high electric field acting on the surface of the nickel substrate, the excited electrons will be prevented from returning to their shells. Instead they will be accelerated by these fields from the nickel surface through the NiO, MgO and vacuum dielectric layers of the X-ray tube to its target. In this way, as a result of the irradiation of the nickel substrate, further electrons will be removed from the cathode. This additional current given off by the cathode can therefore be considered as directly proportional to the intensity of the X-ray photon emission from nickel. This means that

$$I_\lambda \propto i_F$$

where I_λ is the intensity of the X-radiation, containing both tungsten characteristic emission lines as well as its continuum, acting on the cathode. Therefore current emission from the MgO cold cathode can be described as a combination of the following three effects:

1. Initially all of the current emitted from the cathode can be attributed to the changing electric field created within the dielectric layers of the X-ray tube as voltage pulses with negative gradients are applied across the tube (see Figure 3.2.8 and 3.2.9).

2. As soon as X-radiation produced at the target reaches the cathode further electrons are excited and removed from the cathode thus adding to the total tube current. The X-radiation contains both the characteristic lines of tungsten as well as its continuum. These two effects each contribute to the removal of additional electrons from the cathode under the influence of a high electric field. The nickel intensities of its characteristic lines produced by X-irradiating the surface of the cathode are directly dependent on the initial tube current according to equation 3.2.24, which is once again shown below,

$$I_K \propto i\left(V - V_K\right)^{\approx\beta}$$

Since I_K or I_λ is directly proportional to the initial tube current i, the combined fluorescence intensity $\sum P_i$ of nickel (see section 3.2.9), which is directly proportional to the intensity of the initial radiation I_λ, can therefore also be directly related to i. The current produced by the irradiation of the nickel substrate by the tungsten characteristic lines can therefore be expressed by equation 3.2.48 below

$$i_{char} = a \cdot P_i\left(t,i\right) \tag{3.2.48}$$

where i_{char} is the current produced as a result of the irradiation of nickel by the tungsten characteristic lines, a is a constant of proportionality and $P_i\left(t,i\right)$ is the primary fluorescence, which is a function of time and the initial tube current i.

3. The tungsten continuum finally adds to the overall tube current in the same way as the characteristic X-radiation from the target discussed above. The intensity produced by this type of radiation can be expressed by Beatty's formula (equation 3.2.47), which in effect presents an expression for the radiation power due to the nickel substrate also being irradiated by the continuum.

The sum of the photocurrent i_{char} due to the action of the tungsten characteristic X-rays and i_{cont} due to the tungsten continuum acting on the cathode has to be multiplied by an overall fluorescence yield of nickel, which is a quantity that gives the proportion of electrons in a given atomic energy level, that will be available for recombination or, in this case, the number of electrons, that will be emitted as photoelectrons under the influence of a high electric field. For the calculation of photoelectrons emitted from the cold cathode, or alternatively the current i_{char} produced due to the

X-irradiation by the tungsten characteristic lines of the nickel substrate of the cathode, equation 3.2.48 is used. In determining i_{char} theoretically an idealised case presented, in which it is assumed that the proportionality factor a is equal to 1 and all of the electrons excited by X-rays leave their atomic shells as photoelectrons. That this presents an idealised case can be seen in Section 6.2 in Chapter 6, where the measured average photocurrent produced in the X-ray tube constitutes only 4.81% of the total tube current, which shows that the total contribution of the photocurrent to the overall tube current is far leas than the calculations of an ideal photocurrent presented in Table 3.2.14 and Figure 3.2.18 suggest. Hence the measurements in Section 6.2 in Chapter 6 actually show that recombination of nickel electrons excited by X-rays does in fact take place.

One can expect that there will be an initial current rise time during each voltage pulse across the tube until, due to the combined effects of the current i_{field}, which is produced as a result of the formation of high electric fields in the dielectric layers of the cold cathode, and the photocurrent i_{photo}, the current output reaches a maximum value dependent on the maximum current, that the power supply is capable of providing. In order to determine such a current waveform , it is necessary to first of all consider a time interval Δt_n, in which an electron travels from the cathode through the dielectric layers of the X-ray tube to the anode and the X-ray photon subsequently produced upon that electron's collision with the tungsten target returns to the cathode. Initially, during the first time interval Δt_1, electrons will be emitted from the cathode as a result of the changing electric field only. As a result of X-ray photons from the tungsten target interacting with the nickel substrate further electrons are excited and emitted by the cathode as photoelectrons in addition to the electrons emitted due to the changing electric field. Evidently this leads to an increased tube current during the next time interval Δt_2, in which the same process is repeated as before with a higher current, a higher X-radiation intensity, a higher photoelectron emission and hence a higher tube current in the following time interval. This process continues until the total tube current during each pulse reaches the current limit of the power supply. In order to determine the total current rise time t_{rise} we first of all need to calculate Δt_n. The time interval can be expressed as the sum of the time an electron will need to traverse the dielectric NiO, MgO and vacuum layers of the tube from the cathode to the target and the time the resulting X-ray photon will need to travel back to the cathode from the anode. To do that it is necessary to calculate the drift velocities of an electron in the NiO and the MgO layers of the cathode and the relativistic velocity of the electron in the vacuum of the tube under a given electric field. By taking the thicknesses of these layers into account the time periods that the electron requires to cross each of these layers can be determined. The X-ray photon returning to the cathode can be treated as light and will therefore travel at the speed of light $c = 3 \times 10^8$ m s^{-1}. The current per unit cross section area in a conductor is called the current density j, and is expressed by

$$j = \frac{i}{A} = nev_d \tag{3.2.49}$$

where i = the total current through the conducting medium (A);
A = the cross sectional area of the medium (m^2);
n = the concentration of particles (m^{-3});
e = the charge of an electron and (C);
v_d = the drift velocity of moving charges (m s^{-1});

When a charged particle such as an electron moves in an electric field in vacuum, it accelerates continuously [31]. However, the motion of an electric field inside a material such as NiO and MgO is very different because of frequent collisions with the atoms inside the material. In this way the charges flow in a somewhat random motion drifting in the direction of the force due to the electric field across the medium at a velocity v_d. Since $j = \sigma \cdot E$, equation 3.2.49 can be rewritten as

$$v_d = \frac{\sigma \cdot E}{n \cdot e} \tag{3.2.50}$$

The charge concentration n can be obtained by multiplying the number of valence electrons by the number of molecules in the medium. The number of moles and hence the number of molecules in a material can be expressed by equations 3.2.51 and 3.2.52 [32]:

$$\text{no. of moles} = \rho \cdot Vol \cdot (\text{molar mass})^{-1} \tag{3.2.51}$$

and

$$\text{no. of free charges } n = \text{no. of moles} \left(\frac{6.022 \times 10^{23} \text{ molecules}}{\text{mol}} \right) \cdot \text{no. of valence electrons}$$

(3.2.52)

where ρ is the density of the material and Vol is its volume. In Table 3.2.12 the parameters for the calculation of the number of free charges n and hence the drift velocity v_d through NiO and MgO are listed. In the previous sections it was already shown that the cross sectional area of the cathode A = 1.256 cm^2, and d denotes the thickness of each dielectric layer. Note should be taken of the fact, that the values E_{MgO} and E_{NiO} have been taken from equations 3.2.21a and 3.2.21b (see section 3.2.5) respectively.

Table 3.2.12: Parameters for the calculation of electron drift velocities in NiO and MgO with a voltage of $V(t) = -2.83 \times 10^7 t + 8.5 \times 10^4$ Volts applied across the X-ray tube.

Quantity	NiO	MgO
ρ (kg m^{-3})	6.81×10^{-3}	3.58×10^{-3}
d (m)	1×10^{-7}	1×10^{-4}
Vol (m^3) = d x A	6.8×10^{-5}	3.6×10^{-3}
$E = \frac{V(t)}{d}$ (V m^{-1})	$-4.263 \times 10^7 t + 1.279 \times 10^5$	$-5.243 \times 10^7 t + 1.573 \times 10^5$
σ (S m^{-1})	1.138×10^{-3}	9.26×10^{-4}
molar mass (g mol^{-1})	74.6894	40,3044
no. of molecules	6.199×10^{-6}	3.201×10^{-4}
no. of valence electrons	2	4
n (m^{-3})	7.467×10^{18}	7.703×10^{20}

Substituting the above parameters into equation 3.2.50 finally allows us to determine the drift velocities across the NiO and MgO layers:

1. The drift velocity in the nickel oxide layer: $v_d(NiO) = -4.0555\times10^{4}t + 121.676$ m sec^{-1};
2. The drift velocity in the magnesium oxide layer: $v_d(MgO) = -3.9343\times10^{2}t + 1.180$ m sec^{-1};

Having obtained the values for electron drift velocities in the NiO and MgO layers we can now proceed to establishing the time it takes an electron to cross the aforementioned dielectric layers by dividing the above drift velocities by the thicknesses of the respective layers. This operation is illustrated in Table 3.2.13 below.

Table 3.2.13: Parameters for the calculation of time periods that an electron takes to cross the NiO and MgO dielectric layers with a voltage of $V(t) = -2.83\times10^{7}t + 8.5\times10^{4}$ Volts applied across the X-ray tube.

	v_d (m s^{-1})	d (m)	t (s) $= \frac{d}{v_d}$
NiO	$-4.056\times10^{4}t + 121.676$	1×10^{-7}	$t_{NiO} = -2.465\times10^{-12}t + 8.219\times10^{-10}$
MgO	$-3.934\times10^{2}t + 1.180$	1×10^{-4}	$t_{MgO} = -2.545\times10^{-7}t + 8.475\times10^{-5}$

Once an electron enters the vacuum of the tube it is accelerated to velocities that are of the same order of magnitude as the speed of light c. The kinetic energy of an accelerated electron in vacuum can be determined using equation 3.2.53:

$$W_K = eV = \frac{m_e \cdot v^2}{2} \tag{3.2.53}$$

where W_K = the kinetic energy (J),
e = the charge of an electron (1.602×10^{-19} C),
V = the accelerating potential (Volts),
m_e = the mass of an electron (9.11×10^{-31} kg), and
v = the velocity (m s^{-1}) of the electron under the influence of an accelerating potential

The above expression can be reformulated to give the velocity after being accelerated through the potential V:

$$v = \sqrt{\frac{2eV}{m_e}} \tag{3.2.54}$$

If we consider a maximum accelerating potential of 85 kV we obtain a velocity of 1.73×10^{8} m s^{-1}, which is of the same order of magnitude as the velocity of light $c = 3\times10^{8}$ m s^{-1}. Therefore it can be stated, that the motion of the electron in the vacuum space of the tube is relativistic in nature. In

Table 3.2.14 a number of relations are listed both in their relativistic as well as their corresponding classical forms.

Table 3.2.14: Laws of relativistic dynamics [33].

Law	Relativistic Statement	Reduces at low velocities to
Definition of momentum	$p_{rel} = \frac{m_e v}{\sqrt{1 - v^2 / c^2}}$	$p = m_e v$
Definition of kinetic energy	$W_{Krel} = m_e c^2 \left(\frac{1}{\sqrt{1 - v^2 / c^2}} - 1 \right)$	$W_K = \frac{m_e v^2}{2}$
Newton's second law (force ‖ to motion). a = acceleration of electron (m s^{-2})	$F = \frac{m_e a}{\left(1 - \frac{v^2}{c^2}\right)^{\frac{3}{2}}}$	$F = m_e a$
Time to accelerate from velocity u to v in the same direction	$t_{rel} = \frac{m_e}{F} \left(\frac{v}{\sqrt{1 - v^2 / c^2}} - \frac{u}{\sqrt{1 - u^2 / c^2}} \right)$	$t = \frac{m_e}{F}(v - u)$
Force on charge in electric field	$F = eE$	$F = eE$
Velocity of electron after being accelerated through potential V	$v_{rel} = \sqrt{\frac{2eV}{m_e} \frac{1 + \frac{e}{m} \frac{V}{2c^2}}{\left(1 + \frac{e}{m} \frac{V}{c^2}\right)^2}}$	$v = \sqrt{\frac{2eV}{m_e}}$

The relativistic velocity of the electron at the point at which it reaches the target and the time it takes to get there is of particular interest. From Table 3.2.14 we therefore need to consider the following two expressions:

$$t_{rel} = \frac{m_e}{F} \left(\frac{v}{\sqrt{1 - v^2 / c^2}} - \frac{u}{\sqrt{1 - u^2 / c^2}} \right) \tag{3.2.55}$$

and

$$v_{rel} = \sqrt{\frac{2eV}{m_e}\frac{1+\frac{e}{m}\frac{V}{2c^2}}{\left(1+\frac{e}{m}\frac{V}{c^2}\right)^2}} \tag{3.2.56}$$

where m_e is the rest mass of the electron and is equal to 9.11×10^{-31} kg while m is the relativistic mass, which we can determine from equation 3.2.57, the expression relating the rest mass of an electron to its relativistic mass when accelerated to the velocity v_{rel}. The relativistic statement for the momentum in Table 3.2.14 is sometimes interpreted to mean that a rapidly moving particle undergoes an increase in mass. Hence if the mass at zero velocity (the rest mass) is denoted by m_e, then the relativistic mass m is given by

$$m = \frac{m_e}{\sqrt{1 - v^2/c^2}} \tag{3.2.57}$$

In equation 3.2.55 u is the initial velocity of the electron as it leaves the MgO layer and enters the vacuum. Therefore the initial velocity u of the electron in vacuum can be equated to the drift velocity of the electron in the MgO layer. However, since $v_d(MgO) = u << v$ the term $\frac{\left[v_d(MgO)^2 = u^2\right]}{c^2}$ becomes negligible. By the same token $v_d(MgO) << v$, so that the term $\frac{u}{\sqrt{1-u^2/c^2}} = \frac{v_d(MgO)}{\sqrt{1-v_d(MgO)^2/c^2}}$ in equation 3.2.55 becomes negligible compared to $\frac{v}{\sqrt{1-v^2/c^2}}$ as well. Thus t_{rel} in 3.2.58 can be approximated as

$$t_{rel} = \frac{m_e}{F}\left(\frac{v}{\sqrt{1-v^2/c^2}}\right) =$$

$$\frac{m_e}{eE}\left(\frac{v}{\sqrt{1-v^2/c^2}}\right) =$$

$$\frac{m_e}{e\frac{V}{d_{VAC}}}\left(\frac{v}{\sqrt{1-v^2/c^2}}\right) \tag{3.2.58}$$

The electric field across the vacuum space is obviously a function of time since the accelerating potential across the tube is also time dependent. Therefore, with the anode-cathode spacing being equal to 0.056 m (see Section 3.1.3) the electric field in the vacuum can be expressed as

$$E(t) = \frac{V(t)}{d_{VAC}} =$$

$$\frac{-2.83 \times 10^{7} t + 8.5 \times 10^{4}}{0.056} \text{ V m}^{-1} \qquad (3.2.59)$$

By substituting $V(t)$ for V and equation 3.2.57 into 3.2.56 we obtain the following expression for v_{rel}:

$$v_{rel} = \sqrt{\frac{2 \cdot 1.6 \times 10^{-19}\,\text{C} \cdot \left(-2.83 \times 10^{7} t + 8.5 \times 10^{4}\ \text{Volts}\right)}{9.1 \times 10^{-31}\,\text{kg}} \frac{1 + \frac{1.6 \times 10^{-19}\,\text{C}}{\left(\frac{m_e}{\sqrt{1 - v^2 / c^2}}\right)} \frac{\left(-2.83 \times 10^{7} t + 8.5 \times 10^{4}\ \text{Volts}\right)}{2\left(3 \times 10^{8}\,\text{m}\,s^{-1}\right)^2}}{\left(1 + \frac{1.6 \times 10^{-19}\,\text{C}}{\left(\frac{m_e}{\sqrt{1 - v^2 / c^2}}\right)} \frac{\left(-2.83 \times 10^{7} t + 8.5 \times 10^{4}\ \text{Volts}\right)}{\left(3 \times 10^{8}\,\text{m}\,s^{-1}\right)^2}\right)}}$$

where

$$v = \sqrt{\frac{2eV}{m_e}} = \sqrt{\frac{2 \times 1.6 \times 10^{-19}\,\text{C} \cdot \left(-2.83 \times 10^{7} t + 8.5 \times 10^{4}\ \text{Volts}\right)}{9.1 \times 10^{-31}\,\text{kg}}} = \sqrt{-9.952 \times 10^{18} t + 2.989 \times 10^{16}}\ \text{m}\,s^{-1}.$$

Hence

$$v_{rel} = \left(-9.952 \times 10^{18} t + 2.989 \times 10^{16}\right)\text{m}\,s^{-1} \sqrt{\frac{1 + \frac{1.6 \times 10^{-19}\,\text{C}}{\left(\frac{9.1 \times 10^{-31}\,\text{kg}}{\sqrt{1 - \left(-9.952 \times 10^{18} t + 2.989 \times 10^{16}\,\text{m}\,s^{-1}\right)^2 / \left(3 \times 10^{8}\,\text{m}\,s^{-1}\right)^2}}\right)} \frac{\left(-2.83 \times 10^{7} t + 8.5 \times 10^{4}\ \text{Volts}\right)}{2 \times \left(3 \times 10^{8}\,\text{m}\,s^{-1}\right)^2}}{\left(1 + \frac{1.6 \times 10^{-19}\,\text{C}}{\left(\frac{9.1 \times 10^{-31}\,\text{kg}}{\sqrt{1 - \left(-9.952 \times 10^{18} t + 2.989 \times 10^{16}\,\text{m}\,s^{-1}\right)^2 / \left(3 \times 10^{8}\,\text{m}\,s^{-1}\right)^2}}\right)} \frac{\left(-2.83 \cdot 10^{7} t + 8.5 \cdot 10^{4}\ \text{Volts}\right)}{\left(3 \times 10^{8}\,\text{m}\,s^{-1}\right)^2}\right)}}$$

(3.2.60)

where the units are in m s^{-1}. The modified expression for v_{rel} can now be used in equation 3.2.58 to obtain the time t_{rel}, or t_{VAC} as we shall denote it from now on, that an electron needs to cross the vacuum space of the X-ray tube. An X-ray photon produced by an electron colliding with the target can be treated as light and therefore we can say that its speed $v_{PHOTON} = c = 3 \times 10^8 \, m \, s^{-1}$. Such a photon will need to traverse the vacuum, MgO and NiO dielectric layers of the tube to reach the nickel substrate of the cathode again. Thus the time t_{PHOTON} it will take for the photon to reach the nickel will be equal to $\frac{d_{NiO} + d_{MgO} + d_{VAC}}{v_{PHOTON}}$, where d_{NiO}, d_{MgO} and d_{VAC} are once again the NiO layer thickness (1×10^{-7} m), the MgO layer thickness (1×10^{-5} m) and the cathode-anode spacing (0.056 m) respectively. Therefore t_{PHOTON} will have a constant value of 1.937×10^{-10} seconds. Thus the time interval Δt, namely the sum of the time intervals that an electron will need to traverse the dielectric NiO, MgO and vacuum layers of the tube from the cathode to the target and the time the resulting X-ray photon will need to travel back to the cathode from the anode, can be expressed as the sum of $t_{NiO,n}$, $t_{MgO,n}$, $t_{VAC,n}$ and t_{PHOTON} i.e.

$$\Delta t_n = t_{NiO,n} + t_{MgO,n} + t_{VAC,n} + t_{PHOTON} \tag{3.2.61}$$

It is important to point out that when the nickel substrate of the cathode is irradiated obviously a certain amount of the X-radiation will merely pass through the material without actually having any effect on the nickel. Therefore it is necessary to only take into account the radiation absorbed by the nickel. This can be done simply by considering a parallel monochromatic X-ray beam of intensity I_0 incident on a given homogeneous material as shown in Figure 3.2.16 [22]. After the beam has passed through a thickness x of the material its intensity is reduced to I_x due to the absorption and scattering phenomena. This attenuation process obeys the Lambert law

$$\frac{I_x}{I_0} = exp(-\mu \cdot \rho \cdot x) \tag{3.2.62}$$

where $\frac{I_x}{I_0}$ is the amount of radiation relative to the total initial radiation I_0 that passes through the material. While ρ denotes the density of the material μ is the *mass attenuation coefficient* because it refers to the mass of the material per unit section, and is usually expressed in $cm^2 \, g^{-1}$. The mass attenuation coefficients in terms of incident photon energy are tabulated for a number of elements in Appendix 4. The graph in Figure 3.2.17 illustrates how the attenuation coefficient for nickel μ_{Ni} changes with respect to photon energy or, in the case of the X-ray tube, with respect to the accelerating potential V, which is a function of time (see equation 3.2.19, section 3.2.6). Hence, from the curve in figure 3.2.17 μ_{Ni} can be expressed as a function of time and so the amount of radiation $\frac{I_x}{I_0}$ passing through the nickel substrate of the cathode becomes a function in terms of the time varying voltage applied across the tube.

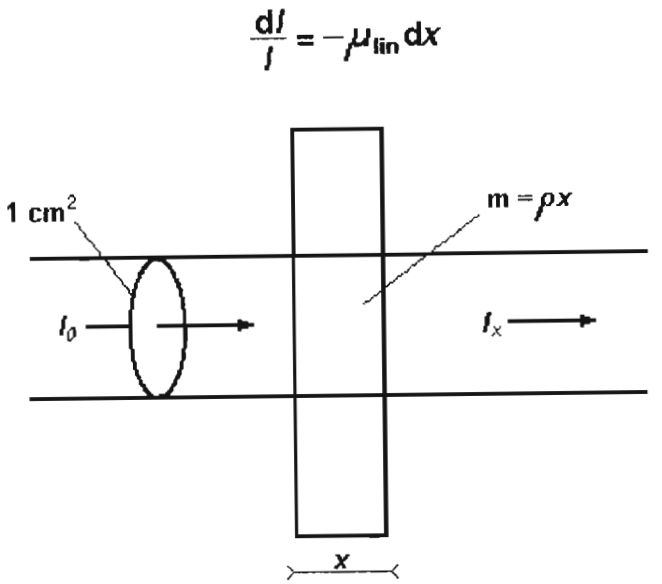

Fig. 3.2.16: Transmission of X-rays through a layer of material [22].

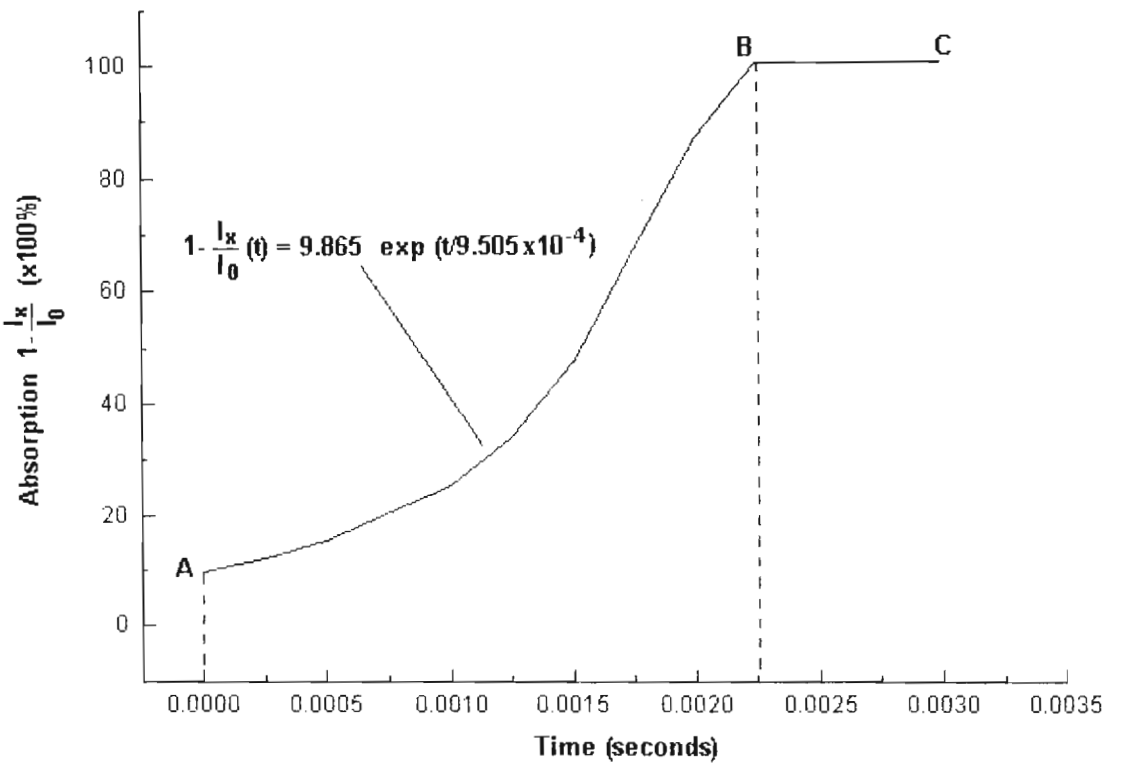

Fig. 3.2.17: Absorption of X-radiation for nickel as a function of time.

The points in Figure 3.2.17 were plotted taking the values of the absorption coefficients for nickel (see Table A4, Appendix 4) and substituting them into equation 3.2.62, where the density ρ is equal to 8.9 g cm^{-2} for nickel and x is 0.02 cm, the thickness of the nickel substrate in question. From these calculations the relative amount of X-radiation absorbed by the nickel, $1-\frac{I_x}{I_0}$, can be obtained and plotted against the corresponding photon energies or accelerating potentials as listed in the table in Appendix 4, and so be expressed as a function of the applied X-ray tube voltage $V(t)$. However, the accelerating potential applied across the X-ray tube is $V(t)=-\frac{8.5\times10^4}{0.003}t+8.5\times10^4$ Volts (see equation 3.2.19), which is the potential applied across the tube in terms of time. Therefore the absorption $1-\frac{I_x}{I_0}$ can be plotted as a function of time as shown in Figure 3.2.17. By applying a linear fit in the graph in Figure 3.2.17 above between points A (t = 0 sec) and B (t = 0.00225 sec), $1-\frac{I_x}{I_0}$ becomes

$$1-\frac{I_x}{I_0}(t)=9.865\cdot exp(t/9.505\times10^{-4})\%\ , \tag{3.2.63}$$

a time-dependent function. By the same token the portion of the curve between points B (t= 0.00225 sec) and C (t=0.003 sec) can be expressed as:

$$1-\frac{I_x}{I_0}(t)=100\% \tag{3.2.64}$$

The curve fitting in Figure 3.2.17 was accomplished using Microcal Origin V4.0.

We have now established expressions for the current that will be produced in the X-ray tube due to the changing electric field, the photocurrent resulting from the characteristic and the continuous spectrum form the tungsten target and the amount of radiation that will be absorbed by the cathode resulting in the aforementioned photocurrent, as well as an approximation for a time interval Δt_n, at the end of which the total current, which is the sum of the field current and photocurrent, changes due to the combined effects of a changing electric field in the dielectric layers of the tube and consequently changing amounts of radiation that excite further electrons in the cathode. Therefore to estimate a rise time for the current pulse across the tube it is necessary to start with an initial current, which is due to the field only, from which one can then derive the amount of characteristic and continuous radiation produced at the tungsten target or anode of the tube due to that initial current. By multiplying the relative amount of characteristic line and continuous radiation by the absorption equation 3.2.63 for nickel the amount of radiation absorbed by the nickel substrate of the cathode at the end of the first time interval Δt_1 can then be obtained, and so the amount of photocurrent due to this absorbed radiation produced at the same time can be obtained. The sum of the initial current and the photocurrent can then be used as the initial emitted current value for the next time period Δt_2. At time $t_1=0\,\text{sec}$ the initial current $i_{ini,1}$ due to the field only will be 18.29 mA (see Figure 3.2.9, section 3.2.6). At that instant the time needed for an

electron to cross the NiO layer and the MgO layer can be found simply by substituting $t_1 = 0\,\text{sec}$ into the expressions for $t_{NiO,1}$ and $t_{MgO,1}$ from Table 3.2.13, and are found to be 8.219×10^{-10} seconds and 8.475×10^{-5} seconds. To find v_{VAC} it is once again necessary to substitute $t_1 = 0\,\text{sec}$ into equation 3.2.60, which gives an electron velocity when accelerated through a potential of 85 kV of 1.544×10^{8} m.s^{-1}. Having obtained that quantity the time an electron needs to cross the vacuum space of the tube at $t_1 = 0\,\text{sec}$ by applying the value obtained for v_{VAC} in equation 3.2.58 can now be found. It can therefore be found, that $t_{VAC,1}$ is equal to 6.739×10^{-10} seconds. The total time for an electron to reach the anode is thus equal to the sum of $t_{NiO.1}$, $t_{MgO,1}$ and $t_{VAC,1}$, namely 8.475×10^{-5} seconds. At that instant, however, the emitted electrons strike the target producing X-ray photons containing both the characteristic line and the continuous spectra. To calculate the effect of characteristic line spectra on the photocurrent one needs to use the intensity expression $\sum P_i(t)$ from Table 3.2.11 during the initial time interval $0 \rightarrow t_1$ of the voltage pulse across the X-ray tube. The term I_λ can be directly replaced by $i_{ini,1} = 18.29$ mA since the two terms are directly interchangeable (see section 3.2.11). Hence with $\sum P_i(t) = \frac{168277.34t + 512.82}{28333t + 85} I_\lambda$ the photocurrent produced in the cathode due to the characteristic line radiation of tungsten acting on it becomes

$$i_{char}(t) = \frac{168277.34t + 512.82}{28333t + 85} i_{field} = \frac{168277.34t + 512.82}{28333t + 85} i_{ini,1} \qquad (3.2.65)$$

Therefore we obtain a value of 110.30 mA for i_{char} at time $t = t_{NiO,1} + t_{MgO,1} + t_{VAC,1} = 8.450\times10^{-5}$ seconds and $i_{ini,1} = 18.29$ mA. In addition further electrons will be emitted as a result of the tungsten continuum acting on the cathode. From equation 3.2.47 we can see, that the integrated spectral continuum I_{int} is in fact an expression for the power of the backradiation emanating from the cathode after its irradiation. This can be translated into an emission current due to Bremsstrahlung during the first time interval Δt_1 at time $t = t_{NiO,1} + t_{MgO,1} + t_{VAC,1} = 8.45\times10^{-5}\,sec$ as follows:

$$I_{int,1} = \left(1.4\times10^{-9}\right) Z i V^2 =$$

$$\left(1.4\times10^{-9}\right)\cdot 74 \cdot 18.29\times10^{-3}\,\text{A}\cdot\left[-2.83\times10^{7}\left(8.45\times10^{-5}\,\text{sec}\right) + 8.5\times10^{4}\,\text{Volts}\right]^2 \approx$$

$$12.93\ \text{W};$$

The current emitted due to the continuum can now be obtained by dividing the power value for the radiation obtained by the voltage at time $t = t_{NiO,1} + t_{MgO,1} + t_{VAC,1} = 8.45\times10^{-5}\,sec$. Therefore the current emitted due to the action of the continuous radiation on the cathode $i_{cont,1}$ becomes

$$i_{cont,1} = \frac{I_{int,1}}{V(t)} =$$

$$\frac{12.93 \text{ W}}{(-2.83 \times 10^{7} (8.45 \times 10^{-5} \text{ sec}) + 8.5 \times 10^{4}) \text{ Volts}} \approx$$

$$0.157 \text{ mA};$$

The photocurrent i_{P_1} emitted at the end of the first time interval Δt_1 is the sum of $i_{char,1}$ and $i_{cont,1}$, and is equal to 110.457 mA. However, it is important to take into account, that this would be the case if all of the radiation were absorbed by the cathode. As discussed earlier in this section only a fraction of the radiation will be absorbed by the cathode. To obtain this fraction and hence the photocurrent emitted due to this absorbed radiation only it is necessary to multiply the photocurrent $i_{photo,1}$ by the factor $1 - \frac{I_x}{I_0}(t)$ (see equations 3.2.63 and 3.2.64), which is directly proportional to the photocurrent. Once again I_x is the amount of radiation that passes through the cathode unimpeded and I_0 is the total radiation produced at the tungsten target. Unlike the characteristic line spectra and the continuum, which are produced as the electrons collide with the target after travelling through the NiO, MgO and vacuum dielectric layers of the tube $t = t_{NiO,1} + t_{MgO,1} + t_{VAC,1} = 8.45 \times 10^{-5} \, sec$ after the start of the voltage pulse $V(t)$ across the structure, the photocurrent $i_{photo,1}$ will be produced at the end of Δt_1, namely at $t_2 = t_{NiO,1} + t_{MgO,1} + t_{VAC,1} + t_{PHOTON} \approx 8.45 \times 10^{-5}$ sec. Using equation 3.2.63 as the absorption factor at t_2 the following expression is obtained:

$$1 - \frac{I_x}{I_0}\left(8.450 \times 10^{-5}\right) / 100 =$$

$$\frac{9.865 exp[(8.45 \times 10^{-5}) / (9.505 \times 10^{-4})]}{100} =$$

$$0.108;$$

Therefore the photocurrent $i_{photo,1}$ produced at the end of the first time interval Δt_1 will be

$$i_{photo,1} = \omega \times \left[1 - \frac{I_x}{I_0}(t_2)\right] \times \left(i_{char,1} + i_{cont,1}\right) =$$

$$(0.108) \cdot (110.3 \text{ mA} + 0.157 \text{ mA}) \approx$$

$$11.30 \text{ mA};$$

where ω is the overall fluorescence yield of nickel, i.e. $\omega = \omega_K + \omega_L = 0.392 + 0.005 \approx 0.4$ (see Appendix 6), which has to be included since it is a measure of the proportion of electrons in an atom which actually leave the atom under the influence of X-radiation. We can now determine the current $i_{ini,2}$ at the start of the next time interval Δt_2:

$$i_{ini,2} = \omega \cdot (i_{ini,1} + i_{photo,1}) =$$

$$7.32 \text{ mA} + 4.52 \text{ mA} =$$

$$11.84 \text{ mA};$$

We have now obtained the value for the initial current $i_{ini,2}$ for the next time interval Δt_2. In Table 3.2.14 the parameters for the first ten iterations or time intervals are shown.

Table 3.2.14: List of total tube current $i_{ini,n}$ (mA) at various points in time t_n (mA) and the corresponding variables that determine the tube current values.

n	t_n (sec)	$t_{NiO,n}$ (sec)	$t_{MgO,n}$ (sec)	$t_{VAC,n}$ (sec)	$i_{ini,n}$ (mA)	$i_{photo,n}$ (mA)	i_n (mA)
1	0	8.19×10^{-10}	8.45×10^{-5}	7.93×10^{-10}	7.32	4.52	11.84
2	8.45×10^{-5}	8.17×10^{-10}	8.42×10^{-5}	7.99×10^{-10}	11.84	8.60	20.44
3	1.69×10^{-4}	8.15×10^{-10}	8.40×10^{-5}	8.05×10^{-10}	20.68	16.07	36.74
4	2.53×10^{-4}	8.12×10^{-10}	8.37×10^{-5}	8.11×10^{-10}	36.74	31.18	67.92
5	3.36×10^{-4}	8.1×10^{-10}	8.35×10^{-5}	8.19×10^{-10}	67.92	62.94	130.86
6	4.20×10^{-4}	8.07×10^{-10}	8.32×10^{-5}	8.26×10^{-10}	130.86	132.34	263.20
7	5.03×10^{-4}	8.05×10^{-10}	8.30×10^{-5}	8.35×10^{-10}	263.20	290.45	553.66
8	5.86×10^{-4}	8.02×10^{-10}	8.27×10^{-5}	8.44×10^{-10}	553.66	170.08	723.74
9	6.69×10^{-4}	8×10^{-10}	8.25×10^{-5}	8.53×10^{-10}	923.74	242.44	966.18
10	7.51×10^{-4}	7.97×10^{-10}	8.22×10^{-5}	8.63×10^{-10}	966.18	352.84	1319.02

In spite of the continuous decrease in the electric field across the dielectric layers of the X-ray tube, and hence a decrease in i_{field}, one can expect the initial tube current $i_{ini,n}$ to increase throughout the duration of a voltage pulse $V(t)$ across the tube assuming that all the electrons excited by the radiation in the nickel base add to the current emission of the cathode. This can be explained by the fact, that the total tube current i_n at the beginning of every time interval Δt_{n+1} at time t_{n+1} will always be a multiple of the total tube current i_{n-1} at the beginning of the previous time interval Δt_n at time t_n. Hence it can be expected, that the current waveform will level off at the current limit of the power supply and remain at that level until $V(t)$ reaches zero again. This is illustrated in the graph in Figure 3.2.18, where tube current $i_{ini,n}$ is plotted versus time t_n. The values were taken from Table 3.2.14 above.

In Figure 3.2.18 it can be seen, that the emitted current will start emitting at approximately 30 mA at the onset of the voltage pulse. This, however, is an idealised case. In Figure 6.1 (see Section 6.1, Chapter 6) it can be seen, that the measured current pulse has in fact a rise time of approximately 0.5 msec while the rise time of the voltage pulse is negligible (see Figure 6.2, Chapter 6). In order

to theoretically establish the waveform of a current pulse one also needs to take the current fall time t_{fall} into account. By substituting the expression for the voltage pulse across the tube $V(t) = -2.83\times10^{7}t + 8.5\times10^{4}$ Volts into equation 3.1.13 (see Section 3.1.3) a relation was obtained in Section 3.1.3 the space charge limited tube current (see equation 3.1.14):

$$i(t) = (-2.83\times10^{7}\,t + 8.5\times10^{4})^{\frac{3}{2}} \cdot \left(5.53\times10^{-7}\,t + 9.154\times10^{-8}\right) \text{ Volts}$$

This function is plotted in Figure 3.1.7. By equating the aforementioned expression to the maximum tube current limit of 30 mA as set by the pulsed power supply t is found to be equal to 0.002837 s. This represents the time after the onset of the current pulse in the X-ray tube, at which point the tube current will start to decay to 0 mA under the effects of space charge. The fall time of the current pulse is therefore the time period between t = 0.002837 s and the total duration of a single voltage pulse discharge across the tube, which is 0.003 s. Hence t_{fall} = 0.003 s – 0.002837 s = 0.000163 s.

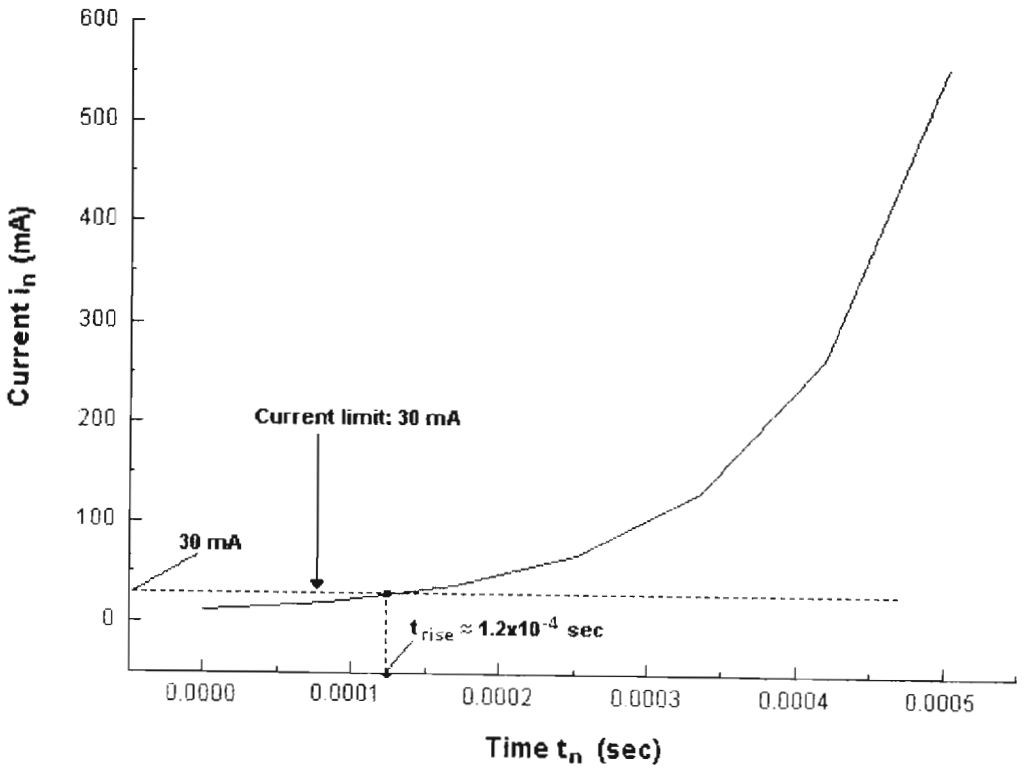

Fig.3.2.18: Graph illustrating how the total tube current i_n changes with t_n.

The following two parameters hav now been theoretically established with respect to every current pulse flowing through the X-ray tube:

1. The rise time t_{rise}, which is approximately 0.00012 sec (see Figure 3.2.18), of each current pulse, where the tube current is produced primarily as a result of the presence of electric fields in the dielectric layers of the tube (see Section 3.2.2) as well as the emission of photoelectrons from the cold cathode (see Section 3.2.7). In Figure 6.1 (see Chapter 6) it can be seen, that the rise time of each current is approximately equal to 0.0004 sec, which is a value of the same order of magnitude as 0.00012 sec, which has been predicted above.

2. The fall time t_{fall}, which is equal to 0.000163 s, due to the decaying voltage pulse across the tube and hence the resultant current emitting effects of space charge in the tube once the tube current drops below 30 mA. The maximum space charge current is directly dependent on the voltage, that is applied between the cathode and the anode of the X-ray tube (see equation 3.1.14). Hence as the voltage across the tube drops off to smaller values, so the maximum current limit due to space charge effects decreases as well, and once its value decreases below the maximum power supply current of 30 mA becomes the limiting factor on the total tube current.

The resultant ideal current pulse is plotted in the figure below against the voltage discharge across the X-ray tube.

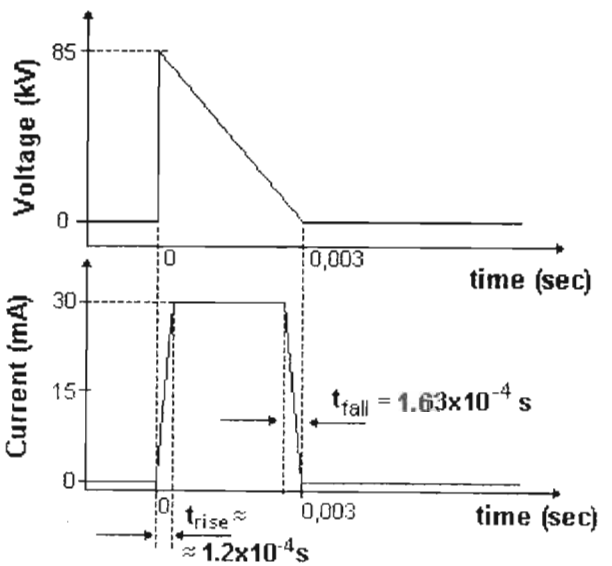

Fig.3.2.19: X-ray tube voltage and current pulse plotted on the same time scale.

The current waveform of each pulse illustrated in Figure 3.2.19 above represents an ideal case, in which all of the electrons excited in the nickel base of the cathode by the X-radiation produced at the target of the tube are assumed to add to the total tube current in the form of photoelectrons. In reality, however, it is to be expected, that some of the excited electrons have a tendency to fall back into their shells emitting nickel characteristic secondary X-radiation rather than be emitted from the cathode thus reducing the overall photocurrent i_{photo} and hence the total tube current. This can be attributed to the fact, that there exist transition probabilities or transition rates for the nickel electrons excited by the X-radiation produced at the target of the X-ray tube [20]. An atomic

transition rate is the probability per second that an atom in a certain energy level will make a transition to some other energy level [54].

3.2.12 RADIATION BY MOVING CHARGES

Before concluding this chapter it is necessary to point out the fact, that the accelerated electrons in the X-ray tube emit electromagnetic radiation as they progress from the cathode to the anode. Of particular interest is the total radiation emitted by the accelerated particles as well as the angular distribution of their radiation and the frequency spectrum [15]. For nonrelativistic motion the radiation is described by the Larmor result [15],

$$P = \frac{2}{3}\frac{e^2 \dot{v}^2}{c^3} \tag{3.2.66}$$

where P = the radiative power of the accelerated charge (Watts);
e = the charge of an electron (1.6×10^{-19} C);
$\dot{v}$ = the acceleration of the charge (m s^{-2});
c = the speed of light (m s^{-1});

The expression in equation 3.2.66 can also be expressed in terms of unit solid angle [15]:

$$\frac{dP}{dQ} = \frac{e^2 \dot{v}^2}{4\pi c^3}\sin^2\Theta \tag{3.2.67}$$

The term $\sin^2\Theta$ in equation 3.2.67 exhibits the characteristic angular dependence of the radiated power. In the case of the accelerated charges undergoing relativistic motion it is the relativistic momentum p_{rel} of the particle that must be taken into consideration [15]. According to *Jackson* [15] the power of the radiation emitted by an accelerated charge moving along a linear path at relativistic speeds can be described by the following relation:

$$P = \frac{2}{3}\frac{e^2}{m^2c^3}\left(\frac{dp}{dt}\right)^2 \tag{3.2.68}$$

where dp is the momentum of the accelerated particle. By recalling the relativistic form of momentum for a charged particle from Table 3.2.14, which is

$$p_{rel} = \frac{m_e v}{\sqrt{1 - v^2/c^2}}$$

where m_e = the mass of an electron (9.1×10^{-31} kg);

v = the nonrelativistic velocity of the electron which is equivalent to $\sqrt{\frac{2eV(t)}{m_e}}$.

The relativistic momentum can also be expressed as

$$p_{rel} = \frac{m_e\sqrt{\frac{2eV(t)}{m_e}}}{\sqrt{1-\frac{2eV(t)}{m_e c^2}}} = \frac{m_e\sqrt{\frac{2e(-2.83\times10^7 t + 8.5\times10^4)}{m_e}}}{\sqrt{1-\frac{2e(-2.83\times10^7 t + 8.5\times10^4)}{m_e c^2}}} \qquad (3.2.69)$$

where $V(t) = -2.83\times10^7\, t + 8.5\times10^4$ Volts represents the accelerating potential across the X-ray tube for every voltage pulse that is discharged across it (see equation 3.2.19, Section 3.2.6). Equation 3.2.69 is plotted against time in the graph in Figure 3.2.20 from t_1 = 0 s to t_2 = 0.003 s, which is the duration of a pulse. The plot can also be described by equation 3.2.70, which is a second order polynomial approximation obtained by simple curve fitting:

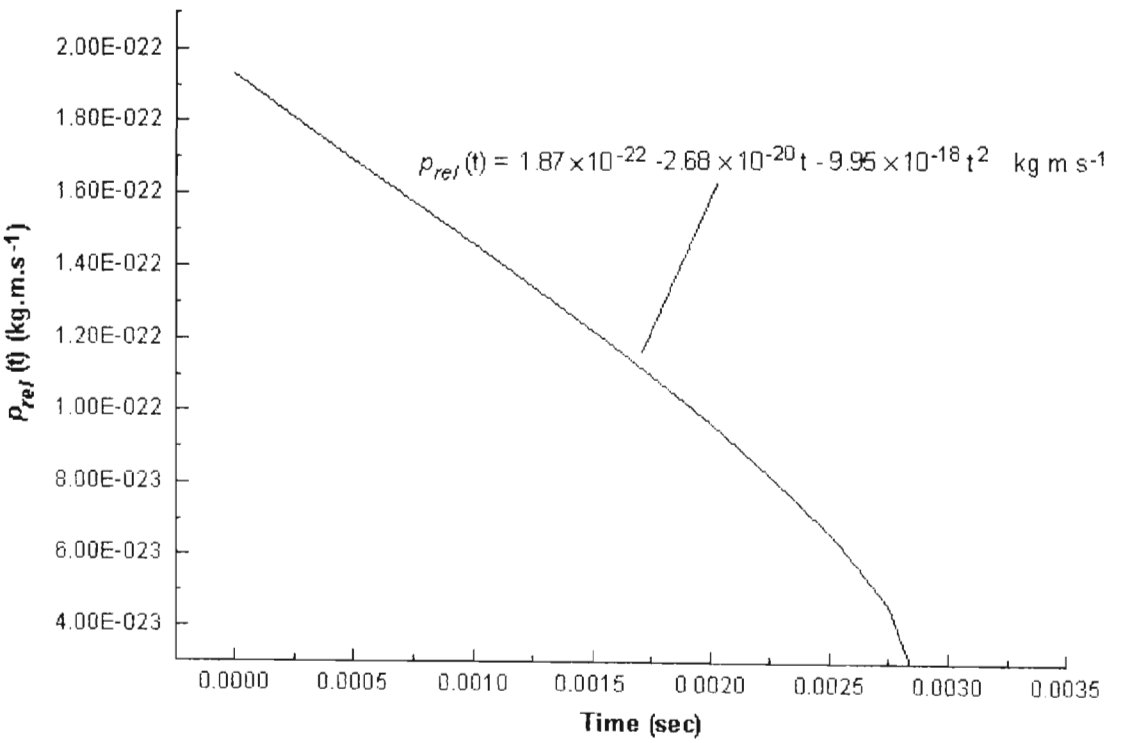

Fig.3.2.20: Plot of relativistic momentum p_{rel} versus time t.

$$p_{rel}(t) = 1.8698 \times 10^{-22} - 2.6761 \times 10^{-20} t - 9.9472 \times 10^{-18} t^2 \qquad (3.2.70)$$

To find the average relativistic momentum that a particle undergoes during one pulse across the tube from time $t_1 = 0$ s to $t_2 = 0.003$ s $p_{rel}(t)$ in equation 3.2.70 must be integrated from t_1 to t_2 with respect to time and divided by the total duration of one pulse, which is 0.003 seconds, i.e.

$$p_{rel}(t)_{AVE} = \frac{\int_{t_1}^{t_2} (1.87 \times 10^{-22} - 2.68 \times 10^{-20} t - 9.95 \times 10^{-18} t^2)\,dt}{t_2 - t_1} = \qquad (3.2.71)$$

$$1.57 \times 10^{-22} \text{ kg m s}^{-1};$$

If this value is substituted into equation 3.2.68 for the term dp over the total pulse duration dt = 0.003 s, the average radiated power for an accelerated electron in the X-ray tube is found to be equal to 2.096×10^{-42} Watts. What is of interest, however, is the total average power radiated by all the accelerated charges per voltage pulse. In Section 3.1.2 (see Figure 3.1.3) it was shown, that the total average current per pulse is 6.67 mA. Since current can also be expressed as the amount of charge dQ flowing through an area in a time dt [31], the current through the area, denoted by i, is

$$i = \frac{dQ}{dt} \qquad (3.2.72)$$

The total charge passing through the tube during each pulse can thus be found to be equal to the product of the current and the duration of one pulse. Therefore the charge passing through the tube per pulse can be approximated as being equal to $dQ \quad i.\ dt = (0.00667\ \text{A}) \cdot (0.003\ \text{s}) = 2 \times 10^{-5}$ C. Having determined the net charge dQ flowing through an area, the number of charges or electrons moving from the cathode to the anode of the tube per pulse applied can be found by dividing dQ by $e = 1.6 \times 10^{-19}$ C, which is the electric charge of an electron. The number of electrons n is thus found to be approximately 1.25×10^{14}. It can be seen, that the total average power radiated by all the accelerated charges per voltage pulse discharged across the tube is:

$$P_{TOTAL\ AVE} = n \times P_{AVE} =$$

$$(1.25 \times 10^{14}) \cdot (2.096 \times 10^{-42})\ \text{W} =$$

$$2.618 \times 10^{-28}\ \text{W},$$

which is negligible compared to the overall average power of 141.83 Watts dissipated in the X-ray tube (see Section 3.1.2). Furthermore the radiation of the accelerated electrons changes as they accelerate towards the anode. As can be seen in Figure 3.2.21 the angular distribution is tipped forward more and more as it increases in magnitude [19]. The angle θ_{max} for which the intensity is a maximum is

$$\theta_{\max} = \cos^{-1}\left[\frac{1}{3v/c}\left(\sqrt{1+15v^2/c^2}-1\right)\right] \rightarrow \frac{\sqrt{1-v^2/c^2}}{2}, \qquad (3.2.73)$$

where the last form is the limiting value for $v/u \rightarrow 1$. Even for $v/u = 0.5$, corresponding to electrons of approximately 80 keV kinetic energy, $\theta_{max} = 38.2°$.

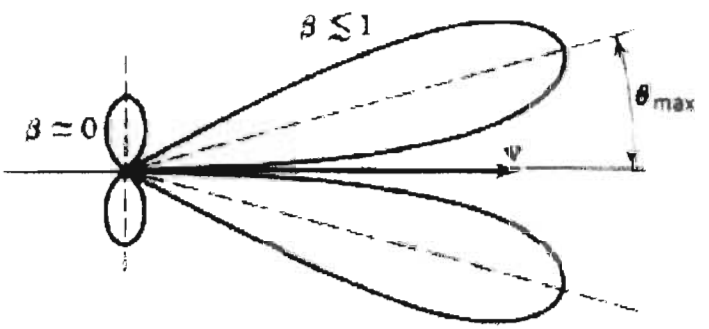

Fig.3.2.21: Radiation pattern for a charge accelerated in its direction of motion. The two patterns are not to scale, the relativistic one having been reduced by a factor of approximately 100 for the same acceleration [15].

For relativistic particles θ_{max} is very small being of the order of the ratio of the rest energy of the particle to its total energy [15]. At the point at which the electrons leave the cathode of the tube and move at relatively low velocities towards the target the peak intensity of radiation will be at approximately right angles to the direction of motion of the particle. Only once θ_{max} approaches 0° as the particle accelerates does the radiation of the moving charge affect the target even though the effects of that radiation on the production of X-rays at the target are negligible as shown earlier. However, this does suggest that X-radiation, no matter how low in intensity, will in fact be produced by the interaction of the radiation of the accelerated electrons with the target even before the electrons themselves arrive at the anode of the X-ray tube.

3.2.13. SUMMARY

In this section the author set out to establish and further the theory of electron emission from a MgO cold cathode when subjected to high electric fields within its dielectric layers as well as X-radiation produced at the target of the X-ray tube. After discussing the field emission from MgO cold cathodes a model was presented by the author, whereby the emission of electrons from MgO can be initiated and sustained by placing a high electric field that decreases rapidly with time across the tube thus avoiding the need for a triggering device, which is necessary for initiating electron emission from MgO under constant electric field conditions. The emission of electrons under a changing electric field can be explained with Ampère's law from Maxwell's equations, according to which a negative changing electric field across a medium creates a magnetic field $\nabla x\mathbf{B}$, which in turn results in current flow $\mathbf{j}$ in the medium. It is this current which represents the field-dependent emission of electrons from the MgO cold cathode. Furthermore, due to the geometry of the tube (see Section 3.1), part of the X-rays generated at the target of the X-ray tube interact with the nickel substrate of the MgO cathode exciting further nickel electrons in the process, which, under the influence of the accelerating potential across the tube and hence the cathode, are then accelerated towards the surface of the cathode and thereafter towards the target of the X-ray tube. The photoelectrons emitted in this way add to the field emitted current to produce the total tube current for every voltage pulse across the tube. In Section 3.2.11 it can also be seen, that the emitted electrons travel at relativistic velocities when traversing the vacuum space of the tube towards its anode, a fact that has to be taken into account when calculating the effect of the photocurrent in the tube on the total tube current (see Section 3.2.11). Theoretically the tube current should increase continuously as the voltage pulse discharges across the tube. However, this is limited to the maximum current that the power supply can provide. Furthermore the effects of space charge must also be taken into account. Once the voltage across the tube becomes low enough to make the maximum tube current limit due to space charge lower than the maximum current limit set by the power supply, the total tube current starts to drop off to zero as the voltage pulse across the tube decays to zero. In this way it was finally possible to establish the theoretical rise time, which is equal to 0.00012 sec, and the fall time of every current pulse, which is equal to 0.000163 s. Thus the overall current waveform of the X-ray tube was determined and is illustrated in Figure 3.2.19. Note should be taken of the fact, that the current waveform of each pulse represents an ideal case, in which all of the electrons excited in the nickel base of the cathode by the X-radiation produced at the target of the tube are assumed to add to the total tube current. In reality, however, some of the excited electrons tend to fall back into their shells emitting nickel characteristic secondary X-radiation thus reducing the overall number of emitted photoelectrons and their contribution to the total tube current. Finally the accelerated electrons in the X-ray tube also emit electromagnetic radiation as they move at relativistic velocities from the cathode to the anode. The angle between the direction in which the intensity of the radiation produced by the accelerated charge is at a maximum and the direction in which it moves is denoted by θ_{max}. This angle is very small for relativistically moving particles. Only once θ_{max} approaches 0° does the radiation of the moving charge affect the target of the X-ray tube. The total average power radiated by all the accelerated charges per voltage pulse discharged across the tube is equal to 2.618×10^{-28} Watts, which is negligible compared to the overall average X-ray tube power output of approximately 142 Watts. Thus the effects of that radiation on the production of X-rays at the target are negligible.

4. The Construction of the X-ray Tube

4.1. INTRODUCTION

This chapter discusses the materials used in the construction of the X-ray tube and how they are processed in the manufacture of the tube. The most important aspect in the manufacture of an X-ray tube is the use of the materials and the techniques applied in joining them, so as to produce a vacuum device, that can maintain the desired vacuum levels for a long period of time giving it a longer useful life-time. The materials used in the manufacture of the tube are the ceramic components, which fulfil the dual purpose of vacuum envelopes and an electrical insulator separating the different electrical contacts. The electrical contacts on the other hand will consist of disk shaped metal components that are separated by the ceramic tubing of the X-ray device.

Ceramic materials have been introduced in the manufacture of tubes in industry primarily as an alternative to glass. Ceramic has a number of advantages over glass. It is mechanically stronger, allows for the automatic assembly of tube structures, withstands higher temperatures and greater heat shock than glass, has superior dielectric properties, and does not suffer a change in its characteristics when exposed to nuclear radiation. Tubes made with ceramic envelopes can therefore be outgassed at much higher temperatures during pumping than tubes with glass envelopes. According to *Kohl* [19] this therefore allows for the attainment of higher vacuum levels and hence a longer life-time and greater emission density obtainable from oxide cathodes. The design of the end-window cold cathode X-ray tube follows the principle of a "stacked assembly" in which the active disk shaped electrodes are made of the metal and insulated from each other by ceramic spacers. The external shape of the tube is thus typically cylindrical. The metal-to-ceramic seals thus formed between the electrodes and the ceramic envelopes have to be processed in such a way, that the resulting stresses present in the seal are sufficiently reduced, so as not to cause any cracking in either the seal or ceramic, which would result in damage of the tube and a subsequent deterioration of the vacuum.

The chief disadvantage of ceramic tubes is that they are not transparent, and this makes it very difficult to perform internal visual inspections of a ceramic tube. However, the advantages of using ceramic instead of glass for the manufacture of vacuum tube envelopes far outweigh the disadvantages, and so have become very popular in the vacuum device industry. This chapter aims to familiarise the reader with the type of ceramics and metal components used in the manufacture of the X-ray tube, and will then proceed to briefly describe metal-to-ceramic sealing techniques before going on to present a detailed outline of the method used in joining the components of the end-window cold cathode X-ray tube.

4.2. METAL-TO-CERAMIC SEALING

After briefly discussing the history of metal-to-ceramic sealing *Kohl* [19] describes a number of techniques, that can be used in this regard. The earliest method employed was that of cold welding metal to ceramic. This is the simplest procedure and can be followed by pushing two surfaces together and allowing for the surface forces to do the permanent coupling once the molecules of the adjacent metal and ceramic surfaces have been brought into sufficiently close contact. Workers have observed the frictional adhesion of metal to ceramic surfaces. The joining

is typically accomplished by pushing a copper-plated steel cylinder of smaller inner diameter than the outer diameter of the ceramic cylinder onto the latter under considerable pressure to effect a seal at room temperature which afterwards can be exposed to temperatures as high as 550°C and heat cycled many times [19]. The main disadvantage of this technique is the necessity for large, mechanically strong components that can withstand the pressures applied during metal-to-ceramic sealing.

As the need for small ceramic vacuum tubes arose early in the 1950s [19] alternative methods for joining ceramic to metal had to be applied in industry. The alternative approaches tended towards processes, in which a metallized layer was formed on the surface of the ceramic, which could then be brazed to metal [19][41]. In one of these processes, referred to as the soldered seals method, soldered seals are formed by the reduction of salt solutions of precious metals including silver, gold, palladium and platinum [19][34]. The most commonly used material here is silver, which is applied to the ceramic surface in the form of flakes in an organic carrier. The metallic layer formed by the reduction of the metal from the solution is then sintered and finally joined to other metal parts by soft soldering [34]. A similar method to the one just described includes the metallization of ceramic surfaces by firing a mixture of a metal powder on their surfaces and glazing them. After applying this mixture to an organic carrier, the coat is then fired in a protective atmosphere to form the metallized layer [19][34].

One of the more commonly used brazing techniques, however, is one that uses sintered metal powder seals [19]. As it is a fairly standard technique employed in modern industry *Kohl* [19] proceeds to describe it in closer detail, and it shall be briefly outlined below. The sintered metal powder process requires several steps to produce a brazed joint between the ceramic and the metal. Firstly finely devised powders of tungsten, molybdenum, rhenium, or iron in a suitable suspension of nitro-cellulose lacquer are applied singly or in combination by brushing or spraying on the clean and smooth ceramic surface. This metal powder coating is then sintered to the ceramic by firing in a hydrogen atmosphere at temperatures ranging from 1300°C to 1500°C [19]. Sintering is a process whereby a metal powder is heated to a temperature of approximately 0,7 to 0,9 times the melting point of that metal. This temperature, while not high enough to melt the metal, is sufficiently high to form bonds between the metal particles. Particles of the same metal will join together by diffusion, which will usually result in a shrinking of the bulk of the metal powder. After sintering, the strength, ductility, thermal and electrical conductivities will have increased, but, on the other hand, the joint will show a strong tendency towards porosity [34]. After the first sintering operation at elevated temperature, a thin film of copper or nickel is applied by means of electroplating, or the reduction of oxide powders in a hydrogen atmosphere at a temperature of about 1000°C. The metallized ceramic is then joined to the metal part by conventional brazing methods in a controlled-atmosphere furnace [19], where by adding magnesium oxide, titanium oxide, barium oxide, or calcium oxide, either to the ceramic body or the metal powder mixture applied to its surface, the adhesion of the metal powder coating and the strength of the seal is improved. The metallized ceramic part is then assembled with the metal components of the tube and finally a metal-to-ceramic seal is formed by brazing the entire structure after placing a filler metal, in the form of a washer, between the ceramic and the metal parts. The sintered metal powder process therefore requires three firing operations. The *active alloy process*, which presents the most recent technique employed in metal-to-ceramic sealing, competes directly with the sintering process, and, compared to the latter, generally tends to produce better vacuum seals while at the same time being more practical as it requires only a single firing operation to produce a vacuum tight seal. This method will be applied in the

manufacture of the end-window cold cathode tube, and shall be described in detail in the following section.

4.3. ACTIVE ALLOY BRAZING

The active alloy soldering process employs titanium and zirconium as diffusion materials that show great affinity for glass and ceramics. At elevated temperatures reactions between titanium and zirconium and the ceramic crystal lattice take place more vigorously. In the presence of other metals at the interface with which titanium forms solid solutions, a bond is established between the ceramic body and the metal member with which the ceramic was put into contact during the assembly of the tube [19]. Titanium oxide and zirconium oxide are highly refractory ceramics, and it is a well established fact that ceramics are constituted of a number of different oxides. It therefore follows that titanium and zirconium will, under favourable conditions, reduce some of these oxides and combine with the released oxygen as long as active gases, such as oxygen or nitrogen, are not present in the atmosphere in which the seal is being made. Titanium and zirconium are known as active metals by virtue of their relative chemical activity [34]. Titanium for instance cannot be processed in ceramic crucibles as it will react with the ceramic, and so it is usually processed in its liquid form in water cooled copper crucibles. All that needs to be done to produce the necessary reactions to obtain vacuum tight seals, is to put titanium or zirconium in contact with the two ceramic surfaces, or between a ceramic and a metal surface. As the exclusion of an oxygen atmosphere is essential during the firing process for a seal to be effected, the active alloy seal has to be made under high vacuum, or in a very pure hydrogen, argon or helium atmosphere. The purity of the active metals themselves and the atmosphere is of critical importance [19]. Precautions have to be taken to ensure that oxides are not released from the metal surfaces during the brazing operations. Thus careful cleaning of all components prior to their being joined in an active alloy process must not be overlooked. While one way of applying titanium, or zirconium for that matter, to the ceramic and metal surfaces is to paint them with a titanium or zirconium hydride and nitro-cellulose lacquer mixture in a thin, uniform layer either by brushing or spraying the surfaces in question, and then heating the parts to 900°C to form a tight bond, a far more practicable approach is the use of a titanium alloy in the form of a washer, placing it between the components and then firing them at temperatures of 950°C. These titanium alloys typically contain silver, copper, nickel, tin or lead, and are preferable to pure titanium, which, when used as a brazing medium, would require brazing temperatures of 1710°C. Hence the approach of using alloys for the active alloy process shall be pursued. The brazing alloy, that shall be used for joining the components of the X-ray tube, consists of titanium, silver, copper and indium. The use of such a brazing alloy promises a most effective and simple method of producing a seal, as the alloy can merely be cleaned and then placed in the form of a washer between the metal and the ceramic. After the components are placed under pressure and heated to a temperature of 950°C a vacuum tight seal is formed. According to *Hensley* [34] the chemical reaction that actually takes place during the formation of the seal is as follows:

$$3Ti + Al_2O_3 \rightarrow 3TiO + 2Al$$

While the excess titanium and aluminium are dissolved in the braze filler material, the ceramic material Al_2O_3, also known as alumina, and TiO bond together by diffusion. The alloy used for brazing the X-ray tube components is the active solder alloy CH4 from *Degussa AG*. Below is a

listing of the composition of that particular alloy as well as other alloys belonging to Degussa's CH family.

Table 4.1: Composition of CH active solder alloys by Degussa [42].

	%Cu	%Ag	%Ti	%In
CH1	19.5	72.5	3.0	5.0
CH2	-	96.0	4.0	-
CH3	6.0	91.0	3.0	-
CH4	26.5	70.5	3.0	-

According to *Weise* [42] CH4 has a soldering temperature of 950°C and a melting temperature of 803°C to 857°C, and has been used successfully in joining Al_2O_3 to steel containing iron and nickel or iron, nickel and cobalt to form vacuum tight seals.

4.4. STRESS IN JOINTS DUE TO THERMAL EXPANSION

A very important aspect of joining metal to ceramic is the type of metal used. According to *Kohl* [19] and *Weise* [42] it is essential to use a metal for the tube components, that has thermal expansion properties similar to ceramic. It is a well established fact, that differences in expansion coefficients between the ceramic and the metal will ultimately lead to stresses in the joint. The best solution therefore is to avoid the development of such stresses in the first place by ensuring that the mismatch in expansion coefficients is as minimal as possible. In Figure 4.1 a plot of the expansion versus temperature is shown for a number of materials. The ceramic, that is used for the manufacture of vacuum envelopes for the X-ray tube, is of the type DEGUSSIT AL23 manufactured by Degussa. According to Degussa's technical data on their ceramic products [43] AL23 is composed of the following materials and displays characteristics as outlined in Table 4.2 below.

Table 4.2: Properties of DEGUSSIT AL23 [43].

	DEGUSSIT AL23, Sintered aluminium oxide
Chemical composition	>99.5% Al_2O_3
Structure	dense
Melting point, °C	2030
Working temperature, °C	1900
Thermal expansion 0-1000 °C, m/m °C	8.1×10^{-6}
Compressive strength, kg/cm²	30000
Bending strength, kg/cm²	3800
Tensile strength, kg/cm²	2650
Electrical Breakdown strength, kV RMS/mm (at 20 °C)	22

Table 4.2 (cont.): Properties of DEGUSSIT AL23 [43].

	DEGUSSIT AL23, Sintered aluminium oxide
Behaviour in oxidising atmospheres	resistant
Behaviour in reducing atmospheres	resistant
Behaviour in high vacuum	resistant
Behaviour in high vacuum or H_2 with W and Mo	resistant

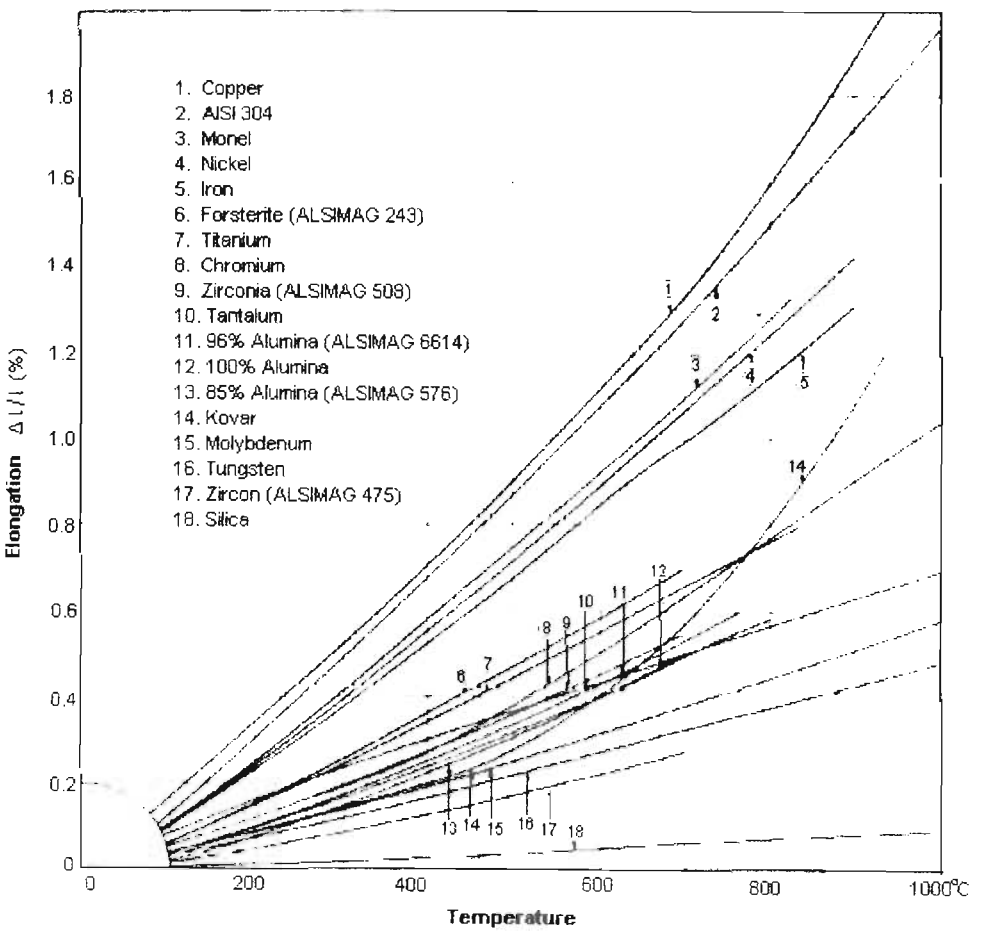

Fig. 4.1: Percentage elongation for vacuum materials [19]. Note that Kovar is an alternative designation for Dilver P.

From Figure 4.1 it can be seen, that the metal alloy Kovar has a percentage elongation very close to that of 100% alumina, especially for temperatures of up to 700°C. Note should be taken of the fact, that Kovar has so far been generally referred to as Dilver P, the name that it is currently

trading under, and therefore the author shall return to using this designation for that particular type of steel throughout the remaining sections of this chapter. Figure 4.1 also shows that copper for instance is least suitable for joining to ceramics. This has been verified by *Hensley* [34], who produced experimental copper-to-ceramic seals using the brazing alloy CH4, which, although resulting in mechanically strong bonds formed between the copper and the ceramic, failed to be vacuum tight. Similarly poor results were obtained for nickel and monel, and were also attributed to the stresses formed in the joints. For the purpose of clarity, it is important to note, that actual stresses do not occur in the active braze joint, but in the ceramic adjoining it. Therefore the actual limiting factor in joining metals to ceramic is not the active solder alloy itself, but rather the ceramic. From the above considerations Dilver P can therefore be considered as the ideal metal to be joined to ceramic to form stress free and vacuum tight joints.

4.5. THERMAL SHOCK

Another characteristic related to the thermal expansion coefficient of ceramics is that of thermal shock. Thermal shock refers to the temperature range that a ceramic component can withstand without rupture. The Schott-Winkelmann equation for the sudden cooling of a body is a measure of thermal shock [34][44]:

$$\Delta T = \frac{\sigma}{E\alpha} \cdot \sqrt{\frac{h}{g c_h}} W \tag{4.1}$$

where ΔT = the tolerable temperature range (°C);
σ = the tensile strength (Pa);
E = the elastic modulus (Pa);
α = the expansion coefficient (K^{-1});
h = the thermal conductivity (W m^{-1} K^{-1});
g = the density (kg m^{-3});
c_h = the specific heat (J kg^{-1} $°C^{-1}$);
W = a shape factor dependent on the geometry of the part;

In the case of an X-ray tube thermal shock has to be viewed in a serious light because of the heat developments during its operation, which can be considerable. It is therefore important to establish what temperature range a particular metal-to-ceramic seal can withstand without becoming leaky or undergoing complete rupture. Because ceramics generally tend to be stronger in compression than in tension [19], the effects of thermal shock become noticeable during the cooling down of a joint after having undergone heating. In the next section the joining of Dilver P discs to a ceramic tube with an outer diameter of 30 mm and an inner diameter of 25 mm will be described. The cooling curve profile that the heating cycle will have to follow once the joint has been brazed at a temperature of 950°C will be of special importance if rupture of the ceramic due to an excessively rapid cooling rate is to be avoided.

4.6. BRAZING AND TESTING OF EXPERIMENTAL METAL-TO-CERAMIC SEALS

Since X-ray tubes display a tendency towards the development of high anode temperatures it is necessary to ensure, that the vacuum tight metal-to-ceramic seals of the tube can operate within a certain temperature range without causing cracking of the ceramic along the joints, which results in the loss of tube vacuum. It was therefore decided to build an experimental tube as shown in Figure 4.2, which would be tested for the maximum temperature ranges, that its metal-to-ceramic seals could withstand without cracking. The experimental tube consisted of two metal discs separated by a ceramic vacuum envelope. In order to provide a pumping port for the tube a copper stem with an outer diameter of 9 mm and an inner diameter of 8 mm was fed through and brazed to one of the metal discs as illustrated in Figure 4.2. Before attempting to braze a metal-to-ceramic seal it is necessary to ensure a flat and smooth finish of the metal and ceramic surfaces, where the vacuum tight braze is to be formed. The metal discs, that were punched out of 1 mm thick Dilver P sheeting, had a diameter of 38 mm. Therefore the surface oxides, that tend to form on metal surfaces, had to be removed from the Dilver P metal discs mechanically, namely by polishing them with 1200 grit sandpaper. To remove any oils or fats from the metal surfaces, the discs were then first cleaned in distilled water in an ultrasonic bath. The latter procedure was then repeated by ultrasonically cleaning the metal in an ethanol bath. The ceramic tubes were processed in the same manner. However, since ceramic tends to be very hard, mechanical polishing of the ceramic surfaces, where a seal was to be formed, was accomplished by diamond polishing on a diamond saw. Tubes of 40 mm length were prepared, and then assembled in a jig as illustrated in Figure 4.2 below with CH4 washers placed between the ceramic and metal parts. The function of the jig is to keep the tube components in perfect alignment during the brazing of the seals (see Figure 4.2). In this way the parts were assembled in a vacuum furnace and compressed by a weight of approximately 500 g.

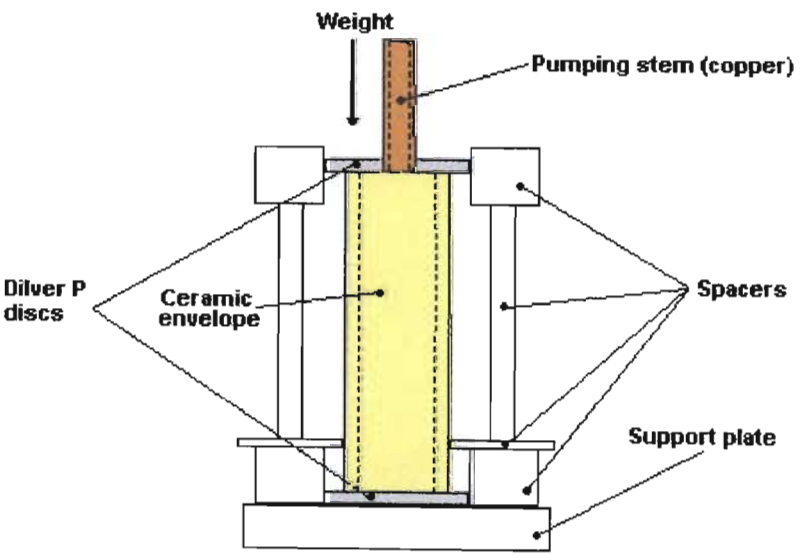

Fig. 4.2: Jigging of the experimental ceramic tubes prior to brazing.

The temperature profile used for the brazing procedure is shown in Figure 4.3. According to *Hensley* [34] a cooling rate of 23°C/min consistently produced mechanical failure of the ceramic in the form of cracks forming in the ceramic sleeve adjacent to the metal-to-ceramic seal. After modifying the cooling rate to 7°C/min he finally obtained vacuum tight seals formed between the Dilver P components and the ceramic tubes. It is evident that the lower the cooling rate the more the stresses present in the joint are reduced if not eliminated. As illustrated in Figure 4.3 the author introduced a cooling rate of 5°C/min from 960°C to 250°C, at which point the heating cycle came to an end. The tube was then allowed to cool down to room temperature inside the furnace for 120 minutes. After the brazing of the tube was completed using the temperature curve in Figure 4.3 the metal-to-ceramic seals thus formed were allowed to cool down to room temperature. The joints of the tube were then tested by heating the tube in a furnace in air to a temperature of 60°C. After cooling down to room temperature again, the tube was then mounted on a vacuum pumping station as illustrated in Figure 4.4.

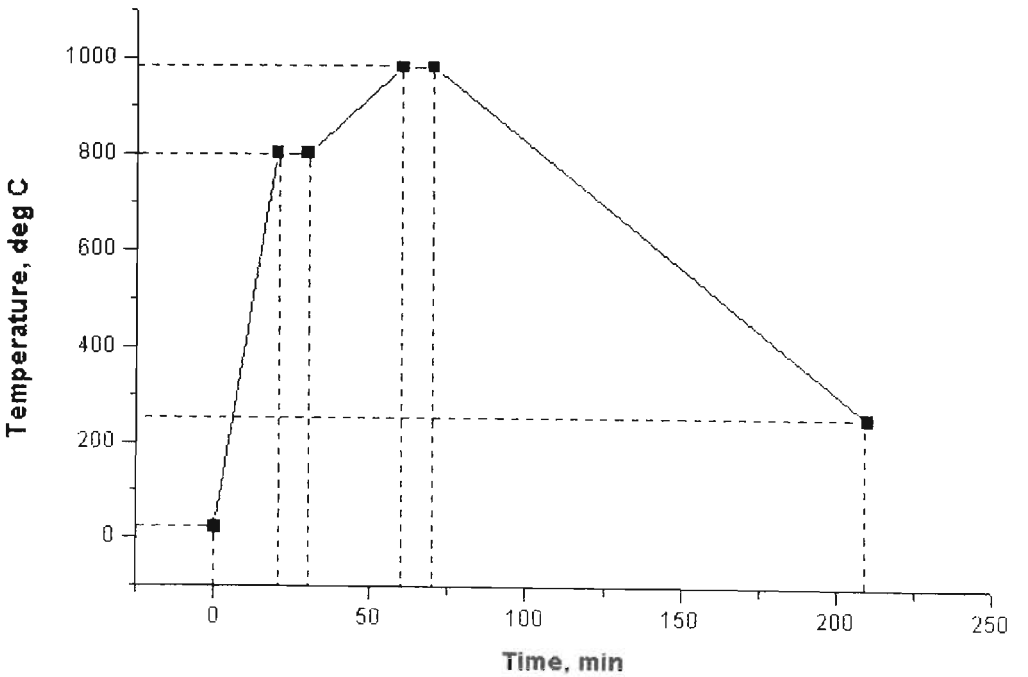

Fig. 4.3: Active brazing temperature profile [34].

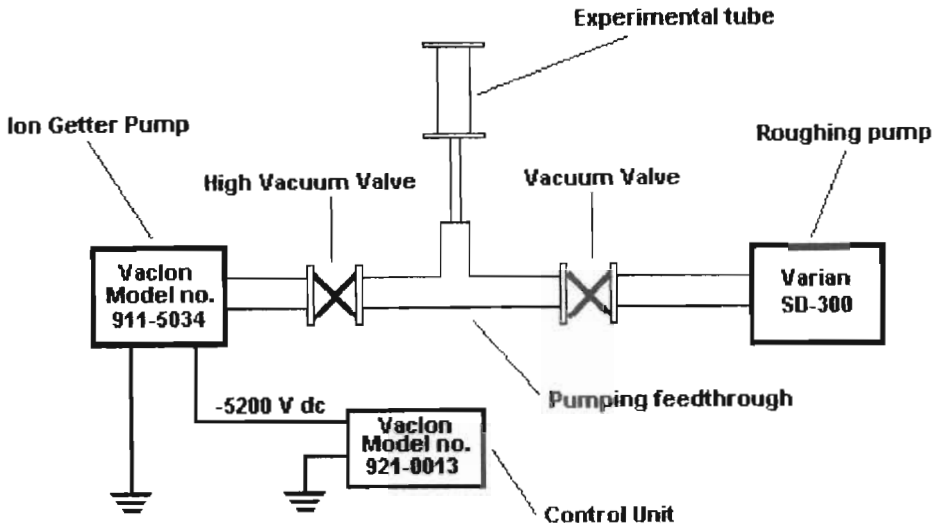

Fig. 4.4: Vacuum pumping station used in the testing of metal-to-ceramic seals.

The tube was pumped through its copper stem, which was attached to the vacuum feedthroughs of the vacuum pumping station via a vacuum tight copper ring seal. As can be seen in Figure 4.4 the vacuum pumping station operates on two vacuum pumps. With the high vacuum valve closed the roughing pump, which is capable of providing maximum pressures of 10^{-3} Torr, was engaged first to pump air out of the tube. As a pressure of 10^{-3} Torr was reached, the ion getter pump, with an operating pressure range of 10^{-2} Torr to 10^{-11} Torr, was then set into operation after the high vacuum valve was opened (see Figure 4.4), and the tube was pumped down to a pressure of 10^{-5} Torr. This procedure was repeated for temperatures of 90°C, 120°C, 140°C, 160°C and 180°C for three samples of the experimental tube described above. The results obtained are shown in Table 4.3 below.

Table 4.3: Maximum pressures that tubes 1, 2 and 3 as shown in Figure 4.2 were pumped down to after they were heated up to a temperature T.

	Maximum pressure (Torr) in tube no. 1	Maximum pressure (Torr) in tube no. 2	Maximum pressure (Torr) in tube no. 3
T=60°C	10^{-5}	10^{-5}	10^{-5}
T=90°C	10^{-5}	10^{-5}	10^{-5}
T=120°C	10^{-5}	10^{-5}	10^{-5}
T=140°C	10^{-5}	10^{-5}	10^{-5}
T=160°C	10^{-5}	10^{-5}	10^{-5}
T=180°C	10^{-1}	8×10^{-2}	5×10^{-2}

In Table 4.3 one can see, that the metal-to-ceramic seals of the tubes were capable of maintaining vacuum pressure levels of 10^{-5} Torr after they were heated to temperatures of 60°C, 90°C, 120°C, 140°C, 160°C and 180°C, and allowed to cool down to room temperature following each of the aforementioned temperature levels. However, for a temperature of 180°C it was no longer possible to pump the tubes to pressures below 10^{-3} Torr. By visually inspecting the tube joints under a microscope it was noted, that cracks along the ceramic adjacent to the metal-to-ceramic seals had developed in the tubes after they were exposed to a temperature of 180°C. From these observations it can therefore be concluded, that tubes with vacuum tight seals between the metal Dilver P and ceramic, where the solder alloy CH4 is used to braze the joint, should not be heated above a temperature of approximately 160°C if damage to the seals is to be avoided. It is for this reason that cooling of the ceramic X-ray tube while operating it becomes absolutely essential. The above results also confirmed the fact, that the formation of stresses along a metal-to-ceramic seal typically occur, if cooling of the seal from a high temperature occurs at too fast a rate. It is therefore essential, that a low rate of cooling be applied to a metal-to-ceramic seal after it has been brazed, so as to minimise the development of stresses between the metal and the ceramic along the joint.

4.7. ASSEMBLY OF THE X-RAY TUBE

Before the X-ray tube described in chapter 3.1 was assembled, jigged and brazed following the same procedure as the one described in section 4.6 above a number of metal-to-metal brazes had to be completed in order to produce the individual metal components of the tube. Metal-to-metal seals had to be made between the tungsten target of the anode and the Dilver P ring supporting it, which serves as an electrical contact of the anode (see Figure 3.1.17, Section 3.1.5), as well as between the stainless steel focusing lens and its Dilver P support (see Figure 3.1.1, Section 3.1.1). In the same way the cathode support of the X-ray window-cold cathode structure, which was manufactured from stainless steel, had to be brazed onto the Dilver P cathode-window support (see Figure 3.1.11, Section 3.1.4). In order to realise the aforementioned metal-to-metal seals special brazing alloys for different metal-to-metal seals were used. The brazing alloys, manufactured by WESGO, are listed in the table below together with their properties.

Table 4.4: Specifications for WESGO brazing alloys. The data is taken from the WESGO brazing alloy datasheets [51].

Brazing Alloy	Composition	Liquidus, °C	Solidus, °C	Characteristics
PALCO	Co: 34%-36%; Pd: 64%-66%;	1235	1230	Lowest vapour pressure in its melting range. Wets Molybdenum and Tungsten.

Table 4.4 (cont.): Specifications for WESGO brazing alloys. The data is taken from the WESGO brazing alloy datasheets [51].

Brazing Alloy	Composition	Liquidus, °C	Solidus, °C	Characteristics
NIORO	Au: 81%-83%; Ni: 17%-19%;	950	1000	Will "wet" Tungsten and Molybdenum, as well as Copper, Dilver P, Stainless Steel. Excellent flow.
NICORO	Au: 34%-36%; Cu: 61%-63%; Ni:2.75%3.25%;	1030	950	Excellent wetting and flow on Dilver P, Copper, Nickel and Steel.

The alloy NICORO was used for all the metal-to-metal brazes except for the joining of tungsten to the Dilver P support of the anode, where a vacuum tight joint was produced with PALCO as the brazing alloy. The brazing of the focusing lens and the cathode was accomplished by placing a NICORO ring (see Figure 4.5) and allowing the welding process to take place at a temperature of 1050°C for a period of ten minutes. The brazing of the tungsten target to its support was effected in the same manner at a vacuum furnace temperature of 1250°C for the same period of time. The copper pumping stem was brazed to the anode using NICORO as the brazing alloy only after the tungsten target was brazed onto its support at the higher temperature of 1250°C necessary for brazing with the alloy PALCO.

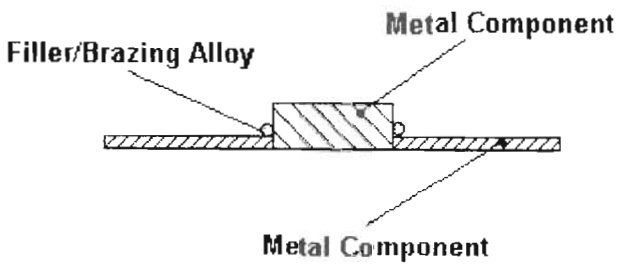

Fig. 4.5: Example of a brazing ring or filler placed at a metal-to-metal joint prior to brazing.

After the completion of the metal-to-metal joints as well as the metal-to-ceramic seals, the X-ray tube was virtually fully assembled with only the X-ray window remaining to be added to the tube

structure. Thus before the tube could be mounted on the vacuum pump station the aluminium window had to be assembled onto the tube. This was accomplished by joining a thin 0.1 mm thick aluminium foil over the window opening with a vacuum tight adhesive, thus producing a so-called "Torr seal", and mechanically fastening it with an aluminium washer or window support (see Figure 3.1.11, section 3.1). The aluminium window could only be mounted after the brazing of the tube was complete, since the melting point of aluminium, which is 660.1°C, is far lower than the active brazing temperature of 960°C. In order to determine the pressure, which a cold cathode X-ray tube should be pumped down to, the mean free path length of the electrons travelling through the tube should be taken into consideration. The mean free path length is the mean distance travelled by a particle between collisions [37]. At relatively high pressures, where molecules collide with each other far more frequently than with the vacuum chamber walls, gas flow is referred to as viscous flow. At low pressures, on the other hand, molecules collide with the vacuum system walls more frequently than with each other. This type of gas flow is known as molecular flow. With molecular flow in the X-ray tube the molecules of the rest gas, air in this case, collide with each other to a far lesser extent while the tube is operated. In the same way it can be stated, that electrons travelling towards the anode of the tube will be far less likely to loose energy by colliding with each other or the rest gas molecules before reaching the target provided that the pressure inside the tube is low enough to allow for molecular flow. From a theoretical point of view this is desirable as a greater number of electrons, which have not lost any energy while propagating towards the target due to collisions with other particles in the tube, will thus be capable of transferring more energy to the X-radiation produced by the electrons' collisions with the target of the X-ray tube. As shown in chapter 3.1 the electrons have to travel from the cathode to the anode through a distance of 0.056 metres. This means, that for molecular flow to occur the mean free path length should be greater than 0.056 metres. According to *Young* [31] the mean free path length, which is denoted by λ, can be expressed by the following equation:

$$\lambda = \frac{k \cdot T}{133{,}3 \cdot 4\pi\sqrt{2} \cdot r^2 \cdot P} \tag{4.2}$$

where k = Boltzmann's constant (1.38×10^{-23} J K^{-1});
T = Temperature (K);
P = Pressure (Pa);
r = radius of the rest gas molecules (m);

To determine the maximum permissible air pressure inside the X-ray tube for molecular flow to occur λ has to be equated to the cathode anode spacing of the tube, which is 0.056 metres. The temperature T can be approximated at 293 K, which is room temperature. The radius r of an air molecule is approximately 2×10^{-10} m according to *Young* [31]. Substituting these values into equation 4.2 a pressure value of 7×10^{-4} Torr is obtained. This presents the maximum pressure, that the tube should be operated at. According to *Templeman* [52], however, who conducted experiments with cold cathode X-ray tubes, the gas pressure of a cold cathode X-ray tube should be in the "soft" vacuum range (10^{-3} Torr to 10^{-4} Torr) to permit the passage of electrons from the cathode to the X-ray producing target in a so-called "dark" discharge. Higher pressures would result in a luminous discharge, as in a neon lamp, with only a small potential drop across the tube, while lower pressures would result in no current flow regardless of the voltage applied [52]. Incidentally the pressure range of 10^{-2} Torr to 10^{-4} Torr represents a transition from viscous to molecular flow [37]. This means that the "soft" vacuum range of 10^{-3} Torr to 10^{-4} Torr falls into

the pressure range, where both viscous and molecular flow occurs. This observation was verified by the author (see Chapter 6), who found that no current flow took place in a tube with a hard vacuum at a gas pressure of 6×10^{-5} Torr whilst high voltage pulses were applied across the X-ray tube. Operating the same type of tube, however, at a higher gas pressure of 7×10^{-4} Torr, which falls within the soft vacuum range mentioned above, resulted in the production of a tube current, and hence X-radiation, during the operation of the X-ray tube.

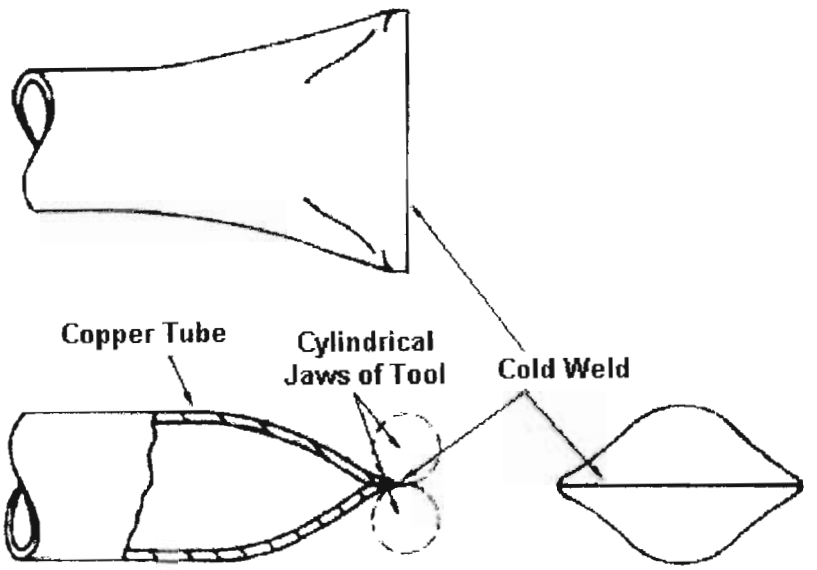

Fig. 4.6: Technique used to squeeze-off or pinch-off the copper tubulation between the tube and the pumping station [37].

The setup for the vacuum pumping station as illustrated in Figure 4.4 was used to pump down the X-ray tube. After the desired pressure of 7×10^{-4} Torr was attained, it was necessary to separate the tube from the pumping station. The technique used to separate the tube from the pumping station is illustrated in Figure 4.6. As already mentioned in the preceding section the soft copper tubulation was used to make the vacuum connection between the tube and the pumping station. This tubulation was molecularly clean on its internal surfaces after having been baked along with the tube during the active brazing cycle. By squeezing the tubulation with a special tool, the internal mating surfaces of the copper were forced to flow together to form a cold weld. In Figure 4.7 the different X-ray tube components prior to brazing and assembly are shown.

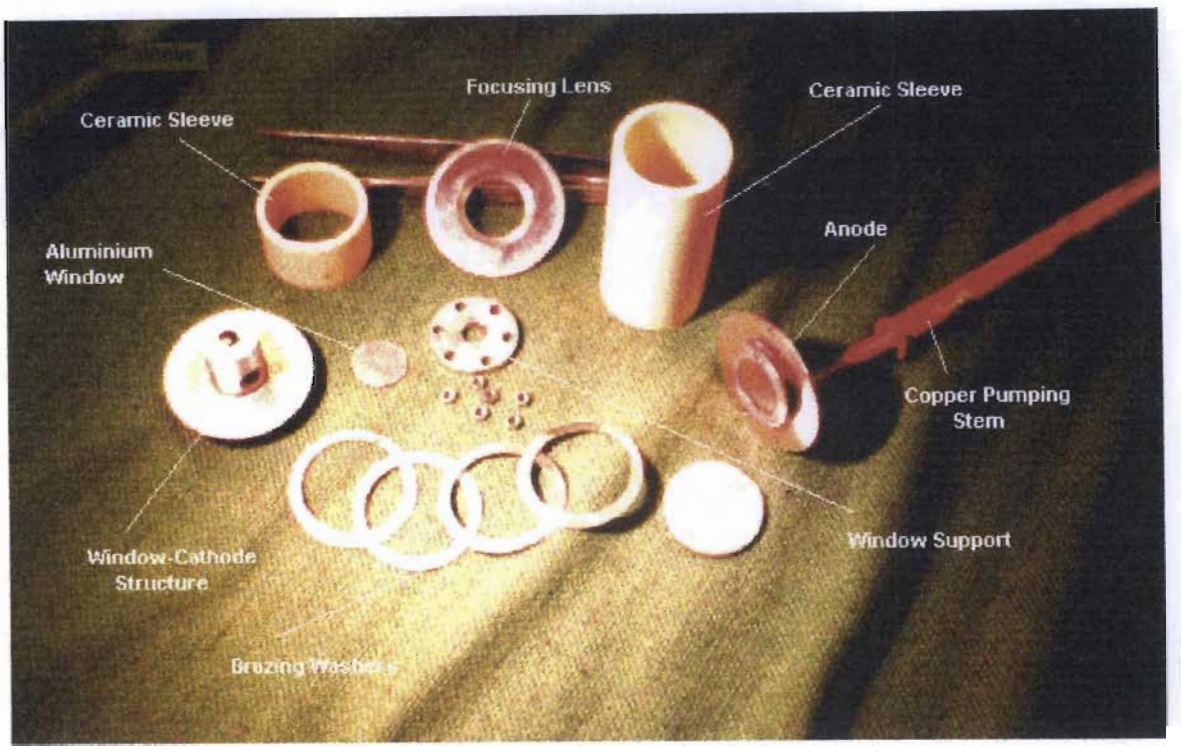

Fig. 4.7: The components of the end-window cold cathode X-ray tube.

4.8. OUTGASSING

Outgassing is a process by which any gas molecules not drifting freely in the tube, i.e. attached to the inner surfaces of the tube, are removed [34]. This was accomplished by elevating the temperature of the tube to release the bonded gas molecules while the device was pumped down. In this way the inner surfaces of the tube were allowed to expand and release molecules trapped in the minuscule creases and cracks of the inner ceramic surfaces of the tube. The operating temperature should never exceed the outgassing temperature, so as to ensure that no further molecules would be released from the inner surfaces of the device during its life-time. At the same time, however, it is also necessary to ensure that the maximum allowable temperature for the entire tube is not exceeded. In the case of the end-window cold cathode X-ray tube the maximum allowable temperature is 160°C, a limit imposed by the sealing adhesive of the X-ray window, namely the "Torr seal" (see Section 4.7).

4.9. LEAD SHIELDING AND HIGH VOLTAGE INSULATION OF THE X-RAY TUBE

After successfully assembling, brazing and pumping the X-ray tube it is necessary to insulate the high voltage contact of the tube, which is the anode of the X-ray tube, from its surroundings, so that electrical spark over through air from the anode to other electrodes or electrical contacts can be avoided. This was accomplished by potting the X-ray tube in transformer high voltage insulation epoxy, which has a dielectric breakdown strength of 11 kV/mm. The tube was coated

in a 20 mm thick layer of epoxy thus allowing the anode of the tube, which would have to operate under voltages of up to 85 kV with respect to the grounded cathode of the tube, to withstand voltages of up to 220 kV without the insulation layer breaking down. Because the tube produces X-radiation not only in the direction of the X-ray window, but also sideways through its vacuum envelope, it was also necessary to place a cylindrically shaped lead shield of 1.5 mm thickness around the tube, so that all X-radiation leaving the tube sideways through its ceramic envelope would be absorbed. The resulting structure was then placed inside a PVC cylinder with an inner diameter of 100 mm and an outer diameter of 110 mm. The remaining space between the PVC sleeve and the lead shielding was then filled out with insulation epoxy. The potted tube surrounded by lead shielding is illustrated in Figure 4.8.

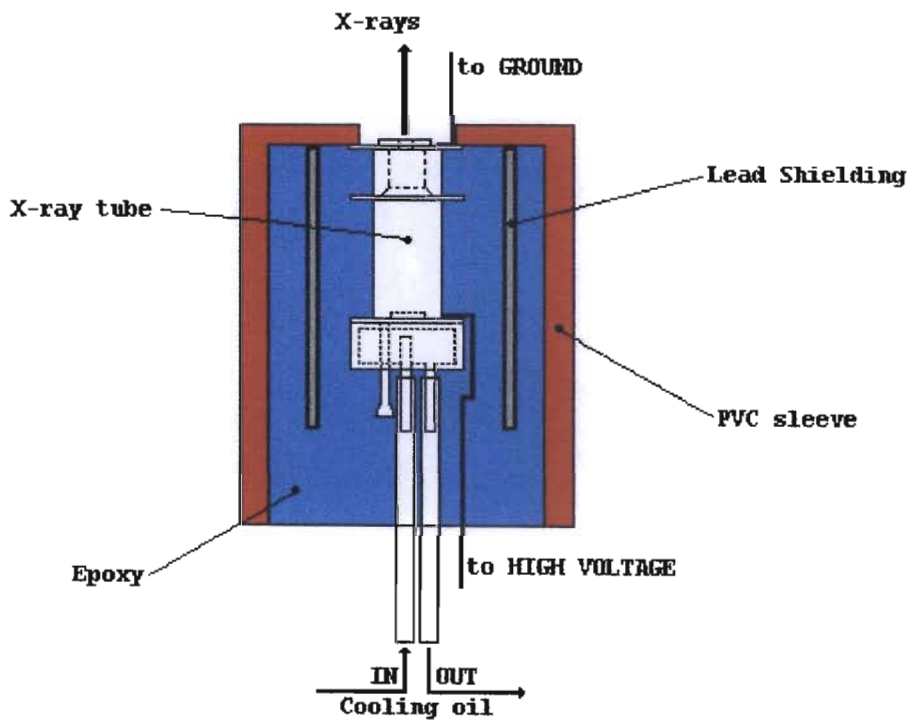

Fig. 4.8: The insulated X-ray tube with lead shielding.

4.10. SUMMARY

In this chapter the construction of the X-ray tube was discussed in closer detail. Central to this problem is the metal-to-ceramic sealing technique, which needs to be applied when joining the ceramic components of the tube to its metal parts. After briefly presenting the reader with a number of conventional techniques used to manufacture vacuum tight metal-to-ceramic seal it was finally decided to use the active alloy process. Unlike the method of sintered metal powder metal sealing, the active alloy process was chosen, because it proved to be a faster way of producing vacuum tight seals of the same quality as those effected by the sintered metal powder process. The active alloy technique required only one firing cycle at lower brazing temperatures

than those necessary in the sintered metal powder process. At the same time the ceramic surfaces which were to be joined to metal did not need to be treated with metallic coatings prior to the braze of the seal. In order to reduce the stresses between the ceramic and the metal in the joint, which usually results in cracking of the seal, a metal had to be chosen with a similar expansion coefficient to that of 99.9% alumina ceramic used in this case. The metal best suited for that purpose was the steel alloy Dilver P. The active alloy process was first tested on the seals of a set of three experimental tubes. The vacuum tightness of the seals was investigated by pumping the tubes to a pressure of 10^{-5} Torr after heating the tubes up to a certain temperature and allowing them to cool down to room temperature again. It was found, that the ceramic along the joints of the tubes tended to crack following their exposure to temperatures of approximately 180°C. After the occurrence of such cracking it was no longer possible to pump the tubes down to pressures below 10^{-3} Torr proving that the tubes had become leaky. A further constraint on the operating temperature of the tube was posed by the vacuum tight adhesive of the aluminium X-ray window, which in order to retain its vacuum tight properties should not be heated to temperatures above 160°C according to *Varian*, the manufacturer of the adhesive. It was therefore suggested, that the X-ray tube operating temperature be kept below 160°C, so as to prevent any thermal damage to the tube during its life-time. Finally, after the X-ray tube was assembled and brazed, it was established, that in order for a satisfactory current emission to take place in the tube, an X-ray tube pressure of between 10^{-3} Torr and 10^{-4} Torr would be required, and so a tube pressure of 7×10^{-4} Torr was chosen. In the end a brief description of how the X-ray tube was electrically insulated was given. This was followed by the application of lead shielding to the X-ray tube structure, so as to ensure, that any side radiation exiting the tube through its ceramic envelopes would be absorbed and not given off to the environment.

5. The Spectrometer Set-up for the Evaluation of the X-ray Tube

5.1. INTRODUCTION

In modern analytical chemistry many techniques are available for the determination of elemental compositions of materials samples. Instrumental methods include a variety of *spectroscopic* or *spectrometric* techniques, which depend on the analysis of some portion of the electromagnetic spectrum emitted or absorbed by the sample under the conditions of analysis. The spectra are characteristic of the elements present in the sample (and, in some cases, of the form in which they are present), and analysis is made by comparing results from the sample analysed with those obtained under the same conditions from calibration standards. In order to produce spectra of a given sample irradiated by an X-ray tube as efficiently as possible, it is necessary to optimise certain X-ray tube parameters. These X-ray tube parameters include the potential applied to the anode and cathode of the device, which affects both the penetrating power and the intensity of the resulting X-radiation, the electron current through the tube, which has a direct effect on the intensity of the X-radiation, as well as the photoefficiency of the X-ray tube cathode, the primary radiation distribution of the tube and the spectra obtained from a given sample obtained by irradiating that particular sample using the X-ray tube. This chapter discusses the X-ray fluorescence (XRF) spectrometer set-up (see Figure 5.1), which was used as a test station for the evaluation of the aforementioned cold cathode X-ray tube parameters. Furthermore it was also necessary that the measured data be recorded for subsequent analysis. These tasks were carried out quickly and repeatedly by recording the measured data on a personal computer, which was linked to a HP 54601A multichannel oscilloscope via a HP-IB interface (see Figure 5.1). The radiation intensity distribution of the X-ray tube on the other hand was determined by measuring the primary radiation of the X-ray tube at different angles to the X-ray tube target using a Geiger counter (see Figure 5.4). Finally the ability of the tube to excite elements contained in a given sample was tested by operating the X-ray tube in the spectrometer set-up shown in Figure 5.1 and analysing the spectra of the sample elements using AMPTEK's XR-100T-CZT and XR-100T X-ray detector systems. In Figure 5.1 it can be seen, that either the AMPTEK XR-100T-CZT cadmium zinc telluride X-ray detector for higher energy measurements or the AMPTEK XR-100T silicon detector for higher energy resolution measurements may be used with the 'AMPTEK MCA 8000A' multichannel analyser, a software package used for the analysis of X-ray spectra characteristic of the elements present in the sample. Apart from determining the presence of certain elements in a particular sample, the X-ray spectra thus obtained also gave a direct indication of the intensity of the spectra. The spectra intensity, which is displayed by the multichannel analyser in counts per second (cps) on the y-axis of the spectra display, is a quantity, which is directly dependent on the X-ray tube current (see Chapters 2 and 3.2), but is also indicative of the concentrations of the various sample elements relative to each other. In order to protect the user of the spectrometer from harmful X-rays it was necessary to irradiate the samples in a chamber with lead lined aluminium walls, which shields the environs of the spectrometer from the primary radiation of the X-ray tube and the secondary radiation containing the characteristic spectra of the sample elements. Furthermore the high voltage power supply, which, when in operation, was found to have produced electromagnetic impulses (EMI) harmful to electronic devices, had to be placed in an EMI shielding enclosure. In this case the chamber consisted of 2.2 cm thick aluminium laid out with 5 mm thick PVC on the inside to prevent any spark over from the high voltage power supply to the aluminium walls of the chamber. In the following sections the methods, which were used for measuring the typical X-ray tube current

and voltage characteristics, the MgO cold cathode photoefficiency as well as the distribution of the primary radiation intensity of the X-ray tube are described in detail.

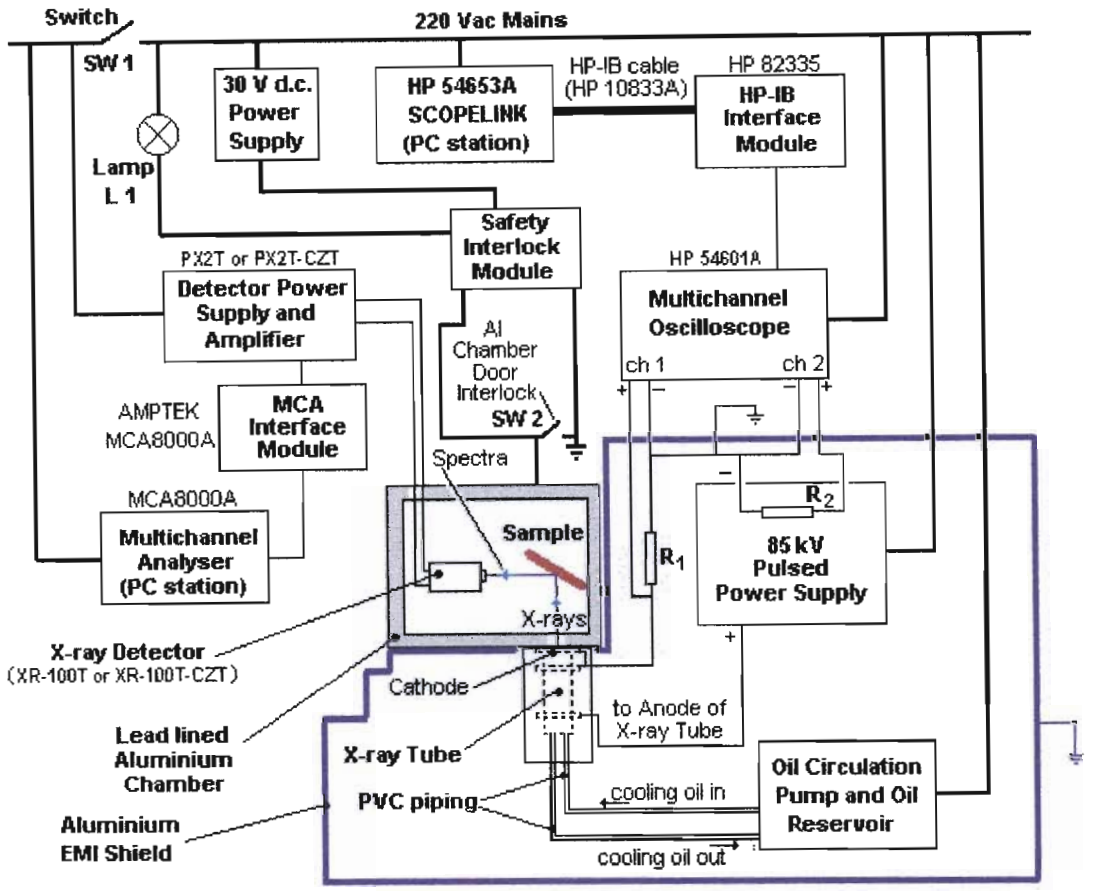

Fig. 5.1: The X-ray fluorescence spectrometer set-up, in which the cold cathode X-ray tube was evaluated.

5.2. MEASUREMENT OF THE X-RAY TUBE CURRENT AND SUPPLY VOLTAGE

The current through the X-ray tube was measured via the voltage drop across a 10 Ω measuring resistor (resistor R_1 in Figure 5.1) connected in series with the X-ray tube between its cathode and the ground of the 85 kV pulsed power supply. This means that the tube cathode, which had to be connected to ground, was in fact offset from ground during the operation of the X-ray tube. If one assumes a maximum tube current of 30 mA, then the maximum equivalent voltage drop for that particular current across R_1, or alternatively the tube cathode offset from ground, can be easily computed as 300 mV according to Ohm's law. For a maximum tube voltage of 85 kV the error thus introduced would be 3.53×10^{-4} % which is insignificant. Assuming a maximum current of 30 mA with a voltage of 1 kV across the tube the error would rise to 0.0353 %, which can also be considered negligible. Hence it can be said that the introduction of a 10 Ω measuring resistor in

series with the X-ray tube did not alter the performance of the tube in any significant way at all. The voltage drop across resistor R_2 on the other hand (see Figure 5.1 and Figure 5.2) gave an indication of the voltage drop across the X-ray tube. Resistor R_2 was in fact part of a resistor-capacitor voltage divider network connected in parallel with the pulsed power supply output. The so-called parallel arrangement of resistors and capacitors is a well-known technique used for attenuators within electronic measuring instruments, and is often referred to as a compensated resistor voltage divider [50]. Their chief advantage over pure resistor divider networks is the fact, that they have a better unit step response, which means that the final voltage build up across the resistors is much faster. For this reason the resistor-capacitor divider is typically used for the measurement of high impulse voltages. The resistor values are typically in the range of several kΩ, while the capacitor values are of the order of some 100 pF. The circuit diagram of the particular resistor-capacitor divider network, which was internal to the power supply unit, is shown in Figure 5.2 below. The divider network shown in Figure 5.2 consisted of twenty-eight 47 MΩ high voltage resistors and resistor R_2, which had a value of 33 kΩ, connected in series. High voltage ceramic capacitors of 470 pF were connected in parallel with each of the resistors. With a maximum power supply output voltage of 85 kV the maximum voltage drop V_2, that could be measured across R_2, was equal to 2.125 V (see Figure 5.2). The current and voltage waveforms were displayed on a PC station using the graphic oscilloscope display software package 'Scopelink HP 54653A'. This data was then processed from the oscilloscope to the PC station via a HP-IB interface module (see Figure 5.1).

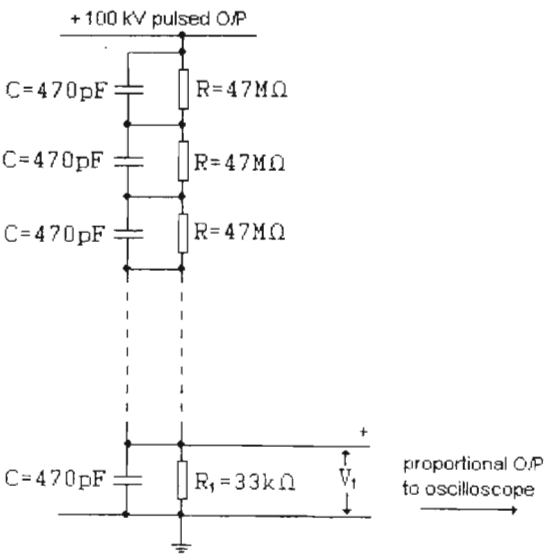

Fig. 5.2: Proportional voltage measurement from the power supply output.

5.3. DETERMINATION OF THE PHOTOEFFICIENCY OF THE MgO COLD CATHODE

In Section 3.2.11, Chapter 3, it was pointed out that the cold cathode of the X-ray tube, once irradiated by the primary radiation produced at the target of the tube, will emit photoelectrons raised to a higher energy state by the X-radiation in addition to the field emitted electrons. According to *Pollehn* [49] photoemission is a three step process:

1. Absorption of a photon elevating an electron into a state of higher energy.

2. The motion of the electron through the material.

3. The escape of the electron into the vacuum.

In an ideal cathode, all photons arriving at the cathode will release an electron into the vacuum, giving 100 per cent quantum efficiency. However, losses occur in all three steps mentioned above. In the case of the MgO cold cathode of the X-ray tube not all of the photons arriving at the cathode were absorbed. Some of the X-ray photons passed through the nickel substrate of the cold cathode losing some or no energy at all in the process (see Section 3.2.11, Chapter 3). The photoefficiency of the X-ray tube was measured by comparing the average current flow through the X-ray tube with that of a tube that did not contain a tungsten target. Such a tube, which in effect constituted a diode, had the same structure as the X-ray tube albeit without the tungsten target at which X-radiation would have been produced. Therefore the field current emission characteristics of the diode were assumed to be virtually identical to that of the X-ray tube. Ideally no X-radiation induced photocurrent should have been produced in the diode due to the absence of a tungsten target. The average current through the diode is denoted $i_{AVE,\ DIODE}$ as opposed to the average X-ray tube current $i_{AVE,\ X\text{-}RAY\ TUBE}$. The photoefficiency of the X-ray tube relative to the diode can be expressed as the ratio of the average X-ray tube photocurrent $i_{ave,\ photo}$, which is equal to $i_{AVE,\ X\text{-}RAY\ TUBE} - i_{AVE,\ DIODE}$, and $i_{AVE,\ X\text{-}RAY\ TUBE}$ (see equation 3.2.67, Section 3.2.12):

$$\text{photoefficiency} = \frac{i_{AVE,\ X-RAY\ TUBE} - i_{AVE,\ DIODE}}{i_{AVE,\ X-RAY\ TUBE}} \cdot 100\% \qquad (5.1)$$

where $i_{AVE,\ DIODE}$ is equivalent to the average field current $i_{ave,\ field}$ while $i_{AVE,\ X\text{-}RAY\ TUBE}$ is representative of the total average current through the X-ray tube containing both the photocurrent and the field current. This, however, is not quite true since the diode did produce X-radiation which primarily resulted from the interaction of the accelerated electrons with the anode of the diode, which in this case consisted of a Dilver P plate. This means that some X-radiation containing iron characteristic lines was produced, which acted on the cathode of the diode.

5.4. MEASUREMENT OF THE PRIMARY RADIATION INTENSITY DISTRIBUTION OF THE X-RAY TUBE

In order to determine the absolute intensity of the primary X-radiation from the X-ray tube the total intensity had to be measured at the window of the tube. The total radiation intensity of the primary beam produced by an X-ray tube can be measured with either an X-ray detector or a Geiger-Müller counter tube. When measuring the radiation intensity emanating from an X-ray

tube window one is actually determining the primary X-radiation intensity. As described in Section 5.5 the characteristic X-ray spectra obtained from the multichannel analyser with an X-ray detector displays the total intensity values for different X-ray photon energies. This means that in order to determine the total radiation intensity the spectra of the primary radiation has to be integrated in terms of energy. With a Geiger-Müller tube the total number of photons arriving at the Geiger-Müller tube window is counted for a given time interval. The multichannel analyser (MCA), on the other hand, has the advantage of allowing the user to obtain spectra via the X-ray detector in the form of the total number of counts per energy channel (see Section 5.5) as well as the total number of counts received from the X-radiation for the given region of interest (ROI). The region of interest is the energy range in the spectrum that the user can choose. This can obviously be just a section of the measured spectra, for which the integrated intensity is then measured, or spectra which spans across the entire energy range of all the elements of the periodic table.

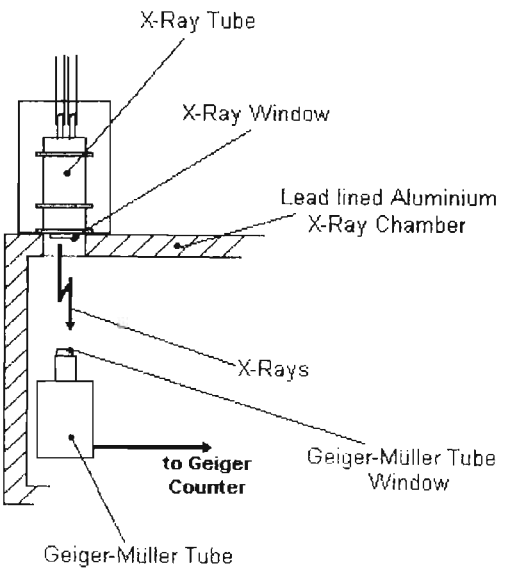

Fig. 5.3: Measurement set-up for the determination of the absolute primary radiation intensity of the X-ray tube.

The direct measurement of the primary spectra emanating from an X-ray tube window by the XR-100T-CZT or XR-100T detector is not recommended, however, since X-radiation arriving at the detector window with intensities above 1000 counts per second (cps) usually leads to detector saturation [47]. For this reason the Geiger-Müller tube was used in order to determine the integral primary radiation intensity of the cold cathode X-ray tube. The measurement set-up for this experiment is illustrated in Figure 5.3. Furthermore it was also necessary to determine the radiation distribution of the X-ray tube in order to establish at what angles to the target face of the tube maximum radiation intensities were produced. The radiation distribution of the X-ray tube

was measured at angles between -45° and 90° to the target face of the X-ray tube (see Figure 5.4). For this experiment a tube was used that did not contain a lead shield as shown in Figure 4.8 in Chapter 4, so that the radiation emanating from the side of the tube could also be measured as illustrated below.

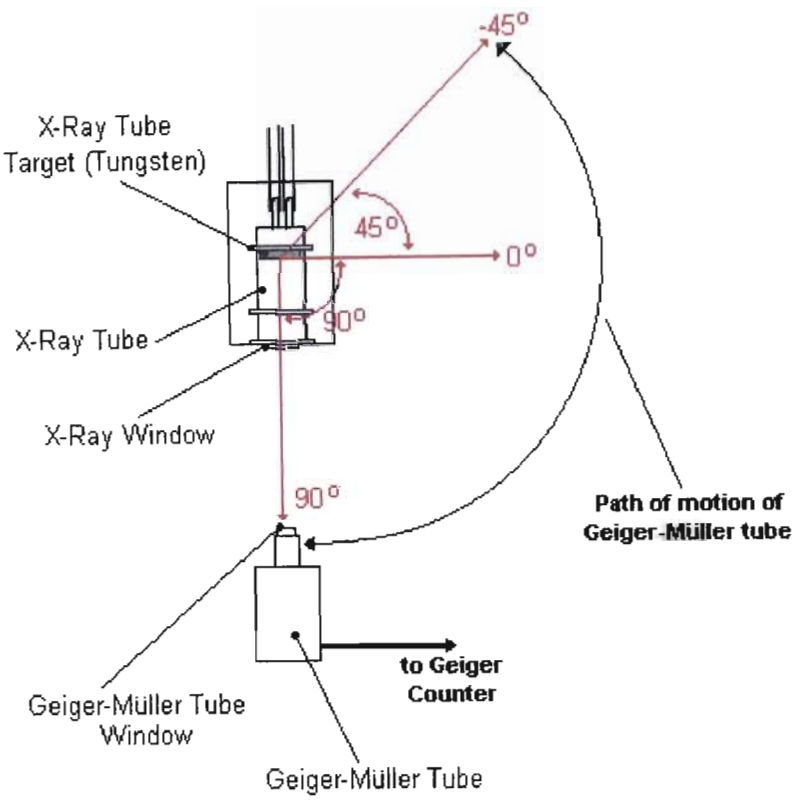

Fig. 5.4: Set-up for the measurement of the radiation distribution of the X-ray tube.

As shown in Figure 5.4 the measurement was conducted at angles between -45° and 90° to the X-ray tube target surface. The radiation distribution thus obtained was symmetrical about the axis of the tube. The measurements were taken from -45° to 90° in 15° steps.

5.5. X-RAY SPECTRA ANALYSIS USING THE COLD CATHODE X-RAY TUBE

The X-ray spectra were recorded using AMPTEK's XR-100T-CZT and XR-100T detector systems with the multichannel analyser 'AMPTEK MCA 8000A', which was run on the Windows 95 operating system. In Section 5.5.1 the XR-100T-CZT cadmium zinc telluride detector is described, which can be used for measuring X-ray and gamma ray spectra at energies

of up to 200 keV [47]. The XR-100T silicon detector on the other hand, which is described in Section 5.5.2 below, is designed for higher resolution measurements of X-ray spectra containing energies below 20 keV. Both detectors were used for measuring characteristic spectra of samples irradiated by the cold cathode X-ray tube (see Figure 5.1). The XR-100T-CZT cadmium zinc telluride detector, when used in conjunction with the cold cathode X-ray tube in the spectrometer set-up illustrated in Figure 5.1, allowed for the recording of spectra at energies up to 85 keV, an energy value corresponding to the maximum acceleration potential of 85 kV that was applied across the tube (see Section 3.1.2, Chapter 3), while the XR-100T silicon detector enabled the user to measure spectra at relatively higher energy resolutions at energies up to 20 keV [47]. Both of the aforementioned detectors are fully compatible with the 'MCA 8000A' multichannel analyser [47] (see Figure 5.1 and Figure 5.5).

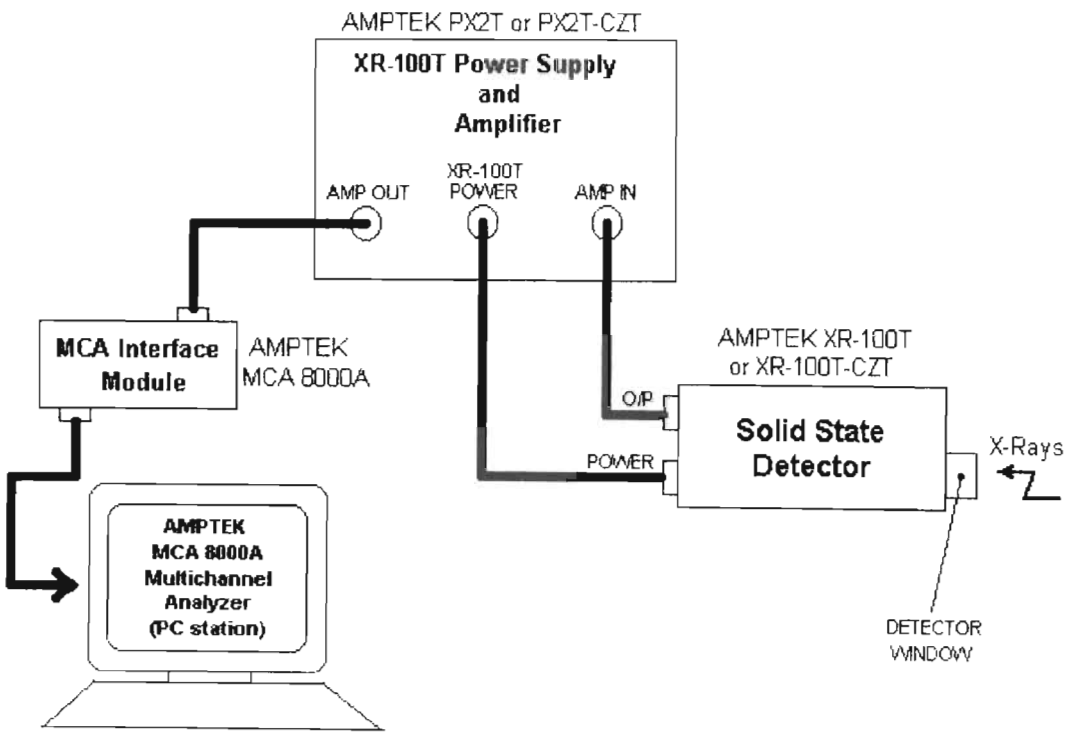

Fig. 5.5: The X-ray detector system and multichannel analyser of the spectrometer, in which either the XR-100T silicon or the XR-100T-CZT cadmium zinc telluride detectors can be used [47].

5.5.1. THE XR-100T-CZT CADMIUM ZINC TELLURIDE X-RAY DETECTOR

The XR-100T-CZT detector unit uses a $3 \times 3 \times 2$ mm^3 cadmium zinc telluride (CZT) detector that is integrated into a hermetic TO-8 package, that has a light tight, vacuum tight 250 μm or 10 mils beryllium window [47]. Upon striking the window of the XR-100T-CZT detector X-rays interact with the cadmium zinc telluride atoms to create an average of one

electron-hole pair for every 5.0 eV of energy lost in the cadmium zinc telluride layer of the detector. Depending on the energy of the incoming radiation, this energy loss is dominated by either the photoelectric effect or Compton scattering. The probability or efficiency of the detector to 'stop' the incoming radiation and create electron-hole pairs increases with the thickness of the cadmium zinc telluride layer, which in the case of the XR-100T-CZT is equal to 2 mm or 80 mil [74]. Electron-hole pairs created by radiation, which interacts with the cadmium zinc telluride near the back contact of the detector, are translated into voltage pulses, which are fed by the charge sensitive PX2T-CZT preamplifier to the 'MCA 8000A' multichannel analyser interface module, which links the PX2T-CZT preamplifier with the multichannel analyser software (see Figure 5.5). The spectra are displayed by the multichannel analyser in the form of an x-y plot, where the intensities are shown in the form of counts per second on the ordinate while the radiation energies can be observed on the abscissa. The energies are displayed in the form of energy channels. It should be noted that any measurements displayed by the multichannel analyser are meaningless as long as the system is not calibrated according to a particular energy peak of a given element. The channel in which this peak is then recorded serves as the reference channel, relative to which the energy peaks shown in other channels are then measured in terms of the characteristic energy, that they represent. Needless to say once the characteristic energies have been evaluated, the respective elements from which they were emitted in the sample can then be identified. The electron-hole pairs also result in fluctuations of charge collection times. These fluctuations are observed as rise time variations of the voltage step at the output of the charge sensitive preamplifier PX2T-CZT. As a result the acquired spectra suffer from increased counts due to the measured continuum and degraded energy resolution [47].

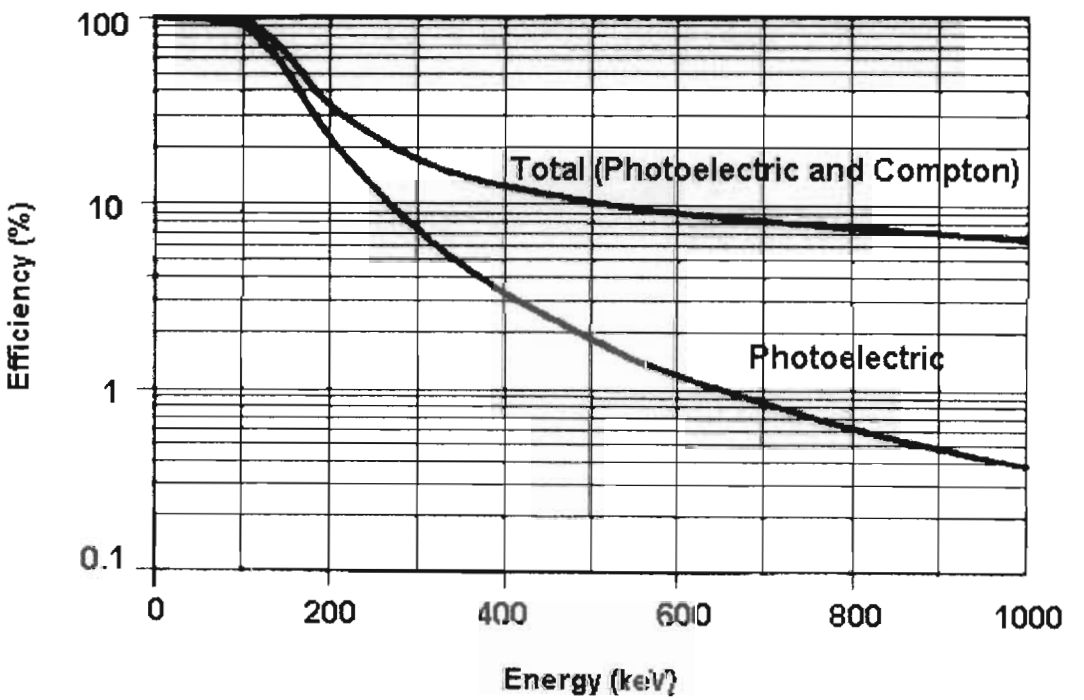

Fig. 5.5.1: The detection efficiency for the 2 mm thick XR-100T-CZT ($Cd_{0.9}Zn_{0.1}Te$) detector [47].

As shown in Figure 5.5.1 the XR-100T-CZT detector is best suited for detecting X-ray, or gamma ray photons for that matter, at radiation energies up to 100 keV at an efficiency of 100% [47]. If a photon is recorded due to the photoelectric effect taking place in the cadmium zinc telluride layer of the detector, the efficiency drops off sharply to approximately 20% at X-ray photon energies of 200 keV. According to the manufacturer of the XR-100T-CZT, detection of photons at energies above 200 keV is not recommended.

5.5.2. THE XR-100T SILICON X-RAY DETECTOR

While the principle of operation of the XR-100T detector is similar to that of the XR-100T-CZT cadmium zinc telluride detector, there are a number of notable differences in the characteristics of the two detectors. In the case of the XR-100T detector a silicon PIN diode is used as a detector. The X-rays, which interact with the silicon atoms of the detector, create one electron-hole pair for every 3.62 eV of energy lost in the silicon. According to the manufacturer [47][48] the XR-100T has a minimum energy resolution of 200 eV, which means that radiation is detected in 200 eV energy increments. For the high energy cold cathode X-ray tube, which has been designed specifically for the detection of X-ray photons with energies of several keV the XR-100T energy resolution offers a high degree of accuracy. It can therefore be expected, that some of the electron-hole pairs interacting with the silicon are collected more slowly than normal events resulting in smaller than normal voltage pulses from the PX2T shaping amplifier, which can increase the background noise in an energy spectrum and create false peaks. The PX2T amplifier (see Figure 5.1 and Figure 5.5), which also incorporates a power supply for the XR-100T detector, prevents these pulses from being counted by the multichannel analyser. The desirable pulses on the other hand are fed from the amplifier output terminal to the MCA via the 'AMPTEK MCA 8000A' multichannel analyser interface module, which links the PX2T amplifier to the multichannel analyser software (see Figure 5.5). Furthermore, as can be seen in Figure 5.5.2, the XR-100T detector, which has a silicon thickness of 300 μm or 12 mil, is best suited for the detection of X-ray photons with energies below 10 keV, where the detection efficiency is close to 100 % [47]. Thereafter it drops off rapidly to an efficiency of about 1.5 % at photon energies of 85 keV (see Figure 5.5.2). This means, that while the detector is capable of detecting virtually all photons striking its window at energies below 10 keV its ability of detecting photons will decrease dramatically as the energies of the photons rise above 10 keV. Since the number of photons detected at a particular energy is directly proportional to the radiation intensity displayed in counts per second by the multichannel analyser at that particular energy it can be expected that characteristic radiation intensity peaks at energies above 10 keV will be less pronounced with increasing energy as compared to characteristic lines of elements with excitation energies below 10 keV. According to AMPTEK [47] the XR-100T detector is best suited for measuring energies at 10 keV and below. The measurement of excitation lines above 20 keV is not recommended [47].

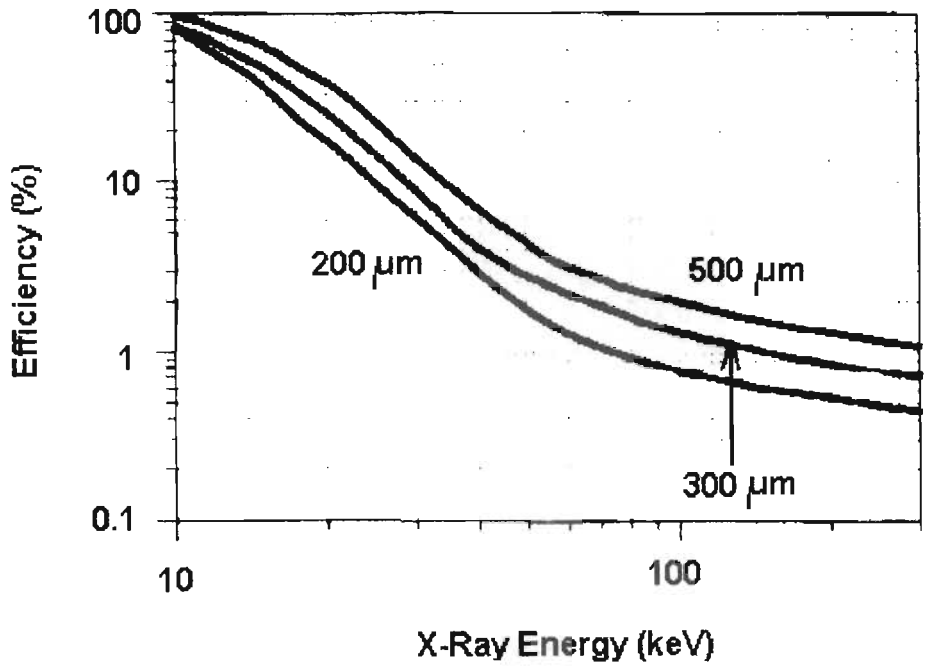

Fig. 5.5.2: The detection efficiency of the XR-100T silicon detector [47].

5.6. SAFETY AND PROTECTIVE DEVICES

In order to provide for the safety and protection from radiation of personnel operating the spectrometer, in which the cold cathode X-ray tube was tested, a number of safety measures had to be taken. The lead lined aluminium chamber (see Figure 5.1), into which the chemical sample to be analysed was placed, had the function of absorbing any harmful X-radiation emanating from the tube that could escape to the outside environment. The chamber door was fitted with an interlock switch SW2 (see Figures 5.1 and 5.6) which only closes when the chamber itself is closed. With SW2 open the supply voltage of 30 Volts is removed from the safety interlock device (see Figure 5.6) thereby disabling the relay switch SR1, which, when closed, connects the spectrometer to the 220 Volt mains line. A further safety feature in the interlock safety device is lamp L1, which merely serves to indicate or warn that the spectrometer is in operation and that therefore X-rays are produced. With L1 dysfunctional or removed from the circuitry the base current of T1 is removed resulting in 0 Volts being applied to the negative input of OP1, which serves as a comparator. This in turn results in a comparator output of 0,8 Volts which is not enough to turn on transistor T2, which requires a base voltage $V_{B,T2}$ of at least $V_{D1} + V_{D2} = 1.4$ Volts for operation. In this way no current can flow through the coil of the relay switch SR1 and so SR1 remains open thus keeping the spectrometer effectively disconnected from the 220 Volt mains line.

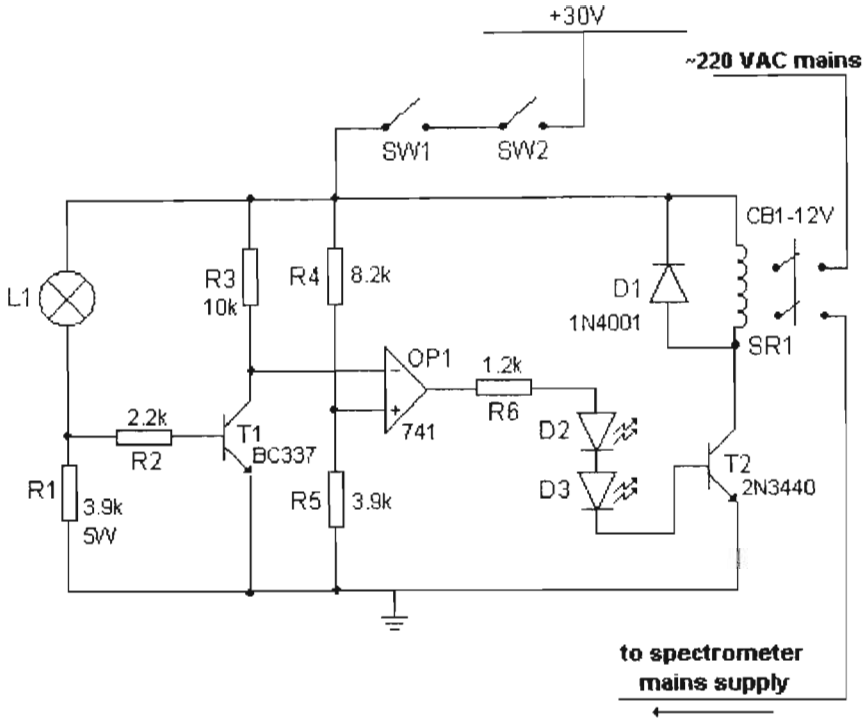

Fig. 5.6: The interlock safety device.

In order to shield the electronic circuitry of the spectrometer from the electromagnetic impulses produced by the power supply it was necessary that the power supply be placed inside an aluminium shield of 2.2 cm wall thickness. According to *White* [53] aluminium has the property of shielding electromagnetic pulses only in certain frequency intervals for a given aluminium shield thickness. Therefore aluminium of 2.2 cm thickness will shield frequencies given in Table 5.1 below.

Table 5.1: Electromagnetic impulse frequencies between 30 Hz and 300 kHz, at which 2.2 cm thick aluminium can be used as an electromagnetic shield [53].

Shielding Frequency (Hz)
60
110
190
305
600
1000
1580
3300
6000
10000

In Table 5.1 it can be seen that 2.2 cm thick aluminium can be used for electromagnetic shielding at an impulse frequency of 110 Hz, which closely corresponds to the repetition rate of 111 Hz of the output voltage waveform produced by the X-ray power supply (see Section 3.1.2, Chapter 3).

5.7. SUMMARY

In this chapter the spectrometer in which the cold cathode X-ray tube was set up for testing is described. As the main concern of this study is the performance of the X-ray tube for XRF spectrometry, the spectrometer was used primarily for the characterisation of the X-ray tube. After presenting a method for the measurement of the characteristic X-ray tube currents and voltages, a method for determining the photoefficiency of the cold cathode of the X-ray tube was illustrated in Section 5.3. It was shown that for the particular case of the X-ray tube the photoefficiency of the MgO cold cathode could be expressed as the ratio of the average photocurrent and the total current of the X-ray tube, which consists of both a photocurrent and a field current. In the measurement of the photoefficiency of the X-ray tube it was assumed that the average diode current was representative of the field emitted current in the X-ray tube. Thus it was possible to establish a value for the average photocurrent, which is the difference between the total average current and the average field current of the X-ray tube, and consequently the photoefficiency. A very important X-ray tube parameter is the intensity distribution of the primary radiation produced by an end-window X-ray tube. Since the radiation could not be measured directly at the X-ray tube window with the XR-100T and XR-100T-CZT detectors as this approach would have resulted in the detectors being saturated and possibly even damaged, a Geiger counter was used instead (see Section 5.4). Finally the tube was tested as an X-ray source in a spectrometer by detecting and analysing the spectra produced from samples irradiated by the tube. In Section 5.5 the functions of the XR-100T-CZT and the XR-100T X-ray detector systems, in conjunction with the 'AMPTEK MCA 8000A' multichannel analyser to detect and evaluate characteristic X-ray spectra from samples, were discussed. In Section 5.5.1 the reader was introduced to the XR-100T-CZT detector for high-energy measurements of X-ray and gamma ray spectra, while in Section 5.5.2 a brief description of the XR-100T silicon detector for higher energy resolution X-ray spectra measurements was given. Finally the safety features of the spectrometer were discussed, namely the safety interlock device for the prevention of operating the spectrometer with an open X-ray chamber, which would have allowed for hazardous radiation to escape to the environment, as well as the EMI shielding chamber which had the function of protecting electronic circuitry from potentially damaging electromagnetic impulses produced by the X-ray power supply (see Section 5.6).

6. Experimental Results

6.1. THE X-RAY TUBE CURRENT AND VOLTAGE CHARACTERISTICS

The measured current and corresponding voltage characteristics of the X-ray tube are shown in Figure 6.1 and Figure 6.2 respectively.

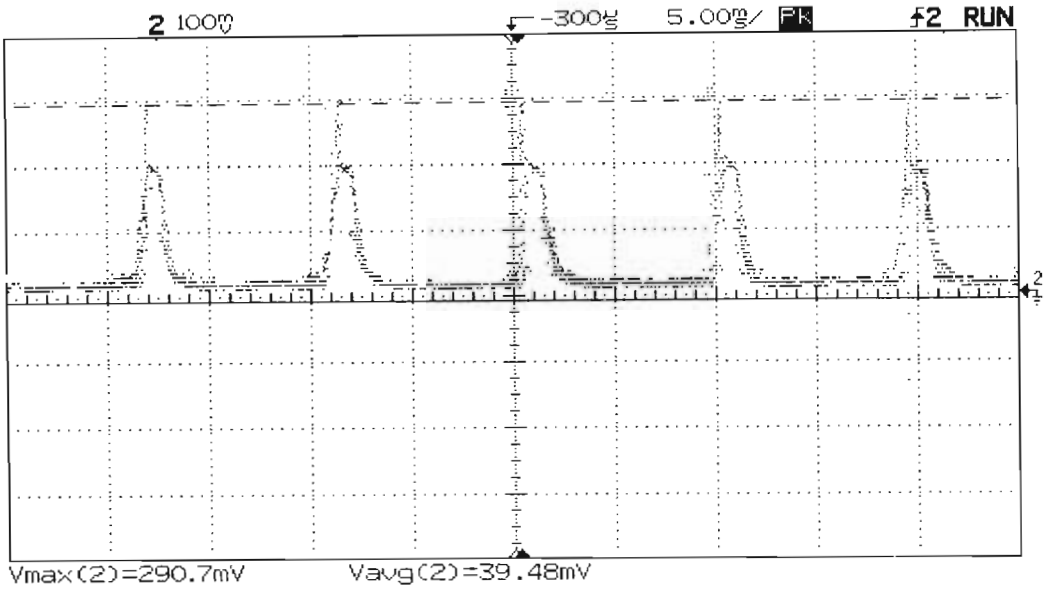

Fig.6.1: The voltage drop across resistor R_1 (10 Ω) which was measured to establish the current characteristics of the X-ray tube.

The waveform in Figure 6.1 was obtained by measuring the voltage drop across resistor R_1 (see Section 5.2, Chapter 5), which has a resistance of 10 Ω. Therefore, with a maximum voltage drop of 290.7 mV and an average voltage drop of 39.48 mV measured across R_1, it was found that the maximum tube current $i_{MAX.\ X\text{-}RAY\ TUBE}$ flowing through the tube was equal to 29.68 mA while the average current $i_{AVE.\ X\text{-}RAY\ TUBE}$ was found to be equal to 3.948 mA. In Figure 6.2 on the other hand a waveform was obtained for the voltage across the tube by measuring the voltage across a proportional resistor divider network (see Figure 5.2, Chapter 5), where 1 V displayed on the oscilloscope corresponded to 40 kV measured across the tube. Therefore, with a maximum voltage $V_{MAX.\ R2}$ = 2.125 V and an average voltage $V_{AVE.\ R2}$ = 0.327 V measured across the measuring resistor R_2 (see Figure 5.2, Chapter 5), it can be seen, that the maximum voltage developed across the X-ray tube $V_{MAX.\ X\text{-}RAY\ TUBE}$ was 85 kV, while the actual average voltage $V_{AVE.\ X\text{-}RAY\ TUBE}$ was found to be equal to 13.08 kV. Therefore the average power P_{AVE}, which is the product of the average tube current $i_{AVE.\ X\text{-}RAY\ TUBE}$ and the average output voltage $V_{AVE.\ X\text{-}RAY\ TUBE}$ (see Section 3.1.2, Chapter 3) was equal to approximately 52 Watts.

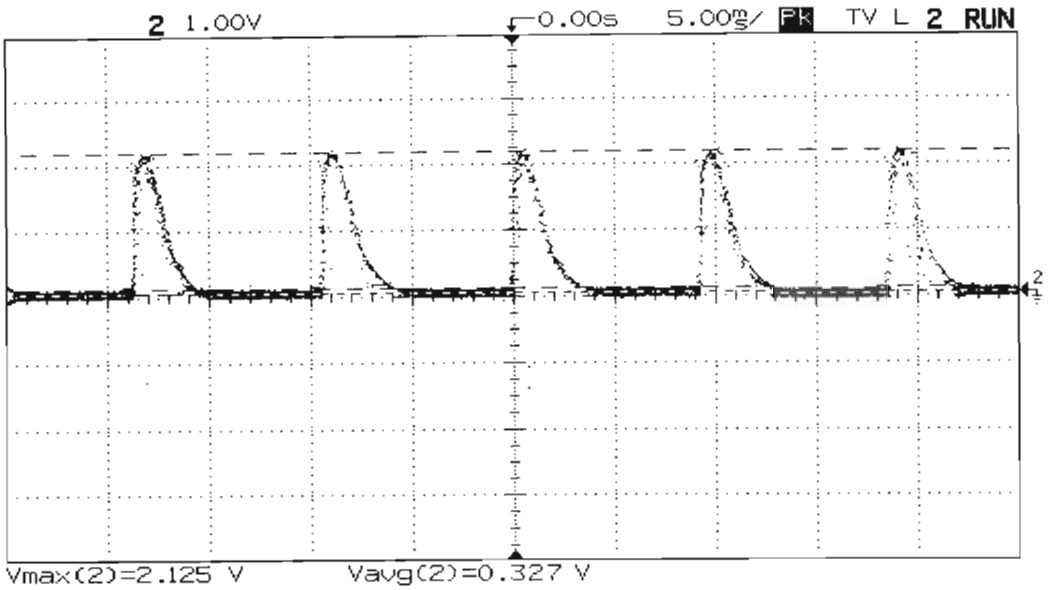

Fig.6.2: The voltage drop across resistor R_2 of the proportional voltage divider network, where 1 V corresponds to 40 kV discharged across the tube.

6.2. DETERMINATION OF THE PHOTOEFFICIENCY OF THE MgO COLD CATHODE

The photoefficiency of the X-ray tube was determined using the measurement method described in Section 5.3 in Chapter 5. In order to establish the photoefficiency of the X-ray tube the average current flow through the X-ray tube was compared to that of a diode, which has the same structure as the X-ray tube, but does not contain the tungsten target at which the current enhancing X-radiation is produced. Using the diode it was thus possible to determine a value for the maximum and average field current, namely $i_{max.\,field}$ and $i_{ave.\,field}$ respectively, flowing through the X-ray tube. The measured current through the X-ray tube is illustrated in Figure 6.1, where the average current $i_{AVE.\,X\text{-}RAY\ TUBE}$ is equal to 3.948 mA (see Section 6.1). As in Figure 6.1 the waveform in Figure 6.4 was obtained by measuring the voltage drop across the 10 Ω measuring resistor R_1, which, as in the previous case of the X-ray tube (see Section 5.2, Chapter 5), was placed in series with the diode. An average voltage drop of 37.58 mV was measured across R_1 (see Figure 6.4) corresponding to an average diode current $i_{AVE.\,DIODE} = i_{ave.\,field} = 37.58$ mV / 10 Ω = 3.758 mA. Similarly a maximum diode current $i_{MAX.\,DIODE}$, or alternatively $i_{max.\,field}$, of 19.69 mA was measured. The photoefficiency of the X-ray tube relative to the diode was finally determined by substituting the measured values for $i_{AVE.\,X\text{-}RAY\ TUBE}$ and $i_{AVE.\,DIODE}$ into equation 5.1 (see Section 5.3, Chapter 5):

$$\text{photoefficiency} = \frac{i_{AVE.X\text{-}RAYTUBE} - i_{AVE.DIODE}}{i_{AVE.X\text{-}RAYTUBE}} \cdot 100\% =$$

$$\frac{3.948\ \text{mA} - 3.758\ \text{mA}}{3.948\ \text{mA}} \cdot 100\% = 4.81\%;$$

The waveform of the voltage drop across the 10 Ω measuring resistor R_1 developed during the operation of the diode is shown in the figure below:

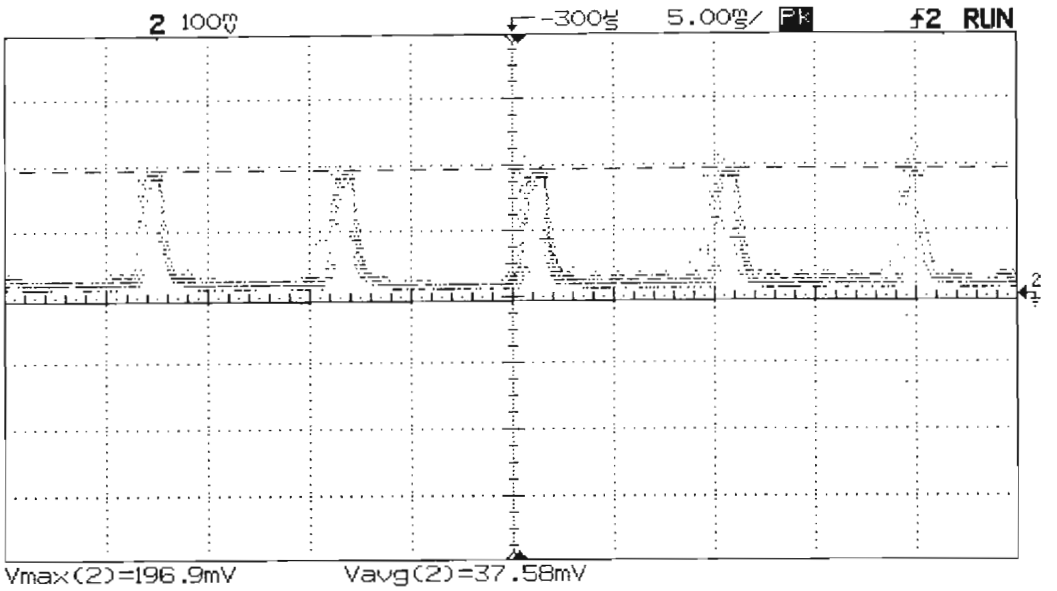

Fig.6.3: The voltage drop across resistor R_1 (10 Ω) during the operation of the diode, which was used to establish the field current flowing through the X-ray tube.

6.3. MEASUREMENT OF THE PRIMARY RADIATION INTENSITY DISTRIBUTION OF THE X-RAY TUBE

The radiation distribution of the X-ray tube was measured from an angle of 90° to -45° to the target face (see Figure 5.4, Chapter 5) in 15° steps at a distance of 60 mm to the centre of the X-ray tube target face at all angles. In order to obtain statistically accurate values for the total intensities measured 15 readings were taken per measuring angle. The intensities are expressed in counts per second (cps) and are listed in Table 6.1 together with the mean values and the standard deviations of the measured intensities for every angle. In Figure 6.5 the mean intensities are plotted against their respective angles of measurement.

Table 6.1: Measured intensity values (counts per second) at various angles to the target face of the X-ray tube.

Read-ing no.	90°	75°	60°	45°	30°	15°	0°	-15°	-30°	-45°
1	1904.5	1909.2	1801.0	1790.8	1850.3	1869.5	1880.2	1308.0	1203.2	685.5
2	1922.5	1886.3	1854.2	1885.6	1832.2	1901.1	1870.0	1297.0	1190.1	975.6
3	1934.2	1828.5	1879.5	1894.2	1847.0	1895.0	1836.5	1312.3	1172.2	964.2
4	1901.2	1860.5	1843.3	1884.2	1860.0	1964.3	1870.2	1342.5	1198.8	998.3
5	1966.5	1893.3	1809.5	1895.3	1839.9	1970.0	1930.0	1358.1	1248.5	987.2

Table 6.1 (cont.): Measured intensity values (counts per second) at various angles to the target face of the X-ray tube.

Read-ing no.	90°	75°	60°	45°	30°	15°	0°	-15°	-30°	-45°
6	1918.3	1790.2	1820.1	1906.1	1851.1	1882.2	1903.3	1318.2	1232.4	893.3
7	1875.4	1819.5	1879.4	1933.2	1880.2	1807.4	1840.6	1289.0	1201.5	1028.2
8	1916.3	1809.6	1883.3	1899.4	1829.5	1904.3	1856.9	1280.8	1192.0	1007.1
9	1869.5	1842.1	1812.5	1895.2	1857.1	1912.3	1929.3	1347.8	1180.0	1012.2
10	1840.3	1843.2	1874.1	1863.1	1859.2	1899.9	1882.5	1368.4	1188.3	852.3
11	1970.2	1806.5	1834.6	1907.3	1873.2	1880.0	1880.6	1340.8	1205.2	981.4
12	1892.3	1861.0	1860.2	1860.5	1860.0	1901.3	1925.4	1338.8	1214.2	1017.4
13	1861.1	1823.4	1792.1	1806.3	1879.1	1841.7	1894.4	1370.5	1228.8	1008.8
14	1863.5	1833.2	1805.0	1891.0	1844.3	1946.6	1911.1	1358.0	1208.0	964.5
15	1930.4	1840.0	1866.5	1860.0	1889.1	1879.5	1850.5	1342.5	1172.8	1029.5
Mean	**1904.41**	**1843.08**	**1841.02**	**1878.15**	**1856.81**	**1897.02**	**1884.10**	**1331.51**	**1202.40**	**960.37**
Std. Devi-ation	**6.17**	**5.81**	**5.68**	**6.14**	**4.20**	**6.52**	**5.57**	**5.37**	**4.67**	**9.51**

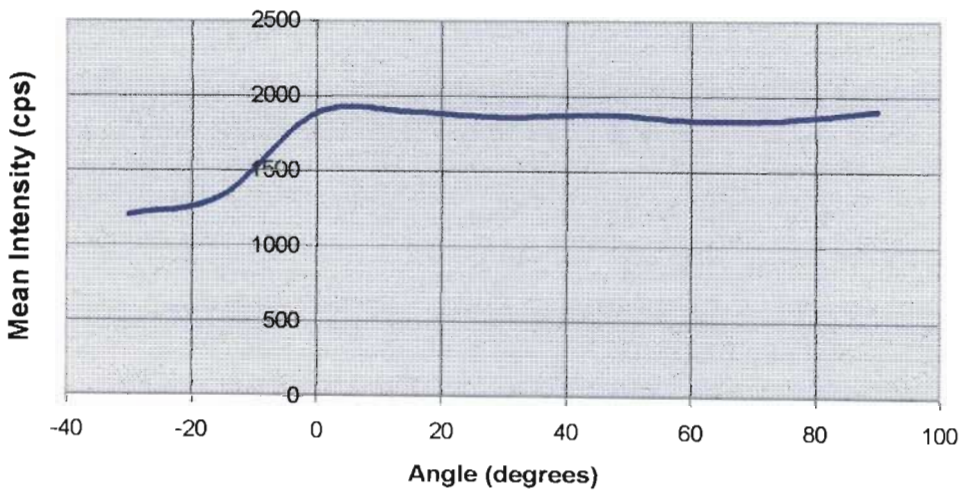

Fig.6.4: Mean radiation intensity versus the angle of measurement.

6.4. SPECTRA ANALYSIS USING THE COLD CATHODE X-RAY TUBE

6.4.1. SPECTRA ANALYSIS WITH THE XR-100-CZT CADMIUM ZINC TELLURIDE X-RAY DETECTOR

In order to determine the channels, in which the K shell excitation lines of the elements to be measured occur, it was necessary to calibrate the multichannel analyser. The channel-excitation energy relationship of the recorded spectra was determined by measuring the K lines of the elements molybdenum (Mo), silver (Ag) and lanthanum (La), which were used as calibration samples. The spectra were measured on a channel scale containing a total of 4096 channels. The channels in which these peaks were recorded are listed in Table 6.2 below:

Table 6.2: The channel-photon energy relationship of the K excitation lines of molybdenum, silver and lanthanum. The photon energies were taken from Tables A5b and A5c (refer to Appendix 9).

Characteristic excitation line	Photon energy (keV)	Channel
Mo $K\alpha_1$	17.478	405
Mo $K\beta_1$	19.607	450
Ag $K\alpha_1$	22.162	511
Ag $K\beta_1$	24.942	575
La $K\alpha_1$	33.440	773
La $K\beta_1$	37.799	877

The spectra of Mo, Ag and La are displayed in Figure A9a in Appendix 9. The 'MCA8000A' multichannel analyser program automatically establishes a channel-excitation energy relationship after the calibration process has been completed. In this case the relationship that was obtained for the above measurement is expressed below, where A denotes the photon excitation energy in keV:

$$\text{Channel} = 23.22A - 1.29 \qquad (6.1)$$

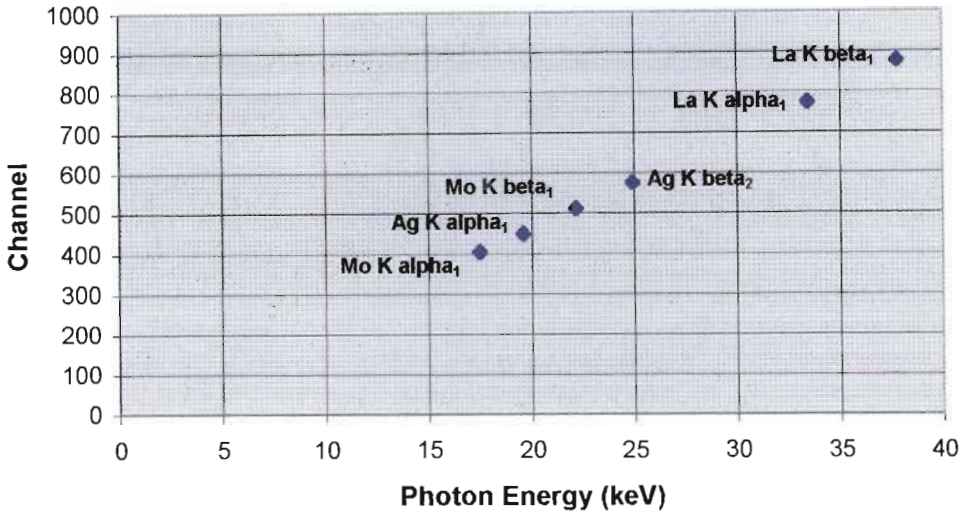

Fig. 6.5: Linear plot of the measured channel number versus the photon energy for the K excitation lines of elements Mo, Ag and La.

The relationship described by equation 6.1 and plotted in Figure 6.5 for the measured K excitation lines of elements Mo, Ag and La is a linear one. The X-ray tube was tested further by measuring the K excitation lines of the elements neodymium (Nd) and gadolinium (Gd) with the multichannel analyser using the XR-100T-CZT detector. According to the relationship in equation 6.1 and the photon energies of the elements of the periodic table listed in Table A5b and Table A5c (see Appendix 5) the theoretical values of the channels for the neodymium and the gadolinium K excitation lines were calculated and are shown in Table 6.3 below:

Table 6.3: Predicted channel values for the K shell excitation lines of elements Nd and Gd.

Characteristic excitation line	Photon energy (keV)	Channel
Nd $K\alpha_1$	37.359	866
Nd $K\beta_1$	42.269	980
Gd $K\alpha_1$	42.983	997
Gd $K\beta_1$	48.718	1130

The spectra obtained for Nd and Gd using the XR-100T-CZT detector are shown in Figure A9b and Figure A9c respectively (see Appendix 9). The neodymium and the gadolinium K excitation lines and their deviations from the predicted channel values listed in Table 6.3 are shown in the table below:

Table 6.4: Measured channel values of the Nd and Gd K excitation lines.

Characteristic excitation line	Photon energy (keV)	Channel	Deviation	Duration of measurement (sec)
Nd $K\alpha_1$	37.359	866	0	301.72
Nd $K\beta_1$	42.269	986	-6	301.72
Gd $K\alpha_1$	42.983	1001	4	249.92
Gd $K\beta_1$	48.718	1134	4	249.92

The continuous spectrum produced by the X-ray tube was obtained by measuring the spectra of a secondary tungsten target, so that the tube characteristics would not be falsified by spectra of any other elements (see Figure 6.6). The maximum energy at which a tungsten continuous spectrum was produced was measured at 84.87 keV (see Figure 6.3). This means that the maximum energy at which electrons were accelerated from the cathode to the anode of the tube was equal to 84.87 keV (see Section 2.6, Chapter 2). This verifies the fact, that a maximum accelerating potential of approximately 85 kV was discharged across the X-ray tube during operation (see Figure 6.2, Chapter 6). As expected the XR-100T-CZT detector had a tendency towards acquiring a relatively high amount of continuous spectra (see Section 5.5.1, Chapter 5 and Figure A9a, Figure A9b and Figure A9c, Appendix 9).

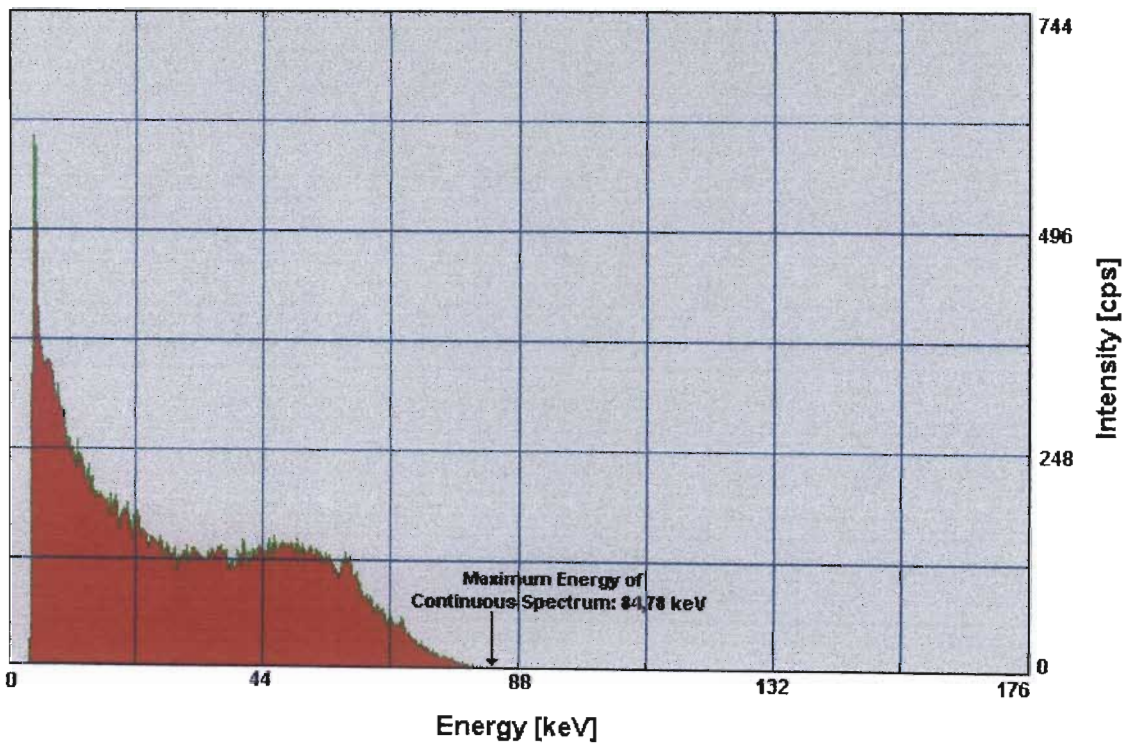

Fig. 6.6: The continuous spectrum of a tungsten secondary target irradiated by the X-ray tube.

In Figure 6.7 the measured channel values of the K lines of molybdenum, silver, lanthanum, neodymium and gadolinium are plotted versus their respective photon energies.

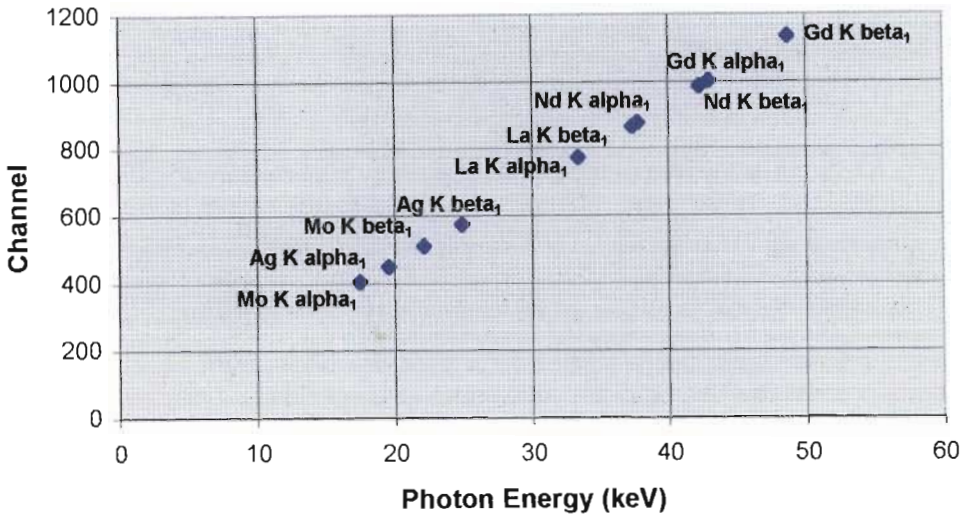

Fig. 6.7: Linear plot of the measured channel number versus the photon energy for the K excitation lines of elements Mo, Ag, La, Nd and Gd.

6.4.2. SPECTRA ANALYSIS WITH THE XR-100T SILICON X-RAY DETECTOR

After the XR-100T-CZT cadmium zinc telluride detector system had been replaced by the XR-100T silicon detector system it was necessary to calibrate the 'MCA 8000A' multichannel analyser as the XR-100T detector records spectra on a lower energy scale as compared to that of the silicon detector described in Section 5.5.1 in Chapter 5. In order to recalibrate the detector system spectra of chromium (Cr), iron (Fe) and nickel (Ni) from a stainless steel 316 sample, zinc (Zn) and copper (Cu) from a brass sample and molybdenum (Mo) were measured. The L lines of lead (Pb) were also measured (see Figure A9d, Appendix 9). As in the case of the XR-100T-CZT detector the gain of the multichannel analyser was set, so that the excitation energies of the samples were recorded on a channel scale containing 4096 channels. The following channels for the different excitation lines were observed:

Table 6.5: The channel-photon energy relationship of the elements Cr, Fe, Ni, Cu, Zn, Mo and Pb. The photon energies were taken from Tables A5b and A5c (refer to Appendix 5).

Characteristic excitation line	Photon energy (keV)	Channel
Cr $K\alpha_1$	5.414	881
Fe $K\alpha_1$	6.403	1040
Ni $K\alpha_1$	7.477	1226
Cu $K\alpha_1$	8.047	1325

Table 6.5 (cont.): The channel-photon energy relationship of the elements Cr, Fe, Ni, Cu, Zn, Mo and Pb. The photon energies were taken from Tables A5b and A5c (refer to Appendix 5).

Characteristic excitation line	Photon energy (keV)	Channel
Zn $K\alpha_1$	8.638	1412
Pb $L\alpha_1$	10.448	1723
Pb $L\beta_1$	12.611	2067
Pb $L\gamma_1$	14.762	2425
Mo $K\alpha_1$	17.478	2856

These values were plotted against the photon excitation energies (see Table A5b and Table A5c, Appendix 5) of the respective elements as shown in Figure 6.8. The relationship described by equation 6.2 once again indicates that the channel-excitation energy relationship is linear. An attempt was also made at measuring the $K\alpha_1$ lines of molybdenum (Mo), tin (Sn) and gadolinium (Gd) at photon energies of 17.478 keV, 25.270 keV and 42.983 keV respectively (refer to Figure A9h, Appendix 9 and Tables A5b and A5c, Appendix 5). The XR-100T detector was unable to reliably detect the Sn and especially the Gd lines due to the low operating efficiency of the detector at energies above 20 keV (see Section 5.5.2 and Figure 5.5.2, Chapter 5). This can be seen in the graph in Figure A9h (see Appendix 9), where the gadolinium $K\alpha_1$ line is barely visible while the $K\alpha_1$ line of tin was detected at a comparatively low intensity with respect to the less energetic molybdenum $K\alpha_1$ line. The elements Mo, Sn and Gd were all measured for a period of 60 seconds each. By extrapolating to a photon energy of 0 keV, which the 'MCA 8000A' multichannel analyser program accomplishes automatically during the calibration process, the following channel-excitation energy relationship was obtained, where A denotes the photon excitation energy in keV:

$$\text{Channel} = 163.71A + 5.88 \qquad (6.2)$$

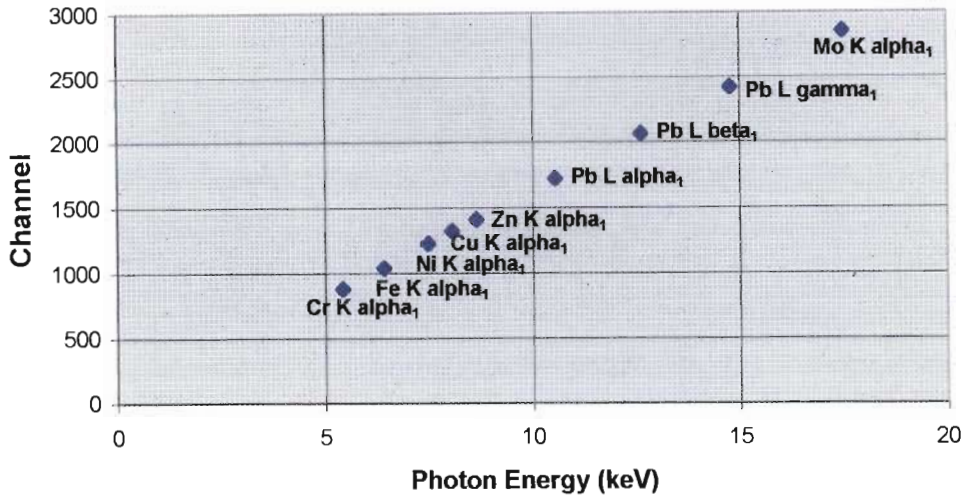

Fig.6.8: Linear plot of channel number versus photon energy for the excitation lines of the elements Cr, Fe, Ni, Cu, Zn, Pb and Mo listed in Table 6.5.

In order to test the X-ray tube the K shell excitation lines of cobaltous acetate, a nickel sample and bromine contained in a barium bromide sample ($BaBr_2.2H_20$) were measured with the multichannel analyser. According to the relationship obtained in equation 6.2 and the theoretical photon energies of the elements of the periodic table listed in Table A5b (see Appendix 5) the theoretical values of the channels for the Co, Ni and Br K shell excitation lines were determined as shown in Table 6.5. These values were then compared to the measured excitation lines, which can be found in the spectra plots in Appendix 9. The excitation line peaks were read out from the plot and are listed in Table 6.6. The spectra of cobaltous acetate, nickel and barium bromide are shown in Figure A9e, Figure A9f and Figure A9g in Appendix 9 respectively.

Table 6.5: Predicted channel values for the Kα line energies of cobalt (Co) in cobaltous acetate.

Characteristic excitation line	Photon energy (keV)	Channel
Co $K\alpha_1$	6.930	1140
Co $K\beta_1$	7.649	1258
Ni $K\alpha_1$	7.477	1230
Ni $K\beta_1$	8.264	1359
Br $K\alpha_1$	11.923	1961
Br $K\beta_1$	13.290	2187

Using the graphs of the spectra obtained for cobaltous acetate, nickel and barium bromide (see Figure A9e, Figure A9f and Figure A9g in Appendix 9) the following channels, in which the Co, Ni and Br K shell photon energies were recorded, were obtained and are listed and plotted in Table 6.6 and Figure 6.9 below:

Table 6.6: Measured channel values of the Co K shell excitation lines.

Characteristic excitation line	Photon energy (keV)	Channel	Deviation	Duration of measurement (sec)
Co $K\alpha_1$	6.930	1226	86	902.12
Co $K\beta_1$	7.649	1358	-100	902.12
Ni $K\alpha_1$	7.477	1226	-4	904.70
Ni $K\beta_1$	8.264	1345	-14	904.70
Br $K\alpha_1$	11.923	1958	-3	901.78
Br $K\beta_1$	13.290	2182	-5	901.78

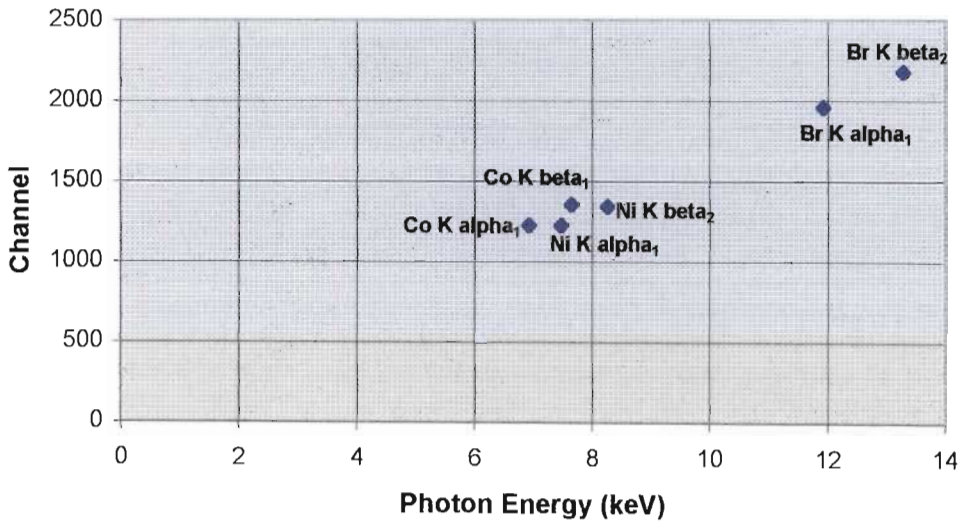

Fig.6.9: Linear plot of channel number versus photon energy for the measured K shell excitation lines of the elements Co, Ni and Br.

7. Discussion of Experimental Results

7.1. THE MEASURED X-RAY TUBE CURRENT AND VOLTAGE

The graphs in Figure 6.1 and 6.2 (see Chapter 6) show the current and voltage characteristics of the X-ray tube respectively when in operation. In Figure 6.1 it can be seen, that the shape of each current pulse flowing through the tube did not in fact level off at 30 mA before decreasing to 0 mA 0.003 seconds after the onset of the pulse (see Section 3.2.11, Chapter 3). Instead the current pulse was observed to peak at 29.68 mA, which roughly corresponds to the current limit of the power supply of 30 mA, only for an instant before gradually decreasing to 0 mA (see Figure 6.1, Chapter 6). This indicates, that the contribution of the photoelectrons to the total tube current was actually far lower than the value of the total tube current predicted in Figure 3.2.19 (see Section 3.2.11, Chapter 3). Consequently the average X-ray tube current was found to be equal to only 3.948 mA as opposed to 10 mA predicted in Section 3.1.2 of Chapter 3. In Section 3.2.11 of Chapter 3.2 it was observed that the predicted tube current presented an idealised case, in which it was assumed that all electrons in the nickel base of the cold cathode excited by the X-radiation would be emitted as photoelectrons. However, in Figure 6.1 it is evident, that the contribution of the photocurrent was much less than predicted (see Section 3.2.11 in Chapter 3). This can be attributed to the fact, that a large number of the excited nickel electrons had a tendency towards returning to their atomic shells rather than leave their host atoms altogether to be emitted as photoelectrons. This suggests that there exist transition probabilities or transition rates for nickel electrons excited by the X-radiation. According to *Eisberg* and *Resnick* [54] an atomic transition rate is the probability per second that an atom in a certain energy level will make a transition to some other energy level. This means that there is a probability at all times, that electrons in the nickel base of the cold cathode affected by X-radiation will experience transitions between different energy levels in the nickel atom itself rather than leave the atom altogether as photoelectrons. In Section 6.2 of Chapter 6 the measured field current is shown, which closely corresponds to the predicted field current i_{field} of the tube (see Section 3.2.6, Chapter 3). The measured average current $i_{ave,\ field}$, or $i_{AVE,\ DIODE}$, was found to be equal to 3.758 mA (see Section 6.2, Chapter 6) as compared to the predicted value of 3.048 mA (see Section 7.2 below and Section 3.2.6 of Chapter 3). Therefore it can be stated, that the predicted average field current $i_{ave,\ field}$ (see equation 3.2.23b, Section 3.2.6, Chapter 3) had a value only 81.11% of the measured average field current. The higher value of the measured average field current can be attributed to the fact that even the diode produced a certain amount of photoelectrons due to X-radiation acting on the cathode of the diode, albeit to a very minimal extent due to the absence of an X-ray target of high atomic number Z, as the electrons collided with the high potential components of the tube. On the other hand the measured maximum field current $i_{max,\ field}$ was equal to 19.69 mA differing from the predicted maximum field current of 18.29 mA by only 7.65 %. The results in Section 6.1 and 6.2 of Chapter 6 show, that the photocurrent i_{photo} contributed to a far lesser extent to the total tube current with the field current i_{field} being the dominant component of the total tube current. Furthermore it was also noted, that the voltage waveform in Figure 6.2 (see Chapter 6) did not in fact follow a precisely linear path as specified by the manufacturer, although it can be seen, that each voltage pulse across the X-ray tube did peak at 85 kV with a subsequent decrease to 0 kV over a pulse duration of 0.003 sec. As a result the average voltage output of the power supply was measured at 13.08 kV (see Section 6.1, Chapter 6) rather than 14.183 kV as specified by the manufacturer (see Section 3.2.1, Chapter 3). Thus with an average measured X-ray tube current of 3.948 mA the total power P_{AVE},

which is the product of the average current and the average voltage, dissipated in the tube was equal to 52 Watts as opposed to 142 Watts predicted in Section 3.1.2 of Chapter 3.

7.2. THE PHOTOEFFICIENCY OF THE MgO COLD CATHODE

In Section 6.2 of Chapter 6 the photoefficiency of the cold cathode of the X-ray tube was determined. In the approach used the measurement of the photoefficiency was accomplished by measuring the average current through a diode, that had the same structure as the X-ray tube, but did not include the target at which the highly energetic X-radiation was produced. With no radiation assumed to be acting on the cold cathode in the diode, and therefore no photocurrent being produced, it can be stated, that the total average current flow through the diode $i_{AVE,\ DIODE}$ was due to the electric fields present in the tube only, and could therefore be assumed to be equivalent to the average field current $i_{ave,\ field}$ present in the X-ray tube. In equation 5.1 (see Section 5.3, Chapter 5) the photoefficiency of the X-ray tube is expressed as the ratio of the average photocurrent $i_{ave,\ photo}$, which is the difference between the total average X-ray tube current $i_{AVE,\ X\text{-}RAY\ TUBE}$ and the average field current $i_{ave,\ field}$, and the total average tube current $i_{AVE,\ X\text{-}RAY\ TUBE}$. With $i_{AVE,\ DIODE} = i_{ave,\ field} = 3.758$ mA and $i_{AVE,\ X\text{-}RAY\ TUBE} = 3.948$ mA (see Section 6.2, Chapter 6) the photoefficiency was thus found to be equal to 4.81% by substituting the measured average current values into equation 5.1 in Chapter 5. The main advantage of measuring the photoefficiency using the above approach was, that the total current through the X-ray tube and the field current through the diode were measured directly. However, since even in the diode some X-radiation is produced as a result of the accelerated electrons striking the different tube components, it follows that some X-radiation did act on the cathode thus enhancing the total current through the tube.

7.3. MEASUREMENT OF THE PRIMARY RADIATION INTENSITY DISTRIBUTION OF THE X-RAY TUBE

In Section 6.3 (see Chapter 6) the radiation distribution of the X-ray tube was recorded starting at an angle of 90° to the target face up to an angle of -45°. The measurements were conducted in steps of 15° at a distance of 60 mm to the target centre. The maximum mean radiation intensity was found to be equal to 1904.41 counts per second (cps) at angle of 90° with a standard deviation of 6.17. At angles of between 75° and 0° the mean radiation intensities decreased somewhat ranging between 1841.02 cps and 1897.02 cps in magnitude with standard deviations of between 4.20 and 6.52. Finally as the angle of measurement became more and more negative the mean radiation intensity decreased progressively. This shows that the parallel electron flow in an end-window X-ray tube resulted in the production of X-rays with a peak intensity at 180° to the direction of the electron flow or, alternatively, at 90° to the X-ray tube target face. The mean radiation intensities between angles of 0° and 75° to the target face were found to be somewhat lower on average and relatively constant, while the mean intensities measured behind the target at angles of -15°, -30° and -45° decreased to 1331.51 cps, 1202.40 cps and 960.37 cps respectively.

7.4. SPECTRA ANALYSIS USING THE COLD CATHODE X-RAY TUBE

X-ray spectra of samples irradiated by the primary X-radiation produced by the cold cathode X-ray tube were measured using both the XR-100T-CZT cadmium zinc telluride X-ray detector for high-energy detection as well as the XR-100T silicon X-ray detector.

In Section 6.4.1 (see Chapter 6) X-ray spectra of different samples were measured with the XR-100T-CZT cadmium zinc telluride detector (see Section 5.5.1, Chapter 5). By measuring the K shell excitation lines of molybdenum, silver and lanthanum it was possible to calibrate the 'MCA 8000A' multichannel analyser by assigning photon energy values from Table A5b and Table A5c in Appendix 5 to the corresponding channels in which the lines of the aforementioned elements were recorded. By plotting the measured channels, in which the aforementioned K lines were detected, versus their respective photon energies (see Table 6.2, Chapter 6) it was observed, that in the case of the XR-100T-CZT detector the channel-excitation energy relationship was a linear one. This relationship is described by equation 6.1 (see Section 6.4.1, Chapter 6), in which the channel, in which a given photon can be detected, is expressed in terms of its energy. Equation 6.1 was then used to predict the channels, in which the K shell excitation lines of neodymium and gadolinium would be recorded. The neodymium $K\alpha_1$ and $K\beta_1$ lines were measured in channel 866 with a deviation of 0 and channel 986 with a deviation of –6 respectively. The time taken to measure these lines was equal to 301.72 seconds (see Table 6.4, Chapter 6). The gadolinium $K\alpha_1$ and $K\beta_1$ lines on the other hand, were measured in channel 1001 with a deviation of 4 and channel 1134 with a deviation of 4 respectively. The time taken to measure the gadolinium lines was 249.92 seconds (see Table 6.4, Chapter6). By plotting the measured channel values of the K shell excitation lines of molybdenum, silver, lanthanum, neodymium and gadolinium against their respective characteristic excitation energies a linear channel-excitation energy relationship was once again observed. In the spectra obtained from a secondary tungsten target irradiated by the X-ray tube (see Figure 6.5, Chapter 6) it can be seen, that the maximum energy of the continuous spectrum measured via the XR-100T-CZT cadmium zinc telluride detector was equal to 84.87 keV. According to equation 2.5 (see Section 2.6, Chapter 2) the term E_0, which represents the accelerating potential applied across the X-ray tube expressed in kV, is equal to the maximum energy E_{max}, which is expressed in keV, of the X-radiation produced by the tube. This relationship was therefore verified by the fact, that the measured continuous spectra had maximum energies of approximately 84.87 keV, which corresponds closely to 85 kV, the maximum value of the measured voltage, that was discharged across the X-ray tube (see Figure 6.2, Chapter 6). The XR-100T-CZT detector proved to have a tendency towards acquiring a high amount of continuous spectra as a result of fluctuations of charge collection times, that take place when electron/hole pairs are created by radiation, that acts on the cadmium zinc telluride detector [47] (see Figure A9a, Figure A9b and Figure A9c in Appendix 9).

In Section 6.4.2 (see Chapter 6) X-ray spectra of different samples were measured with the XR-100T silicon detector. The same procedure in measuring X-ray spectra was followed using the silicon detector (see Section 5.5.2, Chapter 5). Because this detector has the capability of reliably detecting X-ray photons, that have energies of only up to 20 keV, it was necessary to recalibrate the 'MCA 8000A' multichannel analyser for the lower photon energies, that were to be measured. By measuring the K shell excitation lines of chromium, iron and nickel contained in stainless steel, copper and zinc contained in brass and molybdenum on the one hand, and the L shell excitation lines of lead on the other, it was possible to calibrate the multichannel analyser by assigning photon energy values from Table A5b and A5c in Appendix 5 to the corresponding

channels in which the aforementioned lines were recorded. These channel values were plotted against the photon excitation energies for the measured excitation lines in Figure 6.7 (see Section 6.4.2, Chapter 6), where it can be seen that the channel-excitation energy relationship is linear. The linear channel-excitation energy relationship is expressed by equation 6.2, which was established by the multichannel analyser software during the calibration process (see Section 6.4.1, Chapter 6). With the multichannel analyser calibrated the linear channel-excitation energy relationship was further verified by recording the actual spectra of cobaltous acetate, nickel and bromine contained in a sample of barium bromide. Before measuring the K shell excitation lines of these elements equation 6.2 was used to predict theoretical channel values for the Co $K\alpha_1$, Co $K\beta_1$, Ni $K\alpha_1$, Ni $K\beta_1$, Br $K\alpha_1$ and Br $K\beta_1$ excitation lines (see Table 6.2.2, Chapter 6). The Ni $K\alpha_1$, Ni $K\beta_1$, Br $K\alpha_1$ and Br $K\beta_1$ lines were measured in channels 1226, 1345, 1958 and 2182 respectively with deviations from the predicted channel values ranging between –14 and –3 (see Table 6.2.3, Chapter 6). All the aforementioned excitation lines were measured for periods of approximately 900 seconds (see Table 6.5, Chapter 6). The cobalt $K\alpha_1$ and $K\beta_1$ lines, however, were detected in channels with relatively high deviations of –100 and 86 respectively. This would suggest, that by substituting the measured channel values of the Co $K\alpha_1$ and $K\beta_1$ excitation lines, which were found to be equal to 1226 and 1358 respectively (see Table 6.6, Chapter 6), back into equation 6.2, their characteristic photon energies would have been measured as being equal to 7.453 keV rather than 6.930 keV for the $K\alpha_1$ line and 8.253 keV as opposed to 7.649 keV for the $K\beta_1$ line. The deviation of the cobalt excitation lines from the generally linear behaviour of the channel-excitation energy relationship is also clearly evident in the plot in Figure 6.8 (see Chapter 6). Furthermore it was also shown, that due to the low operating efficiency of the XR-100T detector at photon energies above 20 keV, the detector was not suited for measuring energies above that value. This can be seen in Figure A9h (Appendix 9), where the 42.983 keV gadolinium $K\alpha_1$ peak is barely visible, while the tin $K\alpha_1$ line with an energy of 25.270 keV is far less intensive than the less energetic molybdenum $K\alpha_1$ line, which has a photon energy of 17.478 keV.

8. Conclusion

This study offered a deeper understanding of the design and construction methods of pulsed cold cathode X-ray tubes and their application in energy dispersive X-ray spectrometry. After introducing the reader to some general principles of X-ray physics and the parameters involved in the design of X-ray tubes in Chapter 2, the design of the pulsed end-window MgO cold cathode X-ray tube as conceived by the author was presented. Here the main focus was placed on the design and function of the MgO cold cathode, where the author developed a model for the current emission characteristics of the cathode. An important aspect, that had to be taken into account, was the fact, that the current produced by the cathode was not only dependent on the electric fields developed across dielectric layers of the cathode, but also, due to the end-window configuration of the tube, a result of a photocurrent produced by the action of the X-radiation on the cathode. In Chapter 3 a theoretical prediction was made as to the overall current characteristics of the X-ray tube, a quantity that was found to be the sum of the aforementioned field and photocurrents, when in operation. The case presented, however, was an idealised one as far as the production of photocurrent was concerned, where the assumption was made that all of the radiation absorbed within the cathode would result in the release of photoelectrons. In Chapter 4 the reader was introduced to the construction techniques and manufacturing methods of the ceramic X-ray tube. Finally a spectrometer was set up, so as to evaluate the X-ray tube in the following four steps:

1. The evaluation of the X-ray tube current and voltage characteristics (see Section 7.1, Chapter 7).
2. The measurement of the photoefficiency of the MgO cold cathode (see Section 7.2, Chapter 7).
3. The measurement of the absolute primary intensity distribution of the X-ray tube (see Section 7.3, Chapter 7).
4. The measurement of spectra of the higher energy elements molybdenum, silver, lanthanum, neodymium and gadolinium using the XR-100T-CZT detector and the measurements of elements cobalt, nickel and bromine using the XR-100T silicon detector. The spectra were produced by irradiating the aforementioned elements with the X-ray tube (see Section 7.4, Chapter 7).

In step 1 it was found that the overall X-ray tube current was mainly a field dependent one, where the additional photocurrent was present for only an instant at the start of every current pulse and not throughout the duration of each current pulse. This was attributed to the fact that most of the electrons in the nickel base of the cathode, which were excited by the radiation produced in the X-ray tube, were not in fact emitted as photoelectrons, but rather returned to their shells thereby merely releasing further X-ray photons. The maximum and average currents produced due to the changing electric fields present in the pulsed X-ray tube on the other hand were measured at 19.69 mA, deviating by only 7.65 % from the predicted value of 18.29 mA, and 3.758 mA, as opposed to a theoretical value of 3.048 mA, respectively. In step 2 only the field current was measured directly (see Section 7.2, Chapter 7). The photoefficiency, which is the ratio of the photocurrent and the total tube current, was thus found to be equal 4.81%. In step 3, the radiation intensity distribution of the X-ray tube was measured. As predicted it was found, that the tube produced X-rays of maximum intensity in a direction 180° to that of the motion of the accelerated electrons emitted by the cathode of the X-ray tube. In step 4 the performance of the X-ray tube as an X-ray source in an XRF spectrometer was finally tested. The K shell excitation energies of molybdenum, silver, lanthanum, neodymium and gadolinium were

measured using the XR-100T-CZT cadmium zinc telluride detector, which can detect X-ray photons with energies of up to 100 keV at an efficiency of 100%. As a result it was thus possible to measure the entire energy range of the continuous spectrum of the X-ray tube from the aforementioned samples. The maximum energy of the continuous spectrum from a secondary tungsten target irradiated by the X-ray tube was found to be equal to approximately 84.87 keV, which verified the fact, that the maximum voltage developed across the X-ray tube was equal to 85 keV (see Figure 6.2 and Figure 6.3, Chapter 6). With the XR-100T-CZT detector it was therefore shown, that the X-ray tube was indeed capable of producing X-rays at energies sufficient to excite rare earth elements such as lanthanum, neodymium and gadolinium, elements which due to their relatively high critical excitation levels are generally difficult to detect. Finally, further spectra were recorded with the XR-100T silicon detector, which can be used for reliably detecting X-ray photons at energies of up to 20 keV at higher resolution. Together with the Kα lines of the elements chromium, iron, nickel, copper, zinc, lead and molybdenum, which were used as calibration samples for the multichannel analyser, the positions of the channels in which the Kα lines of the elements cobalt, nickel and bromine were recorded, once again showed that the channel-excitation energy relationship displayed by the 'MCA 8000A' multichannel analyser is a linear one. Overall it was shown, that the tube was an excellent light source for X-ray fluorescence (XRF) spectrometry and that elements with relatively high excitation energy levels, such as the rare earth elements neodymium and gadolinium, contained in solutions at concentration levels as low as 100 ppm could be detected in approximately 900 seconds (see Table 6.6, Chapter 6) or less as opposed to conventional spectrometers, which use 2-3 kW continuous current X-ray tubes and can take up to several hours to detect the aforementioned elements at similar concentration levels. Finally the X-ray tube did not only prove to be reliable in that it was tested and run for a total of approximately 200 hours without any deterioration in its performance, but was also free of any practical problems such as overheating, leaking and arcing between its high voltage contacts and their surroundings.

References

[1] J.D.Cobine, Gaseous Conductors: Theory and Engineering Applications, Dover Publications, Inc. New York,1958.

[2] A.M. Shroff, Étude expérimentale de l'émmission électronique autoentretenue d'une couche diélectrique mince (oxyde de magnésium), Annales de radioélectricité, N° 91, January 1968.

[3] A.M. Shroff, Sur quelques traveaux concernant les sources froides d'électrons, Proceedings of the 4th International Congress on Microwaves Tubes, The Hague, September 1963.

[4] A.M. Shroff, Study of the Mechanism of the Self-sustained Electron Emission from Magnesium Oxide, Annual Conference Phys. Electronics, Vol. 26, 1967.

[5] G. Herrman and S. Wagener, The Oxide coated Cathode, Chapman and Hall, 1951.

[6] Dietrich Dobischek, Harold Jacobs and John Freely, The Mechanism of Self-Sustained Emission from Magnesium Oxide, Physical Review, vol. 91, N°4, August 1953.

[7] K. M. Tischer, Der heutige Stand der Kaltkatodenentwicklung, Internationale elektronische Rundschau, vol. 19, N°. 3, 1965.

[8] N. Ya. Basalayeva, T. M. Yekimenko, M. I. Yelinson, D. V. Zernov, Ya. V. Savitskaya, A. A. Yasnopol'skaya, Investigation of some properties of Cold Magnesium Oxide Cathodes with Self Maintaining (Malter type) Emission, Soviet Physics - Solid State, 23 May 1961.

[9] H. N. Daglish, Electron Emission from Cold Magnesium Oxide, The Institution of Electrical Engineers (IEEE), Paper N°. 3344, Jan. 1961.

[10] A. M. Skellett, B. G. Firth, D. W. Mayer, The Magnesium Oxide Cold Cathode and its Application in Vacuum Tubes, Proceedings of the IRE, October 31, 1958.

[11] N. L. Yasnopol'skii, A. E. Shabel'nikova, Investigation of the Field-dependent Electron Emission from Porous MgO Films, Soviet Physics - Solid State, Vol. 10, N°. 1, July 1966.

[12] R. Johannes, K. Ramanathan, P. Cholet, W. Haas, The Role of Avalanching in Cold Emission Devices, IEEE Transactions on Electron Devices, March 11, 1963.

[13] W. Haas, R. Johannes, Thin Film Cold Cathodes, Brit. J. Appl. Phys., vol. 4, 1963.

[14] Martin A. Plonus, Applied Electromagnetics, McGraw-Hill, 1988.

[15] J. D. Jackson, Classical Electrodynamics, John Wiley & Sons, 1962.

[16] Melvin Schwartz, Principles of Electrodynamics, Dover Publications, 1972.

[17] Pieter B. Visscher, Fields and Electrodynamics, John Wiley & Sons, 1988.

[18] R. S. Elliott, Electromagnetics, McGraw-Hill, 1966.

[19] W. H. Kohl, Materials and Techniques for Electron Tubes, Reinhold Publishing Corp., 1960.

[20] David R. Lide, Handbook of Chemsitry and Physics, 74th edition, CRC Press, 1993-1994.

[21] R. H. Fowler, L. Nordheim, Proc. Roy. Soc. London, serie A, vol. 119, pg. 173, 1928.

[22] R. Tertian, F. Claisse, Principles of Quantitative X-Ray Fluorescence Analysis, Heyden & Son, 1982.

[23] R. H. Fowler, The Analysis of Photoelectric Sensitivity Curves for Clean Metals at Various Temperatures, Physical Review, 38 May 1931.

[24] Eugene P. Bertin, Introduction to X-Ray Spectrometric Analysis, Plenum Press, 1978.

[25] Eugene P. Bertin, Principles and Practice of X-ray Spectrometric Analysis, Plenum Press, 1978.

[26] D. B. Matthews, S. U. M. Khan, The Dependence of the Photocurrent at the Metal-Electrolyte Interface on Electrode Potential, Aust. J. Chem., 1975.

[27] P. Venugopala Rao, Mau Hsiung Chen, Bernd Crasemann, Atomic Vacancy Distributions Produced by Inner-Shell Ionization, Physical Review A, General Physics, Third Series, Vol.5, N°. 3, page 997, March 1972.

[28] W. Bambynek, B. Crasemann, R. W. Fink, H. U. Freund, H. Mark, C. D. Swift, R. E. Price and P. Venugopala Rao, Rev. Mod. Phys. 44, pg. 716, 1972.

[29] K. L. Williams, An Introduction to X-ray Spectrometry, Allen & Unwin, 1987.

[30] S. J. B. Reed, Characteristic Fluorescence Corrections in Electron Probe Microanalysis, Brit. J. Appl. Phys. 16, pg. 913, 1965.

[31] Hugh D. Young, Physics, Addison-Wesley Publishing Company, 1992.

[32] T. Moeller et al., Chemistry, with Inorganic Qualitative Analysis, Harcourt Brace Jovanovich, 1989.

[33] Willis W. Harman, Electronic Motion, McGraw-Hill, 1953.

[34] N. P. Hensley, The Construction and Testing of an Experimental TWT, University of Natal, 1990.

[35] D. M. Smith, The Theoretical and Practical Analysis of Low Perveance Pierce electron Guns, University of Natal, 1990.

[36] A. Septier, Focusing of Charged Particles Vol. 1, Academic Press, 1967.

[37] A. S. Gilmour, Jr., Microwave Tubes, Artech House, 1986.

[38] J. R. Pierce, Theory and Design of Electron Beams, D. van Nostrand Company, 1954.

[39] F. Jaundrell-Thompson, W. J. Ashworth, X-Ray Physics and Equipment 2nd Ed., Blackwell, 1970.

[40] F. Kreith, M. S. Bohn, Principles of Heat Transfer, Harper Collins, 1986.

[41] D. G. Burnside, Ceramic Metal Seals of the Tungsten Iron Type, Radio Corporation of America Review, Vol. 15, 1954.

[42] W. Weise, W. Malikowski, W. Boehm, Verbinden von Keramik oder Metall durch Aktivloeten unter Argon oder Vakuum, Degussa AG catalogue on Active Solder Alloy Products, 1990.

[43] Degussa AG datasheet on Ceramic Products, 1998.

[44] W. Espe, Materials of High Vacuum Technology, Vol. 2, Pergamon Press, 1968.

[45] L. Holland, W. Steckelmacher, J. Yarwood, Vacuum Manual, E. and F. N. Spon, 1974.

[46] R. Spatz, K. H. Lieser, Optimization of a Spectrometer for Energy-dispersive X-ray Fluorescence Analysis by X-ray Tubes in Combination with Secondary Targets for Multielement Determination, X-ray Spectrometry, vol.8, no.3, 1979.

[47] Amptek Inc., Operating Manual for XR-100T/XR-100T-CZT X-Ray Detector System and the PX2T/PX2T-CZT Power Supply/Shaper, 1997.

[48] A. C. Huber, J.A. Pantazis, V. T. Jordanov, High Performance Thermoelectrically Cooled X-Ray and Gamma Ray Detectors, International Conference on the Application of Accelerators in Research and Industry, November 1994.

[49] H. K. Pollehn, Chapter 10: Image Intensifiers, Applied Optics and Optical Engineering Vol.6, edited by R. Kingslake, B. J. Thompson, Academic Press, 1980.

[50] E. Kuffel, High Voltage Engineering, 2nd edition, Butterworth-Heinemann, 1998.

[51] Datasheet for brazing filler materials for high vacuum systems, WESGO, 1964.

[52] B. Templeman, The Bell Jar (Electronic version), No. 2, Vol. 3, Winter and Spring, 1994.

[53] D. R. J. White, Electromagnetic Shielding, Materials and Performance, Don White Consultants, 1980.

[54] R. Eisberg, R. Resnick, Quantum Physics of Atoms, Molecules, Solids, Nuclei and Particles, John Wiley & Sons, 1974.

[55] P. Thebock, P. Hils, D. Damjanovic, Article Identification Means, priority: U.K. patent application no. 9722475.2, filed October 1999, RSA patent no. 98/9500, granted July 1999, pending in E.U., Israel, Chile, Brazil, Japan, U.S.A., Australia, Mexico, Argentina, Canada.

[56] P. Thebock, D. Damjanovic, High Energy X-ray Tube, priority: RSA patent application no. PCT/ZA00/00010, filed January 1999.

[57] P. Thebock, Analysis of Chemical Elements, priority: U.K. patent application no. 9722478.6, filed October 1997, RSA patent no. 98/9501, granted July 1999, pending in E.U., Israel, Chile, Brazil, Japan, U.S.A., Australia, Mexico, Argentina, Canada.

Appendix 1. Computer Aided Design Drawings of the Cold Cathode X-ray Tube

1. Ceramic Sleeve
2. Focusing Lens
3. Ceramic Sleeve
4. X-Ray Window
5. Cathode Support
6. Anode/X-Ray Tube Target Structure
7. Cathode and X-Ray Window Structure

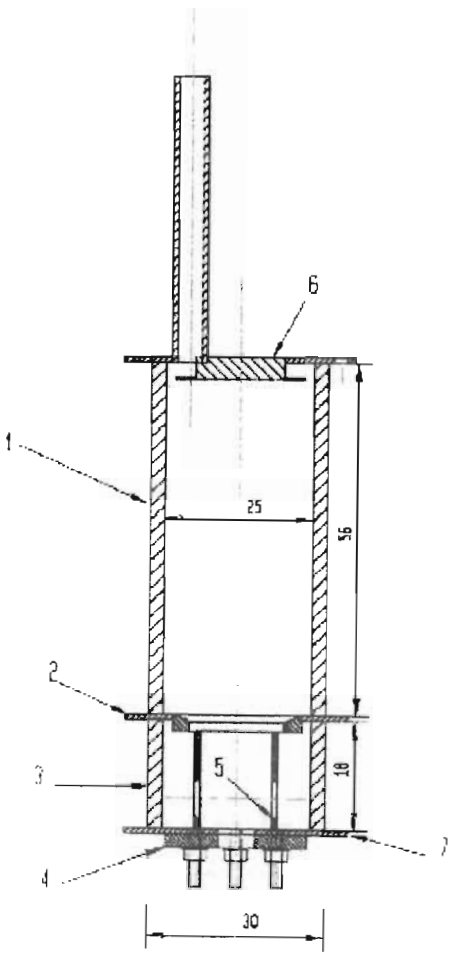

Fig. A1a: Schematic diagram of the cold cathode X-ray tube.

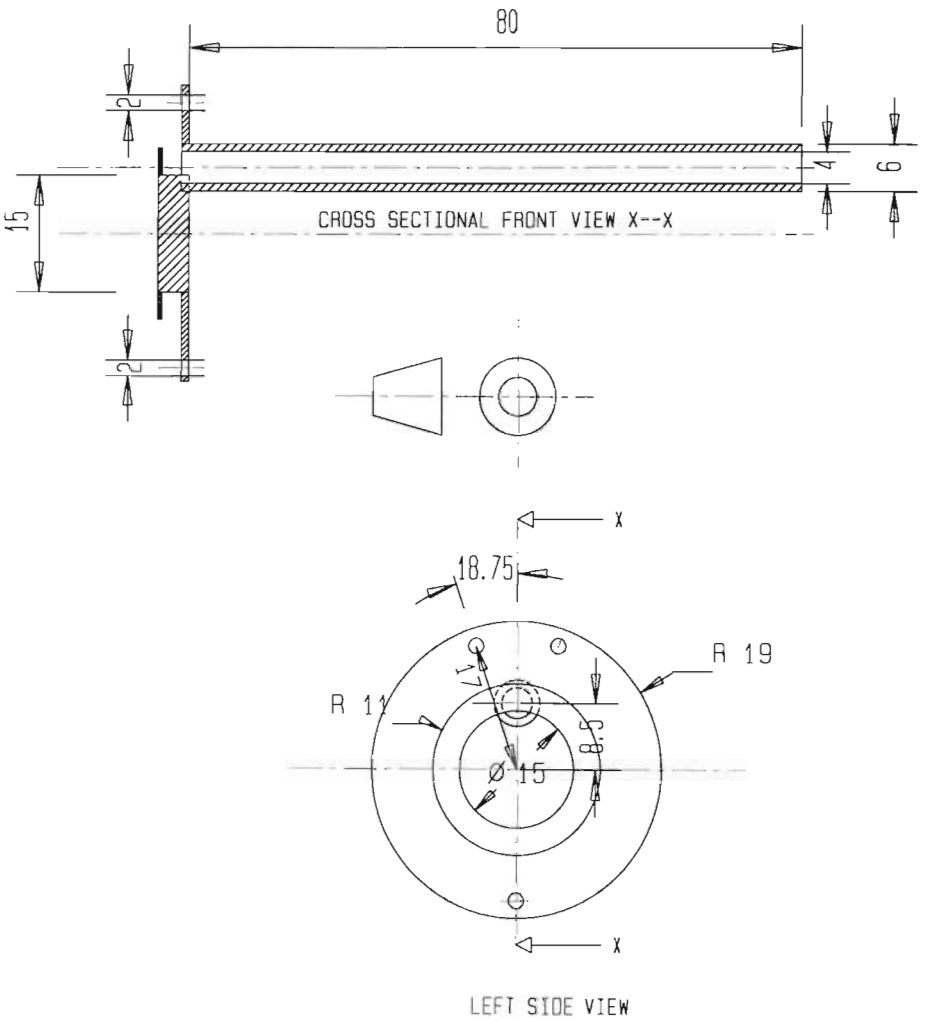

Fig. A1b: Schematic diagram of the anode structure of the cold cathode X-ray tube.

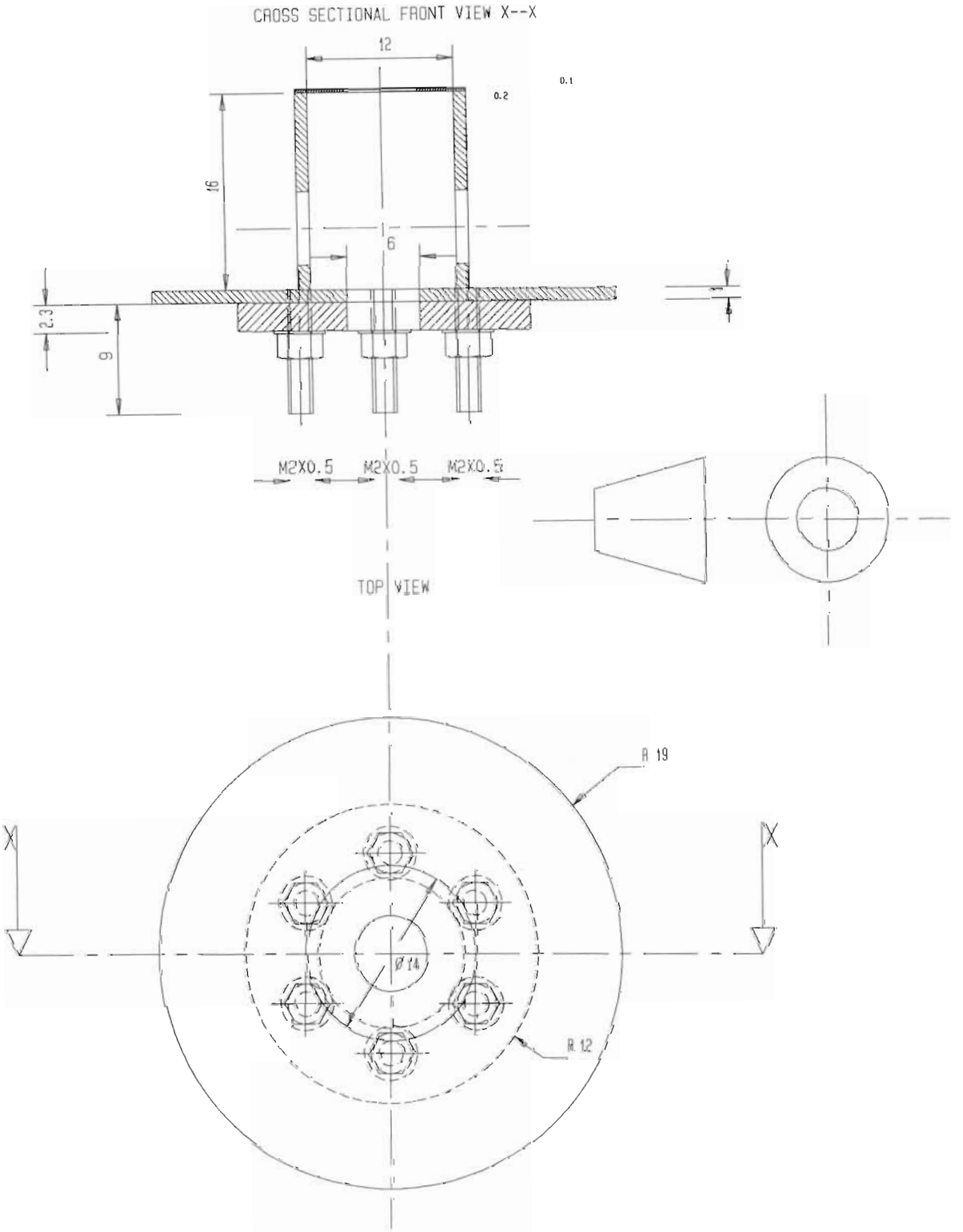

Fig. A1c: Schematic diagram of the cathode-window structure of the cold cathode X-ray tube.

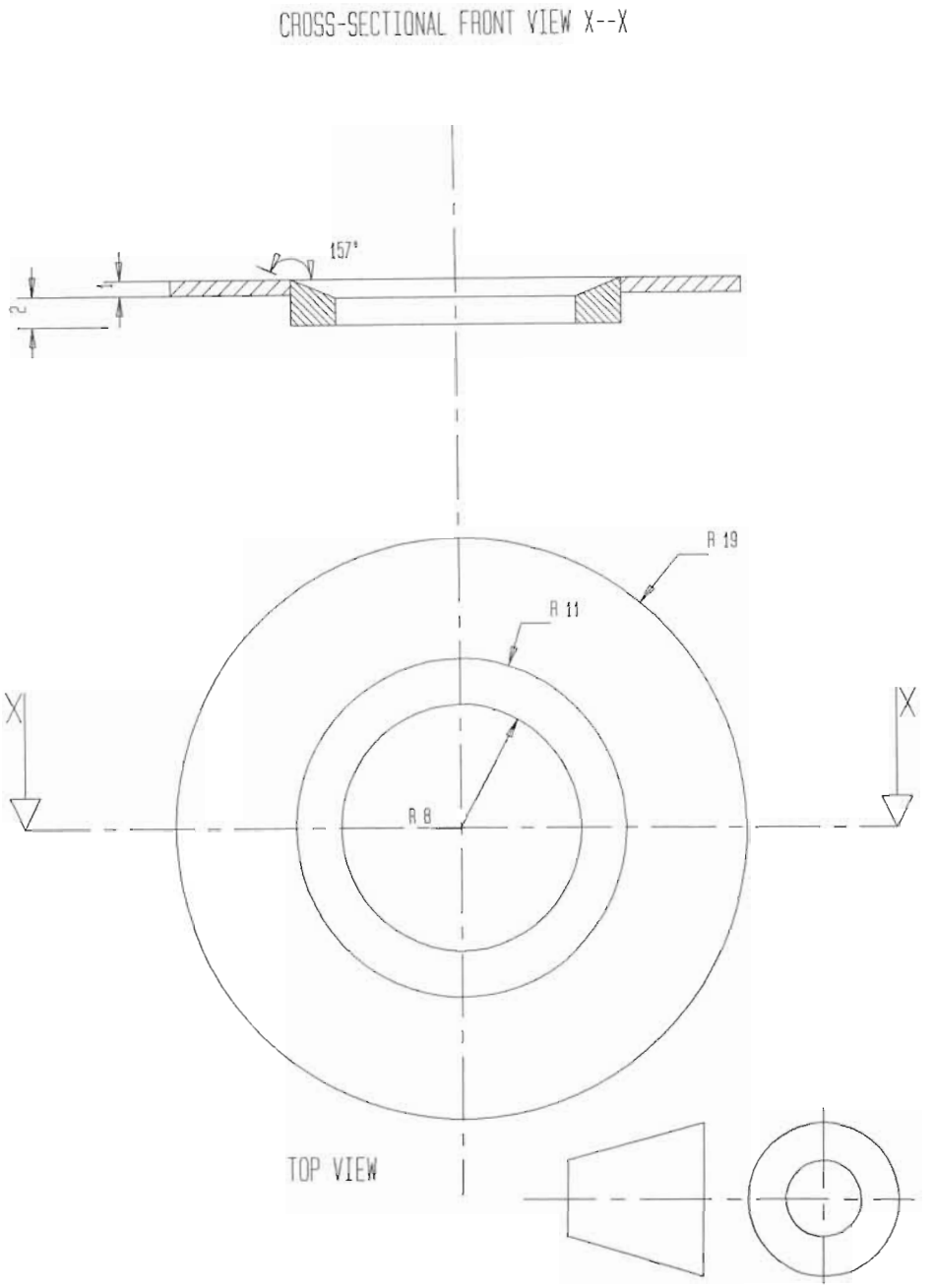

Fig. A1d: Schematic diagram of the focusing lens of the cold cathode X-ray tube.

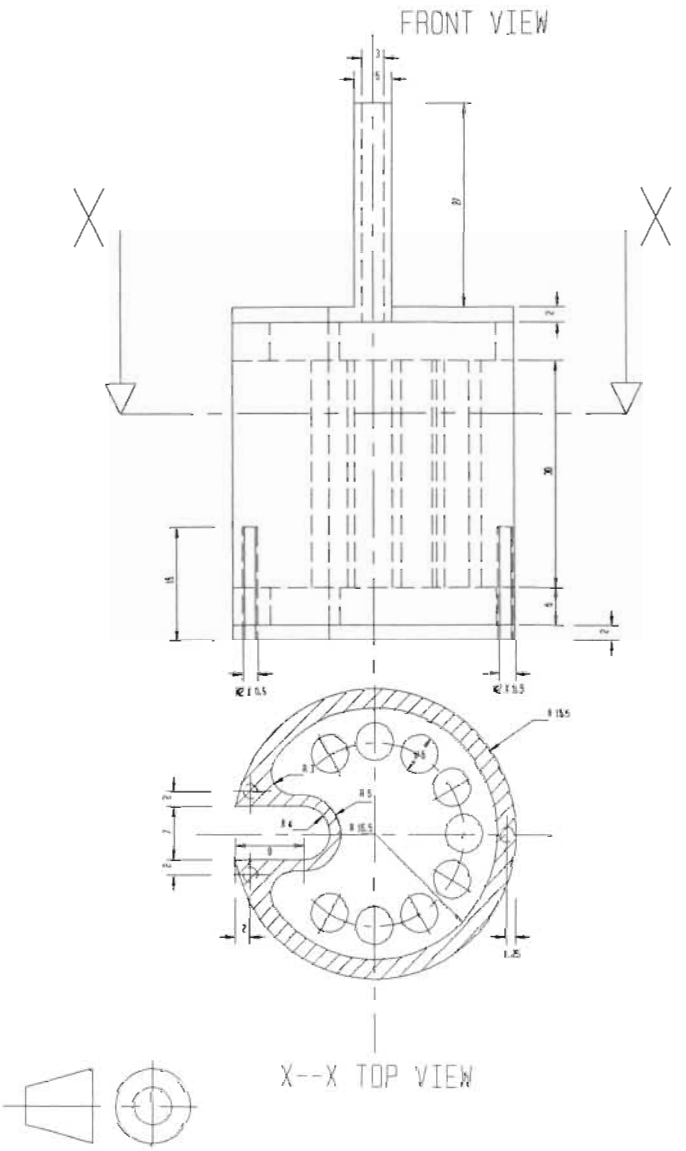

Fig. A1e: Schematic diagram of the cooling block of the cold cathode X-ray tube, which attaches to the anode of the tube.

Appendix 2. Relative Intensities of the Tungsten Emission Lines produced by the Cold Cathode X-ray Tube

Table A2: Relative intensities of the tungsten emission lines produced at the target of the X-ray tube acting on the nickel base of the cathode.

Nickel Emission Line	Tungsten Emission Line acting on Nickel	ω	$\frac{r-1}{r}$	g	E_i	$\lambda_{abs,i}$ (Å)	$P_i(t)$ $(\times I_\lambda)$
$K\alpha_1$	K	0.944	0.873	1	0.824	1.488	$\frac{4342.02t+14.31}{28333t+85}$
$K\alpha_2$	K	0.944	0.873	0.508	0.419	1.488	$\frac{2206.25t+7.27}{28333t+85}$
$K\beta$	K	0.944	0.873	0.135	0.111	1.488	$\frac{586.31t+1.93}{28333t+85}$
KL_1 (A)	K	0.944	0.639	0.185	0.081	12.201	$\frac{4822.17t+14.64}{28333t+85}$
KL_2 (A)	K	0.944	0.639	0.415	0.250	14.104	$\frac{12504.49t+37.90}{28333t+85}$
KL_2 (R)	K	0.944	0.639	0.123	0.074	14.104	$\frac{3706.15t+11.23}{28333t+85}$
KL_3 (A)	K	0.944	0.639	0.410	0.247	14.387	$\frac{12601.71t+38.19}{28333t+85}$
KL_3 (R)	K	0.944	0.639	0.242	0.146	14.387	$\frac{7438.08t+22.54}{28333t+85}$
KL(A)	K	0.944	0.639	1.010	0.609	12.201	$\frac{26326.45t+79.92}{28333t+85}$
KL(R)	K	0.944	0.639	0.365	0.220	12.201	$\frac{9514.01t+28.88}{28333t+85}$
KL_2	K	0.944	0.639	1.375	0.829	14.104	$\frac{41430.52t+125.58}{28333t+85}$
$K\alpha_1$	L	0.304	0.873	1	0.265	1.488	$\frac{1396.60t+4.61}{28333t+85}$
$K\alpha_2$	L	0.304	0.873	0.508	0.135	1.488	$\frac{710.49t+2.34}{28333t+85}$
$K\beta$	L	0.304	0.873	0.135	0.036	1.488	$\frac{188.81t+0.62}{28333t+85}$
KL_1(A)	L	0.304	0.639	0.185	0.036	12.201	$\frac{1552.90t+4.71}{28333t+85}$
KL_2(A)	L	0.304	0.639	0.415	0.081	14.104	$\frac{4026.87t+12.21}{28333t+85}$
KL_2(R)	L	0.304	0.639	0.123	0.024	14.104	$\frac{1193.51t+3.62}{28333t+85}$

Table A2 (cont.): Relative intensities of the tungsten emission lines produced at the target of the X-ray tube acting on the nickel base of the cathode.

Nickel Emission Line	Tungsten Emission Line acting on Nickel	ω	$\frac{r-1}{r}$	g	E_i	$\lambda_{abs,i}$ (Å)	$P_i(t)$ $(\times I_\lambda)$
KL_3 (A)	L	0.304	0.639	0.410	0.080	14.387	$\frac{4058.18t+12.30}{28333t+85}$
KL_3 (R)	L	0.304	0.639	0.242	0.047	14.387	$\frac{295.32t+7.26}{28333t+85}$
KL(A)	L	0.304	0.639	1.010	0.196	12.201	$\frac{8478.01t+25.74}{28333t+85}$
KL(R)	L	0.304	0.639	0.365	0.071	12.201	$\frac{306.84t+9.30}{28333t+85}$
KL_2	L	0.304	0.639	1.375	0.267	14.104	$\frac{13342.03t+40.44}{28333t+85}$
$K\alpha_1$	M	0.018	0.873	1.000	0.016	1.488	$\frac{82.81t+0.27}{28333t+85}$
$K\alpha_2$	M	0.018	0.873	0.508	0.008	1.488	$\frac{42.07t+0.14}{28333t+85}$
$K\beta$	M	0.018	0.873	0.135	0.002	1.488	$\frac{11.18t+0.04}{28333t+85}$
KL_1 (A)	M	0.018	0.639	0.185	0.002	12.201	$\frac{91.95t+0.28}{28333t+85}$
KL_2 (A)	M	0.018	0.639	0.415	0.005	14.104	$\frac{238.43t+0.73}{28333t+85}$
KL_2 (R)	M	0.018	0.639	0.123	0.001	14.104	$\frac{70.67t+0.21}{28333t+85}$
KL_3 (A)	M	0.018	0.639	0.410	0.005	14.387	$\frac{240.29t+0.73}{28333t+85}$
KL_3 (R)	M	0.018	0.639	0.242	0.003	14.387	$\frac{141.83t+0.43}{28333t+85}$
KL(A)	M	0.018	0.639	1.010	0.012	12.201	$\frac{501.99t+1.52}{28333t+85}$
KL(R)	M	0.018	0.639	0.365	0.004	12.201	$\frac{181.41t+0.55}{28333t+85}$
KL_2	M	0.018	0.639	1.375	0.016	14.104	$\frac{789.99t+2.39}{28333t+85}$

Appendix 3. Wavelengths of the principal Emission Lines and Absorption Edges

Table A3a: Wavelengths (Å) of the principal emission lines and absorption edges in the *K* spectrum for elements Z=12 to Z=31 [22].

Element	α_1 KL_{III}	α_2 KL_{II}	β_1 KM_{III}	β_3 KM_{II}	β_2 $KN_{II,III}$	Abs. edge *K*
12-Mg	9.890		9.570	-	-	9.512
13-Al	8.339	8.342	7.982	-	-	7.948
14-Si	7.125	7.128	6.778	-	-	6.738
15-P	6.157	6.160	5.804	-	-	5.784
16-S	5.372	5.375	5.032	-	-	5.019
17-Cl	4.728	4.731	4.403	-	-	4.397
18-Ar	4.192	4.195	3.886		-	3.871
19-K	3.741	3.745	3.454		-	3.437
20-Ca	3.358	3.362	3.090		-	3.070
21-Sc	3.031	3.034	2.780		-	2.762
22-Ti	2.749	2.752	2.514		-	2.497
23-V	2.504	2.507	2.284		-	2.269
24-Cr	2.290	2.294	2.085		-	2.070
25-Mn	2.102	2.106	1.910		-	1.896
26-Fe	1.936	1.940	1.757		-	1.743
27-Co	1.789	1.793	1.621		-	1.608
28-Ni	1.658	1.662	1.500		-	1.488
29-Cu	1.541	1.544	1.392		-	1.381
30-Zn	1.435	1.439	1.295		1.284	1.283
31-Ga	1.340	1.344	1.208	1.208	1.196	1.196
	α_1	α_2	β_1	β_3	β_2	*K*

Table A3b: Wavelengths (Å) of the principal emission lines and absorption edges in the *L* spectrum for elements Z=19 to Z=31 [22].

Element	α_1 $L_{III}M_V$	α_2 $L_{III}M_{IV}$	β_1 $L_{II}M_{IV}$	β_2 $L_{III}N_V$	β_3 L_IM_{III}	β_4 L_IM_{II}	β_5 $L_{III}O_{IV,V}$	β_6 $L_{III}N_I$	γ_1 $L_{II}N_{IV}$
19-K	-	-	-	-	-	-	-	-	-
20-Ca	36.33		35.94	-	-	-	-	-	-
21-Sc	31.35		31.02	-	-	-	-	-	-
22-Ti	27.42		27.05	-	-	-	-	-	-
23-V	24.25		23.88	-	21.19		-	-	-
24-Cr	21.64		21.27	-	18.96		-	-	-
25-Mn	19.45		19.11	-	17.19		-	-	-
26-Fe	17.59		17.26	-	15.65		-	-	-
27-Co	15.972		15.666	-	14.310		-	-	-
28-Ni	14.561		14.271	-	13.180		-	-	-
29-Cu	13.336		13.053	-	12.122		-	-	-
30-Zn	12.254		11.983	-	11.200		-	-	-
31-Ga	11.292		11.023	-	10.359		-	-	-
	α_1	α_2	β_1	β_2	β_3	β_4	β_5	β_6	γ_1

Table A3b (cont.): Wavelengths (Å) of the principal emission lines and absorption edges in the *L* spectrum for elements Z=19 to Z=31 [22].

Element	γ_2	γ_3	γ_4	γ_6	l	η	Absorption edges		
	$L_I N_{II}$	$L_I N_{III}$	$L_I O_{II,III}$	$L_{II} O_{IV}$	$L_{III} M_I$	$L_{II} M_I$	L_I	L_{II}	L_{III}
19-K	-	-	-	-	47.74	47.24	-	42.10	
20-Ca	-	-	-	-	40.96	40.46	-	35.13	35.49
21-Sc	-	-	-	-	35.59	35.13	-	-	-
22-Ti	-	-	-	-	31.36	30.89	-	27.29	
23-V	-	-	-	-	27.77	27.34	-	-	-
24-Cr	-	-	-	-	24.78	24.30	16.70	17.90	20.70
25-Mn	-	-	-	-	22.29	21.85	-	-	-
26-Fe	-	-	-	-	20.15	19.75	-	17.202	17.525
27-Co	-	-	-	-	18.292	17.870	-	15.618	15.915
28-Ni	-	-	-	-	16.693	16.270	-	14.242	14.252
29-Cu	-	-	-	-	15.286	14.900	-	13.014	13.288
30-Zn	-	-	-	-	14.020	13.680	10.350	11.862	12.131
31-Ga	-	-	-	-	12.953	12.597	9.517	10.828	11.100
	γ_2	γ_3	γ_4	γ_6	l	η	L_I	L_{II}	L_{III}

Appendix 4. Mass Attenuation Coefficients of the Chemical Elements

Table A4: Mass attenuation coefficients (cm^2g^{-1}) of the chemical elements at 0.31 – 12.40 Å for elements Z=21 to Z=29 [22].

	Wavelength (Å)																				
Absor-ber	**0.31**	**0.40**	**0.50**	**0.60**	**0.70**	**0.80**	**0.90**	**1.00**	**1.20**	**1.40**	**1.60**	**1.80**	**2.00**	**3.00**	**4.00**	**5.00**	**6.00**	**8.00**	**10.00**	**12.40**	**Absor-ber**
21-Sc	2.00	4.13	7.80	13.1	20.3	29.8	41.6	55.8	91.9	140.	202	178	371	126	276	507	834	1829	3362	6047	**21-Sc**
22-Ti	2.25	4.65	8.78	14.8	22.9	33.5	46.9	62.9	104	158	228	314	419	144	316	582	957	2098	3859	6939	**22-Ti**
23-V	2.52	5.21	9.84	16.5	25.7	37.6	52.5	70.6	116	177	255	352	470	164	359	660	1085	2381	4378	7873	**23-V**
24-Cr	2.81	5.81	11.0	18.4	28.6	41.9	58.6	78.8	130	198	285	393	524	184	404	742	1221	2678	4924	8955	**24-Cr**
25-Mn	3.12	6.44	12.2	20.5	31.8	46.5	65.0	87.6	144	220	317	437	68.5	207	454	835	1374	3014	5542	9966	**25-Mn**
26-Fe	3.44	7.12	13.5	22.6	35.1	51.4	71.8	96.9	160	243	350	57.4	76.6	232	508	934	1537	3370	6197	11140	**26-Fe**
27-Co	3.79	7.84	14.8	24.9	38.7	56.6	79.1	107	176	268	386	63.8	85.1	257	565	1038	1708	3745	6887	12390	**27-Co**
28-Ni	4.16	8.61	16.3	27.3	42.4	62.1	86.8	117	193	294	51.2	70.6	94.1	285	624	1148	1888	4141	7615	8853	**28-Ni**
29-Cu	4.55	9.41	17.8	29.9	46.4	67.9	94.9	128	212	39.2	56.2	77.9	104	314	689	1267	2084	4570	8404	9801	**29-Cu**

Appendix 5. Excitation Energies of the Characteristic Excitation Lines of Elements of the Periodic Table

Table A5a: Critical excitation levels (keV) of the *K* and *L* shells [22].

Element	*K*	*LI*	*LII*	*LIII*	Element	*K*	*LI*	*LII*	*LIII*
3-Li	0.055	-	-	-	**25-Mn**	6.538	-		
4-Be	0.111	-	-	-	**26-Fe**	7.111	-	0.721	0.707
5-B	0.192	-	-	-	**27-Co**	7.710	-	0.794	0.779
6-C	0.284	-	-	-	**28-Ni**	8.332	-	0.871	0.854
7-N	0.400	-	-	-	**29-Cu**	8.980	-	0.953	0.933
8-O	0.532	-	-	-	**30-Zn**	9.661	1.198	1.045	1.022
9-F	0.687	-	-	-	**31-Ga**	10.368	1.303	1.145	1.117
10-Ne	0.867	-	-	-	**32-Ge**	11.104	1.413	1.249	1.217
11-Na	1.072	-	0.0306		**33-As**	11.865	1.529	1.359	1.324
12-Mg	1.303	0.063	0.050	0.049	**34-Se**	12.655	1.653	1.474	1.434
13-Al	1.560	0.087	0.073		**35-Br**	13.470	1.781	1.599	1.553
14-Si	1.840	-	0.101		**36-Kr**	14.324	1.915	1.730	1.677
15-P	2.144	-	0.132		**37-Rb**	15.202	2.063	1.866	1.807
16-S	2.470	-	-	-	**38-Sr**	16.107	2.217	2.009	1.941
17-Cl	2.820	-	-	-	**39-Y**	17.038	2.377	2.154	2.079
18-Ar	3.203	-	-	-	**40-Zr**	17.999	2.541	2.305	2.222
19-K	3.608	-	0.295		**41-Nb**	18.987	2.710	2.464	2.371
20-Ca	4.038	-	0.353	0.349	**42-Mo**	20.002	2.881	2.627	2.523
21-Sc	4.489	-	-	-	**43-Tc**	21.047	3.055	2.795	2.678
22-Ti	4.965	-	0.454		**44-Ru**	22.119	3.233	2.966	2.838
23-V	5.464	-	-	-	**45-Rh**	23.220	3.417	3.145	3.002
24-Cr	5.989	0.742	0.693	0.599	**46-Pd**	24.348	3.607	3.330	3.173

Table A5a (cont.): Critical excitation levels (keV) of the *K* and *L* shells [22].

Element	*K*	*L*I	*L*II	*L*III	Element	*K*	*L*I	*L*II	*L*III
47-Ag	25.517	3.807	3.526	3.351	**68-Er**	57.487	9.757	9.262	8.358
48-Cd	26.716	4.019	3.728	3.538	**69-Tm**	59.380	10.121	9.617	8.650
49-In	27.942	4.237	3.939	3.730	**70-Yb**	61.300	10.490	9.976	8.944
50-Sn	29.195	4.465	4.157	3.929	**71-Lu**	63.310	10.874	10.345	9.249
51-Sb	30.486	4.698	4.382	4.132	**72-Hf**	65.310	11.274	10.736	9.558
52-Te	24.811	4.940	4.613	4.342	**73-Ta**	67.403	11.682	11.132	9.877
53-I	33.167	5.192	4.854	4.559	**74-W**	69.508	12.100	11.538	10.200
54-Xe	34.590	5.453	5.104	4.782	**75-Re**	71.658	12.530	11.954	10.531
55-Cs	35.987	5.721	5.358	5.011	**76-Os**	73.856	12.972	12.381	10.868
56-Ba	37.452	5.996	5.623	5.247	**77-Ir**	76.101	13.423	12.820	11.212
57-La	38.934	6.268	5.889	5.484	**78-Pt**	78.381	13.883	13.272	11.562
58-Ce	40.453	6.548	6.161	5.723	**79-Au**	80.720	14.324	13.736	11.921
59-Pr	42.002	6.834	6.439	5.963	**80-Hg**	83.109	14.842	14.215	12.286
60-Nd	43.574	7.129	6.723	6.209	**81-Tl**	85.533	15.343	14.699	12.660
61-Pm	45.198	7.436	7.014	6.461	**82-Pb**	88.005	15.855	15.205	13.041
62-Sm	46.849	7.748	7.313	6.717	**83-Bi**	90.534	16.376	15.719	13.426
63-Eu	48.519	8.061	7.620	6.981	**88-Ra**	-	19.236	18.486	15.444
64-Gd	50.233	8.386	7.931	7.243	**90-Th**	109.646	20.464	19.683	16.299
65-Tb	52.002	8.717	8.253	7.515	**91-Pa**	-	21.168	20.358	16.765
66-Dy	53.793	9.055	8.583	7.790	**92-U**	115.620	21.771	20.945	17.165
67-Ho	55.619	9.399	8.916	8.068	**94-Pu**	-	23.109	22.253	18.054

Table A5b: Photon energies of the principal *K* and *L* X-ray spectral lines of the chemical elements Z=23 to Z=52 [25].

Element	$K\alpha_1$	$K\alpha_2$	$K\beta_1$	$L\alpha_1$	$L\alpha_2$	$L\beta_1$	$L\beta_2$	$L\gamma_1$
23-V	4.952	4.944	5.427	0.510		0.519	-	-
24-Cr	5.414	5.405	5.946	0.571		0.581	-	-
25-Mn	5.898	5.887	6.490	0.636		0.647	-	-
26-Fe	6.403	6.390	7.057	0.704		0.717	-	-
27-Co	6.930	6.915	7.649	0.775		0.790	-	-
28-Ni	7.477	7.460	8.264	0.849		0.866	-	-
29-Cu	8.047	8.027	8.904	0.928		0.948	-	-
30-Zn	8.638	8.615	9.571	1.009		1.032	-	-
31-Ga	9.251	9.234	10.263	1.096		1.122	-	-
32-Ge	9.885	9.854	10.981	1.186		1.216	-	-
33-As	10.543	10.507	11.725	1.282		1.317	-	-
34-Se	11.221	11 181	12.495	1.379		1.419	-	-
35-Br	11.923	11.877	13.290	1.480		1.526	-	-
36-Kr	12.648	12.597	14.112	1.587		1.638	-	-
37-Rb	13.394	13.335	14.960	1.694	1.692	1.752	-	-
38-Sr	14.164	14.097	15.834	1.806	1.805	1.872	-	-
39-Y	14.957	14.882	16.736	1.922	1.920	1.996	-	-
40-Zr	15.774	15.690	17.666	2.042	2.040	2.124	2.219	2.302
41-Nb	16.614	16.520	18.621	2.166	2.163	2.257	2.367	2.462
42-Mo	17.478	17.373	19.607	2.293	2.290	2.395	2.518	2.623
43-Tc	18.410	18.328	20.585	2.424	2.420	2.538	2.674	2.792
44-Ru	19.278	19.149	21.655	2.558	2.554	2.683	2.836	2.964
45-Rh	20.214	20.072	22.721	2.696	2.692	2.834	3.001	3.144
46-Pd	21.175	21.018	23.816	2.838	2.833	2.990	3.172	3.328
47-Ag	22.162	21.988	24.942	2.984	2.978	3.151	3.348	3.519
48-Cd	23.172	22.982	26.093	3.133	3.127	3.316	3.528	3.716
49-In	24.207	24.000	27.274	3.287	3.279	3.487	3.713	3.920
50-Sn	25.270	25.042	28.483	3.444	3.435	3.662	3.904	4.131
51-Sb	26.357	26.109	29.723	3.605	3.595	3.843	4.100	4.347
52-Te	27.471	27.200	30.993	3.769	3.758	4.029	4.301	4.570

Table A5c: Photon energies of the principal *K* and *L* X-ray spectral lines of the chemical elements Z=56 to Z=82 [25].

Element	$K\alpha_1$	$K\alpha_2$	$K\beta_1$	$L\alpha_1$	$L\alpha_2$	$L\beta_1$	$L\beta_2$	$L\gamma_1$
56-Ba	32.191	31.815	36.376	4.467	4.451	4.828	5.156	5.531
57-La	33.440	33.033	37.799	4.651	4.635	5.043	5.384	5.789
58-Ce	34.717	34.276	39.255	4.840	4.823	5.262	5.613	6.052
59-Pr	36.023	35.548	40.746	5.034	5.014	5.489	5.850	6.322
60-Nd	37.359	36.845	42.269	5.230	5.208	5.722	6.090	6.602
61-Pm	38.649	38.160	43.945	5.431	5.408	5.956	6.336	6.891
62-Sm	40.124	39.523	45.400	5.636	5.609	6.206	6.587	7.180
63-Eu	41.529	40.877	47.027	5.846	5.816	6.456	6.842	7.478
64-Gd	42.983	42.280	48.718	6.059	6.027	6.714	7.102	7.788
65-Tb	44.470	43.737	50.391	6.275	6.241	6.979	7.368	8.104
66-Dy	45.985	45.193	52.178	6.495	6.457	7.249	7.638	8.418
67-Ho	47.528	46.686	53.934	6.720	6.680	7.528	7.912	8.748
68-Er	49.099	48.205	55.690	6.948	6.904	7.810	8.188	9.089
69-Tm	50.730	49.762	57.576	7.181	7.135	8.103	8.472	9.424
70-Yb	52.360	51.326	59.352	7.414	7.367	8.401	8.758	9.779
71-Lu	54.063	52.959	61.282	7.654	7.604	8.708	9.048	10.142
72-Hf	55.757	54.579	63.209	7.989	7.843	9.021	9.346	10.514
73-Ta	57.524	56.270	65.210	8.145	8.087	9.341	9.649	10.892
74-W	59.310	57.973	67.233	8.396	8.333	9.670	9.959	11.283
75-Re	61.131	59.707	69.298	8.651	8.584	10.008	10.273	11.684
76-Os	62.991	61.477	71.404	8.910	8.840	10.354	10.596	12.094
77-Ir	64.886	63.278	73.549	9.173	9.098	10.706	10.918	12.509
78-Pt	66.820	65.111	75.736	9.441	9.360	11.069	11.249	12.939
79-Au	68.794	66.980	77.968	9.711	9.625	11.439	11.582	13.379
80-Hg	70.821	68.894	80.258	9.987	9.896	11.823	11.923	13.828
81-Tl	72.860	70.820	82.558	10.266	10.170	12.210	12.268	14.288
82-Pb	74.957	72.794	84.922	10.549	10.448	12.611	12.620	14.762

Appendix 6. Fluorescent Yields of Elements of the Periodic Table

Table A6: Average values of the K, L and M fluorescent yields of elements Z=6 to Z=79 [25].

Element	*K*	*L*	*M*	Element	*K*	*L*	*M*
6-C	0.001	-	-	**43-Tc**	0.765	0.043	0.001
7-N	0.002	-	-	**44-Ru**	0.779	0.047	0.001
8-O	0.003	-	-	**45-Rh**	0.792	0.052	0.001
9-F	0.005	-	-	**46-Pd**	0.805	0.058	0.001
10-Ne	0.008	-	-	**47-Ag**	0.816	0.063	0.002
11-Na	0.013	-	-	**48-Cd**	0.827	0.069	0.002
12-Mg	0.019	-	-	**49-In**	0.836	0.075	0.002
13-Al	0.026	-	-	**50-Sn**	0.845	0.081	0.002
14-Si	0.036	-	-	**51-Sb**	0.854	0.088	0.002
15-P	0.047	-	-	**52-Te**	0.862	0.095	0.003
16-S	0.061	-	-	**53-I**	0.869	0.102	0.003
17-Cl	0.078	-	-	**54-Xe**	0.876	0.110	0.003
18-Ar	0.097	-	-	**55-Cs**	0.882	0.118	0.004
19-K	0.118	-	-	**56-Ba**	0.888	0.126	0.004
20-Ca	0.142	0.001	-	**57-La**	0.893	0.135	0.004
21-Sc	0.168	0.001	-	**58-Ce**	0.898	0.143	0.005
22-Ti	0.197	0.001	-	**59-Pr**	0.902	0.152	0.005
23-V	0.227	0.002	-	**60-Nd**	0.907	0.161	0.006
24-Cr	0.258	0.002	-	**61-Pm**	0.911	0.171	0.006
25-Mn	0.291	0.003	-	**62-Sm**	0.915	0.180	0.007
26-Fe	0.324	0.003	-	**63-Eu**	0.918	0.190	0.007
27-Co	0.358	0.004	-	**64-Gd**	0.921	0.200	0.008
28-Ni	0.392	0.005	-	**65-Tb**	0.924	0.210	0.009
29-Cu	0.425	0.006	-	**66-Dy**	0.927	0.220	0.009
30-Zn	0.458	0.007	-	**67-Ho**	0.930	0.231	0.010
31-Ga	0.489	0.009	-	**68-Er**	0.932	0.240	0.011
32-Ge	0.520	0.010	-	**69-Tm**	0.934	0.251	0.012
33-As	0.549	0.012	-	**70-Yb**	0.937	0.262	0.013
34-Se	0.577	0.014	-	**71-Lu**	0.939	0.272	0.014
35-Br	0.604	0.016	-	**72-Hf**	0.941	0.283	0.015
36-Kr	0.629	0.019	-	**73-Ta**	0.942	0.293	0.016
37-Rb	0.653	0.021	0.001	**74-W**	0.944	0.304	0.018
38-Sr	0.675	0.024	0.001	**75-Re**	0.945	0.314	0.019
39-Y	0.695	0.027	0.001	**76-Os**	0.947	0.325	0.020
40-Zr	0.715	0.031	0.001	**77-Ir**	0.948	0.335	0.022
41-Nb	0.732	0.035	0.001	**78-Pt**	0.949	0.345	0.024
42-Mo	0.749	0.039	0.001	**79-Au**	0.951	0.356	0.026

Appendix 7. Absorption Jump factors of the Elements of the Periodic Table

Table A7: Absorption jump factors for elements Z=21 to Z=34 [25].

Element	r [K edge]	$(r - 1/r)$ [K edge]	r [L edge]	$(r - 1/r)$ [L edge]
21-Sc	8.58	0.883	-	-
22-Ti	8.53	0.883	-	-
23-V	8.77	0.886	-	-
24-Cr	8.78	0.886	-	-
25-Mn	8.61	0.884	-	-
26-Fe	8.22	0.878	-	-
27-Co	8.38	0.881	-	-
28-Ni	7.85	0.873	2.77	0.639
29-Cu	7.96	0.874	2.87	0.652
30-Zn	7.60	0.868	5.68	0.824
31-Ga	7.40	0.865	5.67	0.824
32-Ge	7.23	0.962	5.70	0.825
33-As	7.19	0.861	4.88	0.795
34-Se	6.88	0.855	4.59	0.782

Appendix 8. Wavelengths of the Absorption Edges

Table A8: Wavelengths of the *K*, *L* and *M* X-ray absorption edges of elements Z=21 to Z=34 [25].

Element	*K*	*LI*	*LII*	*LIII*	*MI*	*MII*	*MIII*	*MIV*	*MV*
21-Sc	2.757	26.800	30.943	31.296	264.440	-	-	-	-
22-Ti	2.497	23.400	26.936	27.290	228.816	-	-	-	-
23-V	2.269	19.803	23.877	24.229	201.484	-	-	-	-
24-Cr	2.070	17.840	21.294	21.637	171.626	-	-	-	-
25-Mn	1.896	16.138	19.086	19.417	150.739	-	-	-	-
26-Fe	1.743	14.650	17.188	17.504	132.991	-	-	-	-
27-Co	1.608	13.333	15.545	15.843	118.175	-	-	-	-
28-Ni	1.488	12.201	14.104	14.387	103.062	-	-	-	-
29-Cu	1.380	11.172	12.841	13.113	91.685	137.152	-	793.498	-
30-Zn	1.283	10.262	11.725	11.987	81.898	116.000	-	546.224	-
31-Ga	1.196	9.416	10.728	10.930	73.146	98.670	107.500	405.000	-
32-Ge	1.116	8.692	9.840	10.089	65.116	89.857	93.488	299.437	-
33-As	1.045	8.067	9.056	9.298	58.581	79.123	82.205	238.357	-
34-Se	0.980	7.456	8.347	8.584	52.835	69.999	72.578	187.662	-

Appendix 9. X-ray Spectra Measurements

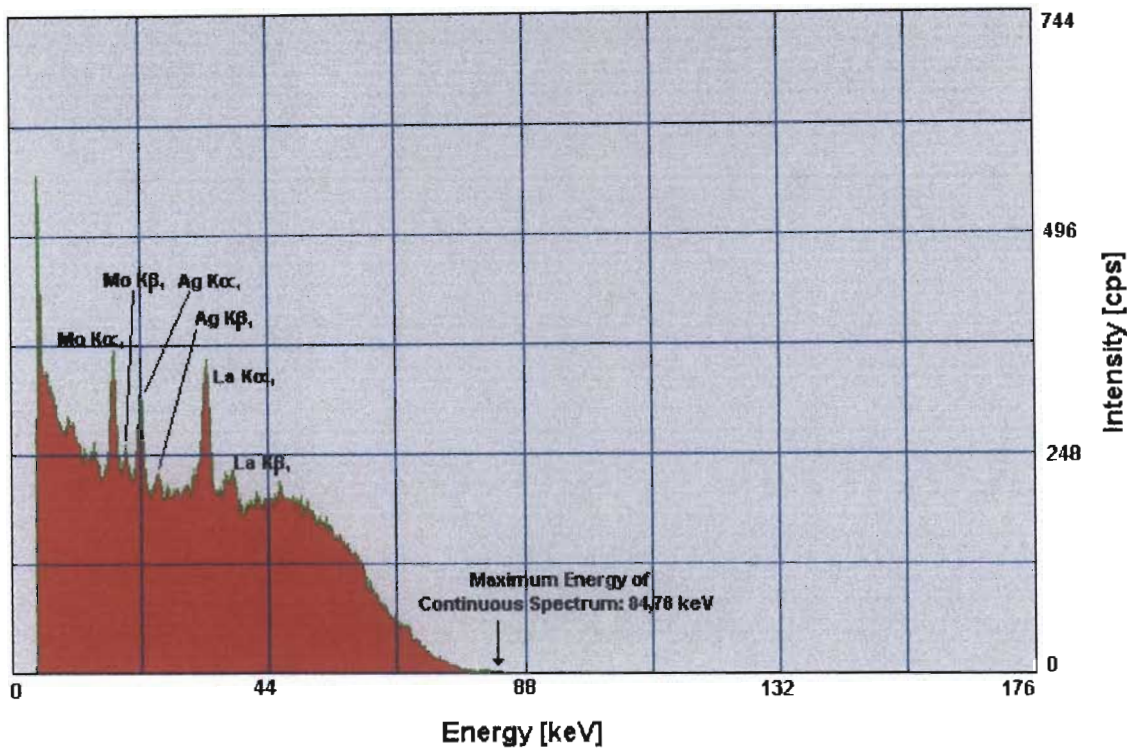

Fig. A9a: Characteristic spectra of elements molybdenum (Mo), silver (Ag) and lanthanum (La) obtained with the AMPTEK XR-100T-CZT cadmium zinc telluride detector.

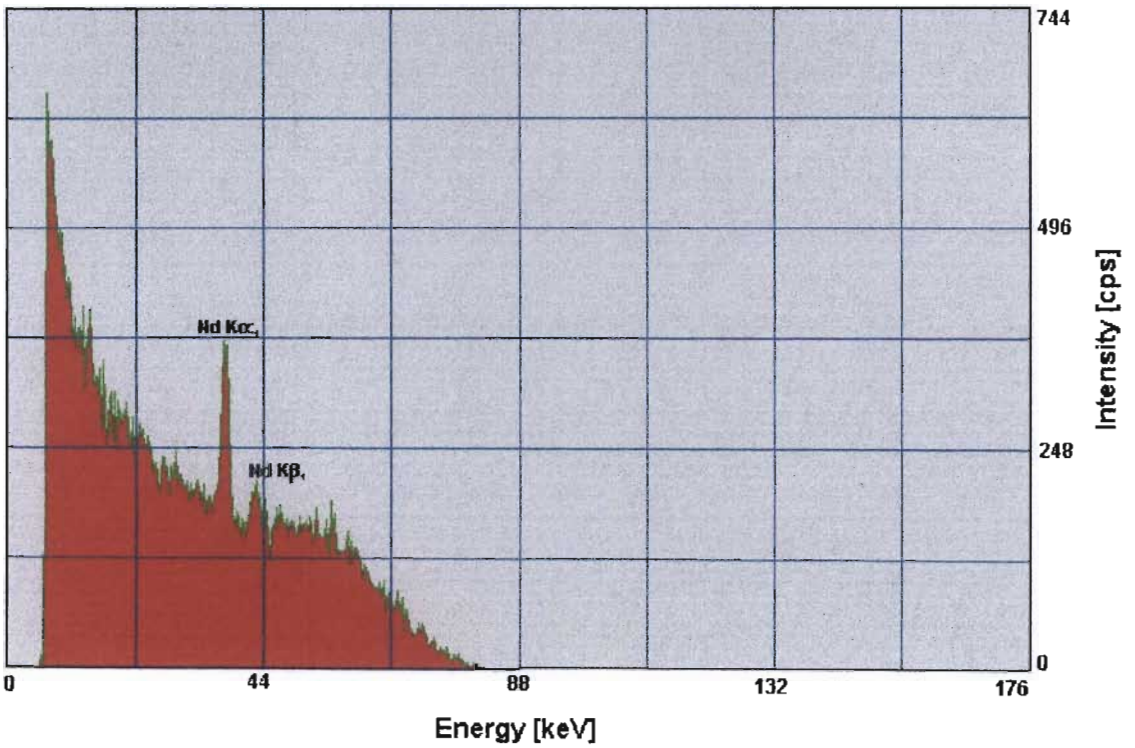

Fig. A9b: Characteristic spectra of neodymium (Nd) obtained with the AMPTEK 100T-CZT cadmium zinc telluride detector.

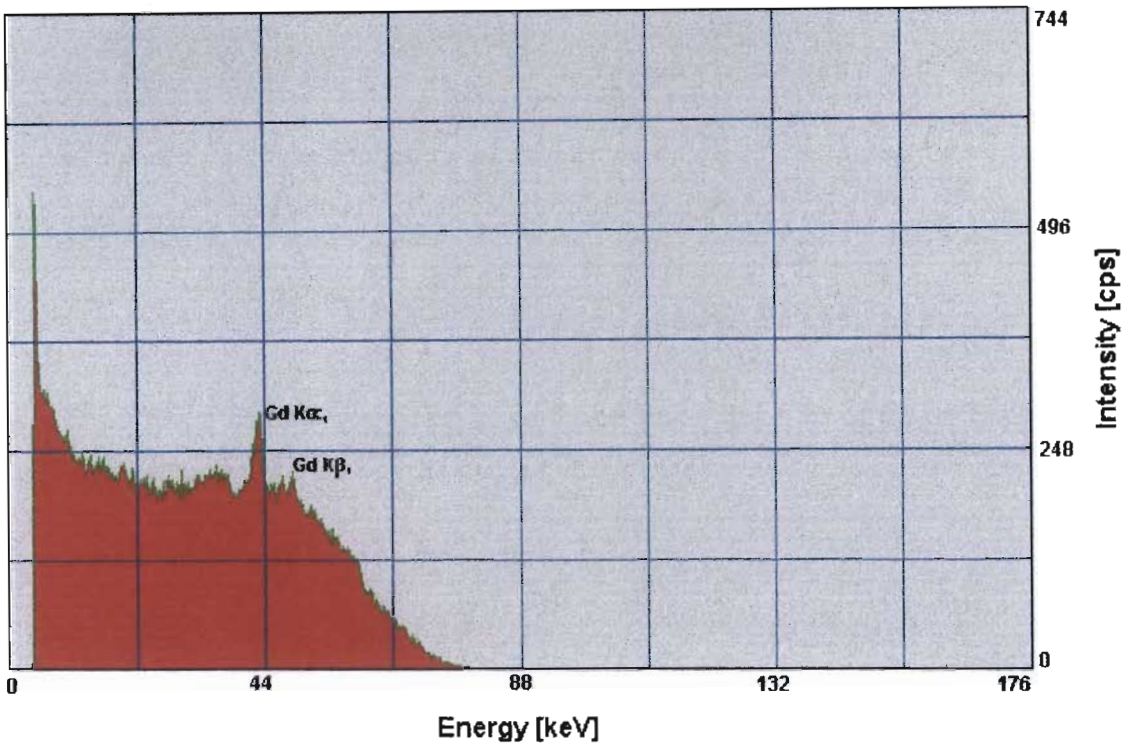

Fig. A9c: Characteristic spectra of gadolinium (Gd) obtained with the AMPTEK XR-100T-CZT cadmium zinc telluride detector.

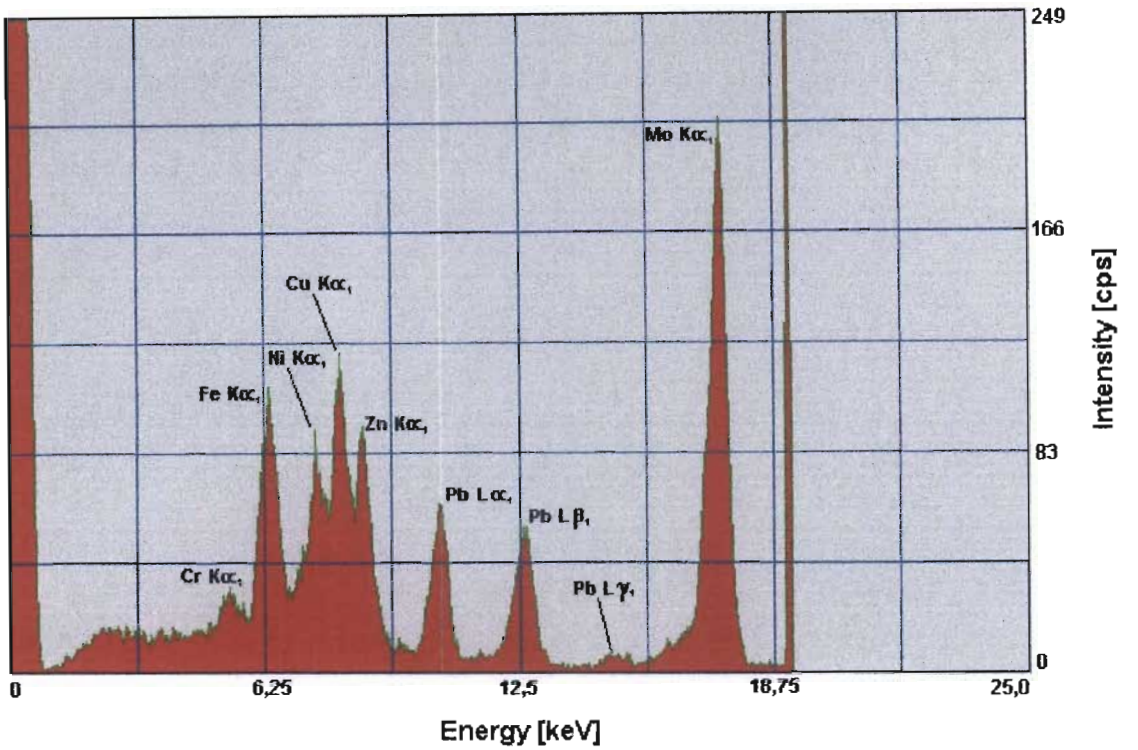

Fig. A9d: Characteristic spectra of elements chromium (Cr), iron (Fe), nickel (Ni), copper (Cu), zinc (Zn), lead (Pb) and molybdenum (Mo) obtained with the AMPTEK XR-100T silicon detector.

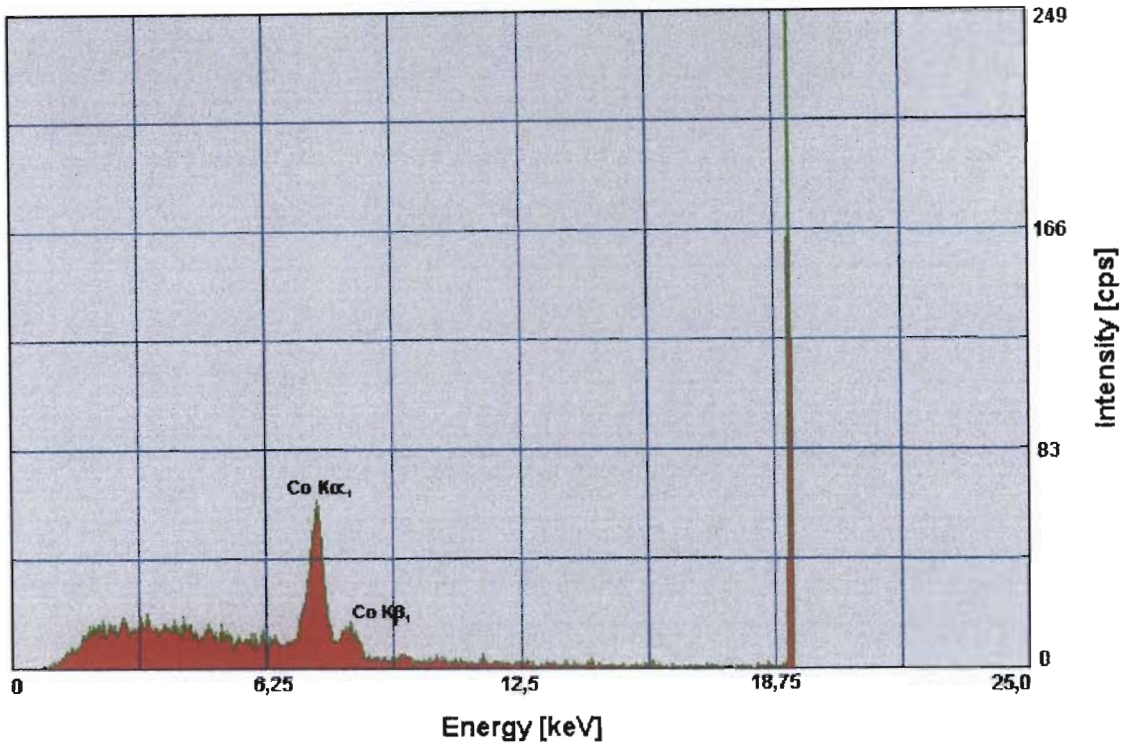

Fig. A9e: Characteristic spectra of cobalt (Co) obtained with the AMPTEK XR-100T silicon detector.

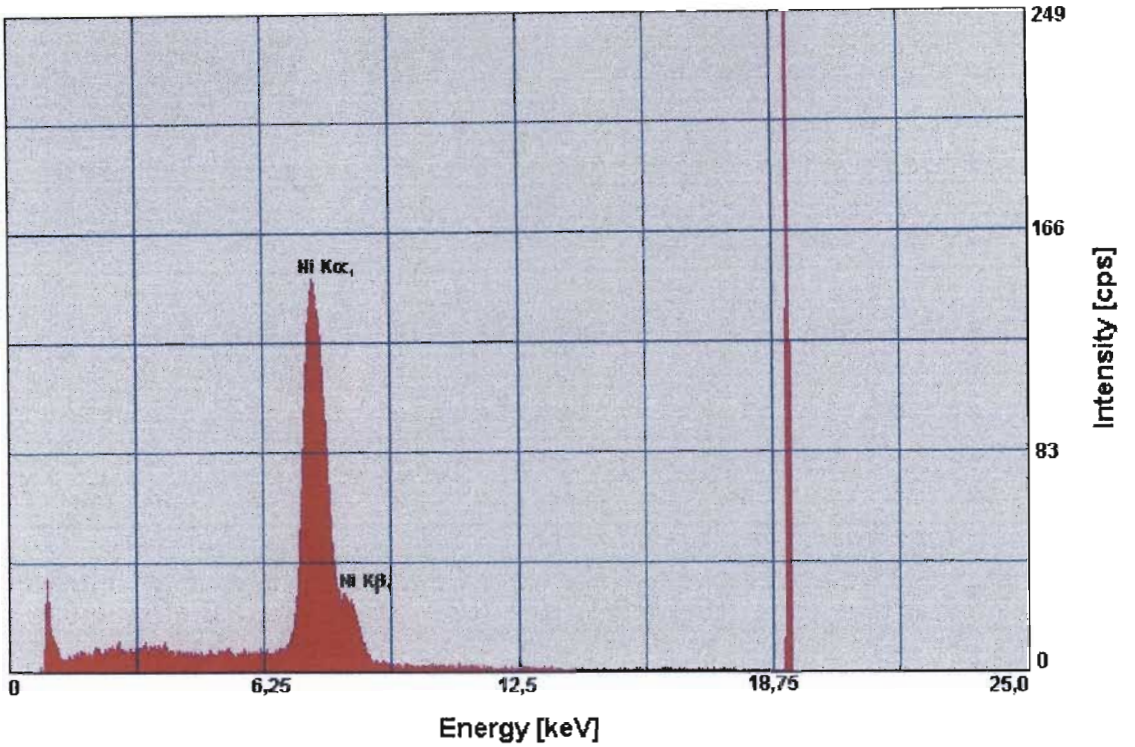

Fig. A9f: Characteristic spectra of nickel (Ni) obtained with the AMPTEK XR-100T silicon detector.

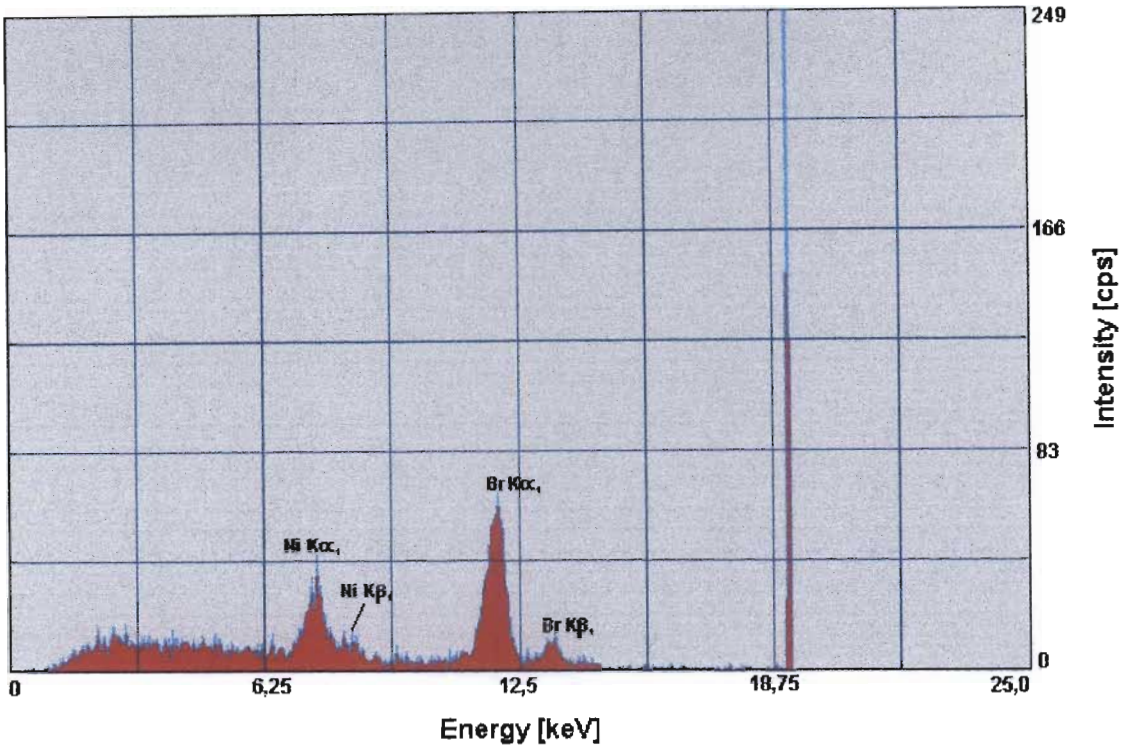

Fig. A9g: Characteristic spectra of bromine (Br) contained in $BaBr_2.2H_2O$ obtained with the AMPTEK XR-100T silicon detector. The nickel characteristic emission lines are also displayed to illustrate their position relative to the bromine characteristic emission lines.

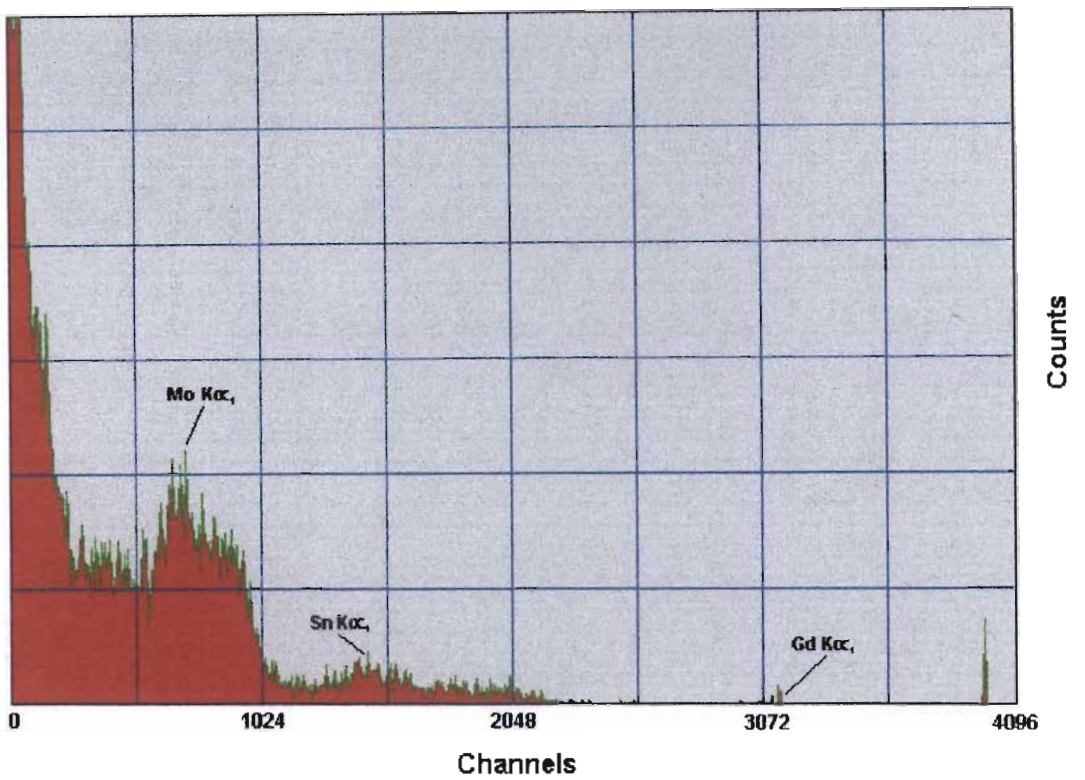

Fig. A9h: The spectra of molybdenum (Mo), tin (Sn) and gadolinium (Gd) using the AMPTEK XR-100T silicon detector.